Stretchable Kirigami devices for biological applications
（生体応用に向けた伸縮性切り紙デバイス）

January, 2020

Doctor of Philosophy (Engineering)

Yusuke Morikawa
森川　雄介

Toyohashi University of Technology

Abstract

Stretchable Kirigami devices for biological applications

Recording technologies for biological signals from the brain [Electroencephalogram (EEG), electrocorticogram (ECoG), local field potentials (LFPs), single unit activity (SUA)], heart [Electrocardiogram (ECG)] and muscle [Electromyography (EMG)] are expected to be used for the treatment of psychiatric and neurological disorders. These technologies can also be used for restoring lost functions, such as brain machine interfaces (BMI) and human–machine interfaces (HMI).

Needle-like penetrating electrodes and film-based surface electrodes are commonly used as electrode devices in *in vivo* experiments. An intimate integration between electrical devices and soft biological tissues can be achieved in case the device's mechanical characteristics (e.g. Young's modulus) are similar to those of the biological tissues in addition to the biocompatibility of the materials used in electrical devices. To this purpose, many flexible and stretchable devices have been developed. Flexible devices usually consist of polymeric materials such as polyimide, parylene, and SU-8. However, the Young's modulus of these materials, which ranges between 2.8 GPa and 5.6 GPa, is about six orders of magnitude higher than those of the biological tissues (e.g. ~1.5 kPa for the brain and 5–40 kPa for a resting muscle). In addition, the Young's moduli of the elastomer materials used in stretchable devices [e.g. ~730 kPa for polydimethylsiloxane (PDMS), ~70 kPa for Ecoflex, and ~350 kPa for poly (styrene-butadiene-styrene) (SBS)] are also large compared to those of the biological tissues. Therefore, there is a possibility that these mismatches may induce tissue damage and malfunction (e.g. ischemia, inflammation). Moreover, the mismatch of Young's modulus of about five orders of magnitude between soft elastomer materials and rigid device components (e.g. transistors and interconnections), may be the cause of failure of the device components due to the large strain applied to the stretchable device.

In this study, a low invasive neuronal interface for biological applications using the Kirigami structure is proposed. The aim is to achieve an intimate integration between electrical devices and soft biological tissues. A remarkable feature of the Kirigami

structure is its high stretchability, which includes a high strain ratio and low effective modulus. Moreover, the characteristics of the Kirigami structure can be controlled by the device design (e.g. slit length and gap of the Kirigami structure) in contrast to the characteristics of conventional stretchable devices, which are decided by the intrinsic characteristics of the materials used.

The stretchability and recording capability of the Kirigami device has been confirmed by the first experiment of the Kirigami bioprobe device. A displacement model of the Kirigami structure was derived to estimate the deformation of the Kirigami structure, which depends on the applied force (stress). In addition, the simulation of the stress distribution in a Kirigami structure has been conducted. The displacement model and the stress distribution results provide an effective and robust method of designing a Kirigami device. A Kirigami device was designed for the ECoG and ECG signal recording from the mouse brain and heart, and fabricated using a microfabrication process, which includes a parylene substrate and embedded platinum layer for electrodes and interconnections. Using the fabricated Kirigami bioprobe device, the electrical and mechanical characterizations were conducted. In the electrical characterization, the impedance of electrodes with interconnections, which was measured in saline solution, exhibited a value of ~300 kΩ. This low value was suitable for the biological signal measurements. Also, the impedance value showed stability under the device's large stretching (~500%) using the Kirigami device, which has a calculated maximum strain of 860%. In the mechanical characterization, it was confirmed that the effective modulus of the Kirigami devices (3.6–23 kPa) is comparable to the Young's modulus of soft biological tissues. The Kirigami devices also exhibited a maximum strain of 470–840% before the film breaking. In addition, the durability of the Kirigami device was also confirmed during a 4,000-cycle strain test in the durability test. The recording capability of the fabricated Kirigami device was confirmed in the ECoG signal recording under the device stretch. Moreover, its recording capability with respect to biological tissues, which shows exhibit deformation, was also confirmed in the ECG signal recording. The above experiments indicated the ability of the Kirigami device to achieve the intimate integration with biological tissues. However, the Kirigami device proposed in the first experiment caused displacement on the biological tissues, which shows their large deformation.

A donut-shaped Kirigami device was proposed to improve the device's stability on biological tissues which shows the large deformation, such as the heart and muscles. The stability of the fabricated donut-shaped Kirigami device on the deformable tissue surface was confirmed during the displacement test using deformable balloon instead of

real biological tissues. The displacement test results exhibit five–to–eight times less displacement in comparison with the displacement caused by the sheet-type Kirigami device proposed in the first experiment. The packaging process using the biocompatible and soluble material of PEG was also proposed to resolve the manipulational difficulty of the highly stretchable Kirigami device. The recording capability and the stability of the fabricated donut-shaped Kirigami device were also confirmed by the biological signal recordings from large deformable tissues, such as the mouse heart and hind limb.

Another challenge faced by the Kirigami device was the integration of its rigid components in the stretchable Kirigami structures to achieve a multifunctional device. An optoelectrical Kirigami device was proposed in the third experiment for the treatment of heart disease. The proposed device includes arrays of light emitting diodes (LED) bonded on the fabricated Kirigami film for optical stimulation and electrodes for ECG signal recording from a mouse's heart in which light-sensitive proteins expressed. No significant resistance changes of the interconnections embedded in the Kirigami structure were observed during the device stretching in its characterization. Moreover, there was no resistance change during the durability test, which included a 300–400 cycle strain test. It was also confirmed that the latch structures had enough fixation force to enable the device's fixation on the heart tissue. The LED functionality test revealed a yield of 100%. The above results successfully demonstrated a highly stretchable device suitable for cardiac tissue defibrillation using optogenetic stimulation.

In this thesis, a displacement model for the Kirigami structure was derived and the stress distribution on the Kirigami device was simulated. Thus, an effective and robust design of an electrical device using the Kirigami structure can be achieved. The remarkable stretchability, electrical and mechanical characteristics, and the stability of the Kirigami device were also confirmed. These characteristics were experimentally demonstrated by the impedance and force measurements during the Kirigami stretching, durability test, displacement of the deformable balloon, and biological signal recordings from the mouse brain, heat, and muscle. The Kirigami device exhibited a low effective modulus comparable to the Young's modulus of soft biological tissues. Such low Young's modulus was not achieved when stretchable devices based on elastomer materials were used. In addition, an integration of the Kirigami device with the rigid electrical components was also demonstrated in the applications for the heart disease treatment. These results indicate the capability of the Kirigami device as appropriate platform of low invasive neuronal interfaces. It is believed that the features of the Kirigami device can be extended to applications involving the integration of electrical components with biological tissues. Moreover, the high stretchability, stability, and unique transformation

of the Kirigami structure will expand possibilities for stretchable electronics including sensors and actuators.

生体応用に向けた伸縮性切り紙デバイス

論文要旨

脳や心臓、筋肉から計測される脳波及び皮質脳波、局所フィールド電位、スパイク、心電図、筋電図の計測は精神疾患や神経疾患の治療、また、切断患者や麻痺患者の失われた機能を補うためのブレイン･マシン･インターフェース(BMI)やヒューマン・マシン・インターフェース（HMI）への応用が期待される。

生体内計測に利用される電極デバイスとして、ニードル型の刺入電極やフィルム型の表面電極がある。生体計測に利用されるデバイスには、埋め込みによる生体への影響を抑えるため、デバイスに使用される材料の生体内の環境における安定性に加えて、機械的な特性（ヤング率など）が生体に対して近いことが望まれる。そのため、多くの柔軟性や伸縮性を有したデバイスが考案されている。しかし、ポリミドやパリレン SU-8 などのポリマー材料を利用した柔軟性デバイスのヤング率（2.8–5.6 GPa）は、柔らかい生体組織(脳: ~1.5 kPa, 筋肉: 5–40 kPa)に対して約 6 桁大きい。加えて、伸縮性デバイスに利用されるエラストマー材料のヤング率[ポリジメチルシロキサン (PDMS): ~730 kPa, Ecoflex: ~70 kPa, スチレン・ブタジエン・スチレンブロック共重合体 (SBS): ~350 kPa]も柔らかい生体に対しては十分に小さいとは言えない。この、生体とデバイスとの特性の不一致は生体への炎症や虚血といったダメージ及び機能不全を引き起こす可能性がある。また、伸縮性デバイスでは、伸縮性材料とそこに埋め込まれた配線や電子部品などとのヤング率の違いにより、デバイスの変形時にそれらの要素が破壊されるという課題がある。

そこで本研究では、生体への親和的なデバイス埋め込みを実現するための、伸縮性 Kirigami 構造を用いた低侵襲な神経インターフェースの提案を行った。Kirigami 構造の大きな特徴は、その高い伸縮性と低いヤング率である。加えて、従来の伸縮性材料を基板として用いた伸縮性デバイスの特性が材料固有の特性によって決定されていたのに対し、Kirigami 構造の特性は、そのスリットの長さや間隔などのデザインによってコントロールすることができる。

Kirigami デバイスの伸縮性及び生体信号の記録は、生体信号記録に向けた Kirigami デバイスの製作を行った最初の実験で確認された。まず、Kirigami 構造

の印加した応力に対する変形モデルの導出及び、Kirigami 構造の変形時に発生する内部応力の検証を行った。これらの結果は Kirigami 構造を用いたデバイスの設計に利用することができる。マウスの脳及び心臓からの皮質脳波及び心電図記録のための Kirigami デバイスの設計を行い、また、微細加工技術を用いてパリレンを基板に、白金を電極及び配線としたデバイスの製作を行った。この、製作した Kirigami デバイスを用いて、電気的及び機械的特性評価を行った。電気的特性評価では、生理食塩水中におけるインピーダンスの計測を行い、その結果約 300 kΩ と生体信号の記録においてインピーダンスが十分低いことが確認された。また、計算上の最大伸縮率が 860%の Kirigami デバイスを用いた場合、伸縮率が約 500%までの領域においてはインピーダンスに大きな変化は見られなかった。加えて、機械的特性評価では製作したデバイスの実効ヤング率がおよそ 3.6–23 kPa と生体のヤング率に匹敵して小さいことが確認された。また、Kirigami デバイスの伸縮率はデバイスの破断に至るまでに 470–840%を示した。耐久試験では 4,000 回の伸縮に対して破断しないことが示された。この、Kirigami デバイスを用いて実際に生体信号の記録を行った結果、デバイスの伸縮状態においてマウスの大脳皮質より皮質脳波の記録が確認できた。また、大きな変形を示す心臓からの心電図計測にも成功した。これらの特性評価及び生体信号の記録実験から、製作したデバイスを用いた生体への親和的な埋め込み及び計測への可能性が示された。しかし、一方で最初に製作した Kirigami デバイスを用いたマウスの心臓からの心電図記録実験から、大きな変形を示す生体組織に対しては、デバイスと生体との界面で滑りが生じることで、変形に十分に追従することが難しいことが分かった。

そこで、この変形する生体組織上におけるデバイスの位置ずれを低減するため、ドーナツ型の Kirigami 構造を有したデバイスの提案を行った。変形する生体上でのデバイスの安定性は、生体を模擬したバルーン上での実験により確認された。その結果、最初に提案したシート型の Kirigami デバイスに対して、ドーナツ型の Kirigami デバイスでは位置ずれをおよそ 5 分の 1 から 8 分の 1 に低減可能であることが確認された。製作したデバイスのパッケージングでは、生体適合性を持ち、水に溶けるポリエチレングリコールを用いて、Kirigami デバイスの動物実験中における取り扱いの難しさを改善した。また、製作したドーナツ型の Kirigami デバイスを用いて、マウスの心臓及び、後脚からの信号計測を行い、デバイスの生体信号計測及び変形する生体上における安定性の検証を行った。

3 つ目の実験では多機能デバイスを実現するための、Kirigami デバイスへの電子部品の実装を用いたデバイスの製作を行った。ここでは、光感受性を有するタンパク質を発現させたマウスの心臓に対して、発作を抑制するための光刺激を行う LED 及び、発作を検出するための心電図計測用電極を有した伸縮性

Kirigami デバイスを提案した。評価用のデバイスを使用した特性評価では、伸縮時における抵抗変化がほぼないことが確認され、また 300〜400 回の繰り返し伸縮時においても大きな変化は見られなかった。また、デバイスを心臓に固定するために設計したラッチ構造が、十分な強度を有していることも確認された。フリップチップボンディングにより Kirigami デバイス上に実装された LED の評価では、実装されたすべての LED が正常に動作することが確認された。これらの結果から、心臓の除細動に用いる光刺激のための LED を実装したデバイスが実現できたことが確認された。

以上のように、本研究では Kirigami 構造を用いたデバイスの設計を行うための、Kirigami 構造の変位モデル及び、構造内での応力の検証を行った。Kirigami 構造の伸縮性及び、電気的・機械的特性、安定性は伸縮時におけるインピーダンス測定及び、フォース計測、変形するバルーン上での位置ずれ試験、そしてマウスの脳、心臓、筋肉からの信号計測により確認された。Kirigami デバイスは従来の伸縮性材料を基板とした伸縮性デバイスでは実現することのできなかった、生体組織に匹敵するヤング率を実現した。加えて、硬い電子部品との一体化も可能であることが心臓発作の抑制を目的とした光刺激デバイスの製作から確認された。これらの結果から、Kirigami 構造が生体への親和的なデバイスの埋め込みを実現するための、プラットフォームとしての可能性を示すことができた。Kirigami デバイスのこれまでにない特徴が、生体への応用に向けたデバイスの可能性を広げ、発展させることが期待される。また、Kirigami 構造の高い伸縮性及び、安定性、独自の三次元的な変形はセンサやアクチュエータをなどの伸縮性エレクトロニクス分野全体へと応用することが可能である。

CONTENTS

Chapter 1: General introduction *1*

1.1 Introduction 1

1.2 Electrodes for *in vivo* biological signal recording 3

1.3 Stretchable devices 7

1.3.1 Stretchable electrode materials 7

1.3.2 Stretchable devices for biological applications 11

1.4 Objective of the present study and organization of the thesis 14

Chapter 2: Kirigami structure *17*

2.1 Introduction 17

2.2 Displacement model for the Kirigami structure 21

2.2.1 Displacement model for the single layered Kirigami structure 22

2.2.2 Displacement model for the multi-layered Kirigami structure 24

2.3 Simulation of the displacement and stress distribution in the Kirigami structure 31

2.3.1 Simulation of the displacement of the Kirigami structure 31

2.3.2 Simulation of the stress distribution in the Kirigami structure 31

2.4 Kirigami film 34

2.5 Conclusions 38

Chapter 3: Kirigami bioprobe device *39*

3.1 Introduction 39

3.2 Design and fabrication of the Kirigami device 39

3.2.1 Design of the Kirigami device 40

3.2.2 Device fabrication 43

3.2.3 Bi-axially stretchable Kirigami bioprobe device 45

3.3 Electrical and mechanical characterization of Kirigami device 47

3.3.1 Impedance characteristics of a Kirigami device 47

3.3.2 Stress–strain curve of the Kirigami device 49

3.3.3 Durability test of the Kirigami structure 52

3.3.4 Stretchability of the Kirigami structure in another layer 56

3.4 Biological signal recording using a Kirigami bioprobe device 59

3.4.1 *In vivo* ECoG signal recording 59

3.4.2 *In vivo* ECG signal recording 63

3.5 Conclusions 66

Chapter 4: Donut-shaped Kirigami device 69

4.1 Introduction 69

4.2 Mechanical properties of the donut-shaped Kirigami structure 71

4.3 Design and fabrication of the donut-shaped Kirigami device 73

4.3.1 Design of the donut-shaped Kirigami device 73

4.3.2 Fabrication of a donut-shaped Kirigami bioprobe device 75

4.4 Characterization of the donut-shaped Kirigami device 78

4.4.1 Electrical characterization of the donut-shaped Kirigami device 78

4.4.2 Displacement test of the donut Kirigami device 80

4.5 Device packaging using PEG scaffold 84

4.6 Biological signal recording using donut-shaped Kirigami bioprobe devices 88

4.6.1 *In vivo* ECG signal recording 88

4.6.2 *In vivo* EMG signal recording 89

4.7 Conclusions 96

Chapter 5: Optoelectrical Kirigami device 98

5.1 Introduction 98

5.2 Design and fabrication of the stretchable optoelectrical Kirigami device 99

5.2.1 Design of the stretchable optoelectrical Kirigami device 100

5.2.2 Device fabrication 101

5.3 Device characterization 106

5.3.1 Resistance of the interconnection embedded in the Kirigami structure 106

5.3.2 Durability of the Kirigami structure 113

5.3.3 Fixation strength of the latch structure 116

5.3.4 LED functionality test 124

5.4 Conclusions 125

Chapter 6: General conclusions and future prospects 126

6.1 Conclusions 126

6.2 Future prospects 128

References *131*

Acknowledgments *145*

List of Publications and Awards *147*

Appendix A *149*

Chapter 1: General introduction

1.1 Introduction

Recording technologies for biological signals from the brain [Electroencephalogram (EEG), electrocorticogram (ECoG), local field potentials (LFPs), single unit activity (SUA)], heart [Electrocardiogram (ECG)] and muscle [Electromyography (EMG)] are expected to be used for the treatment of psychiatric and neurological disorders. These technologies can also be used for restoring lost function[1], [2] Brain machine interface (BMI), brain computer interface (BCI) and human–machine interface (HMI) provide appropriate means to restore the lost functions of severely disabled people who are amputated or paralyzed by neurological neuromuscular disorders, such as amyotrophic lateral sclerosis, brain stem stroke, or spinal cord injury [3]–[9]. BCI and BMI connect the living brain to a computer or to artificial actuators, such as the prosthesis and robot arm, and enable humans to control them directly by electrical signals from brain (Figs. 1.1.1a, b). Another approach to compensate for the lost of functions is the HMI based on the EMG signals (Fig. 1.1.1c) [8], [10]–[12]. In the HMI, a hand prosthesis is controlled by the EMG signals extracted from the residual upper extremity muscle of the amputee. In addition, signal recording and electrical stimulation of the brain can be used for diagnosis and treatment of brain diseases, such as epilepsy, depression and Parkinson's disease [13]–[17]. They are also applicable to the rehabilitation of paralyzed patients [18], [19] (Fig. 1.1.1d). ECG signals allow the detection of heart arrhythmia, which is the major cause of sudden death. Electrical, ultrasound and optical stimulation methods offer defibrillation [20]–[24] (Fig. 1.1.1e).

Biological signals can be recorded using non-invasive and invasive technologies. Non-invasive technologies include functional magnetic resonance imaging (fMRI), positron emission tomography (PET), EEG, near-infrared spectroscopy, and magneto-encephalography (MEG). On the other hand, ECoG, LFP and spikes as well as optical images of cells/neurons can be detected using invasive technologies (Fig. 1.1.2). Applications, such as BMI, BCI, and HMI require the high spatial and temporal resolution of the recorded biological signals using multi-functions. The brain consists of the

fundamental computational unit of cortical minicolumn (~50 μm) which is vertical column through the cortical layers of the brain. Minicolumns comprise perhaps 80–120 neurons and these neurons have similar features [25], [26]. On the other hand, a motor unit innervate dozen to hundreds of muscle fibers depending on the size of muscle. The territory of the motor unit is 5–10 mm in large human muscle (e.g. tibialis anterior muscle

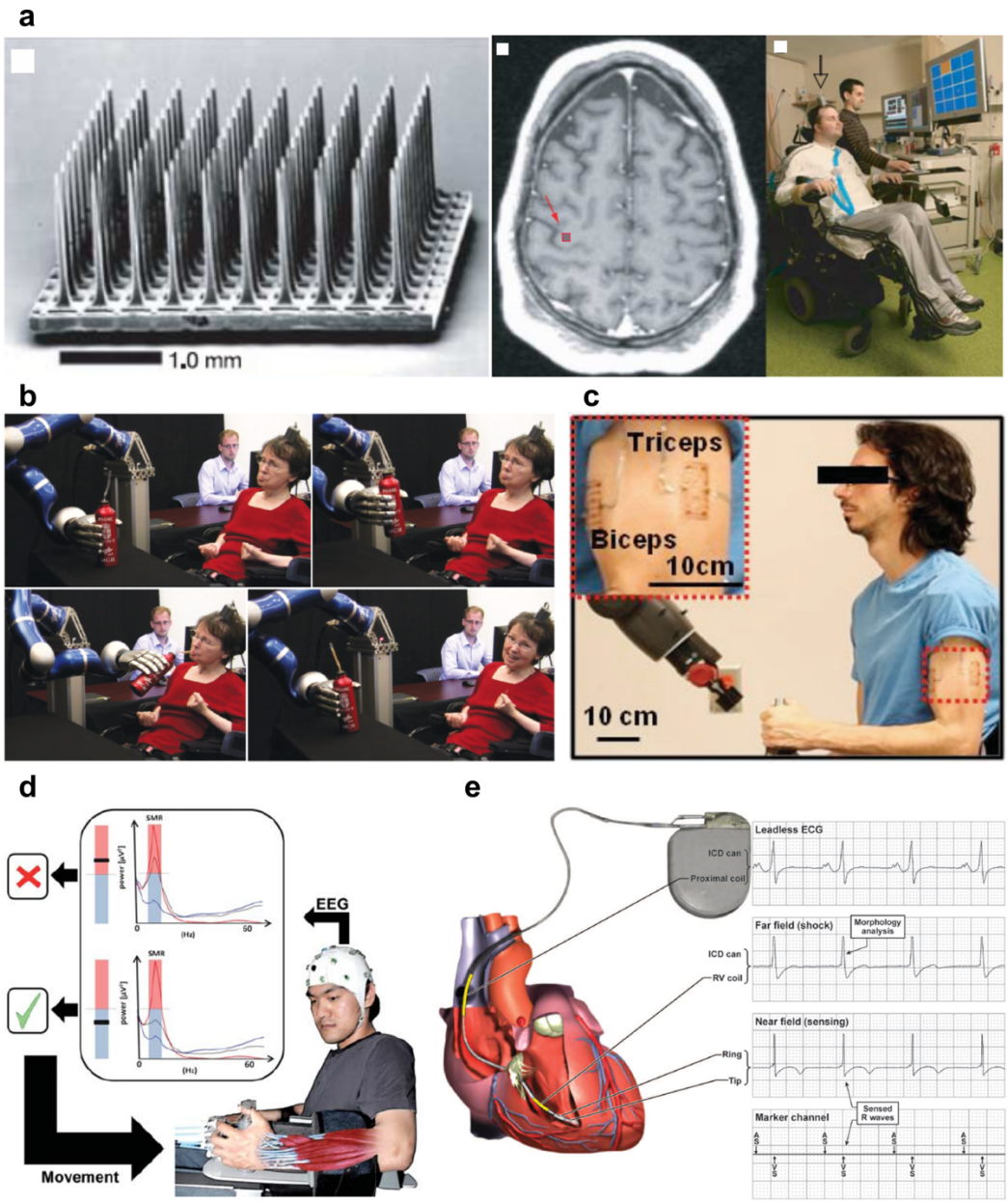

Figure 1.1.1 Applications using biological signals. (a) Brain computer interface based on neuronal signals [6]. (b) Brain machine interface based on neuronal signals [7]. (c) Human–machine interface based on EMG [8]. (d) Rehabilitation using EEG signal [19]. (e) Implanted cardioverter [20].

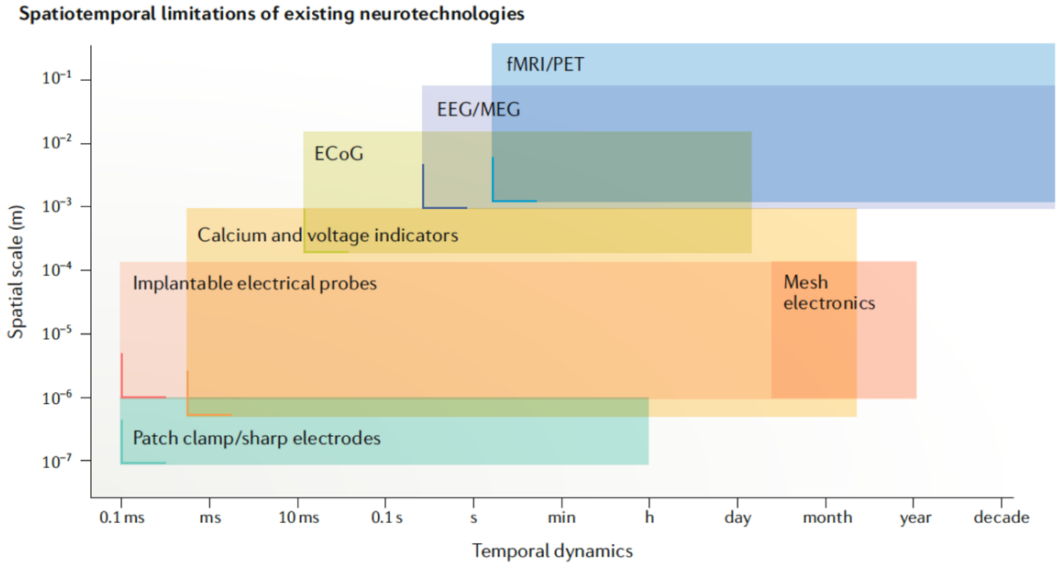

Figure 1.1.2 Spatial and temporal resolution of several recording technologies [2].

consists of 200–300 muscle fibers [27], [28]). However, the separation of these signals from the minicolumn or motor unit is difficult using the signals recorded via surface electrodes [e.g. EEG, surface EMG (sEMG)]. Invasive *in vivo* electrodes offer more accurate and highly resolved spatiotemporal signals compared with those placed outside the tissues [e.g. EEG, sEMG]. The major *in vivo* electrode devices are presented in the next section.

1.2 Electrodes for *in vivo* biological signal recording

The nervous system consists of billions of neurons. Each neuron constantly generates and transmits electro-physiological signals. Therefore, it is required to record spatiotemporally resolved activities of neurons to understand the functions of the brain. Needle- and film-types recording sites are commonly used [29]–[31] as electrode devices for *in vivo* experiments.

Penetrating needle electrodes allow the detection of two different voltage signals of different frequency bands coming from the extra-cellular space. The signals in the low frequency band are LFPs (typically <100 Hz), which present the summed and synchronous electrical activity of multiple neurons. The signals in the high frequency band are action potentials (>250 Hz) of individual neurons and are also known as "spikes". These different types of signals can be separated by applying analogue or digital filtering. A primitive silicon (Si) microneedle electrode array (10 × 10) [29] is presented in Figure 1.2.1a. This type of electrode array has the recording sites only at the tip of each silicon shank. It is called Utah-type microelectrode array. The Michigan-type

microelectrode array, which has the recording sites along the length of each silicon shank [30] is shown in Figure 1.2.1b. The latest high-density Michigan-type microelectrode array is shown Figure 1.2.1c. This array has 960 recording electrodes with multiplexing circuits with 10 mm long and 70 μm wide electrode shanks [32]. As mentioned above, needle electrodes allow the recording of multi-type neuronal signals at high spatial resolution. However, the invasiveness of the needle electrode, which is caused by the device placement into the brain tissue and the mechanical mismatch between the device stiffness and that of the soft tissues, induces the chronic immune response [33]. The response involves the formation of insulating glial scar around the neuronal interface and deteriorate the recording performance. Long-term stability of the neuronal recording is required to enable chronic applications such as BMI and HMI in addition to the spatiotemporal resolution of the recorded signals. The biocompatibility of the neuronal interface includes the chemical compatibility and the mechanical compatibility [34]. Neuronal interface usually consists of the biocompatible materials such as the silicon and noble metals [e.g. gold (Au), platinum (Pt), and iridium] [35], [36]. In addition, surface modification is also use to reduce the immune response [37], [38]. In terms of the mechanical properties of the neuronal interface, biocompatibility achieved by the smaller feature of the implant device and the lower Young's modulus of the materials used in the device. The mechanical wear at the interface between the neuronal implant and tissue is occurred during the constant bodily motion and tissue deformation. The small Young's modulus of the implant device reduce the immune response [36], [39], [40].

As approaches to reduce the invasiveness of the needle electrode in terms of its mechanical characteristics, fine and flexible needles and mesh electrodes are proposed [41]–[45]. A very fine Si microneedle (~5 μm) fabricated using the vapor–liquid–solid (VLS) growth process [41] is shown in Figure 1.2.1d. The high aspect ratio and very fine cone shape of the Si needle enhance its flexibility. Thus, the invasiveness of this probe is reduced [46]. The ultra-flexible nano-electronic thread (NET) electrode [42] is shown in Figure 1.2.1e. This NET electrode exhibits stable signal detection during a long-term implantation without glial scars, which is the maker of the occurred injury to the nervous system. A mesh electronic neural probe with a bending stiffness comparable to the soft brain tissue is shown in Figure 1.2.1f. Its mesh structure with >90% 3D macro-porosity enables inter-penetration of the neurite [47]. The recording capability of multiplexed LFPs and action potentials of a mesh probe is stable for up to ~1 year without a chronic immune response, as demonstrated in [47].

Another way to reduce the chronic immune response caused by the device implantation is the use of film surface electrodes. The common film electrode is able to

detect the ECoG signals, which are recorded from the surface of the cerebral cortex and present the activity of multiple neurons, as well as LFPs recorded using the needle penetrating electrodes. Although the quality of the signals recorded from the brain surface is inferior to that of the signals recorded in the brain tissue using a penetrating electrode, the invasiveness of electrode placed on the brain surface is reduced compared to that of penetrating electrodes, which cause damage to the brain and recording instability. A ultra-thin film electrode device [31] is shown in Figure 1.2.1g. In this report, a ultra-thin film (2.5 μm) and a mesh film supported by bioresorbable substrates of silk fibroin apply minimal stresses on the tissue and enable highly conformal coverage for complex curvilinear surfaces. Because of these ultra-thin film device features, the electrodes embedded in the film device exhibit good contact to the biological tissues and the recorded signals have a high amplitude ratio. A film electrode device with a dense electrode array of 360 channels for sampling large areas of the brain with high special resolution [48] is shown in Figure 1.2.1h. Each electrode needs to be wired individually to form the large electrode array. In this report, the ultra-thin and flexible silicon nano-membrane transistors are transferred and integrated in the electrode array. The electrodes are connected with fewer wires using a multiplexer. Figure 1.2.1i shows the organic material-based, ultra-conformable, biocompatible scalable neural interface array [49]. Although the relatively large electrodes (300 μm × 300 μm) [48] impede the recordings of the single-unit action potentials (spikes) from individual neurons in the general film surface electrodes, this device enables the recordings of the LFPs and spikes from the brain surface using small electrodes (10 μm × 10 μm) without penetrating the brain tissue. A small electrode can be achieved using a conductive polymer of poly(3,4-ethylenedioxythiophene) doped with poly(styrenesulfonate) (PEDOT:PSS) as the interface material. PEDOT:PSS has the high conductivity due to its mixed electronic and ionic conductivity, and high ionic mobility. The high conductivity of the PEDOT:PSS achieve a small impedance magnitude of the small electrode. The film surface electrodes with the low invasiveness and high spatiotemporal resolution can be used for applications regarding the understanding of physiologic and pathologic network activity, control of BMI, diagnosis, and therapy for brain disorders.

Although the flexible devices have lower Young's modulus than the stiff implants consist of silicon and metal, flexible devices still may induce tissue response. Because of the stiffness and Young's modulus of flexible devices and materials used in the devices are not comparable to the stiffness and Young's modulus of the biological tissues. Flexible devices usually consist of polymeric materials, such as polyimide, parylene, and SU-8. The Young's modulus of these materials is in the range 2.8–5.6 GPa

[50]–[52], which is about six orders of magnitude higher than that of the biological tissues (e.g. ~1.5 kPa for the brain and 5–40 kPa for a resting muscle) [53], [54]. These mismatches have the possibility of inducing tissue damage and malfunction (e.g. ischemia,

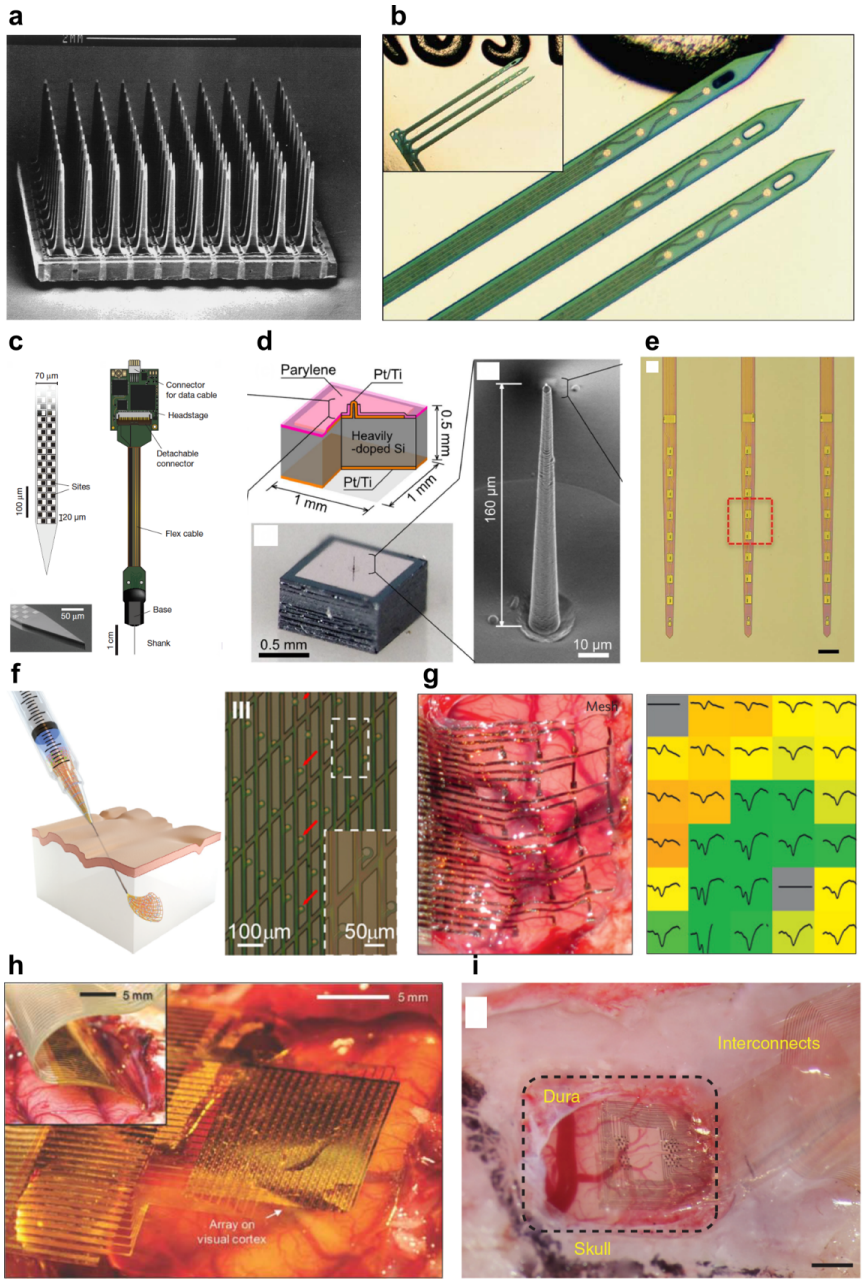

Figure 1.2.1 Electrodes for biological signal recording. (a) Utah array [29]. (b) Michigan probe [30]. (c) Neuropixels [32]. (d) Very fine Si microwire electrode [41]. (e) Ultraflexible nanoelectronic thread (NET) electrode [42]. (f) Mesh electronic neural probe [43], [45]. (g) Ultra-thin film electrode device [31]. (h) High-density electrode array film with multiplexer [48]. (i) Organic material-based, ultra-conformable, biocompatible, and scalable neural interface array [49].

inflammation). The mechanical properties of the neuronal interface should be close to the biological tissues as much as possible [55], [56]. In addition, the huge mismatch of the Young's modulus causes the malfunctions of organs especially for the target tissues or organs have the deformation, such as intracranial pressure, beating, and muscle deformation [57]. Moreover, the device delamination and the displacement of the electrode from the recording point may also cause problems. Device failure may be also induced by device strain of the order of ~1% because of the delamination of the metal layer from the device substrate [58]. Therefore, to record the signals from such deformable tissues, stretchability of the device is also required [59], [60]. According to the literature, the device used on the skin surface requires 100% of the device's strain [61]. In some diseases, the brain expands by ~300% and a high strain is also needed to achieve long term signal recordings in such applications [62], [63].

1.3 Stretchable devices

High stretchability and deformability are promising properties for expanding the applications of flexible film electronics not only to neuronal recording, but also to sensors, actuators, and energy harvesters [64]–[66]. In biological applications, stretchability provides intimate device integration with the biological tissues and device durability. Stretchable devices usually consist of stretchable materials such as polydimethylsiloxane (PDMS), polyurethane (PU), and Ecoflex. These stretchable materials have a Young's modulus of in the range 70–730 kPa, which is about four or five orders of magnitude smaller than that of the polymeric materials. Flexible electrode devices usually consist of flexible polymeric materials and thin film rigid metal materials for the electrode and interconnections. On the other hand, stretchability is required for both the device substrate and the electrode in stretchable devices.

1.3.1 Stretchable electrode materials

Design approaches based on structural stretchable layout and stretchable electrode materials are used to achieve stretchable electrodes. Structural stretchable layouts include the wavy structure, random networks, two-dimensional serpentine interconnections, three-dimensional coiled structures, and nanomeshes [67]. The bi-axially stretchable silicon nanomembrane using the single crystalline silicon with the wavy structure bonded on elastomeric supports [68] is shown in Figure 1.3.1a. The fabrication process of the silicon wavy structure includes the bonding of silicon nanomembrane onto the pre-strain elastomer substrate, followed by the release of the substrate pre-strain. The wavy structure is spontaneously formed during the release of the substrate pre-strain. In this study, the

bi-axially stretchability can be achieved by the two-dimensional pre-strain of the elastomer substrate. This wavy structure can be also achieved by the use of silver nanowires (AgNWs) materials bonded onto the pre-strain silicone substrate [69]. The wavy structure, which is based on a stretchable conductor using AgNWs, exhibits a strain of over 460% without significant resistance increase. The maximum strain within the constant resistance depends on the pre-strain of the device substrate.

The networks of the AgNWs are shown in Figure 1.3.1b. The stretchable electrodes utilizing the networks of metal nanowires are fabricated by embedding randomly distributed metal nanowires under the cured elastic substrates [70]. The details of the fabrication steps are shown in Figure 1.3.1b. Initially, the solution containing AgNWs is casted on the Si wafer. ~1 μm of the film of the AgNWs is deposited on the Si wafer after the solution has been dried. Next, liquid PDMS is coated over the AgNWs film and the AgNWs are embedded in the PDMS. Finally, the stretchable conductor is released from the Si substrate after curing the PDMS. This stretchable conductor exhibits stable electrical characteristic in the strain range 0–50%.

The two-dimensional serpentine interconnects of gold nanowires bonded onto the elastomer [71] are shown in Figure 1.3.1c. The thin metal film is patterned to the serpentine configuration with the specific amplitude–wavelength ratio before embedding to the PDMS. This shape effectively enhances the stretchability of the metal film. The stretchability of the serpentine interconnections depends on the amplitude–wavelength ratio. A large amplitude–wavelength ratio causes high stretchability. Serpentine interconnections with an amplitude–wavelength ratio equal to 0.5 exhibit a strain of 14.2% without interconnections fracturing. In contrast, straight Au nanowires embedded in the PDMS substrate exhibit a fracture when the strain is 2.4%. The maximum serpentine interconnections strain is further improved to 27.2% with an amplitude–wavelength ratio of 1.

Three-dimensional coiled structures consisted of silicon nanowires (SiNWs) on a PDMS substrate [72] are shown in Figure 1.3.1d. Compared to the 2D serpentine interconnections the 3D coiled structure can dramatically improve stretchability because the 3D coiled structure contributes to the prevention of stress concentration in the conductive layer, while the structure is stretched. The coiled structure is fabricated by a controlled buckling process on the elastomeric substrate. SiNWs are transferred onto the ultraviolet/ozone (UVO)-treated PDMS substrate with pre-strain in this buckling process. SiNWs are buckled and formed into the coiled structure when the pre-strain of the PDMS substrate is released. The buckling mode of the SiNWs including the in-plane wavy mode and the three-dimensional coiled mode depend on the UVO-treatment time. The coiled

nanowire exhibits high stretchability up to the failure strain of the PDMS (104%). The single coiled NW exhibits a nearly constant electrical response in a large strain range.

A stretchable Au nanomesh electrode with a PDMS substrate [73] is shown in Figure 1.3.1e. The Au nanomesh is fabricated by the grain-boundary lithography, which involves a bi-layer lift-off metallization process. The grain-boundary lithography use of the bi-layer consists of an indium (III) oxide (In_2O_3) mask layer and a SiO_x sacrificial layer for undercut formation. Initially, the SiO_x layer and the In layer with grains are deposited on the Si wafer. The In_2O_3 mask for the undercut of the SiO_x serves as the formation of the gap between each In grain using nitric acid (HNO_3) etching and thermal oxidation of the In layer. After the undercut of the SiO_x layer, the Au layer is deposited and structured as an Au nanomesh by the lift-off of the the In_2O_3 and SiO_x bi-layer. The Au nanomesh exhibits a stretchability of 160% and the moderate conductivity changes with a one-time strain or after a 1000-cycle strain. However, the stretching mechanism of the nanomesh structure is similar to that of the networks of metal nanowires; in general, the stretchability of the nanomesh is higher than that of metal nanowires. The high stretchability of the nanomesh is caused by the instability and out-of-plane deflection of the stretched nanomesh, while the substrate stabilizes the rupture of Au wires and forms the distributed slits. The stretchability of the nanomesh can be controlled by the mesh size and the wire width.

Novel carbon-based nanomaterials such as carbon nanotubes (CNT), graphene, and their composites as well as materials made using special processing techniques serve as stretchable electrode materials [74]–[77]. The features of the carbon-based electrode materials include their superior mechanical characteristics and relatively lower practical electrical conductivity compared to the traditional thin film metal. In addition, these nanomaterials can be dissolved on solvents due to their small size and fabricated using lower-cost solution processes, such as printing technologies. For comparison, the conventional electrode is made by a metal film, which requires high temperature, vacuum deposition, and chemical etching processing. Stretchable wavy ribbons of CNTs embedded in the elastomer films [74] are shown in Figure 1.3.1f. The CNT ribbons are directly drawn from the spinnable vertically grown multiwalled CNT forests and attached to the Teflon substrate and coated by the thin layer of the sputtered Au/palladium for reduction of the resistance. The CNTs are uniformly aligned along the drawing direction. The CNTs ribbon attached to the Teflon substrate is transferred onto the PDMS film with pre-strain. After the brief contact, the Teflon substrate is peeled off from the PDMS film and only the CNTs ribbon remains on the PDMS because of the difference of the adhesiveness between PDMS and Teflon. The CNT ribbon exhibits out-of-plane buckling

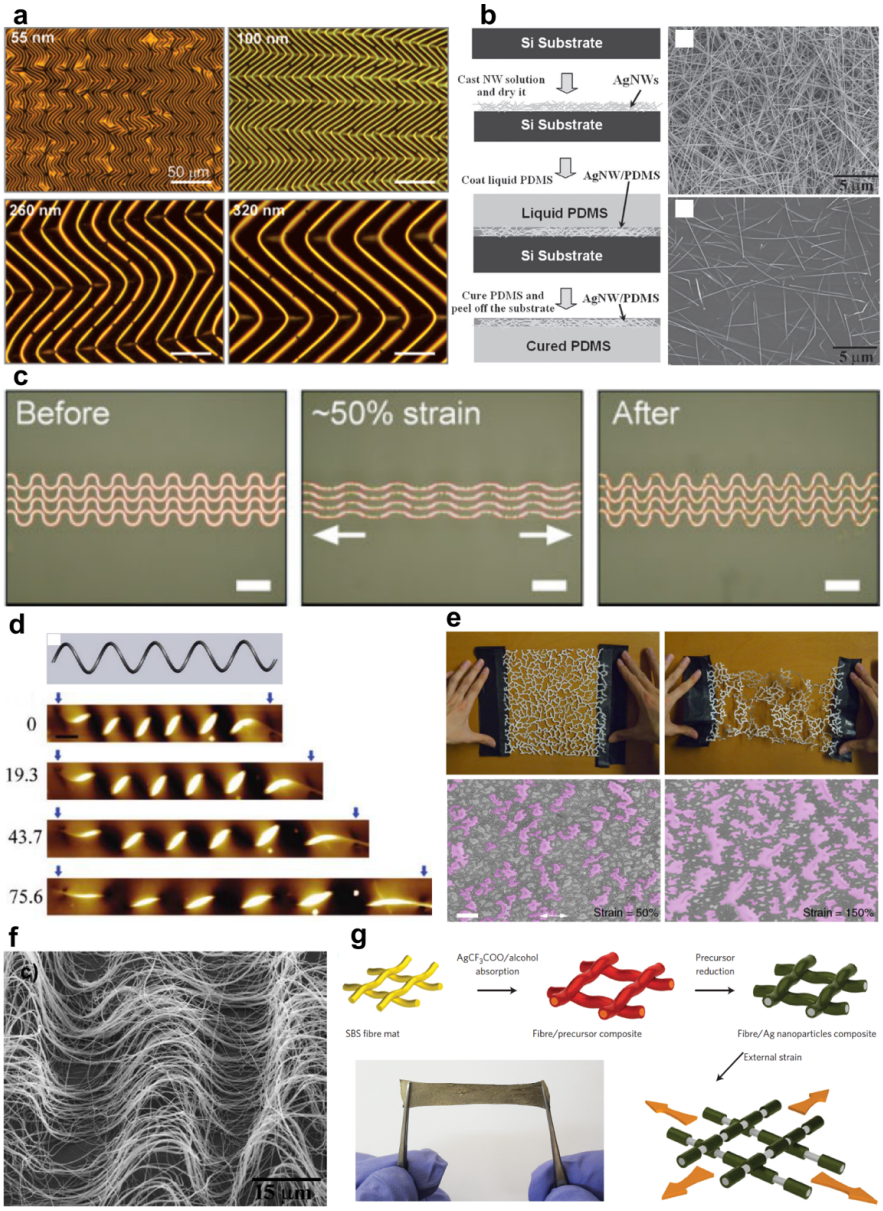

Figure 1.3.1 Stretchable electrode materials (a) Bi-axially stretchable silicon nanomembrane with a wavy structure [68]. (b) Percolating AgNWs networks [70]. (c) Two-dimensional serpentine interconnects of gold nanowires bonded onto the elastomer [71]. (d) Three-dimensional coiled structures consisted of SiNWs on a PDMS substrate [72]. (e) Au nanomesh electrode with PDMS substrate [73]. (f) Wavy ribbons of CNTs embedded in the elastomer films [74]. (g) Composite material of silver nanoparticles and elastomeric fibres [78].

after the release of the pre-strain of the PDMS film. The wavy CNT exhibits a stretchability of 100% with a resistance increase of only about ~4%.

The conductivity of the stretchable electrode can be improved by special processing techniques, which include chemical modifications and distinct additions. This approach is applicable to low-aspect-ratio materials such as metal nanoparticles, metal nanosheets, or conductive polymers, which are different from novel nanomaterials with a high aspect ratio, such as AgNWs or CNTs. Low-aspect-ratio materials have a relatively high resistance compared to AgNWs or CNTs because of the high contact resistance and charge-carrier scattering, and their resistance is not stable under strain. The combination of these low-aspect-ratio materials and special processing techniques improve the electrical characteristics under strain. Stretchable electrode materials using special processing techniques of silver nanoparticles composite materials and elastomeric fibers [78] are shown in Figure 1.3.1g. The composite material is fabricated by the dip coating and reduction process using an electrospun poly (styrene-butadiene-styrene) (SBS) rubber fiber and a silver precursor solution [silver trifluoroacetate in ethanol]. Initially, the rubber fiber is dipped into the silver precursor solution and the solution is absorbed by the fiber. After the absorbed solution has dried, the silver precursor is reduced by a solution of hydrazine hydrate and silver nanoparticles are generated inside the surfaces of the fibers. The composite material exhibits a stretchability similar to that of the elastomer fiber of the SBS. The conductivity of the composite material depends on the fiber thickness, while the material stretches. The higher thickness exhibits more stability with the material strain. The composite material with a fiber thickness of 150 μm exhibits a conductivity of 5400 S cm^{-1} without strain. The conductivity reduces to 610 S cm^{-1} under a 140% strain. Under large strain, the silver shell generated on the surface of the fiber breaks into small pieces. However, the silver nanoparticles percolated inside the fiber preserve their conductivity. Stretchable devices for biological applications, which consists of these stretchable conductors are described in the next section.

1.3.2 Stretchable devices for biological applications

Stretchable electrode materials are applicable to signal recording devices for biological tissues including brain, muscle, heart, and spinal cord [21], [56], [60], [79], [80]. A stretchable ECoG electrode device using a wavy Au nanobelt structure [60] is shown in Figure 1.3.2a. The wavy structure of the suspended Au-electrode is fabricated by transformed gold nanobelts deposited on the thin PDMS film onto the out-of-plane tripod PDMS structure with pre-strain. After releasing pre-strain, the Au nanobelts form the suspended wavy structure on the tripod PDMS film. In this structure, the Au nanobelt is not directly attached to the tripod PDMS film. Therefore, the stress concentration in the conductive metal, which is caused by the mismatch of the mechanical characteristics

between the rigid metal and the soft elastomer materials, can be avoided. The fabricated Au nanobelt exhibits a high stretchability of 130%. A 10,000-cycle strain can be applied without significant change in the conductivity. In this report, the recording capability of the fabricated Au nanobelt electrode was demonstrated during an *in vivo* recording from the surface of a rat's cerebral cortex to monitor intracranial EEG or ECoG. An integrated stretchable microelectrode array (isMEA) device for the interface of neural and muscular surface [79] based on the PDMS is shown in Figure 1.3.2b. The high-density packaging process of the stretchable device using the rigid circuit is difficult compared to the conventional unstretchable film devices. In this report, the isMEA was fabricated and directly integrated within a printed circuit board (PCB) during the device fabrication process. This fabrication process was achieved by embedding the PCB in the uncured PDMS film followed by metallization to configure the electrode and obtain the connection between electrodes and contact pads of the PCB. The recording capability of the device was demonstrated using dissociated neuronal culture grew on the MEA surface and cat's muscle. A multifunctional 3D elastic membrane-shaped device for cardiac measurements and stimulations across the entire epicardium [21] is shown in Figure 1.3.2c. The conventional 2D sheet cannot cover the whole area of the target tissue and the remain of the reliable contact between the electrode or other devices and the tissue surface without using sutures or adhesives. The 3D elastic membrane, which has a shape that matches the epicardium of the heart, achieves the conformal integration of the electronic and optoelectronic components to the surface of the heart by completely enveloping the heart. The 3D multifunctional device was fabricated using a 3D printing model as a substrate for mounting of electronic and optoelectronic components which are separately prefabricated on planar substrates. The 3D heart model with the multifunctional components is coated by the elastomer and the overall format of the device is defined. The stretchable interconnections, which connect the device components, are implemented using serpentine mesh. The recording capability and other functions are confirmed using the rabbit heart in an *ex vivo* experiment. Stretchable and implantable devices for the measurements and stimulations for the spinal cord and sciatic nerve [56], [80] are shown in Figures 1.3.2d and e. The device shown in Figure 1.3.2d is the wireless optical stimulation system. A LED used for optical stimulation is integrated in the elastomeric substrate using stretchable serpentine Ti/Au electrical interconnects. The device shown in Figure 1.3.2e is the electronic dura mater, which has electrodes and a fluid channel for the drug delivery system. The stretchable interconnections and electrodes consist of micro-cracked gold film and platinum-silicone composite, respectively. These soft and thin devices reduce the device invasiveness and their

capability of chronic applications is confirmed by histological tests.

These stretchable electrode materials (Fig. 1.3.1) and devices (Fig. 1.3.2) usually employ elastomer materials (PDMS, Ecoflex, and SBS) as the substrate or supporting layer. These stretchable conductive materials and the devices employing these materials have a great potential for applications related to deformable 3D-shaped soft biological tissues and organs. However, the Young's modulus of such elastomer materials (~730 kPa for PDMS [81], ~70 kPa for Ecoflex [82], and ~350 kPa for SBS [83]) are large compared to the Young's modulus of biological tissues. These tissues have relatively small Young's

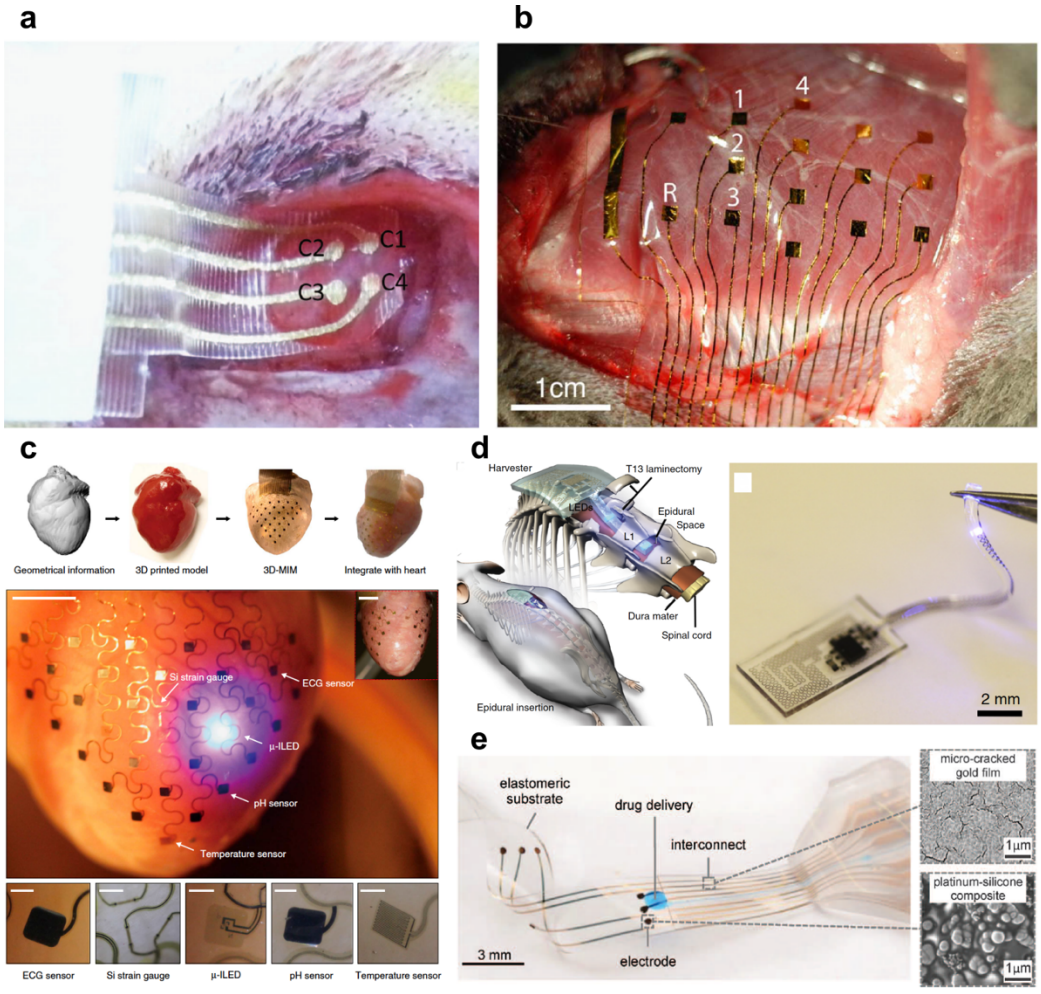

Figure 1.3.2 Biological applications using stretchable devices. (a) ECoG electrode device using a suspended wavy Au nanobelt [60]. (b) Stretchable MEA device based on the PDMS for the neural and muscular surface interface [79]. (c) Multifunctional 3D elastic membranes for cardiac measurements and stimulations [21]. (d) Wireless optical stimulation system for the spinal cord and sciatic nerve [80]. (e) Electronic dura mater for long-term multimodal neural interfaces [56].

moduli (e.g. ~1.5 kPa for the brain and 5–40 kPa for a resting muscle) [53], [54]. In addition, a large deformation of these elastomer-based electronics induces mechanical failure to the device components (e.g. transistors and interconnections) because of the large mechanical mismatch between the elastomer and these device components [13–15]. Also, the strains of conventional devices are limited by the intrinsic elasticity of the device substrate and the interconnections [e.g. silver flakes and serpentine interconnects exhibit stretchabilities of 215% [65] and 300% [66], respectively]. Finally, the volume and surface of the heart exhibit large and rapid changes. Assuming an ontogenetic process and pathological hypertrophy/atrophy, the deformation of brain tissue exceeds 300% [62], [63].

1.4 Objective of the present study and organization of the thesis

In this study, a platform for low invasive neuronal interfaces for numerous biological applications such as the BMI, HMI, and treatment of psychiatric and neurological disorders is proposed. In addition to proper electrical characteristics (low electrical impedance, electrode density, and others), low invasiveness and ability to follow the tissue deformation are required to achieve robust biological signal recordings. To achieve an intimate integration of the device with the soft biological tissues, high flexibility and stretchability of the device is required, which contribute to the reduction of the physical stress induced to the biological tissues and prevent the foreign-body-response. The Young's modulus of the neuronal interface should be similar to that of biological tissues, which is in the kPa range. Current flexible needle penetrating electrodes and film surface electrodes have a Young's modulus, which is about six orders of magnitude higher than that of biological tissues. Moreover, a stretchable electrode using stretchable materials as the device substrate also has a relatively high Young's modulus compared to that of biological tissues. Stretchable devices based on stretchable materials are limited by the intrinsic characteristics of the materials.

One possible way to obtain a low Young's modulus for a stretchable device is the use of stretchable structures [57]. Stretchable structures have the potential to improve the stretchability of flexible and stretchable materials. Stretchability based on stretchable structures enable an unprecedented high stretchability including a high strain ratio of over 1,000% and a low Young's modulus, which is comparable to that of the soft biological tissues. In this study, the highly stretchable neuronal, cardiac, and muscular interfaces are achieved using stretchable 'Kirigami' structures. The Kirigami structures consists of slit patterns embedded in the 2D film and it is compatible with the conventional microfabrication process (e.g. the photolithography technique). Therefore, the utilization

of the Kirigami structures has the ability to achieve the high density of a microelectrode array on a highly stretchable substrate using relatively simple process steps. The Kirigami structures provide a platform to enable an intimate integration of the electronic devices with soft biological tissues for numerous biological applications.

This thesis summarizes the theory of the mechanical characteristics of the Kirigami structures, the effective design and fabrication process of stretchable Kirigami-based biological interfaces, and their mechanical and electrical characterization. A demonstration to confirm the Kirigami's capability in *in vivo* experiments is also presented. The thesis consists of six chapters, and is organized as follows.

Chapter 1 introduce the major neural interfacing technologies and applications using recorded biological signals and the stimulation of biological tissues via neural interfaces. Soft neural interfaces for an intimate device integration with the biological tissues along with stretchable electrode materials required to implement soft electronic devices are also presented. Moreover, objective of this study to overcome issues of current neuronal interfaces is described.

In Chapter 2, the Kirigami structure which is the key component of this study is described. Recently presented stretchable and 3D deformable Kirigami structures along with their applications (including sensors, actuators, and others) are introduced, in the first part. A mechanical model for the estimation of the displacement of the Kirigami structure along with simulation results of the maximum stress occurred in the Kirigami structure are also presented. These results can be used for the effective design of Kirigami devices with the specific mechanical characteristics and robustness.

The first experiment of stretchable bioprobe device using the Kirigami structure is presented in Chapter 3. The ability of the Kirigami structure for biological applications is confirmed in this experiment. Four types of the Kirigami bioprobe devices are designed. Each type has different stretchability and number of electrodes. A bi-axially stretchable Kirigami bioprobe device is also presented. These Kirigami devices are fabricated using a microfabrication process. The electrical and mechanical characteristics of the fabricated Kirigami devices are also presented. The electrical characterization includes impedance measurements of the Kirigami device with and without device strain. The mechanical characterization includes the measurement of the stress–strain curve of the Kirigami device. The measured results are compared with calculated and simulated data. In addition, the endurance test and the stretchability tests of the Kirigami film sandwiched and embedded in another layer assuming an environment of the implantation to the biological tissues are conducted. Biological *in vivo* signal recordings using the fabricated devices in mouse brain cortex and heart are demonstrated. The recording capability of the

fabricated Kirigami device is confirmed by the ECoG signal recording under the device stretch (the electrode interval is adjusted to the distance between the two areas of the cortex for the simultaneous signal recording from multiple brain areas). In addition, the recording capability from biological tissues exhibiting a large deformation is also confirmed by the ECG signal recording.

The donut-shaped Kirigami device is presented in Chapter 4. The Kirigami bioprobe device presented in the first experiment could not follow the deformation of the biological tissues such as heart and muscle. This donut-shaped Kirigami device improve the device stability on biological tissues exhibiting a large deformation. The stability of the fabricated donut-shaped Kirigami device on the deformable tissue surface is confirmed by the displacement test using a deformable balloon instead of a biological tissue. The ECG and EMG signal recordings from a mouse's heart and hind limb are conducted to confirm the recording capability of the Kirigami device from large deformable tissues.

In Chapter 5, an optoelectrical Kirigami device for the treatment of heart disease is presented as another biological application of the Kirigami device. The proposed device includes arrays of LEDs for the optical stimulation and electrodes for the ECG signal recording. Regarding the characterization of the optoelectrical Kirigami device, the change in the resistance of the device interconnection with the thin and thick metal layer during the Kirigami stretching was investigated. The durability of the interconnection with the cycle strain and the fixation force of the latch structures used in the device fixation to the heart tissue were also investigated.

In Chapter 6, the research results are summarized and a discussion of the future prospects of the Kirigami devices is presented.

Chapter 2: Kirigami structure

2.1 Introduction

In the Japanese culture, 'Origami' (ori means 'folding' and gami means 'paper') [84] and 'Kirigami' (kiri means 'cutting') are artistic transformations from a 2D flat sheet/film into numerous 2D and 3D structures through folding, cutting, and gluing techniques. Kirigami designs have been used in material science and engineering to obtain the stretchability and functional 3D structures using not only stretchable materials but also flexible materials. The major deformable structures using the Kirigami patterning are shown in Figure 2.1.1. A stretchable Kirigami film using flexible materials including graphene [85] and nanocomposites [86], is shown in Figures 2.1.1a and b, respectively. These references describe a flexible film, which obtains its tunable mechanical properties (including stretchability), because of the Kirigami patterning embedded in the film. The remarkable feature of the Kirigami structure is that rigid and unstretchable materials can be rendered stretchable compared to other elastomer-based stretchable materials (e.g. a 370% strain for nanocomposites [86]). In addition, unpredictable local failure caused by a large strain in conventional stretchable materials used in stretchable electric devices can be prevented by using the Kirigami structure. This is a way to realize stretchable electronics by utilizing rigid and unstretchable materials, including insulators, metals, and semiconducting materials. Other types of the Kirigami structure using the fractal cut [87] are shown in Figure 2.1.1c. The fractal cut embedded in the film achieves a high stretchability (>800%) and a wide range of desirable programmed shapes and mechanical properties. The hierarchical cut motif and cut level in the film cause the un-uniform deformation of the film and allow it to expand into a unique structure. Kirigami-based 3D mesostructures made of bi-layers of Si nanomembranes and epoxy films [88] are shown in Figure 2.1.1d. In this report, a thin film with the Kirigami slit is transferred and partially bonded onto a pre-strained silicone elastomer material. When the pre-strain is released and the silicone returns to its original shape, the non-bonded area of the Kirigami film exhibits out-of-plane motions via compressive buckling caused by the compressive force of the silicone film. Using this approach, an exceptionally large number of 3D structures

can be obtained.

Using the unique characteristics of the Kirigami structure, which include stretchability, out-of-plane deformation, and others, many applications were proposed. The major applications using the Kirigami structure are shown in Figure 2.1.2. A strain sensor using the Kirigami structure [89] is presented in Figure 2.1.2a. This sensor has serpentine gold traces embedded in thin-film parylene-C with the Kirigami structure. The strain transduction is achieved using the change in DC resistance, which increases linearly with the strain. A solar cell with an optical tracking system, which uses the out-of-plane-

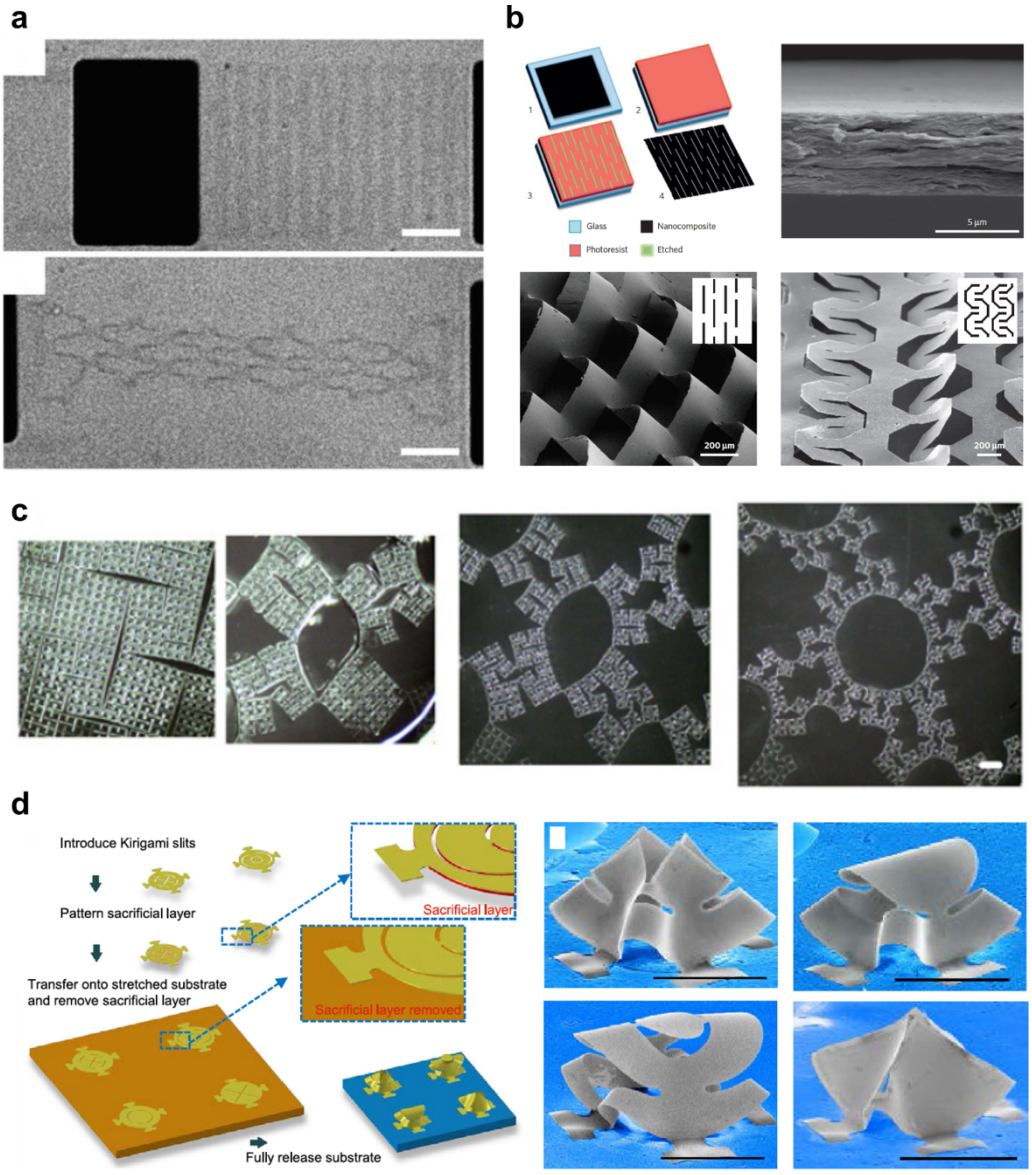

Figure 2.1.1 Proposed major structures using the Kirigami approach. (a) Kirigami film using graphene [85] and (b) nanocomposite [86]. (c) Hierarchical fractal cut [87]. (d) Kirigami-based 3D made of bi-layers of Si nanomembranes and epoxy films [88].

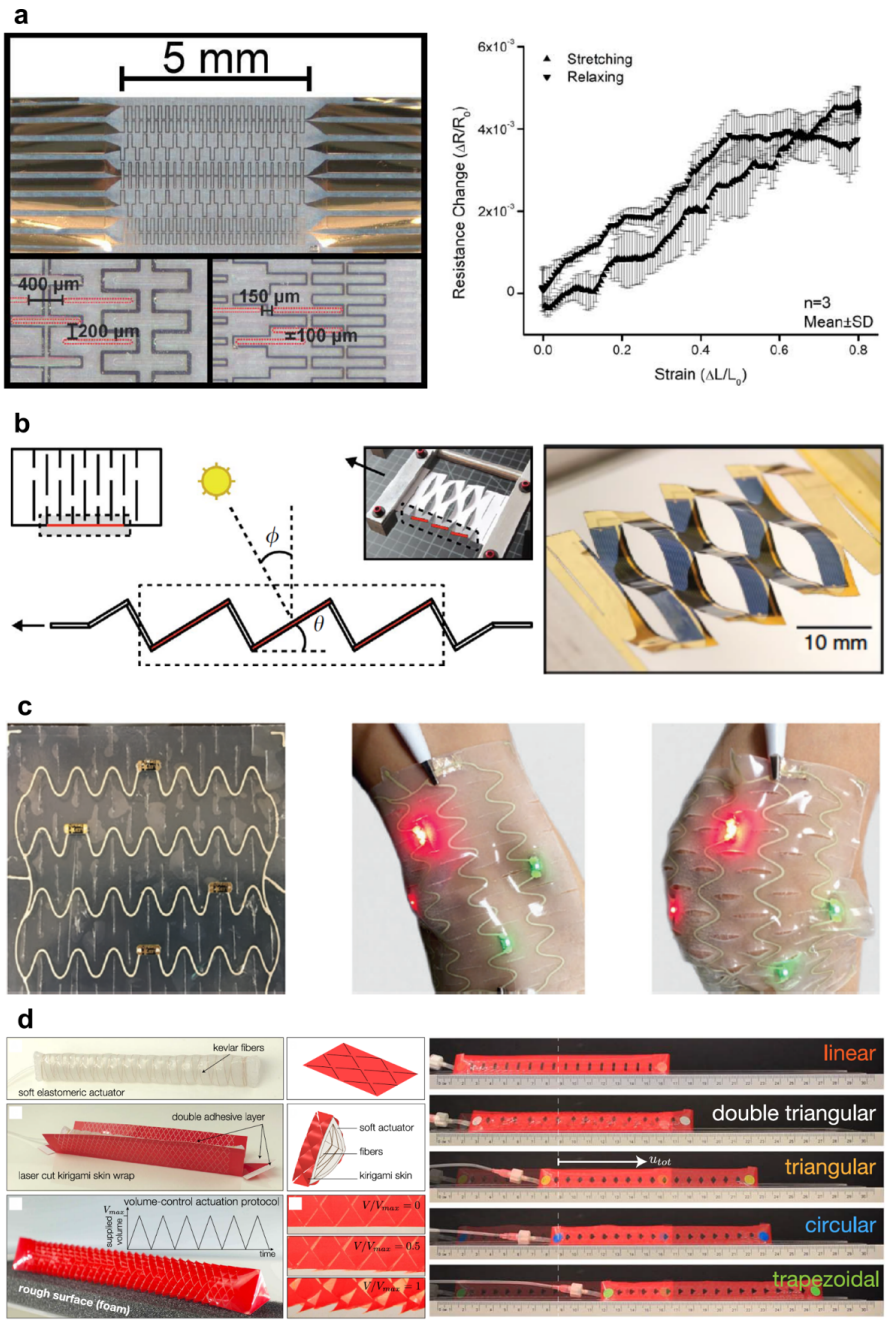

Figure 2.1.2 Applications using the Kirigami structure. (a) Strain sensor embedded in the Kirigami structure [89]. (b) Solar tracking system using the 3D deformation of the Kirigami structure [90]. (c) Enhancement of the adhesiveness of the stretchable sheet using a Kirigami structure [91]. (d) Soft actuator crawl [92].

deformation of the Kirigami structure to maximize electrical power generation [90] is shown in Figure 2.1.2b. The Kirigami cut is embedded in thin-film gallium arsenide solar cells. When the Kirigami film is stretched, each beam with the solar cell is tilted and the

angle of the solar cell can be controlled exactly as the strain of the Kirigami structure. Using this tilt of the solar cell with the Kirigami structure, a low-cost system for solar tracking can be implemented. A stretchable electrical device using an elastomer material with the Kirigami structure [91] is shown Figure 2.1.2c. Here, the Kirigami structure is used to enhance the device adhesion on the deformable surface of the human body without changing the thickness, rigidity, and adhesiveness of the film. The adhesion enhancement achieved by the Kirigami structure is due to the three factors of the shear-lag effect, which reduces the energy release rate compared with the continuous film without slit, partial debonding around the Kirigami slit, and inhomogeneous deformation of the substrate. A soft actuator crawl harnessing the out-of-plane deformation of the Kirigami structure to enhance its crawling capability [92] is given in Figure 2.1.2d. In this study, the mechanical instability of the Kirigami surface induces the transformation from a flat sheet to a 3D-textured surface similar to the snake's skin. The 3D shape of the device surface can be decided by the slit design of the Kirigami structure. The frictional properties of the device surface are also changed by that 3D shape. Using the stretchability and the 3D transformation properties of the Kirigami structure, the capability of the crawler locomotion is simply enhanced without using a complex system, which includes several independently activated actuators. Kirigami structures with good stretchability and deformability are able to replace conventional approaches, which often require complex and costly systems. Many kinds of applications, such as strain sensor and actuators using simple and cost-effective systems, can be implemented using Kirigami structure.

The stretching mechanism of the Kirigami structure, which is similar to the way the origami paper is stretched by cutting a slit pattern with a box cutter (Fig. 2.1.3), is based on the out-of-plane bending deformation of the membranes around each slit. Namely, the bending properties of each membrane dominate the stretchability of the whole Kirigami film system. Compared to in-plane bending deformation of membranes in a similar stretchable structure [93], the out-of-plane bending mechanism realizes a

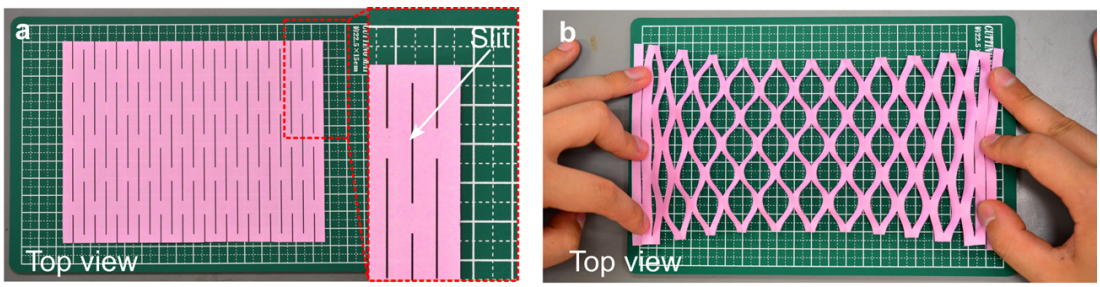

Figure 2.1.3 Deformation of the Kirigami structure patterned in the Origami paper. (a) Before deformation and (b) after deformation.

larger strain for the same strain–force and the effective Young's modulus is smaller than that of the film, which exhibits the in-plane deformation. The mechanical characteristics (effective Young's modulus and maximum strain) can be controlled by the device design (e.g. slit length and slit gap) and the stretchability of the Kirigami structure can exceed that of stretchable materials (e.g. PDMS, SBS, PU, and Ecoflex). Moreover, the Kirigami concept is applicable not only to stretchable materials but also to other non-stretchable (flexible) materials. This property extends the abilities of numerous flexible materials, such as Si nanomembrane, graphene, and nanocomposites.

In this study, stretchable and flexible electronic devices based on the Kirigami structures are presented. These devices can be used as biological interfaces including bioprobe and optical stimulators for applications, such as BMI, HMI, and treatment of heart disease. In addition, the ability to use Kirigami structures as the platform for stretchable electronics is validated and the insights into their design are obtained by utilizing the Kirigami structures. A device based on the Kirigami structure has a great potential, which is particularly exploited in biological applications. Because of its high stretchability, the Kirigami structure is able to achieve an intimate integration of the electronic devices with the soft and deformable biological tissues. Such Kirigami films can be realized by a sophisticated 2D microfabrication process (e.g. the photolithography technique). A stretchable bioprobes device, which uses a Kirigami structure, consists of a multiple layered system composed of non-stretchable materials, such as insulating polymeric materials of parylene-C or polyimide (PI) (both have the same Young's modulus of 2.8 GPa and yield strain of ~3%) for the device substrate. Noble metals, such as Pt or Au (Young's modulus of 168 GPa for Pt and 79 GPa for Au, respectively) with a titanium (Ti) adhesion layer (Young's modulus of 116 GPa) can be used for the electrode layer embedded in the polymer substrate. In the next section, displacement models for single and multi-layered Kirigami structures are extracted using the beam theory for an effective device design utilizing the Kirigami structure.

2.2 Displacement model for the Kirigami structure

To design Kirigami devices with specific mechanical properties, the equation of the relationship between the deformation and induced force was derived. Herein, two types of Kirigami models are considered: a) the single layer model, which consists of the single material (e.g. the Kirigami film without electrical components, such as interconnections) and b) the multi-layer model, which consists of more than two materials (e.g. the Kirigami electrode device, which consists of the substrate and thin metal layer interconnections or other components).

2.2.1 Displacement model for the single layered Kirigami structure

A cantilever beam model can be used to define the stretching properties of a Kirigami structure [86]. For simplicity, herein one unit cell consisting of a slit and beams around the slit (purple colored section in Figs. 2.2.1a, b) is used. The one unit cell can be considered as the combination of eight beams (Figs. 2.2.1c–e) and the displacement of the cantilever beam, $d_{\text{beam_1}}$, is defined as:

$$d_{\text{beam_1}} = \frac{1}{3}\frac{Pl^3}{EI} \tag{2.1}$$

where P is the load, l is the length of the beam, E is the Young's modulus of the material, I is the second moment of the area of the beam. The variable I for a rectangle is given as:

$$I = \frac{wt^3}{12} \tag{2.2}$$

where w is the beam width, t is the thickness of the beam. By substituting equation (2.2) in equation (2.1) the displacement of the single beam, $d_{\text{beam_1}}$, (Fig. 2.2.1e) is given as:

$$d_{\text{beam_1}} = \frac{4Pl^3}{Ewt^3} \tag{2.3}$$

The model shown in Figure 2.2.1d can be considered as a serial connection of the two beams. In this case, the displacement is provided as follows:

$$d_{\text{beam_2}} = \frac{8Pl^3}{Ewt^3} \tag{2.4}$$

As well as the serial connection of two beams, a unit cell can be considered as the serial and parallel connection of the 4×2 of cantilever beams. In this case, the displacement is given as follows:

$$d_{\text{cell}} = \frac{8Pl^3}{Ewt^3} \tag{2.5}$$

The whole Kirigami film consists of an array of the one cell unit. The total

displacement of the device is provided as:

$$d_{total} = \frac{N_c}{N_r}\frac{8Pl^3}{Ewt^3} \tag{2.6}$$

where N_r and N_c are row and column numbers of the cell units, respectively. In the Kirigami structure, the beam length, l, is decided by the slit design of the slit length, L_slit, and the slit gap, L_gap, and is given as follows:

$$l = \frac{L_{slit} - L_{gap}}{4} \tag{2.7}$$

Using the parameters of the slit design (slit length L_slit and slit gap L_gap), the total displacement of the whole Kirigami film in the direction perpendicular to the film plane without considering the rotation of each beam (d_total in Fig. 2.2.1f), can be expressed as:

$$d_\mathrm{total} = \frac{N_\mathrm{c}}{N_\mathrm{r}}\frac{P\left(L_\mathrm{slit} - L_\mathrm{gap}\right)^3}{8Ewt^3} \tag{2.8}$$

This formula suggests that the stretching property of the film is proportional to the column-/row-numbers ratio, $N_\mathrm{c}/N_\mathrm{r}$, while the bending property of each beam contributes to the film's stretchability. The bending property of each beam is defined by the material properties (e.g. Young's modulus) and the geometry (e.g. length, width, and thickness) of the beams. A more accurate expression for the displacement of the film, $d_\mathrm{total,actual}$, considering the rotation of each beam, is given by the Pythagorean theorem (Fig. 2.2.1f) as:

$$d_\mathrm{total,actual} = \sqrt{L^2 + d_\mathrm{total}^2} - L \tag{2.9}$$

where L is the whole length of the Kirigami film prior to stretching. Herein, the actual displacement of the film, $d_\mathrm{total,actual}$, is used for the film stretching tests and the definition of its stretching properties.

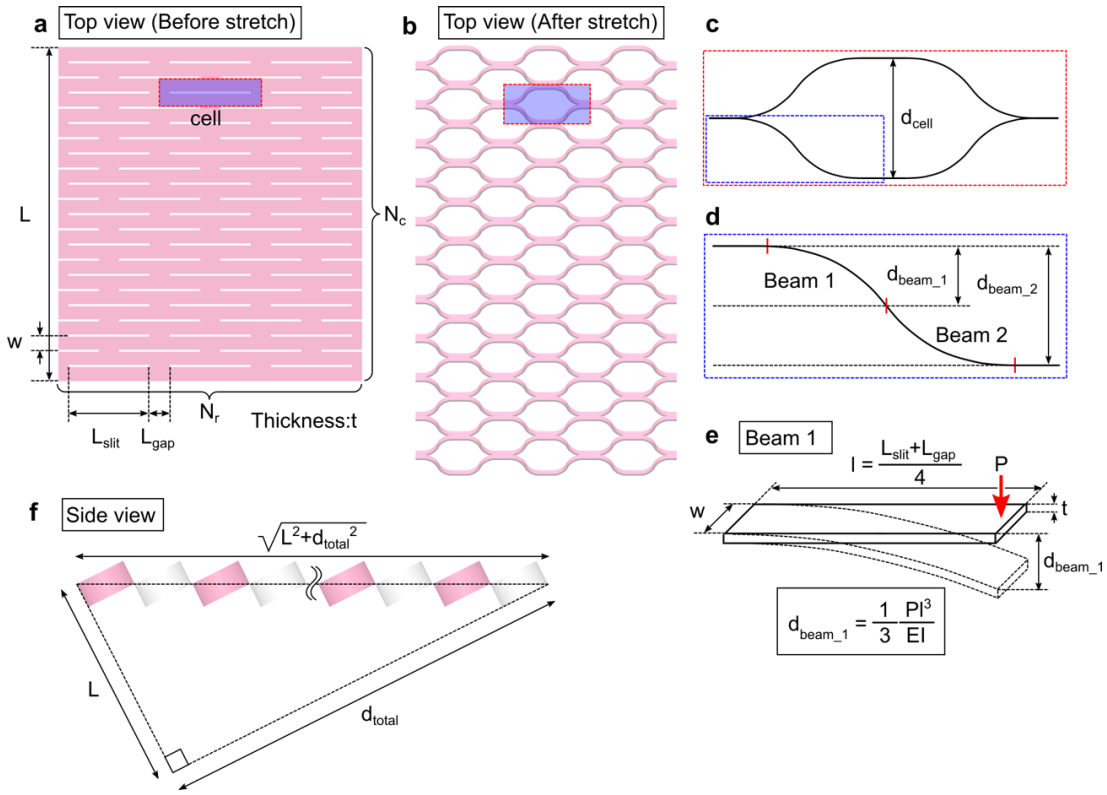

Figure 2.2.1 Derivation of the displacement model for the single layered Kirigami film. (a, b) Schematic diagrams of the stretchable Kirigami film (a: before stretch, b: after stretch) including one unit cell (purple colored), which is used in the modeling. (c) Displacement model for a unit cell of the Kirigami structure. The unit cell consists of the combination of eight cantilever beams. (d) Displacement model for the serial connection of two beams. (e) Displacement model for a single beam. (f) Accurate total displacement of the whole Kirigami film considering the rotation of each beam.

2.2.2 Displacement model for the multi-layered Kirigami structure

Formula (2.9) can be applied to single material-based Kirigami films. Here, the model for multiple layered systems of Kirigami films is further enhanced. Considering the second moment of the area of the beam, I_z, the displacement of the multiple layered Kirigami film can be expressed as:

$$d = \frac{N_c}{N_r}\frac{P\left(L_{slit} - L_{gap}\right)^3}{96EI_z} \tag{2.10}$$

where N_r and N_c are the row and column numbers of the cell units, respectively. E is the Young's modulus of the material. L_{slit} and L_{gap} are the slit length and the gap between

the slits, respectively.

A Kirigami device containing two different materials can be modeled. The cross-section of each beam of the Kirigami device is shown in Figure 2.2.2, where the cross-section is divided into five parts to calculate the second moment of the area, I_z [(1)–(5), Fig. 2.2.2c]. The second moment of area, I_z, is calculated by summing the individual second moment of each part as follows:

$$I_z = I_{z1} + I_{z2} + I_{z3} + I_{z4} + I_{z5} \tag{2.11}$$

The second moments of the area for each part are expressed using the parallel axis theorem. Assuming that each beam consists of a single material (herein, material 1 with a Young's modulus E_1), the width of the other material (material 2 with a Young's modulus E_2) is expressed using the ratio of these Young's moduli (E_2/E_1). The second moments of area for each part, I_{z1}, I_{z2}, I_{z3}, I_{z4} and I_{z5}, can be expressed as:

$$I_{z1} = \frac{b_1 h_{1,2}^3}{12} + e_{1,2}^2 b_1 h_{1,2} \tag{2.12}$$

$$I_{z2} = \frac{b_2 h_{1,2}^3}{12} + e_{1,2}^2 b_2 h_{1,2} \tag{2.13}$$

$$I_{z3} = \frac{b_{3,4,5} h_3^3}{12} + e_3^2 b_{3,4,5} h_3 \tag{2.14}$$

$$I_{z4} = \frac{b_{3,4,5} h_4^3}{12} + e_4^2 b_{3,4,5} h_4 \tag{2.15}$$

$$I_{z5} = \frac{E_2}{E_1}\frac{b_{3,4,5} h_5^3}{12} + e_5^2 \frac{E_2}{E_1} b_{3,4,5} h_5 \tag{2.16}$$

where b_1, b_2, and $b_{3,4,5}$ are the widths of each part, respectively, and $h_{1,2}$, h_3, h_4, and h_5 are the thicknesses of each part, respectively (Fig. 2.2.2b). E_1 and E_2 are the Young's moduli of material 1 and material 2, respectively (Fig. 2.2.2a). $e_{1,2}$, e_3, e_4, and e_5 are the vertical distances between the centroid of each part and the centroid of the entire cross-section of the beam (Fig. 2.2.2c). These distances can be expressed using the distance between the centroid of the entire cross-section of the beam and the bottom of the cross-section, e, as follows:

$$e_{1,2} = e - \frac{h_{1,2}}{2} \tag{2.17}$$

$$e_3 = e - \frac{h_3}{2} \tag{2.18}$$

$$e_4 = h_3 + h_5 + \frac{h_4}{2} - e \tag{2.19}$$

$$e_5 = h_3 + \frac{h_5}{2} - e \tag{2.20}$$

The distance, e, which is defined by the coordinates of the centroid of the entire cross-section of the beam, is calculated from the ratio of the first moment of area and the area of the cross-section as follows:

$$e = \bar{y} = \frac{\int_{(A)} y_1 \mathrm{d}A}{A} \tag{2.21}$$

$$\begin{aligned} \int_{(A)} y_1 dA &= \sum_{i=1}^{5} A_i y_i \\ &= \frac{1}{2} b_1 h_{1,2}^2 + \frac{1}{2} b_2 h_{1,2}^2 + \frac{1}{2} b_{3,4,5} h_3^2 \\ &\quad + b_{3,4,5} h_4 \left(h_3 + h_5 + \frac{h_4}{2} \right) + \frac{E_2}{E_1} b_{3,4,5} h_5 \left(h_3 + \frac{h_5}{2} \right) \end{aligned} \tag{2.22}$$

$$A = \sum_{i=1}^{5} A_i = b_1 h_{1,2} + b_2 h_{1,2} + b_{3,4,5} h_3 + b_{3,4,5} h_4 + \frac{E_2}{E_1} b_{3,4,5} h_5 \tag{2.23}$$

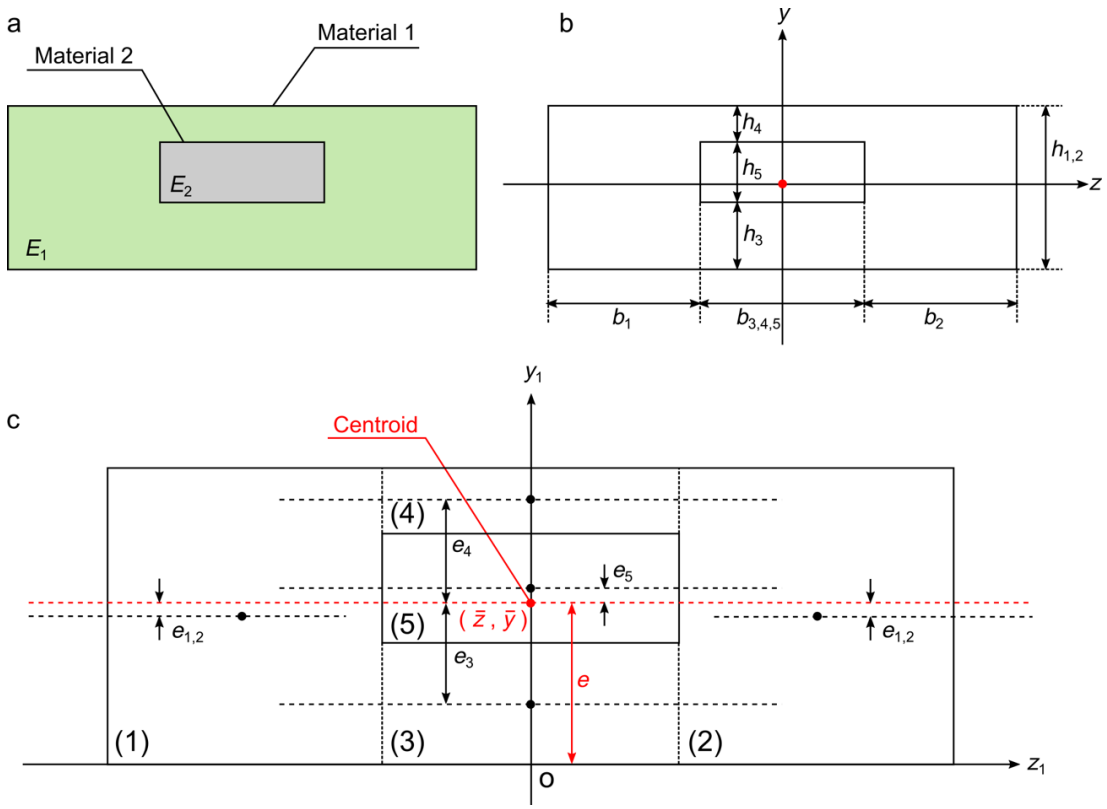

Figure 2.2.2 Cross-section of each beam of the multi-layered system in the Kirigami structure. (a) Schematic diagram of the multi-layered Kirigami structure composed of two materials with Young's moduli E_1 and E_2, respectively. (b) Dimensions of the multi-layered Kirigami structure. (c) Centroids of the entire cross-section of the beam and each divided part.

The modeling of the proposed Kirigami device with a parylene substrate and multiple Pt and Ti metal layers involves further investigation of the aforementioned Kirigami structure, which is based on two different materials (Fig. 2.2.3). The cross-section of the proposed Kirigami device is shown in Figure 2.2.3. Due to the film deposition process, the device's surface has a step over the metal portion (Pt/Ti). Similarly to the aforementioned multi-layered Kirigami model, the cross-section of the beam is divided into six parts [(1)–(6), Fig. 2.2.3]. The second moments of area of each area are expressed as:

$$I_z = I_{z1} + I_{z2} + I_{z3} + I_{z4} + I_{z5} + I_{z6} \tag{2.24}$$

$$I_{z1} = I_{z2} = \frac{(b_{Pa} - b_{Pt})h_{Pa}^3}{3} + e_1^2(b_{Pa} - b_{Pt})h_{Pa} \tag{2.25}$$

$$I_{z3} = \frac{b_{Pt} h_{Pa}^3}{12} + e_2^2 b_{Pt} h_{Pa} \tag{2.26}$$

$$I_{z4} = \frac{b_{Pt} h_{Pa}^3}{12} + e_3^2 b_{Pt} h_{Pa} \tag{2.27}$$

$$I_{z5} = \frac{E_{Ti}}{E_{Pa}} \frac{b_{Pt} h_{Ti}^3}{12} + e_4^2 \frac{E_{Ti}}{E_{Pa}} b_{Pt} h_{Ti} \tag{2.28}$$

$$I_{z6} = \frac{E_{Pt}}{E_{Pa}} \frac{b_{Pt} h_{Pa}^3}{12} + e_5^2 \frac{E_{Pt}}{E_{Pa}} b_{Pt} h_{Pt} \tag{2.29}$$

where b_{Pa} and b_{Pt} are the widths of the parylene beam and the Pt (or Ti)-layer, respectively. h_{Pa}, h_{Pt}, and h_{Ti} are the thicknesses of parylene, Pt, and Ti, respectively. E_{Pa}, E_{Pt}, and E_{Ti} are the Young's moduli of parylene, Pt, and Ti, respectively. e_1, e_2, e_3, e_4, and e_5 are the vertical distances between the centroid of each part and the centroid of the entire cross-section of the beam. These distances can be expressed using the distances between the centroid of the entire cross-section of the beam and the bottom of the cross-section, e, as follows:

$$e_1 = e - h_{Pa} \tag{2.30}$$

$$e_2 = e - \frac{h_{Pa}}{2} \tag{2.31}$$

$$e_3 = \frac{3}{2} h_{Pa} + h_{Ti} + h_{Pt} - e \tag{2.32}$$

$$e_4 = \left(h_{Pa} + \frac{1}{2} h_{Ti} \right) - e \tag{2.33}$$

$$e_5 = h_{Pa} + h_{Ti} + \frac{1}{2} h_{Pt} - e \tag{2.34}$$

Similarly to the two material-based model, the distance, e, can be calculated from the ratio of the first moment of area and the area of the cross-section as follows:

$$e = \bar{y} = \frac{\int_{(A)} y_1 \mathrm{d}A}{A} \tag{2.35}$$

$$\int_{(A)} y_1 dA = \sum_{i=1}^{6} A_i y_i$$
$$= 2(b_{Pa} - b_{Pt})h_{\mathrm{Pa}}^2 + b_{Pt}h_{Pa}(2h_{Pa} + h_{Ti} + h_{Pt})$$
$$+ \frac{E_{Ti}}{E_{Pa}} b_{Pt}h_{Ti}\left(h_{Pa} + \frac{h_{Ti}}{2}\right) + \frac{E_{Pt}}{E_{Pa}} b_{Pt}h_{Pt}\left(h_{Pa} + h_{Ti} + \frac{h_{Pt}}{2}\right) \quad (2.36)$$

$$A = \sum_{i=1}^{6} A_i = 2(b_{\mathrm{Pa}} - b_{\mathrm{Pt}})h_{\mathrm{Pa}} + 2b_{\mathrm{Pt}}h_{\mathrm{Pa}} + \frac{E_{\mathrm{Ti}}}{E_{\mathrm{Pa}}} b_{\mathrm{Pt}}h_{\mathrm{Ti}} + \frac{E_{\mathrm{Pt}}}{E_{\mathrm{Pa}}} b_{\mathrm{Pt}}h_{\mathrm{Pt}} \quad (2.37)$$

The displacement of the Kirigami structure is exhibited by the aforementioned models. However, the displacement close to the maximum strain of the Kirigami structure is gradually saturated. Figures 2.2.4a–f show photographs and schematic diagrams of the

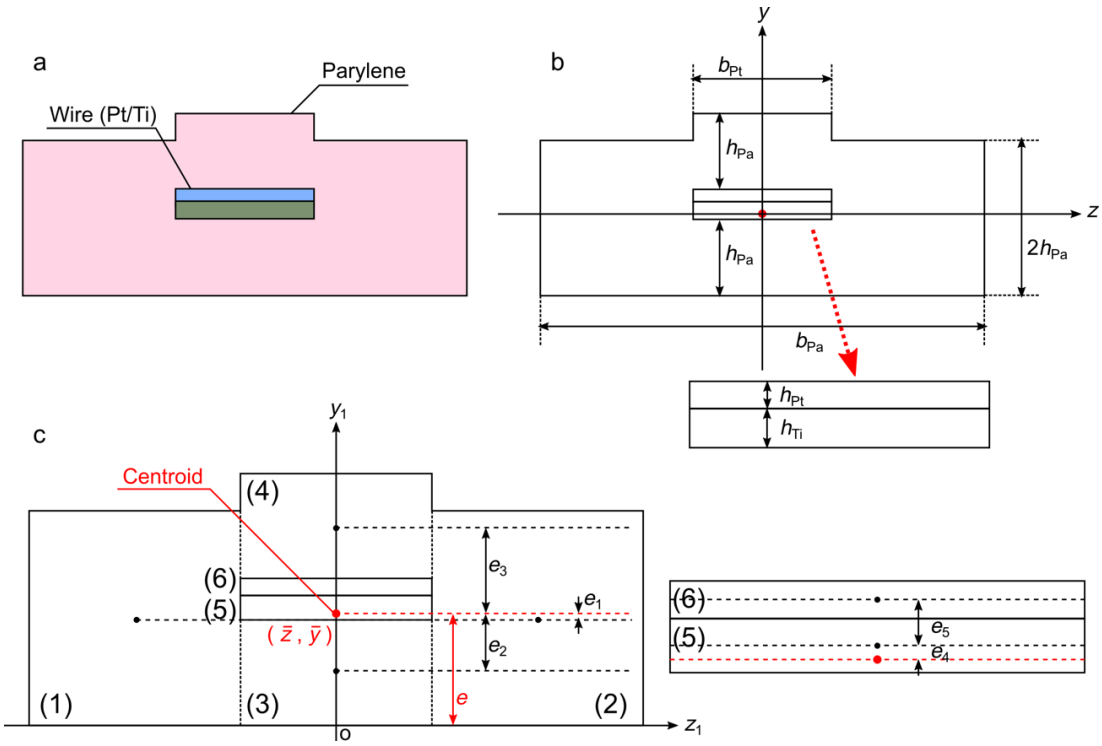

Figure 2.2.3 Cross-section of each beam of the multi-layered Kirigami device proposed in this study. (a) Schematic diagram of the multi- layered Kirigami structure composed of the parylene substrate and multiple Pt and Ti metal layers. (b) Dimensions of the multi-layered Kirigami device. (c) Centroids of the entire cross-section of the beam and each divided part.

Kirigami structure without strain (Figs. 2.2.4a, d) and with maximum strain (Top view: Figs. 2.2.4b, e, Side view: Figs. 2.2.4c, f). The unit cell model stretched to the maximum strain is shown in Figure 2.2.4g. Strain is defined as the ratio of the difference between the length before and after stretch by the initial length. The maximum strain of the Kirigami structure depends on the Kirigami design (Fig. 2.2.4) and is given as:

$$\text{Maximum strain} = \frac{\sqrt{\left(L_{\text{slit}} - L_{\text{gap}}\right)^2 + \left(2(w + w_{\text{slit}})\right)^2} - 2(w + w_{\text{slit}})}{2(w + w_{\text{slit}})} \tag{2.38}$$

where L_{slit} is the slit length, L_{gap} is the slit gap, w is the beam width, and w_{slit} is the slit width. This maximum strain model only considers the bending deformation of the Kirigami structure and excludes the strain of device materials.

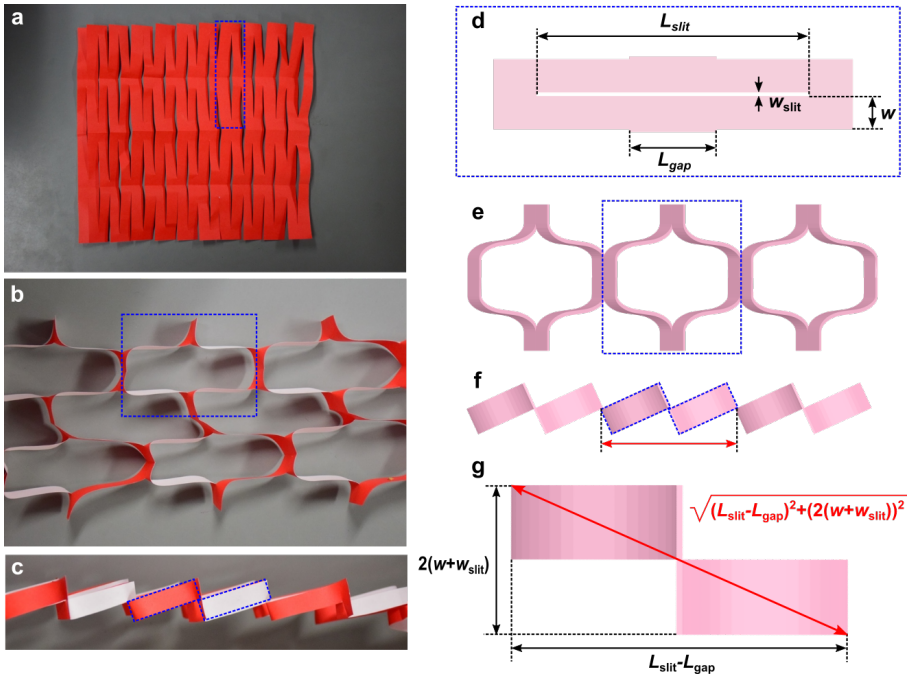

Figure 2.2.4 Maximum strain calculation of the Kirigami structure. (a) Photographs of the top view of the Kirigami structure without strain, (b) with maximum strain, and (c) side view with maximum strain. (d) Schematic diagram of the one cell unit without strain, (e, f) top and side view of the maximum stretched Kirigami structure, (g) side view of the one cell unit with the maximum strain.

2.3 Simulation of the displacement and stress distribution in the Kirigami structure

To achieve an effective design of the Kirigami device, the displacement and stress distribution in the Kirigami structure were simulated using the finite element method (FEM). The simulations were implemented using the commercial software ANSYS (version 15.0, ANSYS, Canonsburg, PA, USA).

2.3.1 Simulation of the displacement of the Kirigami structure

The strain–force characteristics of the Kirigami parylene film were further analyzed by FEM. Here, the model to be simulated consists of a single layer of parylene-C, which has a Young's modulus and a Poisson's ratio of 2.8 GPa and 0.4, respectively. The simulation model of the unit cell, which consists of four parylene beams around a slit, is shown in Figure 2.3.1. The slit length, L_{slit}, slit width, and the gap between the slits, L_{gap}, are 1,600 μm, 10 μm, and 400 μm, respectively, while the beam width, w, is 100 μm. During beam stretching, a downward force was applied to one side between the beams, while the other side was fixed. The simulation z-axis (Fig. 2.3.1c) displacement results and the strain considering beam rotation are presented in Figure 2.3.2. The displacement is saturated as the applied force increases, because the strain reaches the limit of the strain determined by the design of the Kirigami structure. The saturated maximum strain is almost the same as the strain calculated by equation (2.38). The strain–force properties of the whole Kirigami film system were obtained using a combination of the unit cell properties.

2.3.2 Simulation of the stress distribution in the Kirigami structure

To avoid the stress concentration at the edge of each Kirigami slit, the stress distribution in a parylene beam using FEM was investigated. A simulated one-cell unit consisting of a slit and its surrounding beams is shown in Figure 2.3.3a. The dimensions of the simulation model are almost the same as those used for the one-cell model displacement simulation. Two types of slit edges were calculated: a corner-shaped edge (Fig. 2.3.3b) and a circular-shaped edge (Fig. 2.3.3c). The curvature of the corner-shaped edge has a radius of 1 μm. For the circular-shaped edge, the diameter was set to 20 μm.

The stress distribution at each slit edge was calculated by applying a force between the beams (Fig. 2.3.3d). Simulation results for the corner-shaped and circular-shaped edge designs, when applying a force of 100 μN, are shown in Figures 2.3.3e and f, respectively. The corner-shaped edge exhibited a maximum stress of approximately two times larger

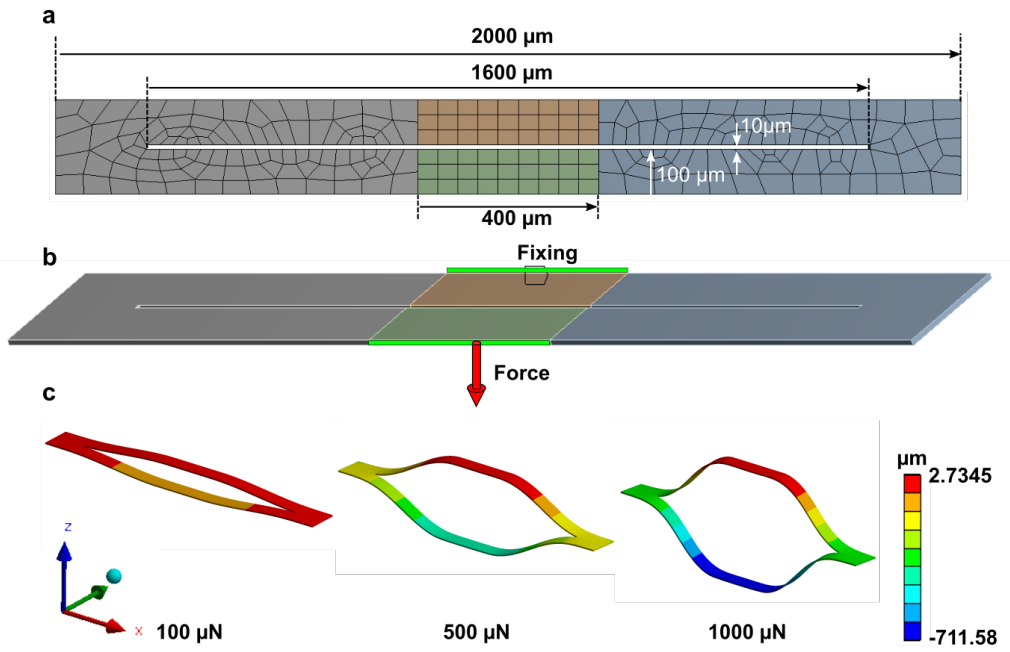

Figure 2.3.1 Simulation of the strain–force characteristics using the one-cell model of the Kirigami structure. (a) One-cell model composed of a slit and four beams. (b) Fixing and force applied to the calculated model. (c) Deformation of the one-cell model with respect to each force. Color bar shows the displacement in the z-axis.

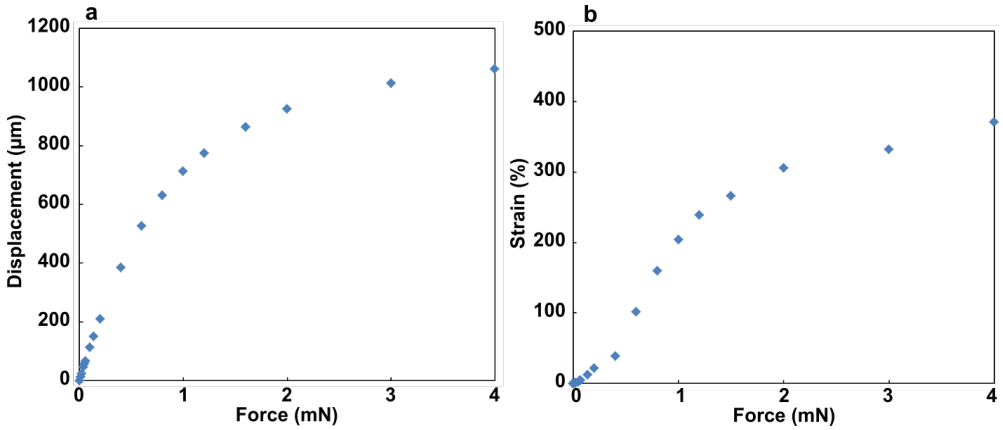

Figure 2.3.2 Simulation results of the displacement and strain of the one-cell model. (a) Displacement depending on the applied force. (b) Strain considering the beam rotation.

than that of the circular-shaped edge. The calculated maximum stress–applied force curves for both edge designs are shown in Figure 2.3.3g. The maximum stress of the corner-shaped edge reached a parylene yield strength of 55 MPa at ~100 μN, while the circular-shaped edge stress reached the yield strength at a two times higher force

(~200 μN). These results indicate that the circular-shaped edge slit design reduces the maximum stress in a film, which results in the beam deformation extending (elastic region) before reaching its yield strength.

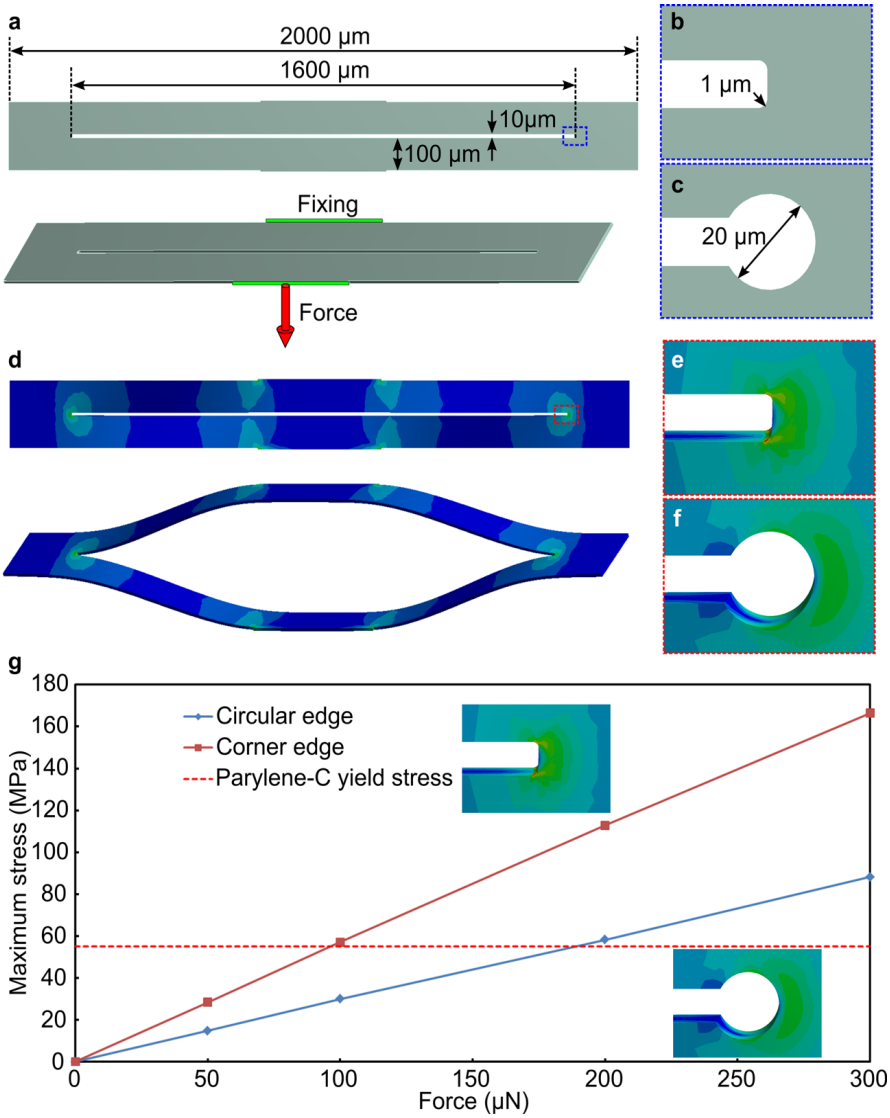

Figure 2.3.3 Calculated maximum stress–applied force curves for both edge designs (circular and corner edges). (a) Simulated one-cell unit consisting of a slit and its surrounding beams. (b, c) Simulated types of slit edges: a corner-shaped edge with a curvature radius of 1 μm (b) and a circular-shaped edge with a diameter of 20 μm (c). (d) Stress distribution at each slit edge calculated by applying a force of 100 μN between the beams. (e, f) Simulation results for the corner-shaped edge design (e) and for the circular-shaped edge design (f). (g) Simulated maximum stress–applied force curves for both edge designs (circular and corner edge).

2.4 Kirigami film

To confirm the stretchability of the Kirigami patterned film, the stretchable Kirigami film realized using a microfabrication process of parylene-C was demonstrated. The designed Kirigami parylene film, which is 40 mm long, 20 mm wide, and 10 μm thick, consists of an array of 5 × 361 slits ($N_r = 5, N_c = 180$) (Fig. 2.4.1a). Here, the designed slit length, L_{slit}, and the gap between the slits, L_{gap}, are 3,400 μm and 600 μm, respectively, while the beam width, w, is ~100 μm. A diamond-shaped-mesh-like parylene film with the same dimensions (40-mm long, 20-mm wide, and 10-μm thick) was fabricated using the same parylene film process for comparison purposes. The designed diamond-mesh parylene film is shown in Figure 2.4.1b. Here, a hole design geometry which is 2,300 μm in height and 1,050 μm in width was used. Consequently, the length and width of each beam around the hole were ~1,300 μm and ~130 μm, respectively. These beam sizes were similar to those used in the Kirigami film (1,400 μm long and ~100 μm wide, Fig. 2.4.1a). With this mesh design, an array of 8 × 63 diamond meshes could be designed in the same film geometry (40 × 20 mm^2). Compared to a Kirigami film with a 5 × 361 slit array in the same film geometry (40 × 20 mm^2), the number of meshes was limited because the diamond holes occupied a larger area in the

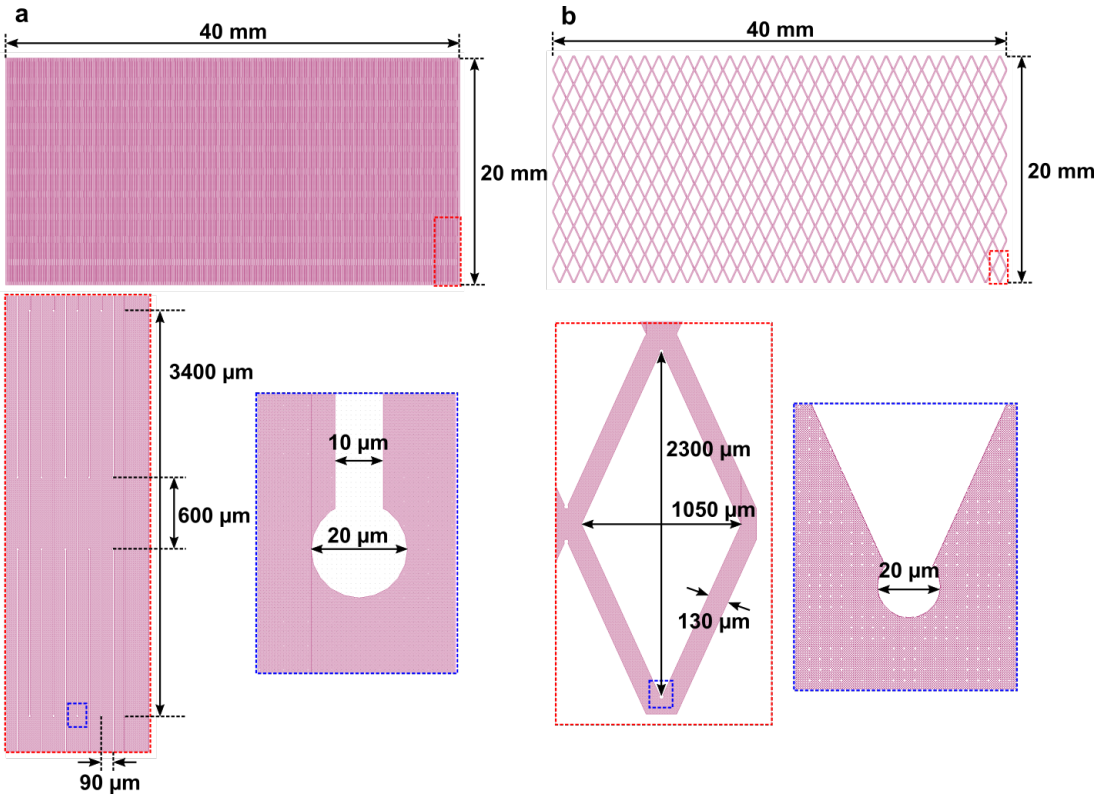

Figure 2.4.1 Stretchable Kirigami and diamond-mesh film designs. (a) Kirigami parylene film and (b) diamond-mesh parylene film.

film than the slit design in the Kirigami film with the same geometry. Each diamond mesh consisted of circular-shaped edges (20 μm in diameter) in a similar way as the slit design of the Kirigami film (Fig. 2.4.1a) to achieve stress reduction in the film (inset in Fig. 2.4.1a).

The fabrication process of each stretchable parylene film was based on some simple steps (Fig. 2.4.2). A 10-μm-thick parylene-C film was deposited on a Si substrate (model PDS2010, LABCOTER). To form the slit patterns, the parylene-C film was etched by oxygen (O_2) plasma with a slit mask of Ti (~80-nm thick), which was patterned by a tetrafluoromethane (CF_4) plasma with a photoresist prior to parylene etching. After removing the Ti mask (CF_4 plasma), the parylene film was released from the Si substrate with ethanol (Fig. 2.4.3).

The fabricated parylene film exhibited great stretching properties as demonstrated in the quantitative analysis (Fig. 2.4.4). Here, each side of the fabricated film was fixed by the clips and expanded (Fig. 2.4.4a). The initial 40-mm-long parylene film could be stretched by 1,100% to a length of 480 mm before the film breaks. The strain of 1,100% is smaller than that of the calculated maximum strain of 1,300%. This is because a number of Kirigami structures placed at each side of the Kirigami film is fixed and cannot be stretched.

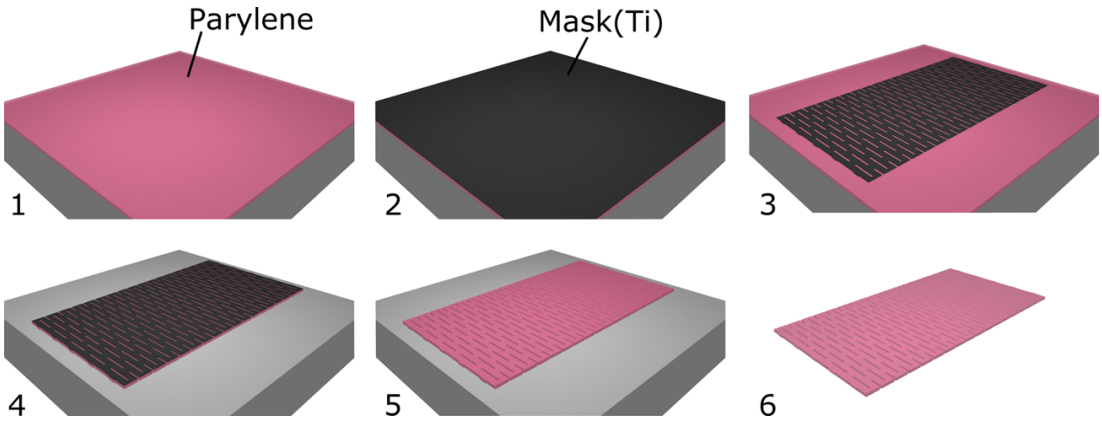

Figure 2.4.2 Fabrication process of the Kirigami-based stretchable parylene film. (1) Deposition of the 10 μm parylene film on the Si wafer. (2) Deposition of the Ti hard mask. (3) Patterning of the Ti hard mask by CF_4 plasma. (4) Patterning of the parylene layer by O_2 plasma using a Ti hard mask. (5) Ti hard mask removal by CF_4 plasma. (6) Release of the Kirigami patterned parylene film from the Si wafer.

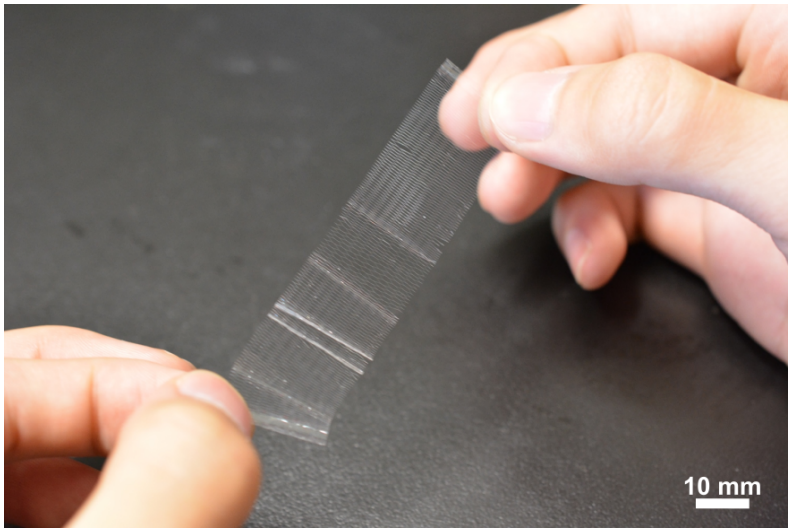

Figure 2.4.3 Photograph of the fabricated Kirigami parylene film (40-mm long, 20-mm wide, and 10-μm thick) consisting of a 5 × 361 slit array ($N_r = 5, N_c = 180$).

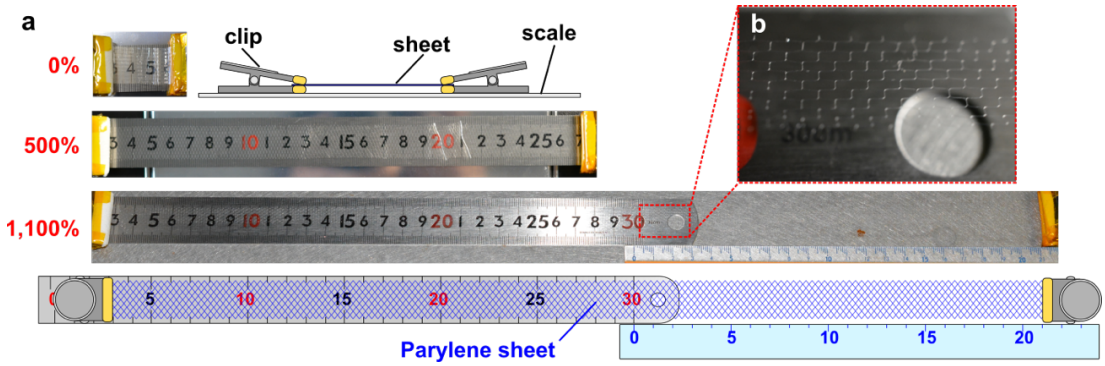

Figure 2.4.4 Kirigami parylene film. (a) Quantitative analysis of the stretchability of the Kirigami film. The initial length of the Kirigami film was 40 mm (0%), which was stretched to 480 mm (1,100%) prior to the film breaking. (b) Maximum stretched Kirigami parylene film.

The stretchability of the fabricated diamond-mesh film was quantitatively analyzed (Fig. 2.4.5). The initial length of the mesh film was 30 mm (0%), which was stretched to 55 mm (83%) prior to the film breaking (Fig. 2.4.5). Since there are fewer meshes (or fewer bendable beams) in the same film geometry (40-mm long, 20-mm wide, and 10-μm thick), the stretchability of the meshed parylene film was limited to ~83% before the film breaks (Fig. 2.4.5). This indicated that the proposed slit array design (Fig. 2.4.4) is suitable to obtain films with high stretchability. As a preliminary test, a Kirigami film with a one-row design was mounted on a beating mouse heart, whose volume and surface area rapidly change (Fig. 2.4.6).

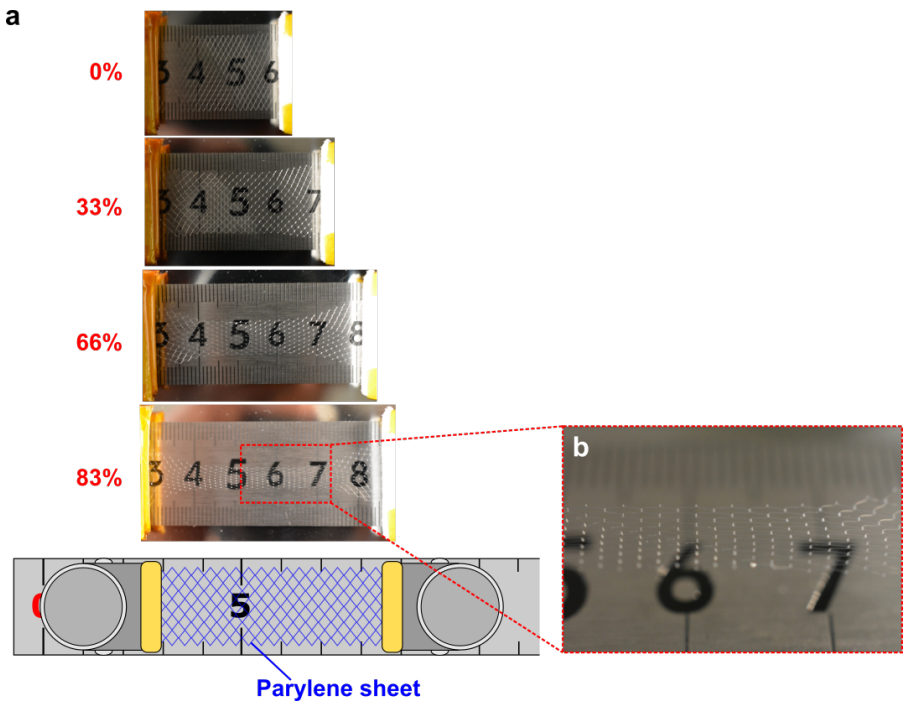

Figure 2.4.5 Diamond-mesh parylene film. (a) Quantitative analysis of the stretchability of the fabricated diamond-mesh film. The initial length of the mesh film was 30 mm (0%), which was stretched to 55 mm (83%) prior to the film breaking. (b) Maximum stretched diamond-mesh parylene film.

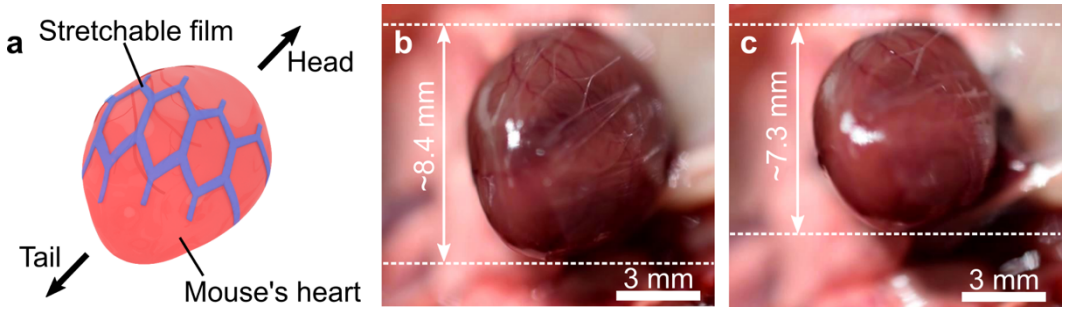

Figure 2.4.6 One-row Kirigami design was mounted on a beating mouse heart. (a) Schematic diagram and (b, c) photographs of the fabricated parylene film placed on a beating mouse heart. The film with one-row design (N_r = 1) follows the heart pulsation during diastole (b) and systole (c).

2.5 Conclusions

In this chapter, the major Kirigami structures and devices proposed, which use a Kirigami structure, were described. Kirigami structures offer stretchability and other multiple functions using flexible or stretchable material (e.g. graphene, nanocomposite, Si nanomembrane, parylene, and PDMS) sheets through 2D and 3D transformations. The Kirigami structures can be applied to the strain sensor, actuator for the solar tracking system, and crawl robot. They also enhance the adhesiveness of the elastic substrate and can be used in many applications utilizing their unique properties of high stretchability, inhomogeneous, and out-of-plane deformations. For the effective design of the devices using the Kirigami structure, displacement models of the Kirigami structure depending on the applied force were derived. The derived displacement models include single layered and multiple layered Kirigami structures. In addition, the simulation model for calculating the maximum strain of the Kirigami structures was also derived. The displacement and the maximum strain of the Kirigami structures depend on the design of the Kirigami slits and the Young's modulus of the materials used in the Kirigami film. Therefore, the mechanical characteristics of the Kirigami structures can be estimated and controlled using these displacement and maximum strain models. For further analysis of the displacement and the stress distributions in the Kirigami structures, the Kirigami stretch was simulated by the FEM. Maximum stress occurred at the slit edge of the Kirigami structure. This stress can be reduced using a circular-shaped edge compared to the corner-shaped edge. The stretchability of the Kirigami film was demonstrated using parylene microfabrication technologies. The fabricated Kirigami film exhibits high stretchability (1,100%) before film breaking. In the next chapter, the design and fabrication process of the Kirigami bioprobe devices based on the derived models along with simulations and demonstrations of the parylene Kirigami film will be presented.

Chapter 3: Kirigami bioprobe device

3.1 Introduction

The deformation model and the stress distribution of the Kirigami structure were derived and simulated in Chapter 2 for the effective design of the stretchable device using the Kirigami structure. In addition, it is confirmed that the Kirigami patterned film exhibited the high stretchability. In this chapter, stretchable bioprobe device using the Kirigami structure is demonstrated to confirm the ability of the Kirigami structure as the stretchable substrate for neuronal interfaces. Electronic devices used in *in vivo* experiments require low invasiveness, which includes matching of the mechanical characteristics to the biological tissues and biocompatibility of the device materials as well as proper electrical characteristics for each particular case. The design and fabrication process of the stretchable Kirigami bioprobe device which is intended for signal recordings from the mouse brain and heart, are described in the first part of this chapter. Electrical, mechanical and other characterizations which are required to achieve the low-invasive neuronal interface, of the fabricated Kirigami devices are confirmed, in the second part. In the third part, biological signal recordings using the fabricated Kirigami device are demonstrated to confirm the recording capability of the fabricated Kirigami device.

3.2 Design and fabrication of the Kirigami device

Based on the displacement model, simulations and demonstration of the Kirigami parylene film described in Chapter 2, the stretchable Kirigami bioprobe device was designed for the ECoG and ECG signal recordings from the mouse brain and heart. The designed Kirigami bioprobe device was fabricated using a microfabrication process, which includes a parylene substrate and embedded platinum layer for electrodes and interconnections.

3.2.1 Design of the Kirigami device

A stretchable Kirigami bioprobe device with a Kirigami patterned area of ~10 × 10 mm^2 was designed. This device consists of 5 × 91 slits of 10 μm width (cell array number of $N_{\mathrm{r}} = 5$, $N_{\mathrm{c}} = 45$) with a slit length, L_{slit}, of 1,600 μm, a gap between the slits, L_{gap}, of 400 μm, and a beam width, w, of 100 μm (Fig. 3.2.1). In Figure 3.2.1a, the pink and gray layers represent the device substrate of the parylene and the electrodes/interconnections of Pt/Ti, respectively. The materials used in this device exhibit biocompatibility and the parylene exhibits high flexibility. This stretchable Kirigami device employs 2 × 5 channels of a microelectrodes array with an electrode gap of 8,000 μm in the vertical direction and 1,980 μm in the horizontal direction. Each recording site of the 50-μm-diameter Pt electrode is connected to the contact pad with a zigzag interconnection (20-μm wide) (Fig. 3.2.1d). Each side of the Kirigami device has a guide structure for easy handling. The calculated maximum strain of this Kirigami device (5 × 45 cell units patterned on a ~10 × 10 mm^2 area) was ~455%. Another type of the Kirigami device, which consisted of 3 × 91 slits ($N_{\mathrm{r}} = 3$, $N_{\mathrm{c}} = 45$) with a different beam design ($L_{\mathrm{slit}} = 2{,}700$ μm, $L_{\mathrm{gap}} = 600$ μm, same $w = 100$ μm), was also designed (Fig. 3.2.2a). This stretchable Kirigami device employs a 2 × 3 channel microelectrodes array (diameter of 50 μm) with an electrode gap of 6,600 μm in the vertical direction and 3,300 μm in the horizontal direction. The calculated maximum strain of this Kirigami device (3 × 45 call units patterned on an area of ~10 × 10 mm^2) was ~860%. Dense Kirigami electrode devices, which have three interconnections (each of a width of 10 μm) embedded in each beam with a width of 100 μm, were also designed (Figs. 3.2.2b, c). The number of electrodes in the high dense Kirigami electrode devices is three times larger than that of the Kirigami devices with a single interconnection (width of 20 μm) in each beam (width of 100 μm) for the same Kirigami structures. The designs of Kirigami bioprobe devices are summarized in Table 3.1.

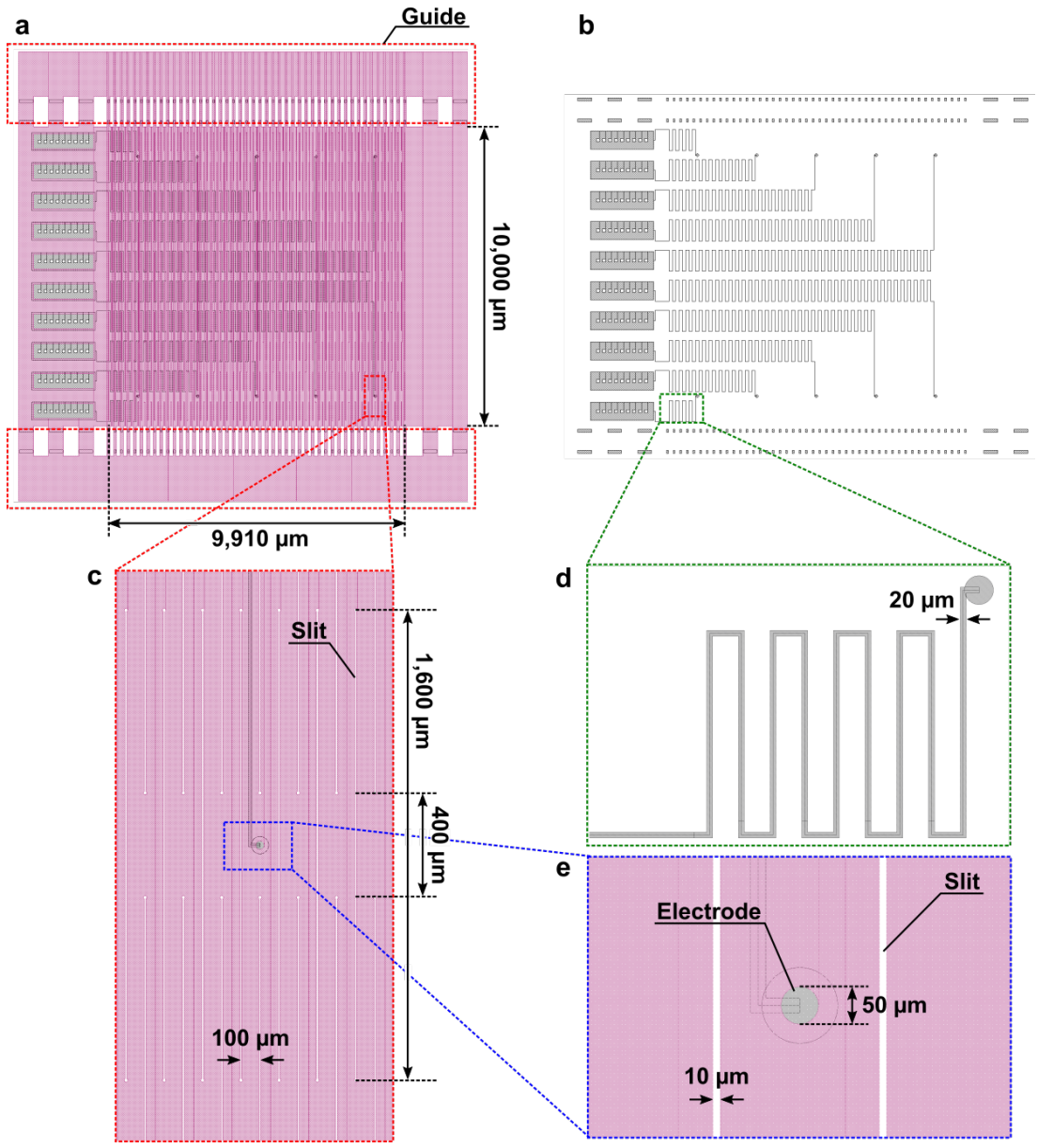

Figure 3.2.1 Design of the stretchable Kirigami bioprobe device (5 × 91 slits). (a) Entire image of the design of the Kirigami bioprobe device with a 2 × 5 channel electrode array (layer colored pink: device substrate of parylene and gray: electrodes and interconnections of Pt/Ti). An easy-to-handle guide for the Kirigami device was placed at each side (top and bottom side in the image). (b) Design of electrodes and interconnections of the Kirigami bioprobe device. (c) Enlarged view of the Kirigami slit patterned in a parylene substrate. (d) Enlarged view of the electrode and interconnections. (e) Enlarged view of the microelectrode with a 50 μm diameter.

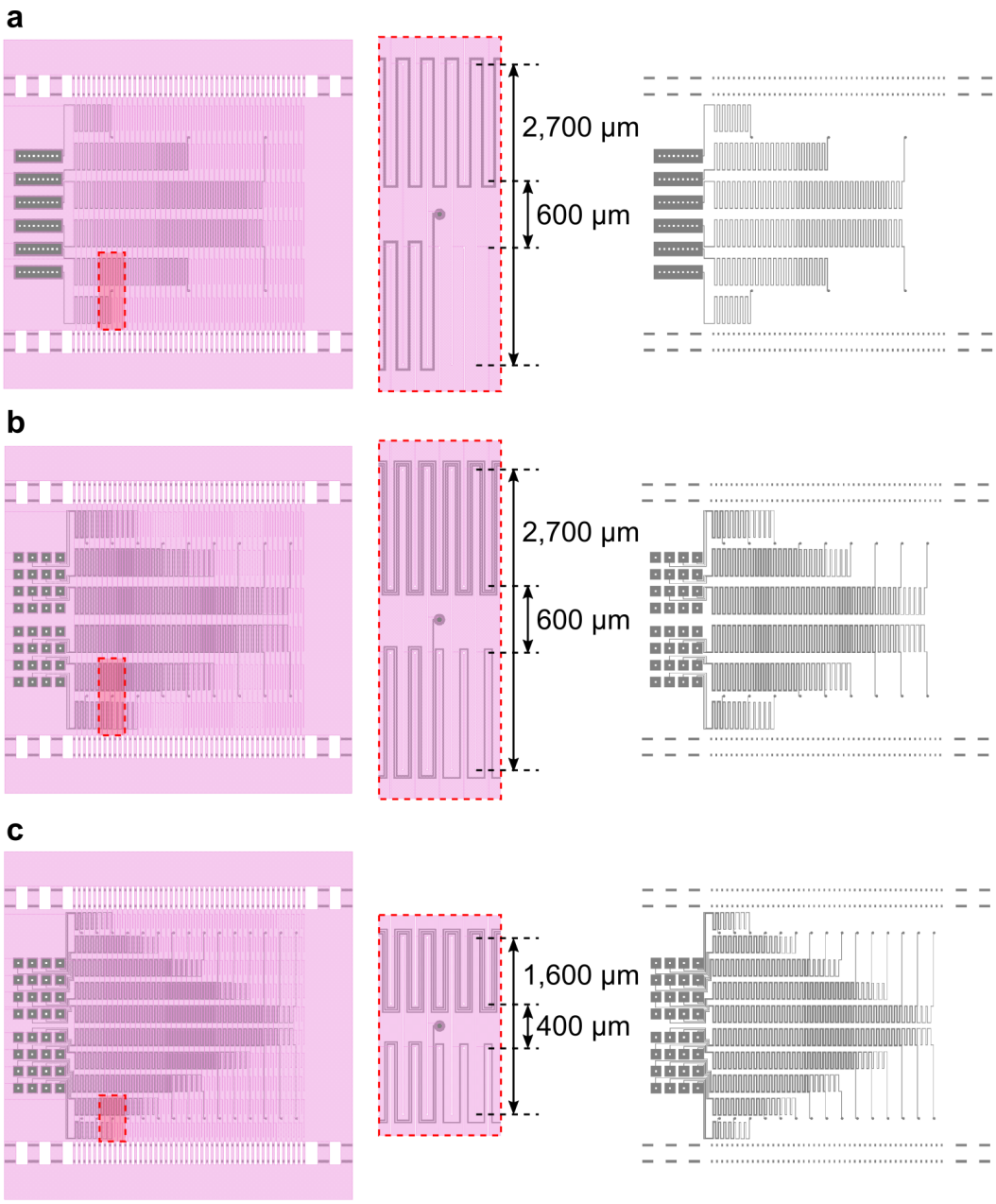

Figure 3.2.2 Alternative design of the stretchable Kirigami bioprobe device (left: entire design, right: interconnection design). (a) A 3 × 91 slit, 2 × 6 channel microelectrodes array. (b, c) high dense Kirigami electrode device with a 3 × 91 slit, 2 × 9 channel microelectrodes array (b) and a 5 × 91 slit, 2 × 15 channel microelectrodes array (c).

Table 3.1 Designs of the stretchable Kirigami bioprobe device

Slit length [μm]	Slit gap [μm]	Beam width [μm]	Film thickness [μm]	Number of cell array column × row	Number of electrode channels	Electrode gap vertical, horizontal [μm]	Maximum strain [%]	Figure No.
1,600	400	100	10	5 × 45	10	8,000 1,980	455	Fig. 3.2.1
2,700	600	100	10	3 × 45	6	6,600 3,300	860	Fig. 3.2.2a
1,600	400	100	10	5 × 45	30	8,000 660	455	Fig. 3.2.2c
2,700	600	100	10	3 × 45	18	6,600 1,100	860	Fig. 3.2.2b

3.2.2 Device fabrication

The fabrication process of the proposed Kirigami-based bioprobe device is shown in Figure 3.2.3. This device consists of an array of microscale planar electrodes for multi-site recording of biological signals. The device fabrication was the same as the parylene film process (Fig. 2.4.2), except that the electrodes were embedded in the film [94], [95]. The device bottom layer was formed by the deposition of a 5-μm-thick parylene-C film on a Si substrate [Fig. 3.2.3(i)]. To form the electrode layer, Pt with an adhesion layer of Ti (40-nm thick for Pt and 60-nm thick for Ti) was sputtered over the bottom parylene layer and subsequently patterned by plasma etchings [argon (Ar) for Pt and CF_4 for Ti] [Figs. 3.2.3(ii-iii)]. Then a 5-μm-thick parylene-C film was deposited over the electrode-/bottom parylene layers to form the device's top layer [Fig. 3.2.3(iv)]. Kirigami slits and electrode sites were structured by patterning both the top and the bottom parylene layers using O_2 plasma with a Ti mask [Figs. 3.2.3(v–vii)]. After removing the Ti mask by CF_4 plasma, the parylene device was released from the Si substrate using ethanol [Figs. 3.2.3(viii–ix)].

The fabricated Kirigami bioprobe device is shown in Figure 3.2.4. The fabricated device on the Si wafer and the release of the device from the Si wafer are shown in Figures 3.2.4a and b, respectively. Figure 3.2.4c shows microscopic images of the Kirigami device, which employs the device Pt electrode and zigzag interconnection patterned in the beam. For *in vivo* recording applications, the fabricated film device was packaged with a polyimide-based flexible printed circuit (FPC) (Fig. 3.2.4d). A fabricated device [a 3 × 91 slit design ($N_r = 3$, $N_c = 45$)] stretched to 650% by tweezers is shown in Figure 3.2.4e.

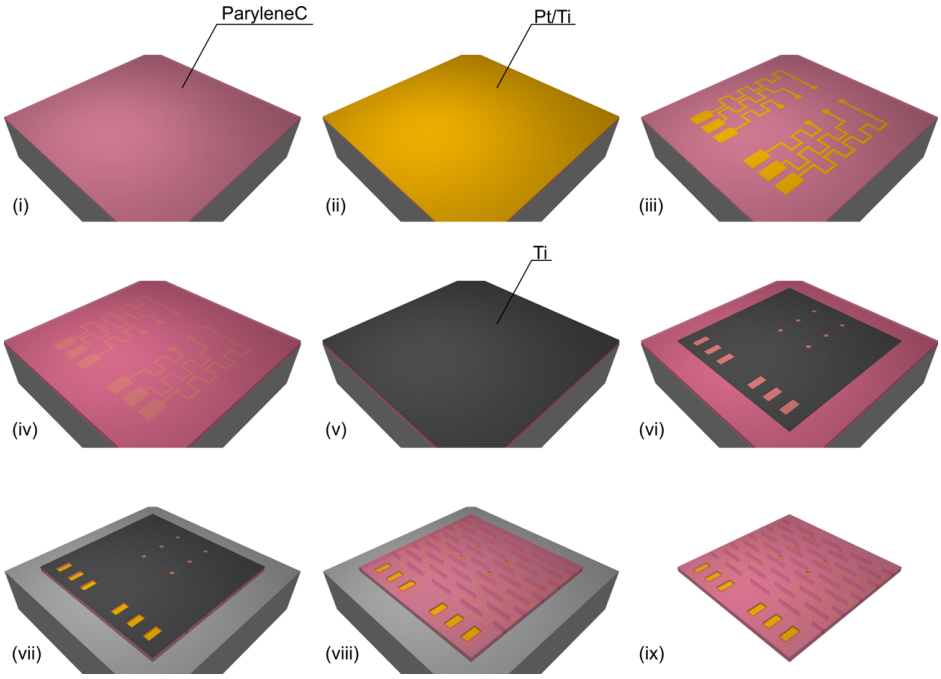

Figure 3.2.3 Fabrication process of Kirigami-based highly stretchable and flexible bioprobe devices: (i) deposition of the bottom layer of parylene-C on a Si substrate, (ii) sputtering of a Pt-electrode layer with a Ti adhesion layer over the parylene layer, (iii) electrodes and interconnections formed by plasma etching (Ar for Pt and CF_4 for Ti), (iv) deposition of the device's top layer of parylene-C over the Pt-electrode layer and the bottom parylene layer, (v) sputtering of a hard mask of Ti over the top parylene layer and (vi) patterning by CF_4 plasma, (vii) patterning of the top and bottom parylene layers by a O_2 plasma using the Ti hard mask, (viii) removal of the Ti mask using CF_4 plasma, and (ix) release of the parylene device from the Si substrate using ethanol.

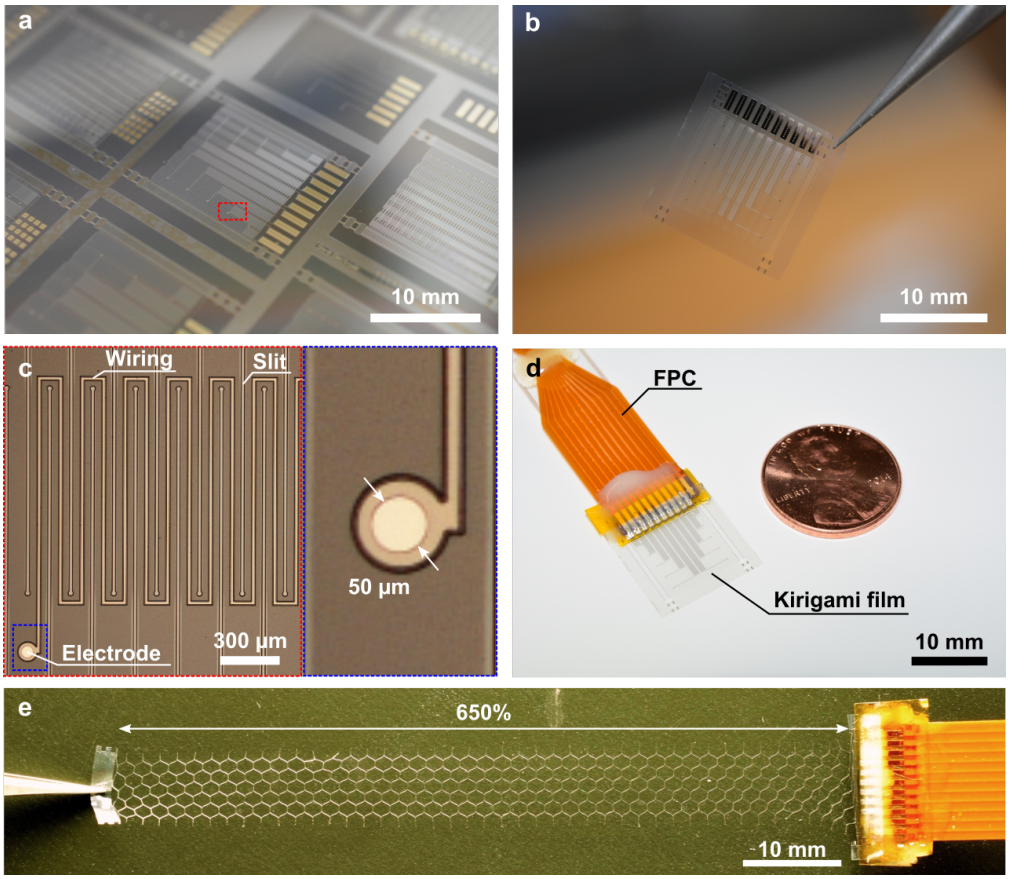

Figure 3.2.4 Fabricated Kirigami bioprobe device. (a) Photograph showing batch-processed devices on a Si substrate. (b) Photograph of the fabricated device after its removal from the Si substrate. (c) Photograph showing the 50-μm-diameter planar Pt-electrode site in a device connected with a zigzag Pt-interconnection. (d) Photograph of a device packaged with a polyimide-based FPC for subsequent *in vivo* applications. (e) Photograph showing a fabricated device [a 3 × 91 slit design ($N_r = 3$, $N_c = 45$)] stretched to 650% by tweezers.

3.2.3 Bi-axially stretchable Kirigami bioprobe device

The aforementioned Kirigami bioprobe device (Fig. 3.2.1) exhibits stretchability in one direction only. However, some biological tissues or organs (e.g. brain or heart) exhibit bi-axial deformation. To enhance the applicability of the Kirigami film, the design of a Kirigami film with bi-axial stretchability was also proposed. The bi-axial Kirigami film was realized by patterning each beam with a zigzag design (Fig. 3.2.5). The designed bi-axial Kirigami film [a 5 × 31 slit design ($N_r = 5$, $N_c = 15$)], is shown in Figures 3.2.5a and b. The fabrication process used was the same as for the parylene film-based bioprobe device process (Fig. 3.2.3). To bi-axial stretchability of the fabricated bi-axial Kirigami

film was demonstrated by placing the Kirigami film on a rubber balloon. The film was stuck to the balloon surface using water drop (Fig. 3.2.5c). The bi-axial stretchability of the film was observed by increasing the volume of the balloon. Figure 3.2.5d shows the Kirigami film as the balloon volume increases, thereby demonstrating the bi-axial stretchability of the film. A photograph showing a Pt-microelectrode site in a bi-axial Kirigami film device (before stretching) is shown in Figure 3.2.5e. The Pt-electrode is connected with a zigzag Pt-interconnection using a zigzag parylene beam.

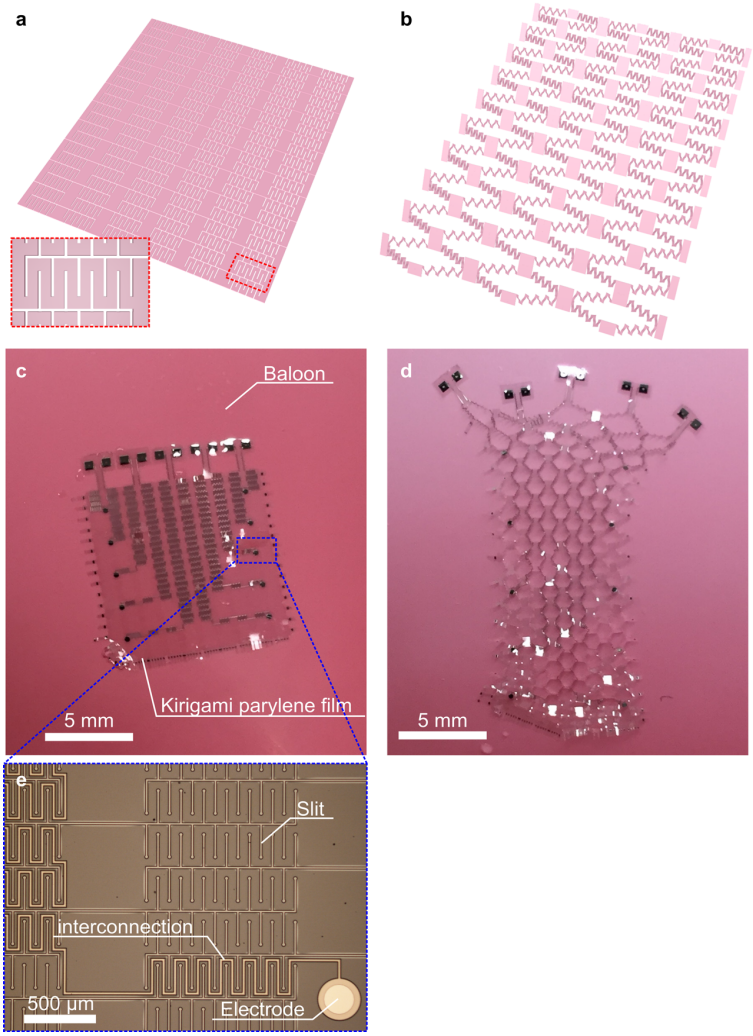

Figure 3.2.5 Bi-axial Kirigami film. (a, b) Schematic diagrams of a bi-axial Kirigami film (a: before and b: after stretching). (c) Photograph of a fabricated film placed on a rubber balloon. (d) Bi-axial stretchability of the film observed by increasing the volume of the balloon. (e) Photograph showing a Pt-microelectrode site in a bi-axial Kirigami film device (before stretching). The Pt-electrode is connected with a zigzag Pt-interconnection using a zigzag parylene beam.

3.3 Electrical and mechanical characterization of Kirigami device

Electrical, mechanical and other characterizations of the fabricated Kirigami devices reveal the practicability of these devices as neuronal interfaces from various perspectives. The electrical characteristics of the electrodes embedded in the fabricated Kirigami devices are confirmed by impedance measurements during the device stretching. As for the mechanical characterizations, the stress–strain curves are obtained by measuring the force of stretch for the fabricated Kirigami devices. In addition, the device durability during repetitive device strain and its stretchability in the out-of-plane-deformation process of the fabricated Kirigami devices, which are confined by another layer assuming the device implantation under the skin, are confirmed.

3.3.1 Impedance characteristics of a Kirigami device

The electrolyte/metal interfacial electrical impedance of the Pt electrode was measured in a phosphate-buffered saline (PBS) solution. Without stretching the film device, which was designed with 5×91 slits, the magnitude of the Pt-electrode impedance was 311 ± 32 kΩ [mean ± standard deviation (SD)] at 1 kHz (Fig. 3.3.1). This impedance is low enough to measure the ECoG signals [96]. The strain-dependent impedance characteristics of the Pt electrodes taken from a Kirigami film device designed with 3×91 slits are shown in Figure 3.3.2. The impedance is independent of the film stretching, when the film is stretched between 0% and 500%. In this stretching regime, the electrical properties of the Pt electrodes do not change because each beam (parylene/Pt/parylene layer system) bends and significant stress concentration does not occur. As the film stretches between 600% and 700%, the electrode impedance drops slightly. This is probably due to the stress induced peeling of the parylene bi-layer and the Pt layer exposed to the PBS solution (e.g. concentrated stress at the beam edge). However, at 800% of film stretching, the electrode impedance increases significantly ($>10^6$ Ω) prior to the film tearing off. This is because a partial breaking of the Kirigami structure around the slit edge occurred at a strain close to the maximum strain of the Kirigami device (860%) and the device interconnections were partially broken.

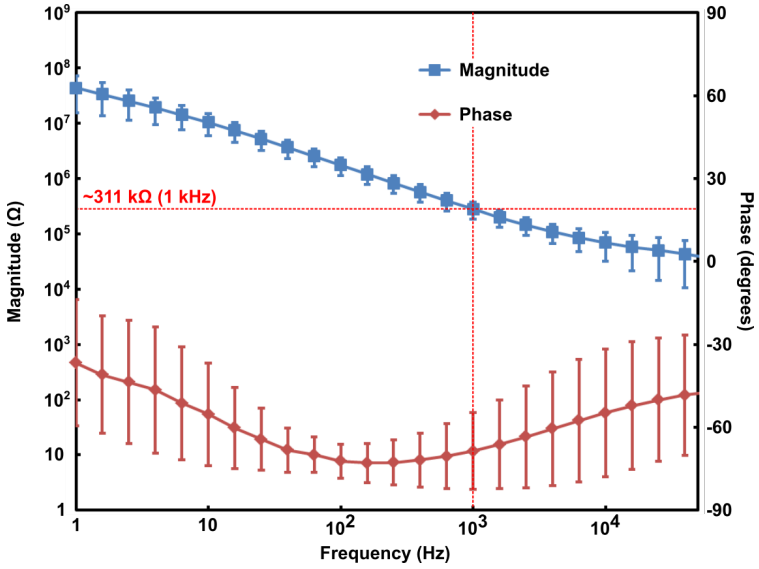

Figure 3.3.1 Impedance of the fabricated Kirigami device without device stretch. Impedance characteristics of the fabricated device measured in PBS without device stretching (0%). Averages and standard deviations for both impedance magnitude and phase characteristics were taken from eight samples; the error bars indicate SD.

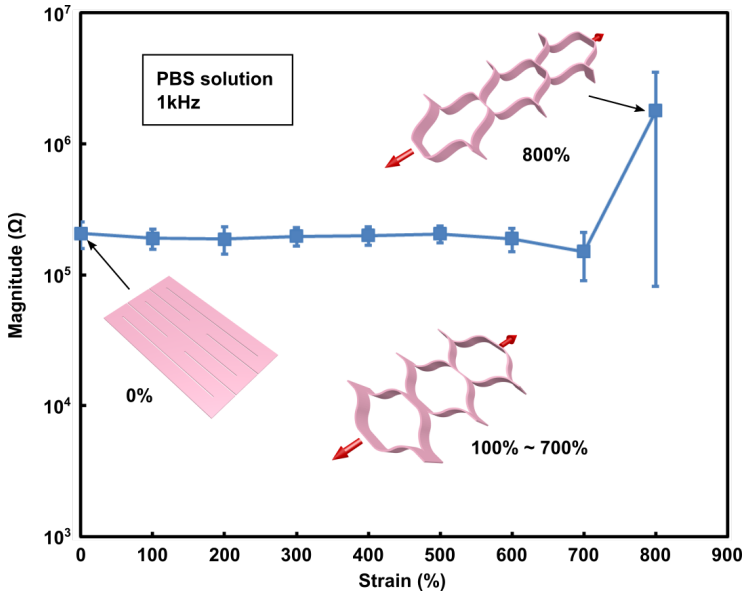

Figure 3.3.2 Impedance of the fabricated Kirigami device during the device stretch. Strain-dependent impedances of the fabricated device at 1 kHz in PBS. Here, the measured device is a film designed with 3 × 91 slits ($N_r = 3$, $N_c = 45$), which is stretched from 0% to 800%. Averages and SD for both impedance magnitude and phase characteristics were taken from 11 samples; the error bars indicate SD.

3.3.2 Stress–strain curve of the Kirigami device

The experimentally measured stress (force)–strain curve for a Kirigami device designed with 5 × 91 slits (green triangles in Fig. 3.3.3a) is included in Figure 3.3.3. The stress–strain curve of the Kirigami device is divided to three deformation regions. In the initial region, where the strain is in the range 0%–20% [Fig. 3.3.3a(i) red dashed square], the beam bending around each slit exhibits the in-plane bending deformation [Fig. 3.3.3b(i)]. In this region, each beam bends to the thicker direction. Therefore, the beam thickness is considered as the designed beam width (w) of 100 μm, which is 10 times thicker than that of the designed beam thickness of 10 μm. As a result, the stress in the initial region increases rapidly. In the second region, where the strain is in the range 20%–250% [Fig. 3.3.3a(ii) blue dashed square], the deformation exhibit its out-of-plane deformation [Fig. 3.3.3b(ii)]. In this region, beam bending occurs in the thinner direction of each beam and the stress is gradually increased as the strain increases. The model derived in Chapter 2 takes into account the out-of-plane deformation of this region. In the third region, where the strain range is above 250% [Fig. 3.3.3a(iii) green dashed square], the film strain becomes saturated due to the limitation of structural deformations [Figs. 3.3.3b(iii), 2.2.4] and the stress is rapidly increased.

The experimentally obtained slope (20%–250% strain) was compared with the values calculated by formula (2.9) (red line in Fig. 3.3.3a) and the fit by the FEM (blue squares in Fig. 3.3.3a). The simulated stress–strain characteristic was derived by the combination of the simulation results for the one-cell unit (Fig. 2.3.1). Since the fabricated device has a parylene thickness of 11 μm (the design value was 10 μm), the same film thickness for both analytical and FEM results was used. Saturation was confirmed by both experimental and FEM data. The maximum strain of the device reaches ~470%. The measurement of the 5 × 91–slit device confirmed that a 9-mN strain–force (0.08 MPa in stress) to the film realizes a high-film stretchability of ~250%. In this regime (20%–250% strain), the film's strain is proportional to the stress (force) (green triangles in Fig. 3.3.3a). The difference in the slope between analytical and experimental values in this second region (20%–250%) is 12.2%, except for the difference in the initial region (0%–20%) (green triangles in Fig. 3.3.3a). One possible reason for this slope difference between experimental and calculated or simulated results is due to the effect of the device fixation in the measurement. Here, each film side is fixed with a ridged chuck for the film substrate, which limits stretching in some beams (~two column cell units) because of the limitation of the deformation in the perpendicular direction to the stretching direction of the Kirigami structure. This edge effect is not considered in the equations or the FEM. In addition, these calculations do not include the effect of the metal

layer (40-nm thick for Pt, 60-nm thick for Ti). For an accurate analysis of the fabricated Kirigami device, the displacement of the multiple layered Kirigami system was calculated, in which each beam consists of the parylene substrate and the embedded Pt/Ti-metal interconnection, using equations (2.24–2.37). By considering the metal layer, the slope difference with and without the metal layer is 0.7%. Since the thickness of the metal layer (Pt/Ti: ~100 nm) in the fabricated device is 110 times smaller than that of the parylene

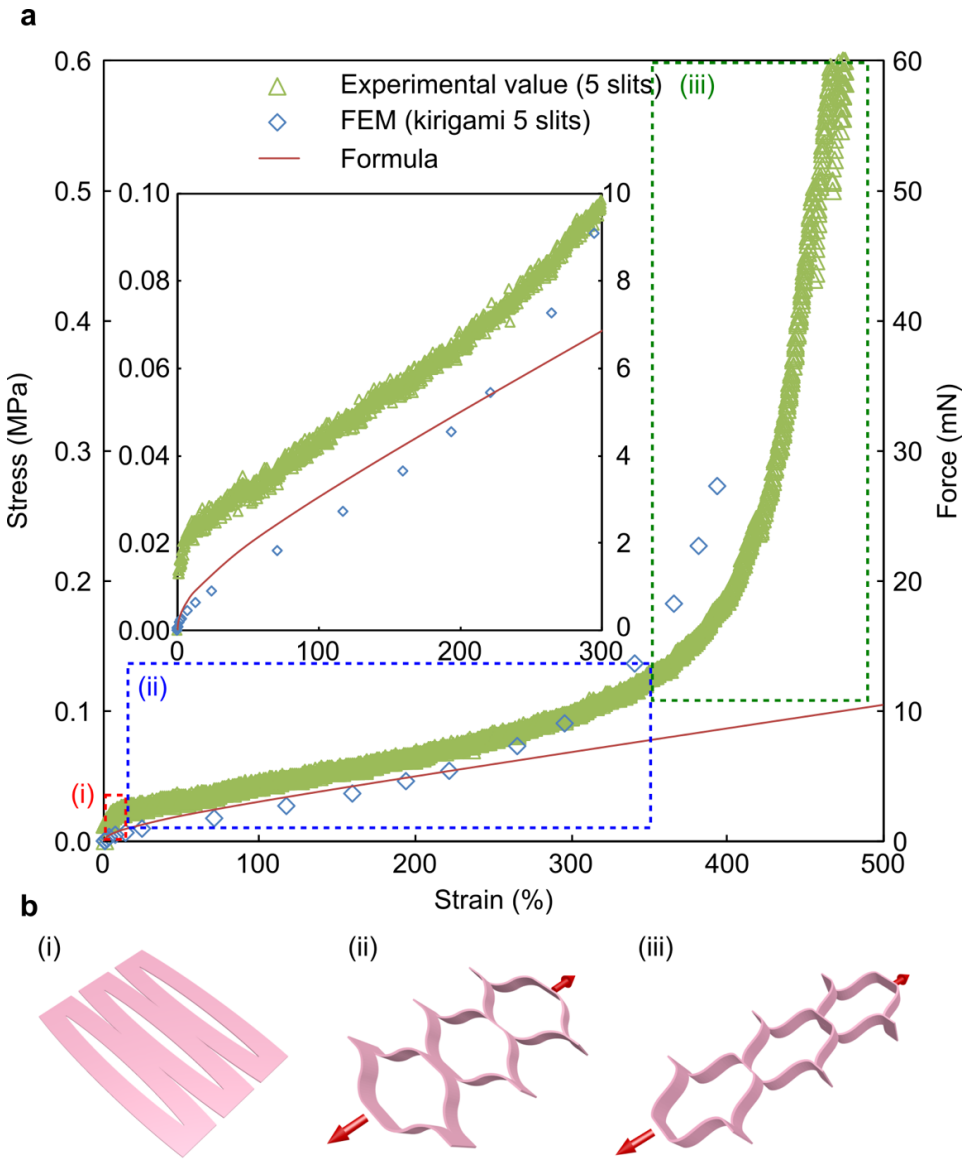

Figure 3.3.3 Mechanical characteristics of the fabricated Kirigami device. (a) Stress–strain curve of the fabricated Kirigami device with 5 × 91 slits ($N_r = 5$, $N_c = 45$, green triangles) calculated using formulas (2.9) (red line) and FEM simulation (blue squares). Inset graph shows the initial region of the stress–strain curve. (b) Stretched Kirigami structure in each stretch region.

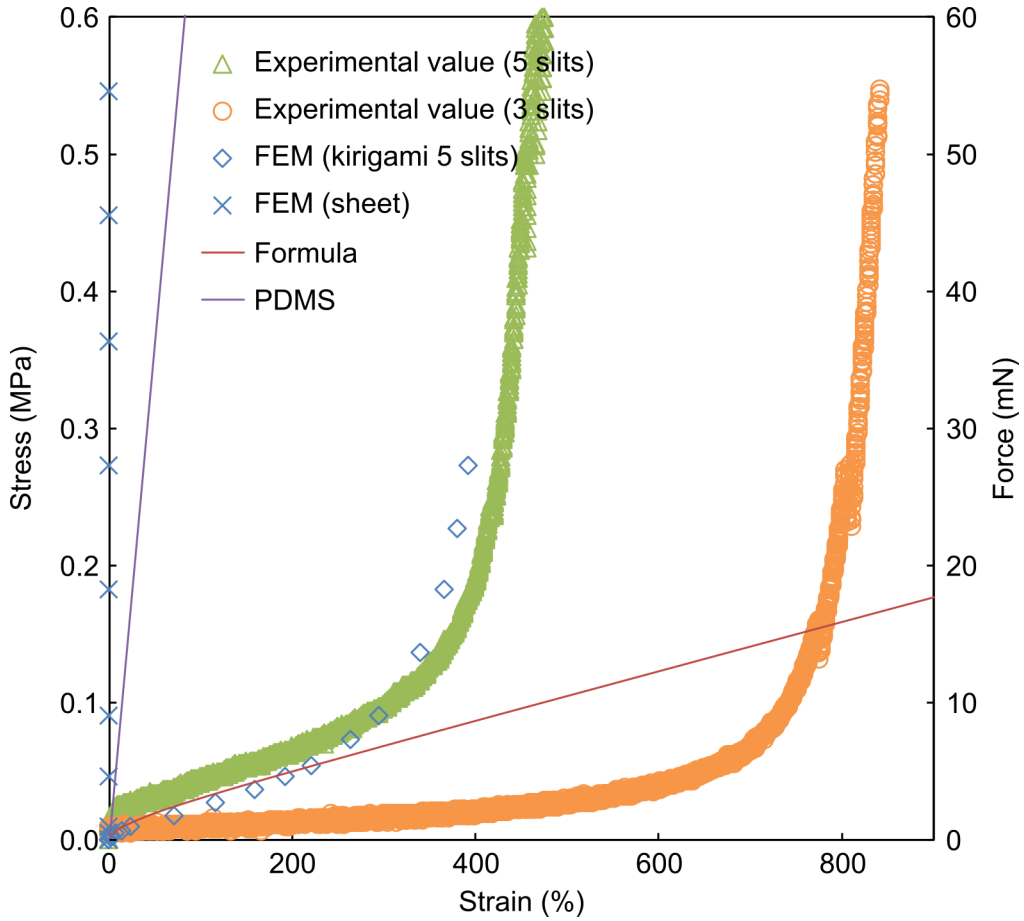

Figure 3.3.4 Experimentally measured strain–strain characteristics of the fabricated Kirigami device. The measured device is a designed film with 5 × 91 slits ($N_r = 5$, $N_c = 45$, green triangles) and 3 × 91 slits ($N_r = 3$, $N_c = 45$, orange circles). The graph also includes calculated values (red line) and FEM simulation values [blue squares correspond to the case with the slit (Kirigami) and blue crosses correspond to the case without the slit (sheet)] and stress–strain characteristic of PDMS [81] (purple line).

device (11 μm), no significant slope differences are observed in this regime. Further considerations of the in-plane mode and the limitation of the stretch at the edge of the Kirigami structure in the calculations offer more accurate data fittings. Both the equations and the FEM values are based on the out-of-plane bending mode and do not consider the in-plane deformation and side effect of the stretch limitation. The other fabricated Kirigami film with 3 × 91 slits exhibits an increased maximum strain of ~840% at 58 mN (0.53 MPa) (orange circles, Fig. 3.3.4).

A parameter was considered for the evaluation of the effective Young's modulus. This parameter, which was taken from the stress–strain curve of the Kirigami device with

5 × 91 slits and 3 × 91 slits (in the second regions: 20%–250% for 5 × 91 slits and 20%–450% for 3 × 91 slits), has a value of 23 kPa and 3.6 kPa, respectively. The effective Young's modulus of the Kirigami device with 5 × 91 slits (23 kPa) is ~30 times lower than that of the conventional elastomer-based stretchable devices with PDMS (730 kPa for PDMS [81]) (purple line in Fig. 3.3.4). The calculated stress–strain curve for a parylene film (Young's modulus of 2.8 GPa) without slits is also included in Figure 3.3.4 for comparison purposes (blue crosses, Fig. 3.3.4).

3.3.3 Durability test of the Kirigami structure

Cycling load tests of the Kirigami film were also conducted. For the evaluation of the Kirigami device, one-row Kirigami devices were fabricated (Fig. 3.3.5). The one-row Kirigami devices consists of 1 × 72 slits of 10 μm width (cell array number of $N_{\mathrm{r}} = 1$, $N_{\mathrm{c}} = 36$). There are two types of the one-row Kirigami devices, which have different device widths, i.e., 2 mm and 3 mm, respectively. The first is the one-row Kirigami device with a slit length, L_{slit}, of 1,600 μm, a gap between the slits, L_{gap}, of 400 μm, and a beam width, w, of 100 μm in the area of ~2 × 8 mm^2 (Fig. 3.3.5a). This one-row Kirigami device exhibits a calculated maximum strain of ~450%. The other design has the Kirigami pattern with a slit length, L_{slit}, of 2,600 μm, a gap between the slits, L_{gap}, of 400 μm, and a beam width, w, of 100 μm in the area of ~3 × 8 mm^2 (Fig. 3.3.5b). This device exhibits a calculated maximum strain of ~900%. In Figure 3.3.5, layers colored pink and gray represent the device's parylene substrate and the electrodes/interconnections of Pt/Ti, respectively. These stretchable Kirigami devices employ a 1 × 6 channel microelectrodes array. As discussed in Chapter 2, each slit edge has a circular-shaped edge to avoid stress concentration at each slit edge. The designs of one-row Kirigami devices are summarized in Table 3.2.

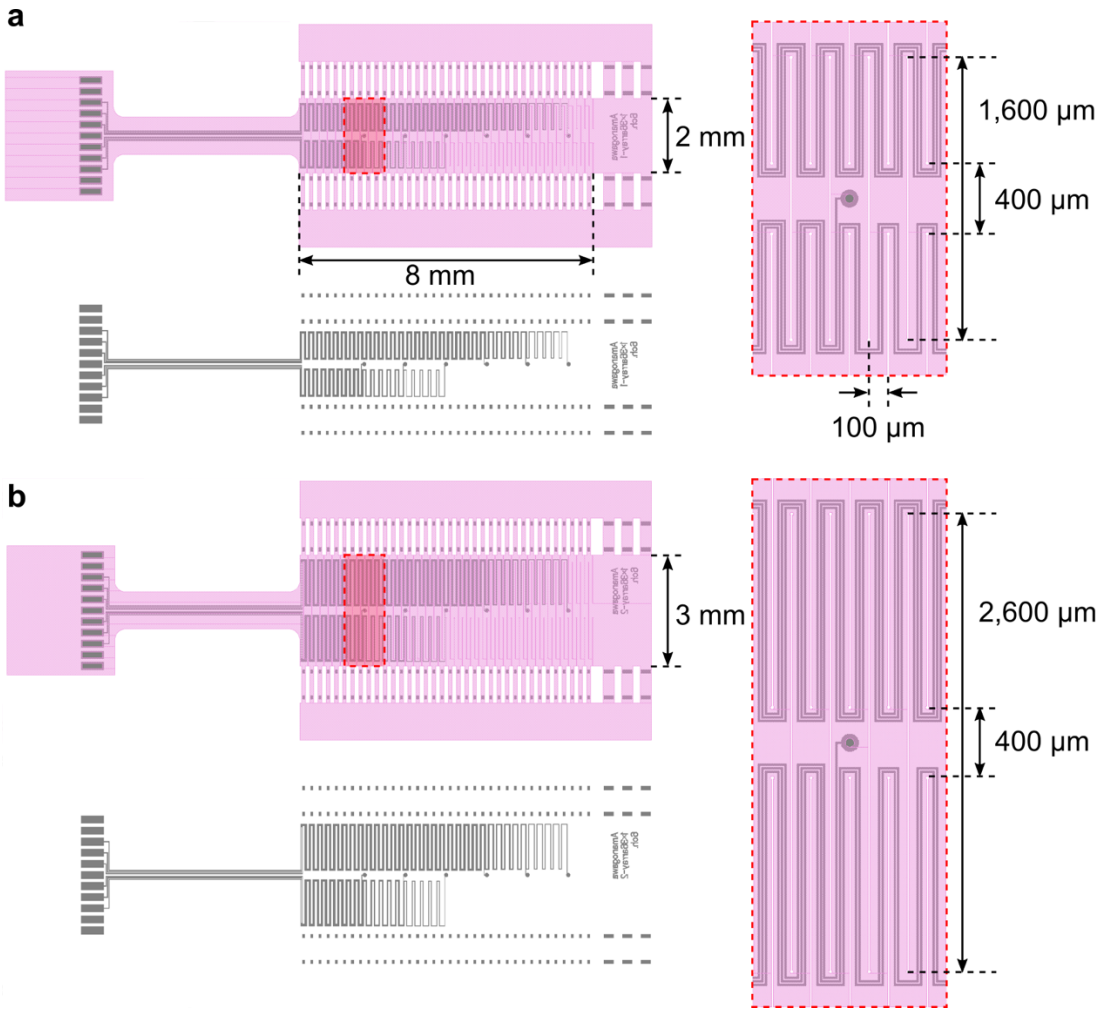

Figure 3.3.5 Design of the one-row Kirigami devices composed of 1 × 72 slits ($N_r = 1, N_c = 36$) for the evaluation of the Kirigami structure. (a) One-row Kirigami devices with $L_{slit} = 1{,}600$ µm, $L_{gap} = 400$ µm, $w = 100$ µm and maximum strain of ~450% and (b) $L_{slit} = 2{,}600$ µm, $L_{gap} = 400$ µm, $w = 100$ µm and maximum strain of ~900%.

Table 3.2 Designs of the one-row Kirigami devices for the evaluation

Slit length [µm]	Slit gap [µm]	Beam width [µm]	Film thickness [µm]	Number of cell array column × row	Number of electrode channels	Electrode gap [µm]	Maximum strain [%]	Figure No.
1,600	400	100	10	1 × 36	6	1,100	450	Fig. 3.3.5a
2,600	400	100	10	1 × 36	6	1,100	900	Fig. 3.3.5b

Using this one-row Kirigami device (width of 2 mm), the durability test of the Kirigami structure was conducted. A 1,000 cycle load was applied to the Kirigami device, while each strain was 125%, 188%, 250%, and 313% (total load cycles = 4,000) (Fig. 3.3.7). The repetitive stretch of the Kirigami device was accurately controlled using a linear actuator (SKR2602A, THK Co., Ltd.), which was driven by a stepper motor (PKP244D23A2, Oriental Motor Co., Ltd.) and a motor driver (L6470, STMicroelectronics Inc.) (Fig. 3.3.6). At the strain range 125%–188%, small cracks were observed at some edges of the slits in the Kirigami film; however, the Kirigami film was not fractured and plastic deformation was not observed. At a 250% strain, plastic deformation slightly occurred and the film did not completely return to its original shape after the stretch was released. For a further strain of 313%, the plastic deformation in the film was increased, as observed in the microscopic image ("313%" in Fig. 3.3.7). Although some film cracks were observed at the edge of the slit, these cracks were not extended during the cycling load test and the Kirigami film was not fractured (not separated).

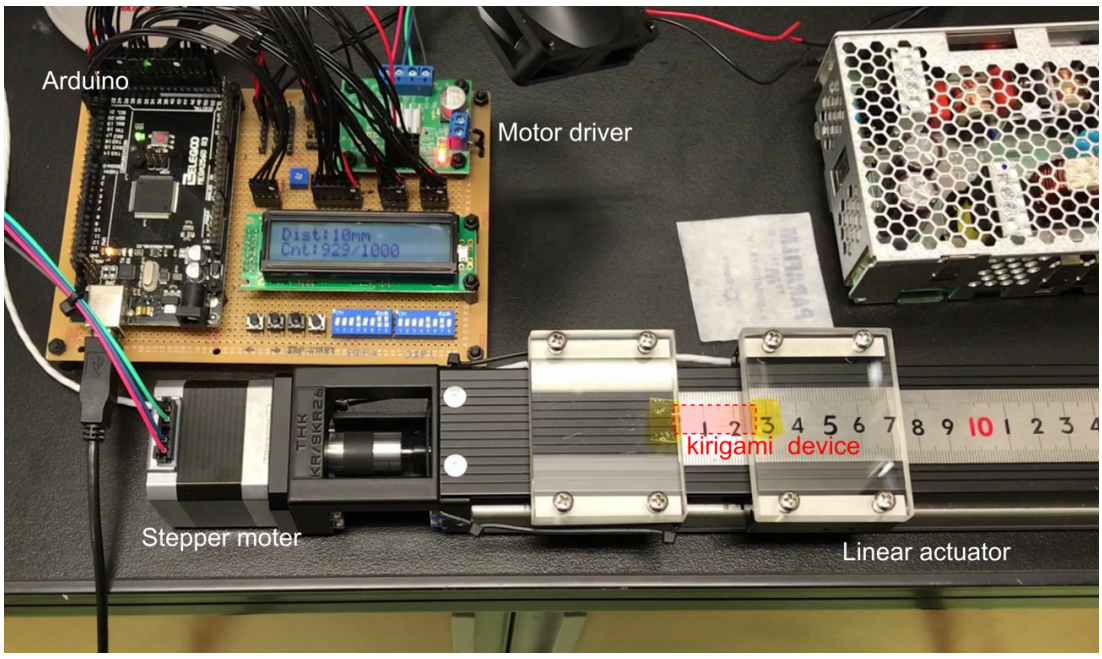

Figure 3.3.6 Linear actuator controlled by a stepper motor and a motor driver for repetitive stretching of the Kirigami device.

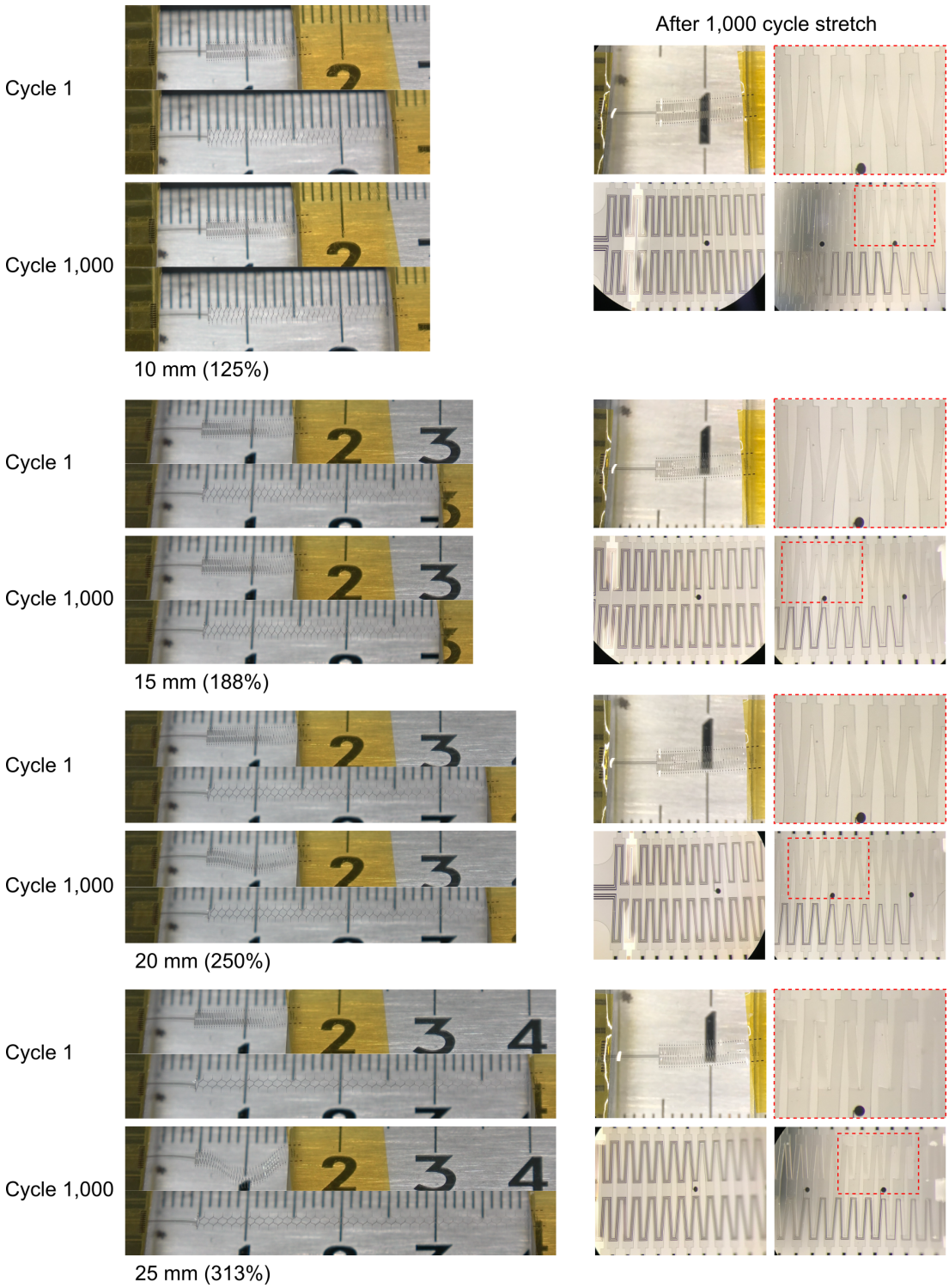

Figure 3.3.7 Durability test of the Kirigami structure. A 1,000-cycle load was applied to the Kirigami device, while each strain was 125%, 188%, 250%, and 313% (total load cycles = 4,000).

3.3.4 Stretchability of the Kirigami structure in another layer

In practical applications, such as long-term recording accompanied by the device implantation into the biological tissues, additional layers (e.g. skin and fat) will be placed over the device during the Kirigami device implantation on the tissue surface. In this case, the out-of-plane deformation of the Kirigami device is confined by these additional layers and the stretchability of the Kirigami device might be affected. Hence, an additional experiment to confirm the stretchability of the Kirigami structure was conducted, while the out-of-plane deformation was confined by another layer assuming that the Kirigami device is implanted to the biological tissues. Two types of experiments using Ecoflex (Ecoflex™ 00-20, Smooth-On, Young's modulus = 56 kPa) instead of using a biological tissue (e.g. skin and muscle) were conducted. In the first one, the Kirigami film (effective calculated modulus: 1.2–4.6 kPa) was sandwiched between two layers of ~1 mm-thick Ecoflex with water (Fig. 3.3.8). In the second one, the Kirigami film was embedded in ~2 mm-thick Ecoflex film (Fig. 3.3.10).

In the first experiment, the Kirigami film which was sandwiched between two ~1 mm-thick Ecoflex layers with water, exhibited a stretchability, which ranged from 0% to 179% (Fig. 3.3.9). However, the Kirigami film in the Ecoflex exhibited a non-uniform stretchability between the left and right parts of the film. This was probably due to fact that a part of the Kirigami film had a strain prior to its sandwiching between the Ecoflex layers (strain = 0%). The left part of the Kirigami film, which had the strain, probably caused a higher contact stress at the interface between the Kirigami film and the Ecoflex

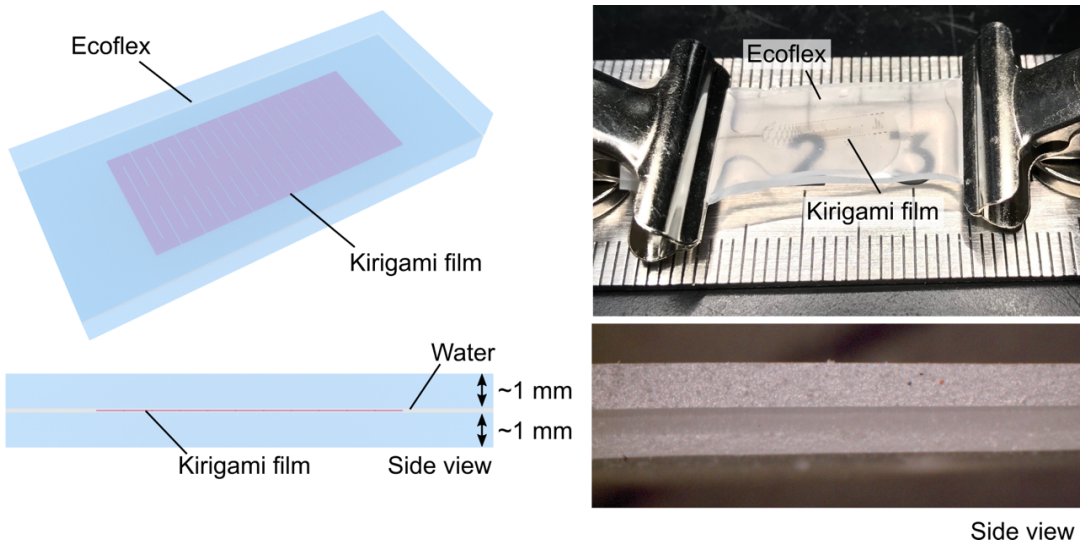

Figure 3.3.8 Schematic diagram and photographs of the stretchability test of the Kirigami film sandwiched between two layers of ~1 mm-thick Ecoflex with water.

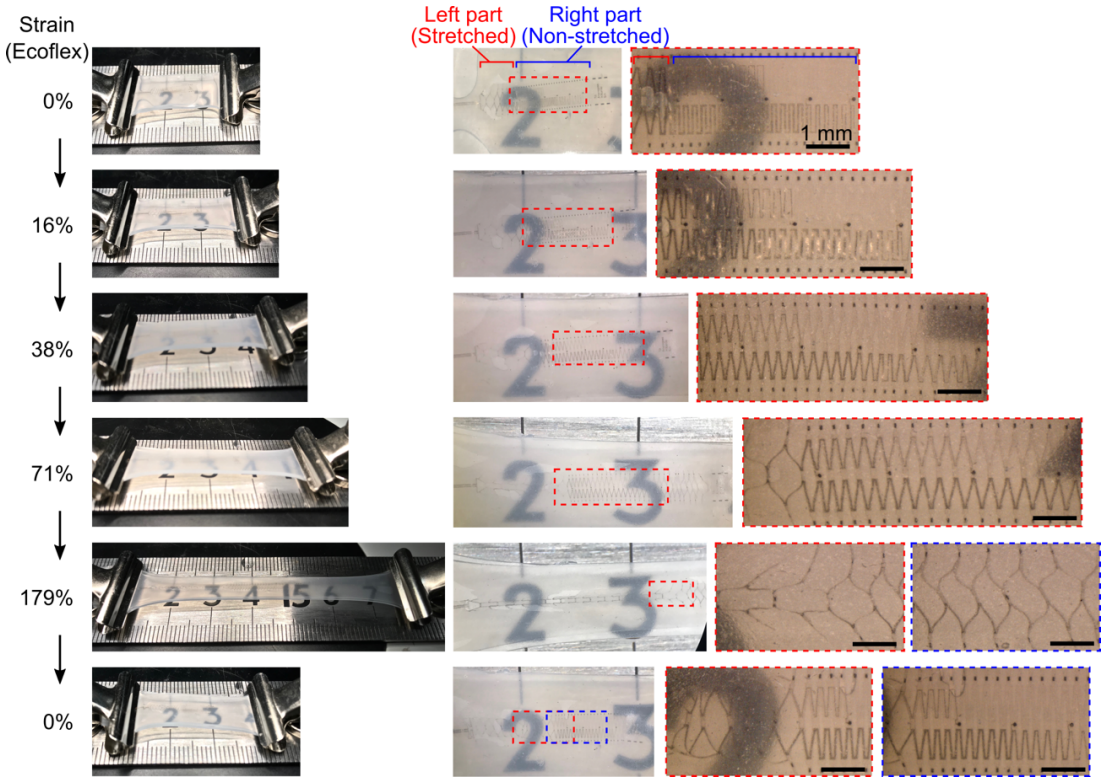

Figure 3.3.9 Stretchability of the Kirigami film sandwiched between two layers of Ecoflex. The strain range of the Ecoflex is 0%–179%.

surface compared to that at the right-hand side. These differences in the Kirigami's uniformity and contact stress induced the non-uniform stretchability of the Kirigami film in Ecoflex. As seen in the picture of a 179%-strain, the left part of the Kirigami (red dashed square in the picture) exhibits a larger strain compared to that in the right part (blue dashed square).

In the second experiment, the Kirigami film, which had the pre-strain in the device's right part, embedded in Ecoflex (total thickness = 2 mm) also exhibited its stretchability (Figs. 3.3.10, 3.3.11). The Ecoflex stretchability ranged from 0% to 130%. The variability of the distance between each beam was needed to enable the Kirigami structure stretchability; hence, the Kirigami film had some strain prior to the Ecoflex embedding (Fig. 3.3.11, 0%). In the strain range 0%–78% of the Ecoflex, the Kirigami film showed no fractures and returned to its original structure, when the stretch was released. However, in the strain of 130% of the Ecoflex, the Kirigami film showed a partial fracture, which remained after the strain was released.

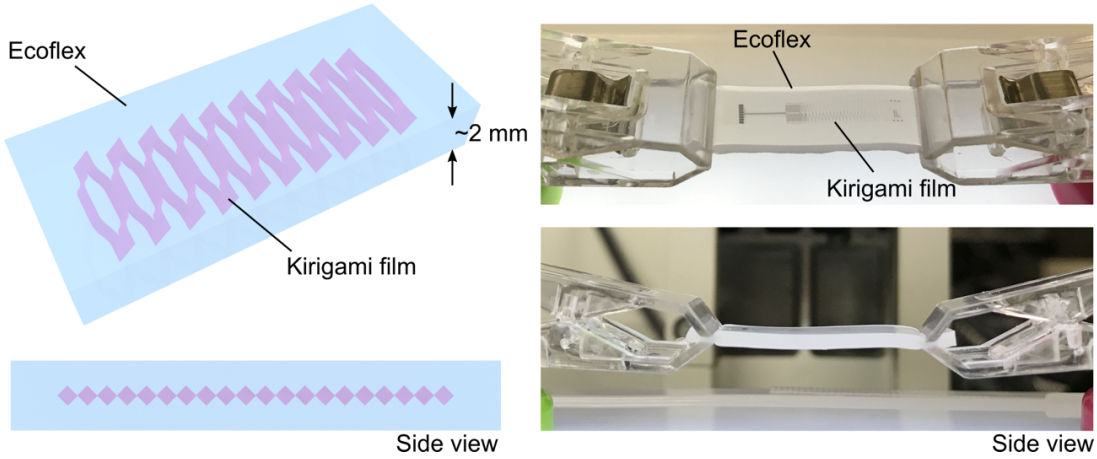

Figure 3.3.10 Schematic diagrams and photographs of the stretchability of the Kirigami film embedded in a ~2 mm-thick Ecoflex film. The Kirigami film had a pre-strain in the device's right part prior to its embedding in the Ecoflex.

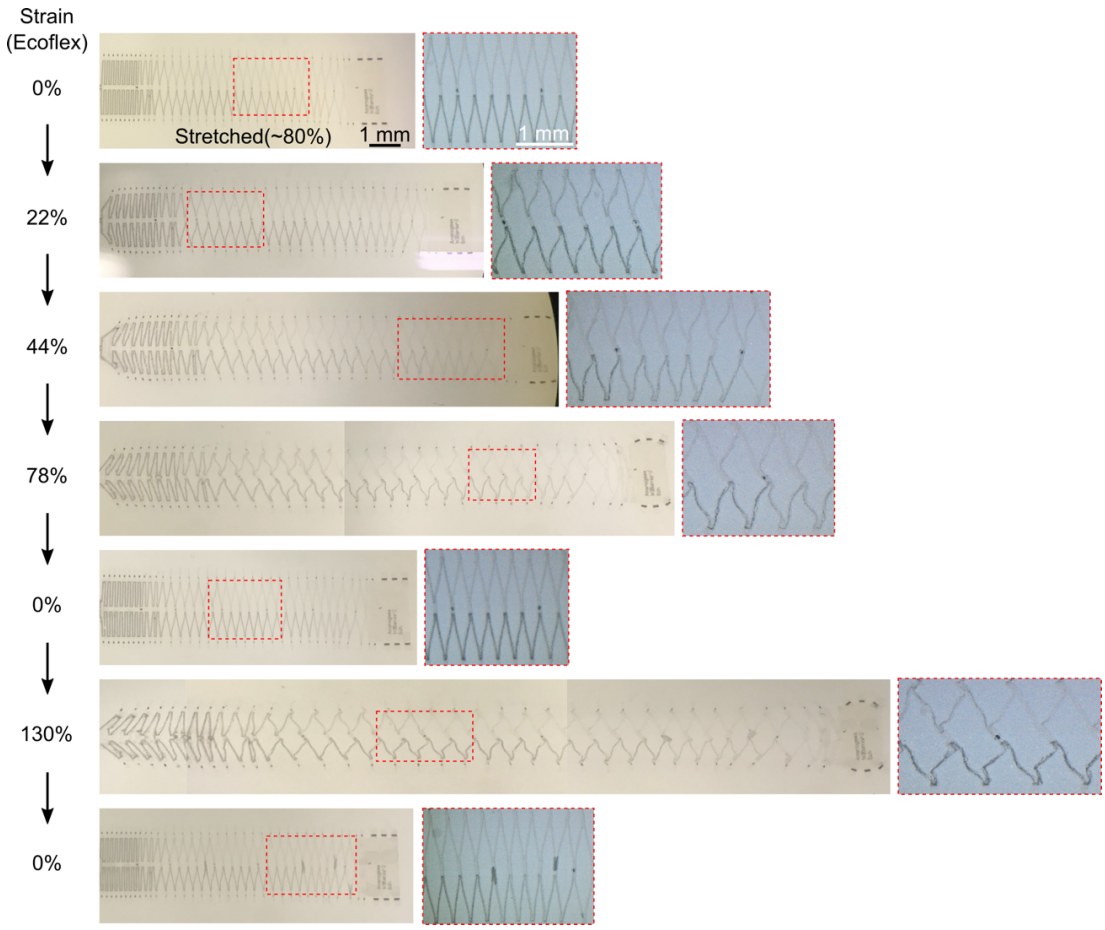

Figure 3.3.11 Stretchability of the Kirigami film embedded in the Ecoflex film. The strain range of the Ecoflex is 0%–130%.

3.4 Biological signal recording using a Kirigami bioprobe device

The recording capability of the fabricated Kirigami device was confirmed in the ECoG and ECG signal recordings from a mouse's brain and heart. In the ECoG recording, the interval of the Pt electrodes embedded in the Kirigami device is adjusted to the distance of two areas of the brain cortex. This is achieved by stretching the Kirigami device to record signals from multiple areas simultaneously. In the ECG recording, the recording capability of the Kirigami device from deformable tissues was confirmed. All experimental procedures regarding mice and animal care were approved by the Toyohashi University of Technology animal experiments committees.

3.4.1 *In vivo* ECoG signal recording

A challenge for highly stretchable, deformable, and flexible bioprobe film devices is the recording of neuronal signals from the brain tissue, which is a soft tissue and has a spherical shape and pulsatile motion in *in vivo* recordings. Recent advances in microfabrication technologies have resulted in the realization of flexible microscale planar ECoG electrode array devices. Their advantage of conformal wrapping onto a brain tissue has been demonstrated [31], [97], [98]. An additional requirement for such devices is that the electrode array must have design variability, such as application-dependent tunable intervals between the electrodes during measurements. Other requirements include conformal wrapping of an *in vivo* brain, which shows an increase/decrease in its tissue volume due to the pulsation of the brain.

A fabricated 5×91 slit Kirigami-based bioprobe device is shown in Figures 3.4.1a and b. This device, which consists of 10 channel planar Pt electrodes [50-μm diameter, 311 ± 32 kΩ (mean ± SD) impedance at 1 kHz], demonstrates the advantage of tunable intervals between the electrodes over the cortical surface of a mouse *in vivo* brain. Here, the mouse's strain, sex, and weight used are C57BL, male, and 17.0 g, respectively. After anesthesia by intraperitoneal injection using urethane (50 μl of 30% solution per 10 g body weight), the head of the mouse was fixed with stereotaxic apparatus (SR-50; Narishige, Tokyo, Japan). Some of the cranium and dura mater (0–5 mm posterior and 1–4 mm lateral to bregma) over the parietal and occipital lobes of the right hemisphere were removed. Then, Ch. 9 and Ch. 8 electrodes were placed on the visual cortex (primary visual cortex, V1, 4 mm posterior and 2.5 mm lateral from bregma) and barrel cortex (primary somatosensory cortex barrel field, S1B, 1 mm posterior and 3 mm lateral from bregma), respectively. To implement simultaneous neuronal recordings from the V1 and S1B of the mouse brain, the positions of the electrodes were aligned with these cortical areas, while the gap between the electrodes increased due to film

stretching (Figs. 3.4.1a, c). After positioning the first electrode of Ch. 9 over the V1, the second electrode of Ch. 8 was positioned over the S1B (3 mm away from the V1) by stretching the film and changing the electrode gap from 2 mm (initial gap, 0% strain) to ~3 mm (50% strain at 3.3 mN). Although the film's strain caused 3D deformation to each beam, which results in a gap between the Pt electrode and the tissue surfaces, this gap could be filled with a conductive solution of saline and each electrode site detects tissue signals via the saline (Fig. 3.4.5). Stimulus-related activity of V1 and S1B was recorded by applying visual and somatosensory stimulations to the mouse's eye and whiskers. The visual stimulation to activate V1 was applied to the mouse's left eye by a white LED (500 ms in duration, 6 s in intervals between trials) (Fig. 3.4.2a). S1B was activated by mechanically stimulating the principal whiskers by an electromagnetic vibrator (2 ms in

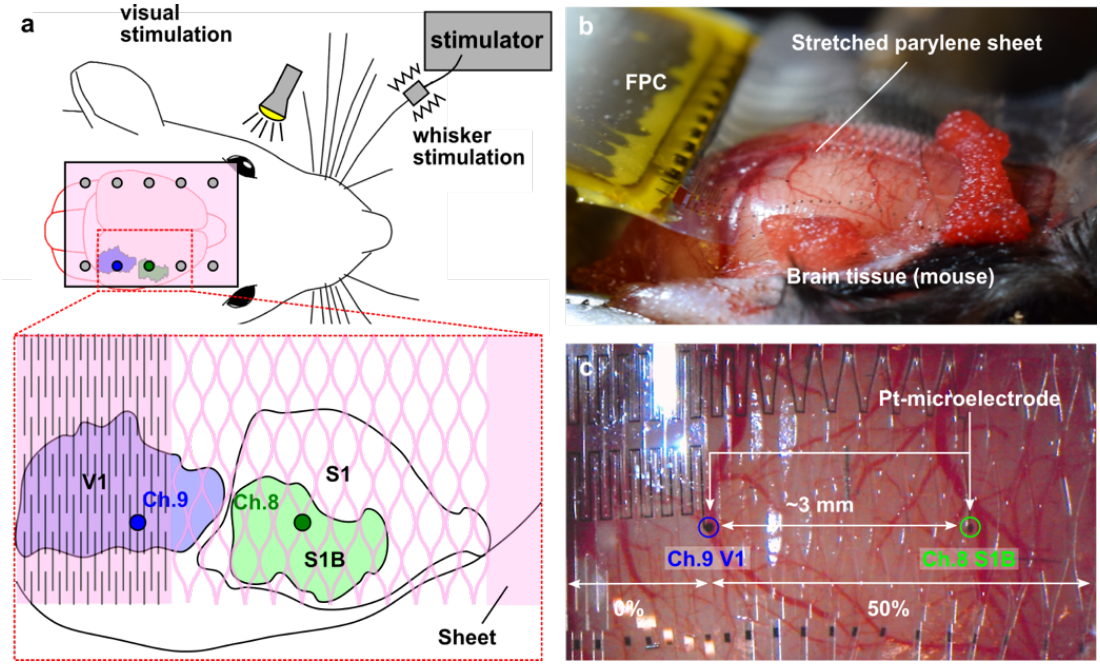

Figure 3.4.1 Schematic diagrams and photographs of the ECoG signal recordings from a mouse *in vivo* brain. (a) Schematic diagrams of the animal experiments and the positions of the Pt electrodes. To achieve ECoG recordings from the visual (V1) and barrel (S1B) cortices of the mouse brain, the gap between the Pt electrodes (Chs. 9 and 8) is changed from 2 mm (initial gap, 0% strain) to ~3 mm (50% strain) by stretching the film. (b) Photograph showing the fabricated Kirigami-based microscale planar electrode (Pt) array device [5 × 91 slits design ($N_r = 5, N_c = 45$)] placed over the cortical surface of a mouse *in vivo* brain, while the electrode positions are adjusted by stretching the film. (c) Photograph of the Pt electrodes (Chs. 8 and 9) after position adjustments, representing the schematic diagram shown in (a).

duration, 6 s in intervals between trials) (Fig. 3.4.2b). The LED and vibrator were driven by a processing system (RZ2, Tucker-Davis Technologies, Alachua, USA). The timing pulse signals of these stimulations were synchronized to acquire the ECoG signals. As a signal reference electrode, a stainless-steel screw was drilled into the skull over the cerebellum.

These Pt electrodes activated the ECoG signals, which ranged from alpha to high-gamma oscillations (8–100 Hz), to be detected (Fig. 3.4.2). During physical whisker stimulation, the Ch. 8 electrode, which was positioned over the S1B, detected the neuronal activities with amplitude of 154 μV_{pp} and a peak time of 54.2 ms from the whisker stimulation (Fig. 3.4.2d). These waveforms are similar to the ECoG signals recorded by conventional ECoG electrodes [97], which suggests that these signals evoked neuronal responses by the stimuli [$p = 1.07 \times 10^{-18}$, n = 100 trials, by paired *t*-test between prestimulus (−200 ms to 0 ms) and poststimulus (0 ms to 200 ms) periods]. While visually stimulating the mouse using a light source, the other electrode (Ch. 9) was placed over the V1 detected neuronal activities with an amplitude of 667 μV_{pp} and a peak time of 80.6 ms from the visual stimulation (Fig. 3.4.2g), which suggests that these signals significantly evoked neuronal responses by the stimuli [$p = 2.04 \times 10^{-78}$, n = 100 trials, by paired *t*-test between prestimulus (−200 ms to 0 ms) and poststimulus (0 ms to 200 ms) periods]. Waveforms recorded by the Ch. 9 electrode during whisker stimulation (Fig. 3.4.2c) [$p = 4.54 \times 10^{-4}$, n = 100 trials, by paired *t*-test between prestimulus (−200 ms to 0 ms) and poststimulus (0 ms to 200 ms) periods] were thought not to be caused by the device crosstalk associated with the parasitic impedance of the device interconnections (250 times larger impedance than the Ch. 9 electrode impedance). In addition, the waveform of Ch. 9 is not similar to the Ch. 8 electrode waveform. The Ch. 9 waveform is probably due to the volume conduction or local spread of the activity around S1B [99].

The time-frequency domain plots for both ECoG signals are also included in Figure 3.4.2. For each stimulation condition, the visual and somatosensory responses were analyzed by averaging the filtered signals (5–100 Hz, first-ordered Butterworth filter) for all 100 trials. The time-frequency domain spectrograms were calculated by the short-time Fourier transform method in a trial-to-trial manner with a sliding time window (Hann window function, width of 500 ms and 1 ms step). The plots were averaged over all trials and then the mean spectrum power during the prestimulus period (–0.1 to 0 sec from stimulus onset) was subtracted to normalize the logarithm of the power. The time-frequency domain plots taken from S1B (Ch. 8) showed that physical stimulation to the mouse whiskers increases the ECoG power in the 8–60 Hz frequency band (Fig. 3.4.2f).

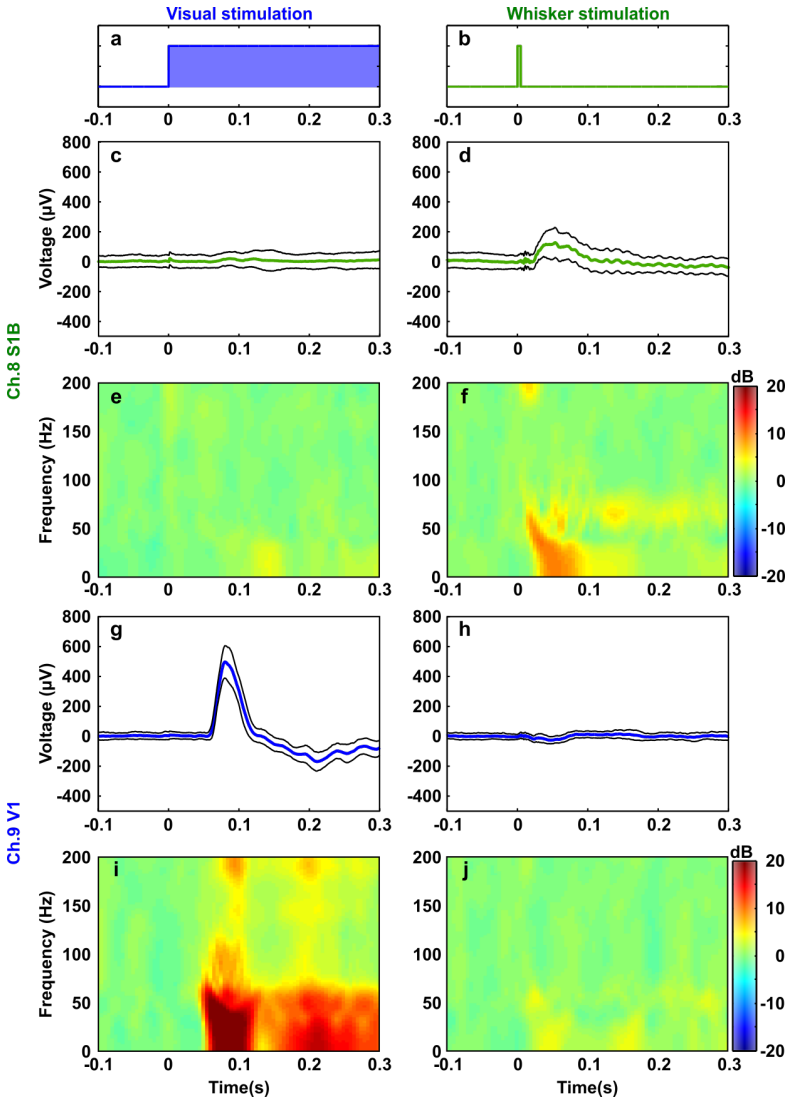

Figure 3.4.2 ECoG signals recorded via the Kirigami device using a mouse *in vivo* brain. (a, b) Visual and whisker stimulation waves. (c–j) Detected ECoG responses using the Pt electrodes via Ch. 8 placed over the S1B (c-f) and Ch. 9 placed over the V1 (g–j) during visual and whisker stimuli. Each panel includes the waveforms and time-frequency domain plots of the recorded ECoG signals. These neuronal responses were detected by Ch. 8 electrode during whisker stimuli and Ch. 9 electrode during visual stimuli, respectively [paired *t-test*, n = 100 trials, $p = 1.07 \times 10^{-18}$ for Ch. 8 (d) and 2.04×10^{-78} for Ch. 9 (g)]. Averages and standard deviations of waveforms were taken from 100 trials.

In contrast, visual stimulation had a negligible impact on the ECoG power (Fig. 3.4.2e). The other time-frequency domain plots of the ECoG signals from V1 (Ch. 9) showed that

the ECoG power in the 8–100 Hz band from V1 (Ch. 9) responds to visual stimulation (Fig. 3.4.2i), but not to whisker stimulation (Fig. 3.4.2j). These results indicate that the ECoG signals with tunable Pt electrodes using the Kirigami design show reasonable stimulus selectivity for each cortical region.

3.4.2 *In vivo* ECG signal recording

Another challenge for flexible bioprobe film devices is their application to organs, which exhibit large and rapid changes in their volume and surface area (e.g. a beating heart). Epicardial ECG signal recordings from a mouse beating heart were demonstrated to confirm the recording capability of the Kirigami device from large deformable tissues. Due to the deformable property of the heart, the strain–force required to stretch the film device should be minimized to follow the natural deformations during heart beating.

A fabricated 5 × 91 slits film device, which consists of an array of 10 planar Pt electrodes (50-μm diameter, ~300-kΩ impedance at 1 kHz) wrapped around a beating mouse heart, is shown in Figure 3.4.3. During a heartbeat, the film device stretches to follow large and rapid (~ 2.5 cycle/sec) changes in the volume and surface area of the heart. During animal preparation, a mouse (strain: C57BL, sex: male, weight: 22.5 g) was deeply anesthetized by an intraperitoneal injection of urethane (50 μl of 30% solution per 10 g body weight). After a thoracotomy, the heart was wrapped with the film device. The device and recording amplifier were connected using a flexible cable, so that the whole

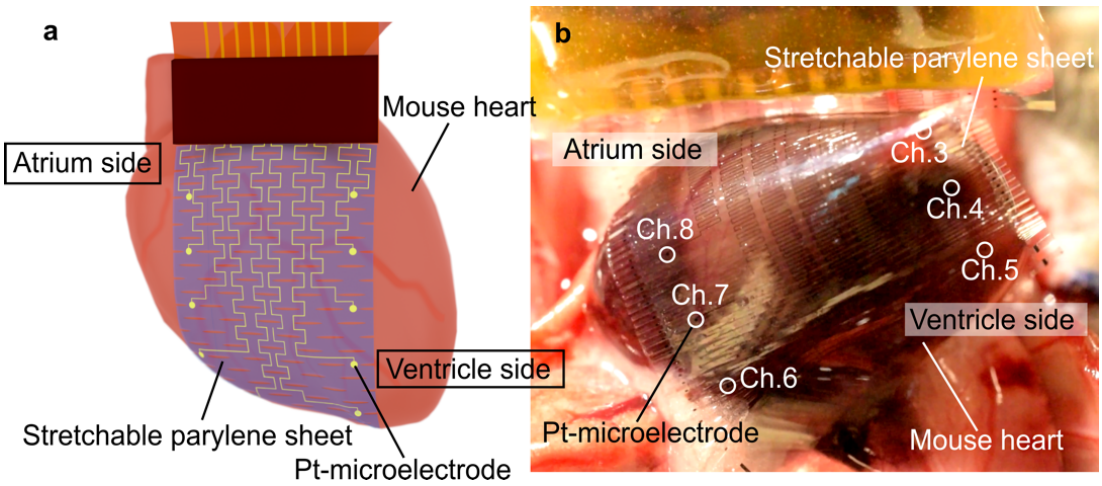

Figure 3.4.3 Schematic diagram and photograph of the ECG signal recordings from a mouse *in vivo* heart. (a, b) Schematic and photograph of the fabricated device [5 × 91 slits design ($N_r = 5$, $N_c = 45$)] wrapped around a beating mouse *in vivo* heart. Sets of Pt electrodes of Chs. 1–5 and Chs. 6–10 were placed over the ventricle side and atrium side of the heart, respectively.

film could move freely. After dropping saline (~20 µl) to keep the surface of the heart and the electrode film wet, the signals were recorded. The reference potential was set to stainless forceps, which clamped the ribs and intercostal muscles to keep the thorax open.

An array of Pt electrodes, Chs. 1–5, was placed over the ventricle side of the heart, while the other array of Chs. 6–10 was placed over the atrium side (Fig. 3.4.3b, Chs. 1, 2, 9, and 10 are not visible in the photograph). The signals detected via the Ch. 7 electrode are shown in Figures 3.4.4a–d; atrial beats are observed without ventricular beats. The recorded signals for the whole recording period of 0–1,200 s and the early period of 0–50 s, are presented in Figures 3.4.4a and b, respectively. Neither shows a significant

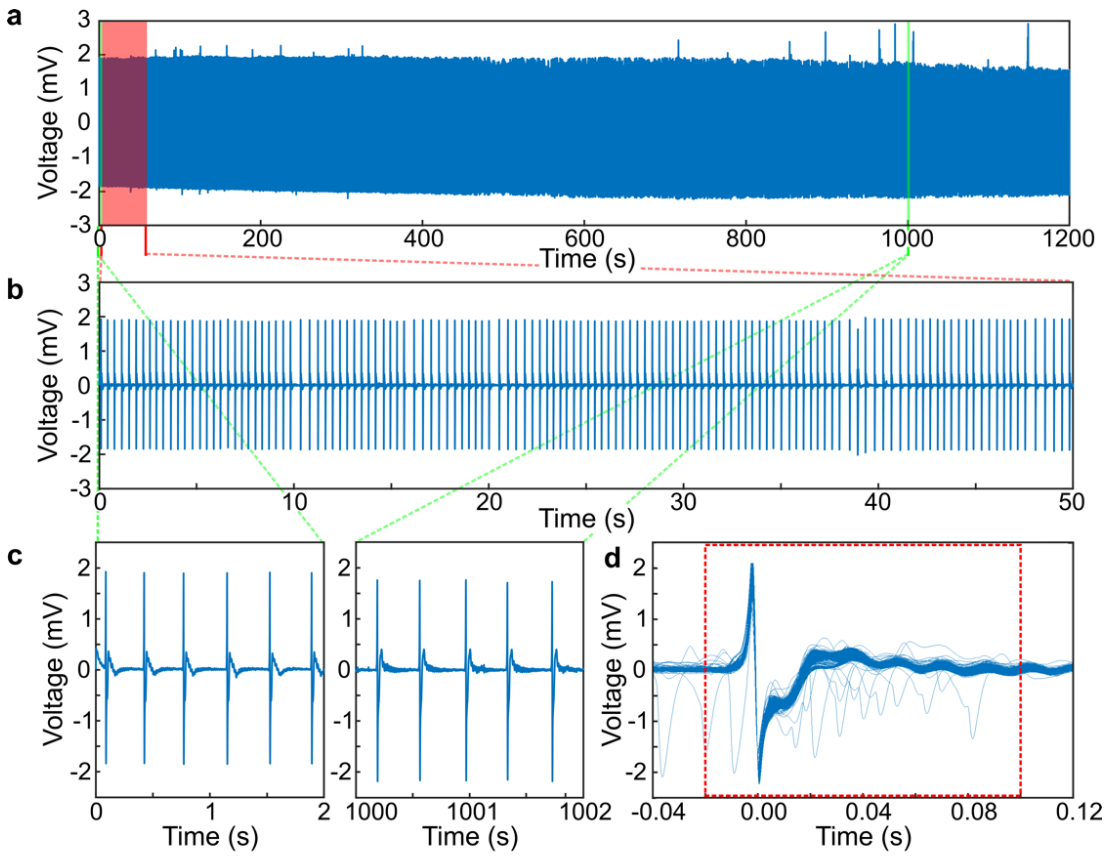

Figure 3.4.4 Recorded ECG signals from a mouse *in vivo* heart. (a) Epicardial ECG signals detected via the Ch. 7 electrode, which was placed on the atrium side of the heart. (b) Recorded ECG signals for the early period of 0–50 sec. (c) Signal waveforms in the early period of 0–2 sec and the later period of 1,000–1,002 sec during the recording for 1,200 sec. (d) Superimposition of waveforms recorded for the whole period of 1,200 sec (number of waveforms: 2988). Red dashed square is consistent with the period used for the ANOVA test.

change in the amplitude of the ECGs during the recording (~4 mV_{pp} in amplitude). The signal waveforms in the early recording period of 0–2 s and the later period of 1,000–1,002 s are shown in Figure 3.4.4c. The superposition of these recorded waveforms across a low threshold voltage of −1.5 mV is shown in Figure 3.4.4d; these waveforms are well superimposed. For further analysis of the waveforms, one–way analysis of the variance (ANOVA) test was performed in the period from −0.02 s–0.10 s (red dashed line area in Fig. 3.4.4d) to confirm the stability of the ECG recording. The ANOVA shows that the effect of the time difference during the ECG recording is vanishingly small compared to the amplitude of the waveforms indicating that the Kirigami bioprobe device stably recorded the ECG signals from the beating heart ($F_{2929, 8751910} = 208930.68$, $p < 0.0001$). The influence of the contraction and the expansion heart motions on the recording stability of the ECG signals was quantitatively analyzed. The signals were verified by a simultaneously recorded video during a regularly beating period without irregular motions of the heart and neighbor muscles (e.g. temporal convulsions due to respiratory failure).

During signal acquisition and processing, the ECoG and ECG signals recorded via the Kirigami devices were differentially amplified using a head amplifier (ZC64, Tucker-Davis Technologies, 1×10^{14} input impedance) with filters (0.35 Hz for the low-cutoff frequency and 7.5 kHz for the high-cutoff frequency). Following signal amplification, the signals were routed to a pre-amplifier/digitizer (PZ2, Tucker-Davis Technologies) and a digital signal processing module (RZ2, Tucker-Davis Technologies). The digitized data were stored on the hard disk of a Windows PC with a sampling frequency of 25 kHz. All off-line data processing were analyzed by signal processing and Statistical MATLAB toolboxes (Mathworks, USA).

As the device stretches, a gap between the electrode and the tissue surface is induced due to the 3D deformation of each beam. The gap width simply follows the film strain and can be calculated using formula (2.8) (Fig. 3.4.5b, red line). In the animal experiments, the gap is filled with a conductive saline solution (resistivity ~62.5 Ω·cm). The conductance of the saline portion between the electrode site and the tissue surface can be calculated by assuming the minimum pathway between them (Fig. 3.4.5). The change in the resistance of the saline portion associated with the device strain is also included in Figure 3.4.5. For a 50% strain, which is the same as that used in the ECoG recording (Fig. 3.4.1a), the calculated saline resistance is 40 kΩ. This resistance is ~8-times lower than the electrolyte–Pt interfacial impedance of 311 kΩ at 1 kHz. As confirmed in both ECoG and ECG recordings, the signals are detected by the Pt electrode

via a conductive saline solution without significant attenuation of the signal's amplitude associated with the gap.

3.5 Conclusions

The design, fabrication process, characterization and recording capability of the Kirigami bioprobe device were described in this chapter. The design and fabrication process of the Kirigami bioprobe device was described in the first part. Two types of Kirigami structures having different numbers of cell arrays ($N_r = 5$, $N_c = 45$ or $N_r = 3$, $N_c = 45$) in the same device area (~10×10 mm^2) and two types of interconnections (single interconnection or three interconnections embedded in each beam) for each Kirigami structure were designed and fabricated. Considering the Kirigami slits patterned in the same area, a smaller number of the array cells in the row direction (N_r), or longer slit length, offers higher maximum strain. However, the low number of the array cells limits the number of array electrodes because of the small beam number used as the path for interconnections. Therefore, the number of Kirigami array cells considering the required stretchability and resolution of the recorded signals for different biological tissues or applications should be decided. The designed Kirigami bioprobe devices were obtained by microfabrication technologies using biocompatible materials (parylene for

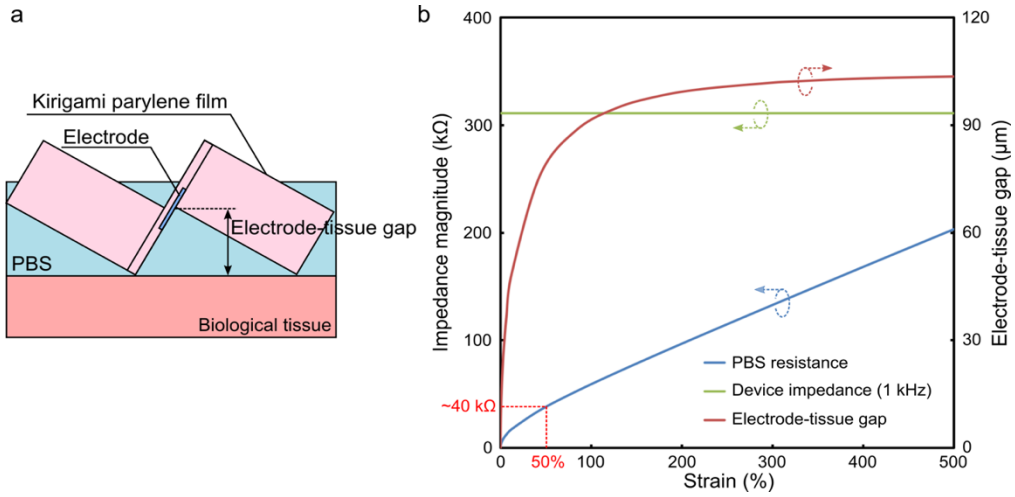

Figure 3.4.5 3D deformation of the Kirigami structure. (a) Schematic diagram of the gap between the microelectrode and the brain tissue surface associated with the film's strain. (b) Calculated gap of the electrode–brain tissue surface associated with the film's strain. The electrical property of the gap is also included in the graph. This is calculated by assuming the minimum pathway between the electrode and the tissue surfaces.

the device substrate and Pt/Ti for the electrode and interconnections). The Kirigami devices were successfully fabricated and exhibit high stretchability. In addition, a Kirigami device with bi-axial stretchability was also designed and fabricated for biological tissues, which exhibit bi-axial deformation. In the second part, the electrical and mechanical characteristics of the fabricated Kirigami devices were described. The Pt electrode embedded in the Kirigami device exhibited an impedance magnitude of ~311 ± 32 kΩ without device strain. This impedance is low enough for the recording of biological signals, such as ECoG signals. The device impedance was not significantly changed in the strain range 0%–500% of the Kirigami device, which has a maximum calculated strain of 860%. In the strain range of over 500%, the impedance was slightly reduced (strain range 600%–700%) and then significantly increased (strain of 800%). These impedance changes were probably caused by the device strain reaching the maximum strain limit, which characterizes the Kirigami design. The mechanical characteristics exhibited by the Kirigami devices with 5 × 91 slits and 3 × 91 slits have an effective Young's modulus of 23 kPa and 3.6 kPa in the strain range of 20%–250% and 20%–450%, respectively. This effective Young's moduli are ~30–200 times smaller than those of the conventional elastomer material of PDMS and are in the same order to those of the biological tissues (e.g. ~1.5 kPa for the brain and 5–40 kPa for a resting muscle). In the durability test using the one-row Kirigami device, the Kirigami device exhibited high durability under a 1,000-cycle ~200% strain. In the stretchability test assuming that the device was implanted into the biological tissues, the Kirigami device maintained its stretchability in another layer of Ecoflex instead of using a biological tissue (e.g. skin and muscle). These results confirmed that the fabricated Kirigami electrode devices can be used for biological signal recordings coming from deformable biological tissues or organs. In the third part, a demonstration of the biological signal recordings from a mouse's brain tissue and heart was presented. This demonstration confirmed the advantages of the device with respect to tunable electrode gaps on the tissue surface with the device stretching and the capability of following the shape of spherical and largely deformable biological samples, such as heart tissues. It was demonstrated that the proposed Kirigami-based microelectrode device can simultaneously record *in vivo* ECoG signals from the visual and barrel cortices of a mouse by stretching the film and tuning the electrode gap. Moreover, *in vivo* epicardial ECG signals can be recorded by wrapping the Kirigami device around a beating mouse's heart, which exhibits large and rapid changes in the volume and surface area. In these animal experiments, where the film stretches <50%, the required forces to strain these films are <3.3 mN. Consequently, the Kirigami design significantly reduces the film's strain–force compared to conventional

stretchable electronics using elastomer substrates. Such a reduction is an important characteristic for stretchable film electronics, particularly for devices attached to soft samples, such as heart or brain tissues, to minimize the device-induced stress to soft biological tissues. In the next chapter, another type of a Kirigami device, which offer a solution to issues faced by the Kirigami device and other stretchable devices, when these devices are applied to large deformable tissues, such as heart and muscles, is described.

Chapter 4: Donut-shaped Kirigami device

4.1 Introduction

In the characterizations of the Kirigami structure described in Chapter 3, it was confirmed that low effective modulus comparable to that of biological tissues could be achieved using Kirigami bioprobe devices (~23 kPa and ~3.6 kPa). These devices exhibit high stretchability under high strain and low effective modulus. They also achieve recording capabilities of signals coming from biological tissues, e.g., from a mouse's brain and heart. The lower effective modulus [compared to conventional elastomer-based stretchable devices (e.g. PDMS)] of these devices enables the minimization of the device-induced physical stress to biological tissues caused by the device placement [55], [81], [100]. However, the Kirigami devices are not able to solve other problems encountered by stretchable devices, such as microelectrode displacement over the wet surface of deformable biological tissues (e.g. heart and muscle).

Usually, signals from deformable tissues, such as heart and muscle, are recorded from the skin surface [ECG and surface EMG (sEMG)]. However, some applications require more accurate signal acquisition. For example, accurate and robust EMG signal recording is necessary in EMG signal-based human–machine interfaces [10]–[12], which allow for prosthesis control in amputated patients. The quality of the sEMG signals recorded via such electrodes is affected by the skin surface conditions, such as conductivity and sweating. Sweating attenuates and filters the EMG signals [101]. Moreover, additional layers (e.g. subcutaneous fat and skin) between the signal source and the electrode cause a difficulty related to the separation of the signals [102]. Therefore, placing the electrode below the skin surface and recording the EMG signals directly from the muscle surface are proposed by some methods to achieve stable EMG signal recordings [102], [103].

Wet electrodes made of conductive gel, hydrogel, or sponge saturated with an electrolyte solution and dry electrodes made of noble metals (e.g. gold, platinum, or

silver), carbon electrodes, and sintered silver or silver chloride are generally used as electrodes to record the sEMG signals [104]. Elastomer and hydrogel with high stretchability and small Young's modulus properties are candidate materials of sEMG signal recording devices [65], [105]. However, as described in Chapter 1, the use of elastomer as the device substrate for EMG signal recordings is problematic because this materials has a higher Young's modulus [e.g. 730 kPa for polydimethylsiloxane (PDMS)] than that of muscle and other tissues (e.g. ~1.5 kPa for the brain and 5–40 kPa for a resting muscle) [53], [54]. Meanwhile, hydrogel cannot maintain robust and conformal contact with the tissues because of dimensional changes in biofluids [106]. Another issue of devices in biofluids is that conventional stretchable devices cannot follow the deformation of the wet tissues (e.g. beating heart) because of the wet tissue surface, which results in device (microelectrode) displacement. The displacement of such electrodes on the muscle surfaces should be minimized in the device application to myoelectric pattern recognition-based prosthesis control [107].

The aforementioned conventional sheet-type stretchable Kirigami bioprobe device [108] placed on the wet tissue of a muscle is shown in Figure 4.1.1a. During muscle contraction, the sheet-type Kirigami device may slip over the tissue because of the "no device fixation mechanism" to the target tissue. Also, the device cannot be stretched or follow the tissue deformation.

To overcome the issue of device displacement, a Kirigami bioprobe able to surround the tissue is proposed. The proposed device is able to stretch and follow the tissue deformation (Fig. 4.1.1b). Kirigami structure is not only applicable to a square or rectangular shaped film but also various other shaped films. Combinations of the Kirigami structure and various shapes of the patterned film offer the various deformations and characteristics. A Kirigami design patterned in a donut-shaped film was implemented in this experiment. This device employs a radially arranged linear array of slits (Fig. 4.1.2). A photolithography-based 2D microfabrication parylene process [94], [95], [109] was used to fabricate the 2D donut Kirigami film; this 2D film can be transformed into a 3D cylindrical shape. The donut-shaped Kirigami device implements the fixation mechanism to the target tissue and the transformed 3D device geometry is suitable for use in numerous spherically or columnar-shaped deformable biological tissues (e.g. heart, brain, upper limb, lower limb, and abdomen). Additionally, an array of microelectrodes is fully integrated within the 3D Kirigami device because of the 2D microfabrication process.

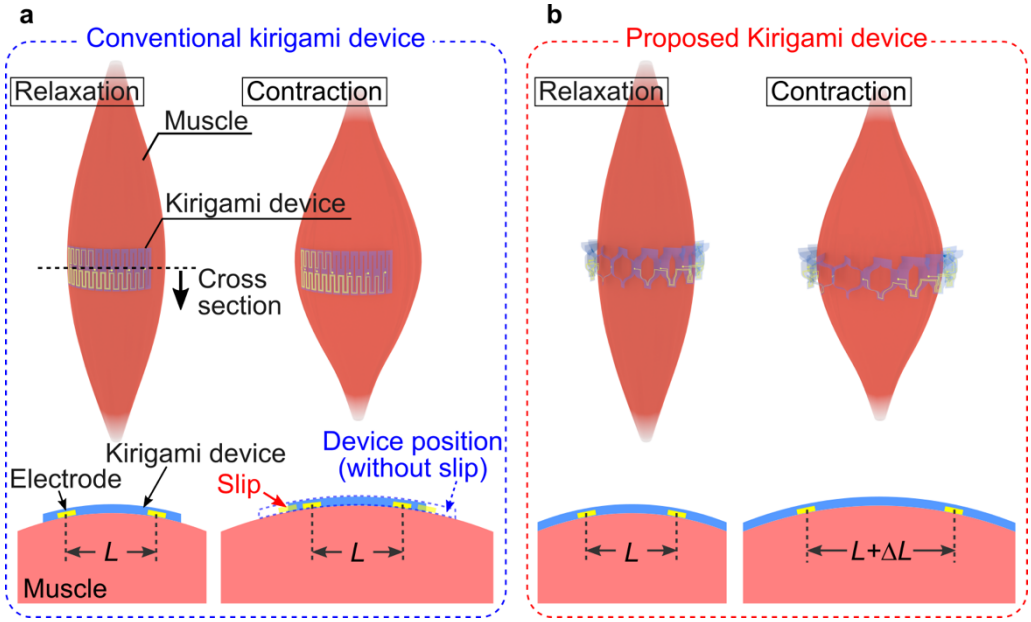

Figure 4.1.1 Displacement issue of the conventional Kirigami bioprobe device. (a, b) Comparison of the device displacement over the tissue (muscle) between the conventional sheet-type device (a, left: relaxation, right: contraction) and the proposed Kirigami device (b).

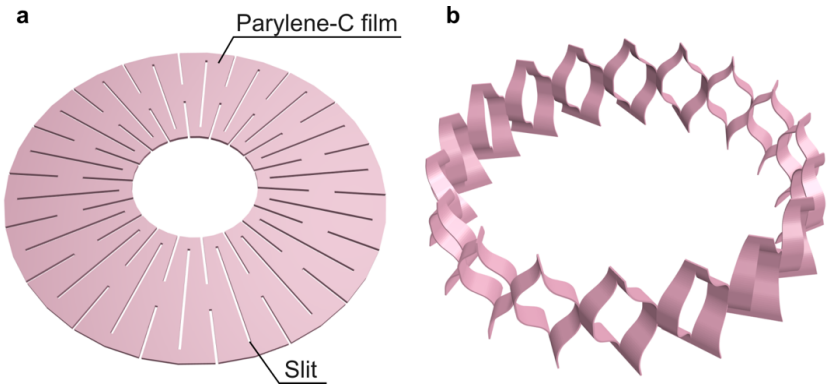

Figure 4.1.2 The proposed donut-shaped Kirigami device. (a) Before device transformation and (b) after device transformation from a 2D donut-shape into a 3D cylindrical shape.

4.2 Mechanical properties of the donut-shaped Kirigami structure

Before the design and fabrication of the device, the stress–strain characteristics of the donut-shaped Kirigami device were obtained using the FEM. The simulations were implemented by the commercial software ANSYS. Similarly to the simulation of the Kirigami structure (Fig. 2.3.1), a one-cell model of the donut-shaped Kirigami film was also used (Fig. 4.2.1). This model consists of one slit and four beams around the slit with

the parylene single layer (Fig. 4.2.1a). In the donut-shaped device design, the combination of the one-cell model using a number of one-cell arrays in each direction along the circle shape and perpendicular to the circle shape can be obtained. An elastomer Young's modulus parameter was used, which was calculated from the device's stress–strain curve (Fig. 4.2.1b). The calculated effective Young's modulus of the donut-shaped Kirigami device was 76 kPa, which is of a similar magnitude to the Young's modulus of resting muscle tissues (5–40 kPa) [54]. The results indicated that the Kirigami design causes lower device-induced stress on tissues than that caused by the stretchable devices (730 kPa for PDMS-device). It is confirmed that the epicardial mesh device which has the same order of elastic modulus (50 kPa) as the kirigami device did not show any appreciable effect to the heart while the device wrapping the heart [57]. However, the effective modulus of the Kirigami device was still larger than that of the muscle and other tissues (e.g. ~1.5 kPa for the brain) [53]. The effective modulus of the Kirigami device

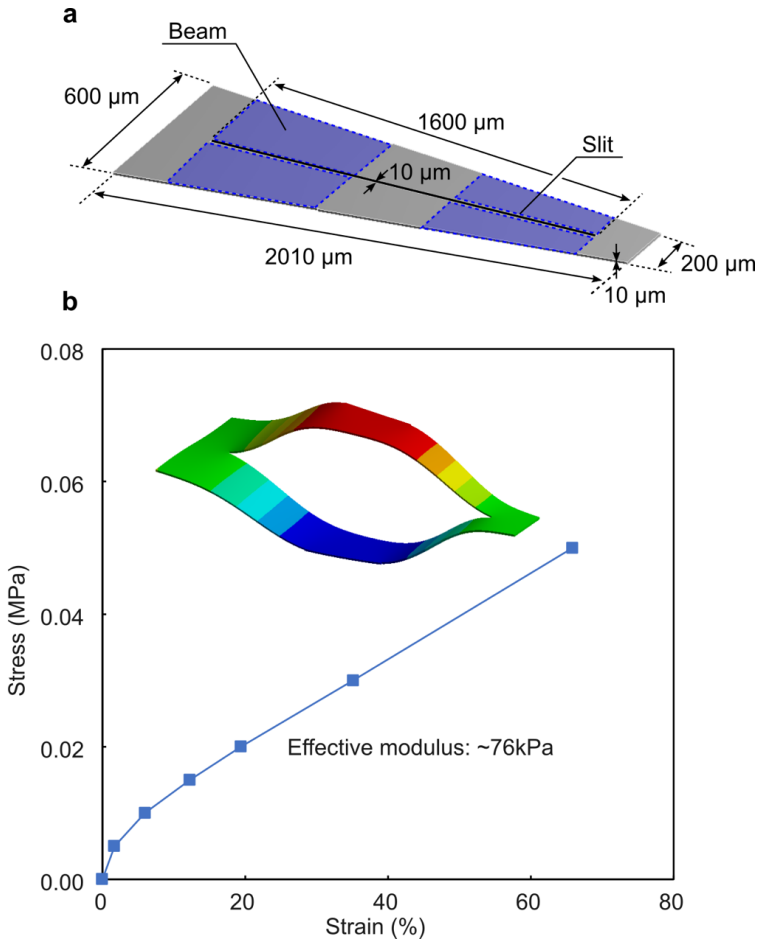

Figure 4.2.1 Mechanical characteristics of the donut-shaped Kirigami film. (a) One-cell simulation model (Fig.4.1.2a, before transformation). (b) Stress–strain curve of the one-cell model.

can be further decreased by changing the dimensions of each beam (or slit) [108] and the material used to fabricate the device. Candidate soft materials for the Kirigami structure include PDMS [110] and Ecoflex [91].

4.3 Design and fabrication of the donut-shaped Kirigami device

Based on the simulation results of mechanical characteristics of the donut-shaped Kirigami structure, the donut-shaped Kirigami bioprobe device was designed for biological signal recordings from the deformable biological tissues such as the heart and muscle. Three types of the donut-shaped Kirigami bioprobe device were designed for ECG and EMG signal recording from a mouse's heart and muscle. These include two types of the single-donut shaped Kirigami device for device characterizations and ECG signal recording and a double-donut Kirigami device for the EMG signal recording (Fig. 4.3.1).

4.3.1 Design of the donut-shaped Kirigami device

The designed donut-shaped Kirigami devices are shown in Figure 4.3.1. Layers colored pink and blue show the parylene and metal interconnection of gold (Au)/Ti. Two single-donut Kirigami devices, which employ 10 channel and 24 channel electrodes, respectively, have the same substrate as the donut-shaped Kirigami. The inner and outer diameters of the donut-shape structure are 2 and 6 mm, respectively, and the film thickness is 10 μm (Figs. 4.3.1a, b). The length and width of each slit in the film are 1,600 and 10 μm, respectively, whereas the slit gap (beam width) ranges from 100 μm (inner side) to 300 μm (outer side). The single-donut Kirigami structure with the 10 channel microelectrodes of 50 μm diameter consists of 27 cells and exhibits a maximum film strain of ~170% (calculated). Au electrodes are embedded along the circle shape (4-mm diameter) with a ~1.3 mm interval. The other single-donut Kirigami with the 24 channel microelectrodes (~0.4 mm interval) consists of 26 cells and exhibits a maximum film strain of ~160% (calculated). Each microelectrode is connected to the bonding-pad through zigzag interconnections. Each slit edge has a circular shape with a 20 μm diameter to prevent the stress concentration confirmed in the simulation results mentioned in Chapter 2. A double-donut-shaped device suitable for EMG signal recording is shown in Figure 4.3.1c. The inner and outer diameters of the inside donut were 2 mm and 5.6 mm, respectively. The inner and outer diameters of the outside donut were 5.8 mm and 8 mm, respectively. The inside donut consisted of an array of 27 cells, whereas the outside donut consisted of an array of 81 cells. The designed maximum strains inside and outside the donuts were ~185% and ~110%, respectively. Slit lengths

of the inner and outer donuts were 1,500 µm and 800 µm, respectively. The double-donut Kirigami employs 10 microelectrode channels along the inner and outer donut-shape (diameter: 3.8 mm and 6.9 mm). The intervals of these electrode arrays were 1,200 and 2,200 µm, respectively and the interval between the inner and outer electrodes was 1,600 µm. The designs of donut-shaped Kirigami devices are summarized in Table 4.1.

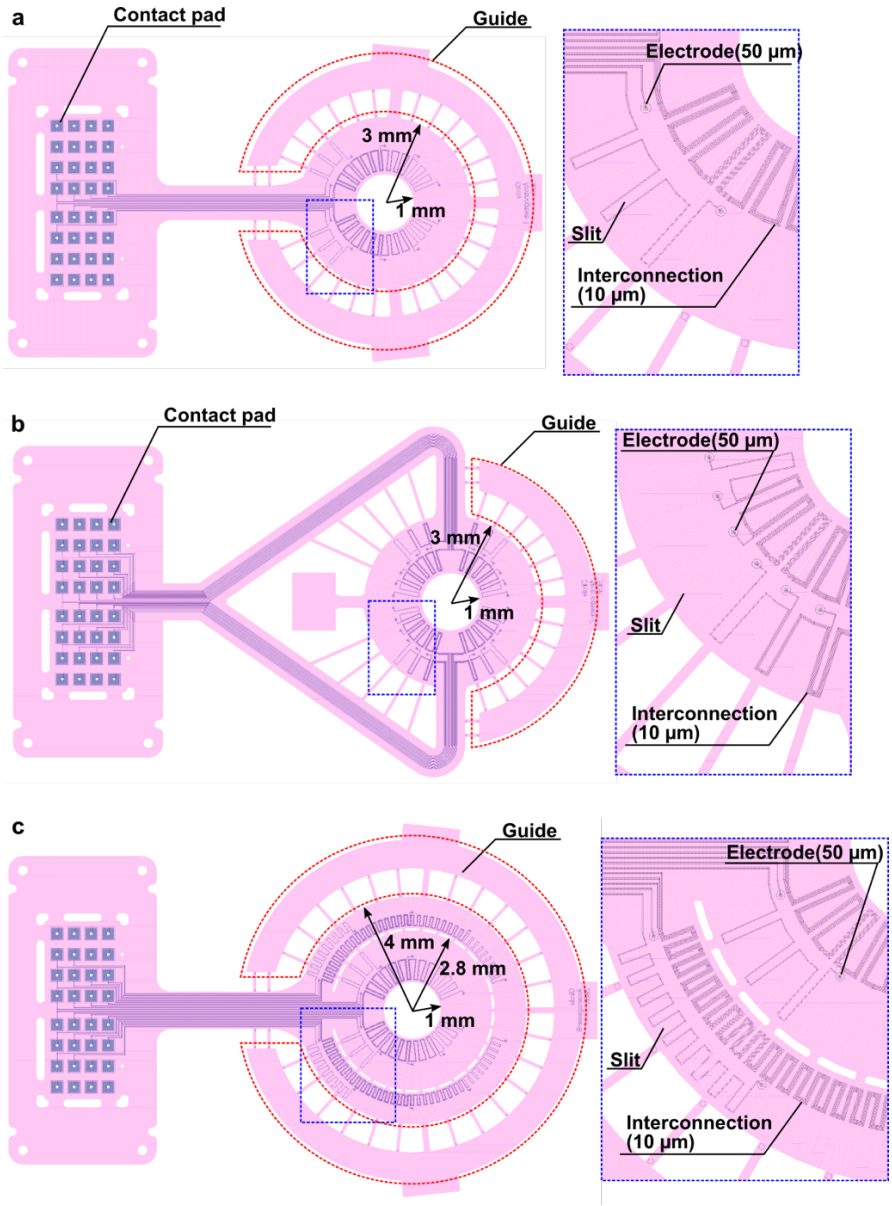

Figure 4.3.1 Designed donut-shaped Kirigami devices. (a) Single donut-shaped Kirigami device with 10 microelectrode channels (~1.2 mm interval) composed of 27 cells and (b) single donut-shaped Kirigami device with 24 microelectrode channels (~0.4 mm interval) composed of 26 cells. (c) Double donut-shaped Kirigami devices with 10 microelectrode channels in each inner and outer donut (~1.2 mm and ~2.2 mm interval).

Table 4.1 Designs of the donut-shaped Kirigami device

Device		Slit length [μm]	Slit gap [μm]	Beam width [μm]	Film thickness [μm]	Number of cell array	Number of electrode channels	Electrode gap [μm]		Maximum strain [%]	Figure No.
Single donut		1,600	400	100-300	10	27	10	1,240		170	Fig. 4.3.1a
Single donut (High density)		1,600	400	100-300	10	26	24	420		160	Fig. 4.3.1b
Double donut	Inside	1,500	300	100-290	10	27	10	1,170	Inside–outside 1,550	185	Fig. 4.3.1c
	Outside	800	300	95-135		81	10	2,130		110	

4.3.2 Fabrication of a donut-shaped Kirigami bioprobe device

Donut-shaped Kirigami bioprobe devices using a parylene-based MEMS process were fabricated (Fig. 4.3.2). Initially, a 5-μm-thick parylene-C film was deposited on a Si substrate as the device's bottom layer [Figs. 4.3.2(i, ii)]. A Au with a Ti adhesion layer (total thickness of Au/Ti = ~100 nm) was formed over the bottom layer by sputtering and plasma etchings (argon plasma for Au and CF_4 plasma for Ti) [Fig. 4.3.2(iii)] to form the device's electrode layer. Next, the Au/Ti layer was covered by another parylene layer (5 μm) [Fig. 4.3.2(iv)]. Both parylene top and bottom layers were patterned by O_2 plasma with a Ti hard mask for the fabrication of the Kirigami substrate [Figs. 4.3.2(v, vi)]. Using this plasma etching process, both electrode sites and bonding pads were exposed simultaneously. Finally, after the Ti layer was removed (CF_4 plasma), the parylene film was released from the Si substrate using ethanol [Figs. 4.3.2(vii, viii)].

Photographs of the fabricated three types of the donut-shaped Kirigami devices are shown in Figures 4.3.3a–c. The insets in Figures 4.3.3a–c are the microscope images of the fabricated device, showing 50-μm-diameter Au electrodes embedded along the circle shape. Each microelectrode was connected to the bonding-pad through zigzag interconnections. The packaged device using the FPC for the electrical characterization and animal experiments is shown in Figure 4.3.3d. The transformation of the fabricated single-donut Kirigami device from a 2D donut shape to a 3D cylindrical shape using a jig is shown in Figure 4.3.3e. It was experimentally confirmed that the stretchability of the fabricated single-donut Kirigami device exhibited >200% strain for the position of electrodes (diameter of 4 mm) without device fracture (separation).

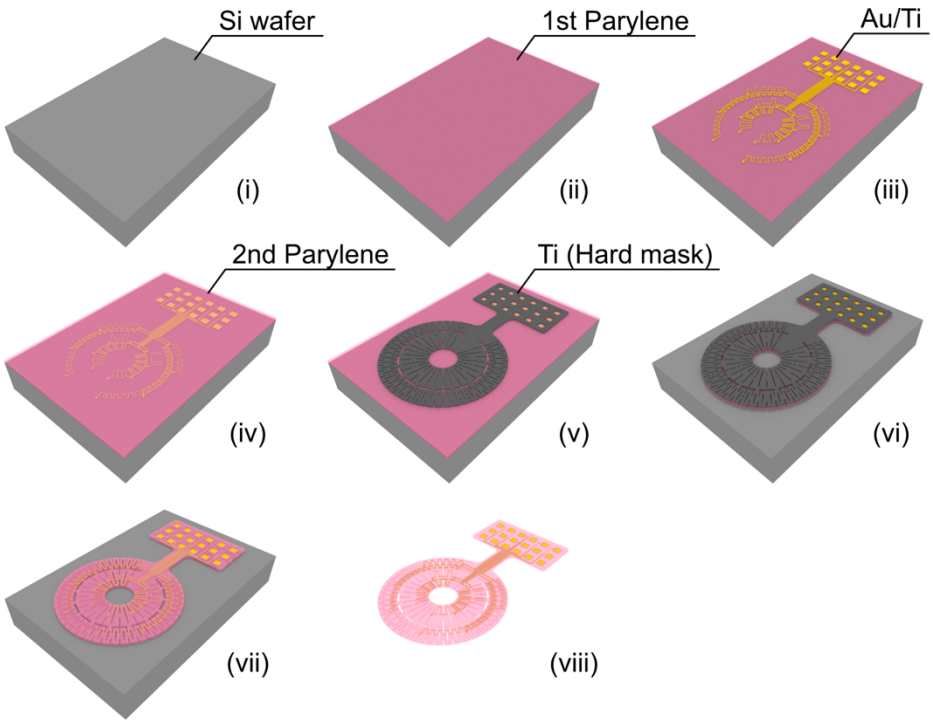

Figure 4.3.2 Fabrication of the donut-shaped Kirigami bioprobe devices. (i–ii) deposition of the first parylene-C on the silicon substrate as the bottom layer, (iii) deposition and patterning of the Au-electrode layer with a Ti adhesion layer, (iv) deposition of the second parylene-C as the top layer, (v) deposition and patterning of the Ti layer as the hard mask, (vi) patterning of both parylene top and bottom layers and exposing electrode sites and bonding pads by O_2 plasma with Ti mask, (vii) removal of the Ti mask and (viii) release of the Kirigami device from the silicon substrate using ethanol.

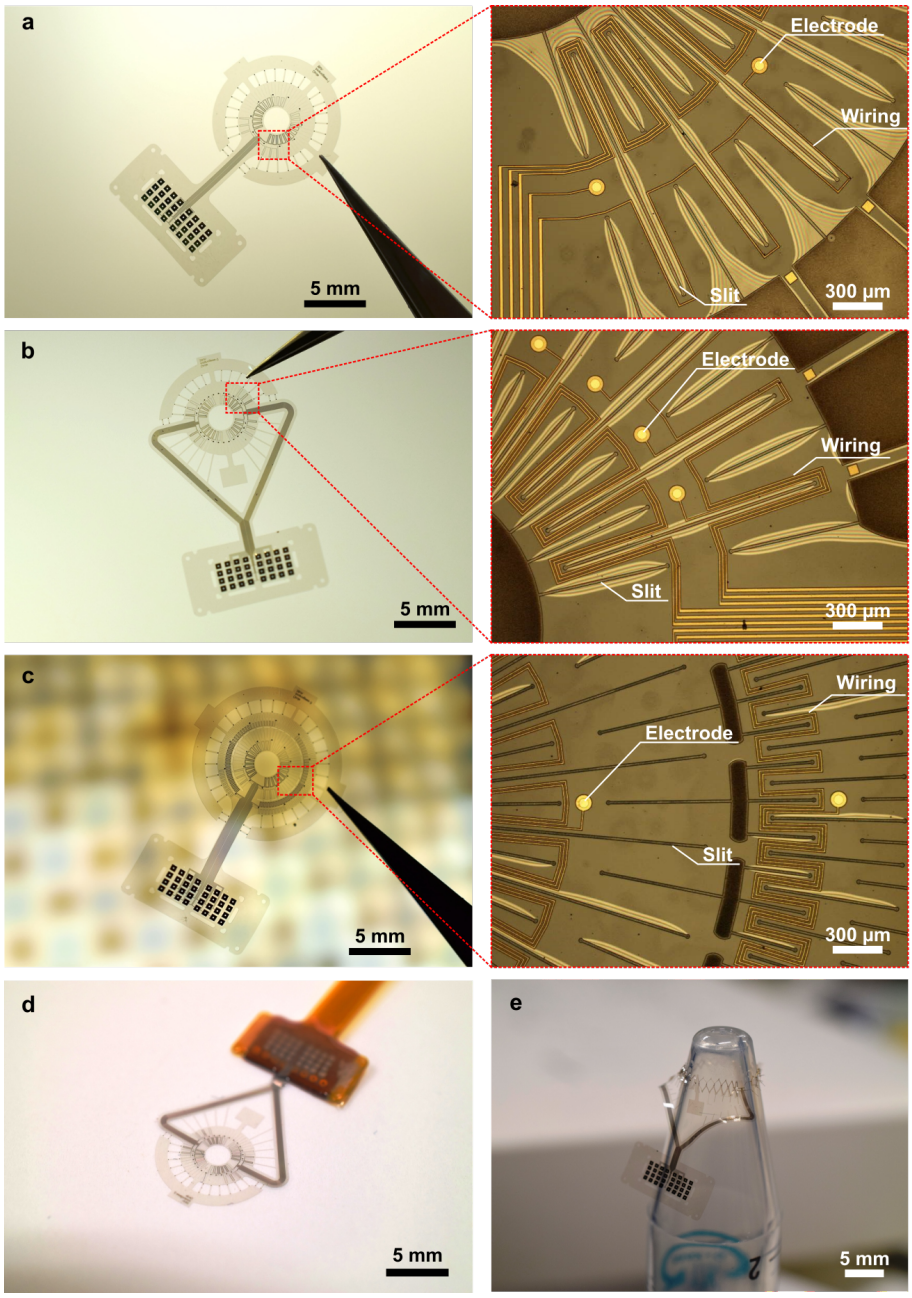

Figure 4.3.3 Fabricated donut-shaped Kirigami device. (a–c) Photographs showing three types of the fabricated donut-shaped Kirigami bioprobe devices: single-donut device with 10 microelectrodes channels (a) and 24 microelectrodes channels, (b) and double-donut shapes with the 10 microelectrodes channels in each donut-shape (c). (d) Packaged donut-shaped Kirigami device with the FPC. (e) Deformed single donut-shaped Kirigami device from a 2D donut shape to a 3D cylindrical shape using a jig.

4.4 Characterization of the donut-shaped Kirigami device

Electrical characterization of embedded microelectrodes and the device displacement test were conducted to confirm the electrical stability and the stability on deformable tissues. The electrical characteristics of the electrodes embedded in the fabricated Kirigami devices are confirmed by impedance measurements during the device stretching. In the displacement test, the deformable balloon was used instead of the deformable biological tissue.

4.4.1 Electrical characterization of the donut-shaped Kirigami device

The electrolyte/metal interfacial impedance magnitude of the embedded Au microelectrode of the single-donut-shaped Kirigami device with the 24 electrode channels, which exhibits a calculated maximum strain of ~160%, was measured in a saline solution. The magnitude of the Au microelectrode's impedance without stretching the device (stretchability = 0%) was ~576 kΩ at 1 kHz (Fig. 4.4.1a). The strain-dependent impedance characteristics of the Au microelectrodes in the single-donut-shaped Kirigami device are shown in Figure 4.4.1b. At a strain range of 0%–100%, no significant changes in the impedance were observed because the film in this condition is deformed by the beam's bending itself and no significant stress was concentrated in the film. At strain ranges of >100%, the value of the impedance was initially decreased but then increased due to the film breaking.

Under this condition, strain-induced stress was concentrated at the slit's edge. Microscopic and scanning electron microscope (SEM) images around the slit edge of the single-donut-shaped Kirigami device after the device was stretched to >200% (until tearing off) are shown in Figure 4.4.2. Simulations results of the stress distribution in the Kirigami structure (Fig. 2.3.3) indicated that the stress concentration occurred in the slit's edge. This stress concentration caused issues regarding the peeling off of the parylene bi-layer and cracks at the slit edge (Fig. 4.4.2). The parylene peeling off caused the exposure of the Au interconnections in the saline solution; the value of the device impedance decreased, since the area exposed to the saline solution was increased. When the cracks extended and reached the interconnections, the value of the device impedance increased due to the film breaking and disconnection of the interconnections.

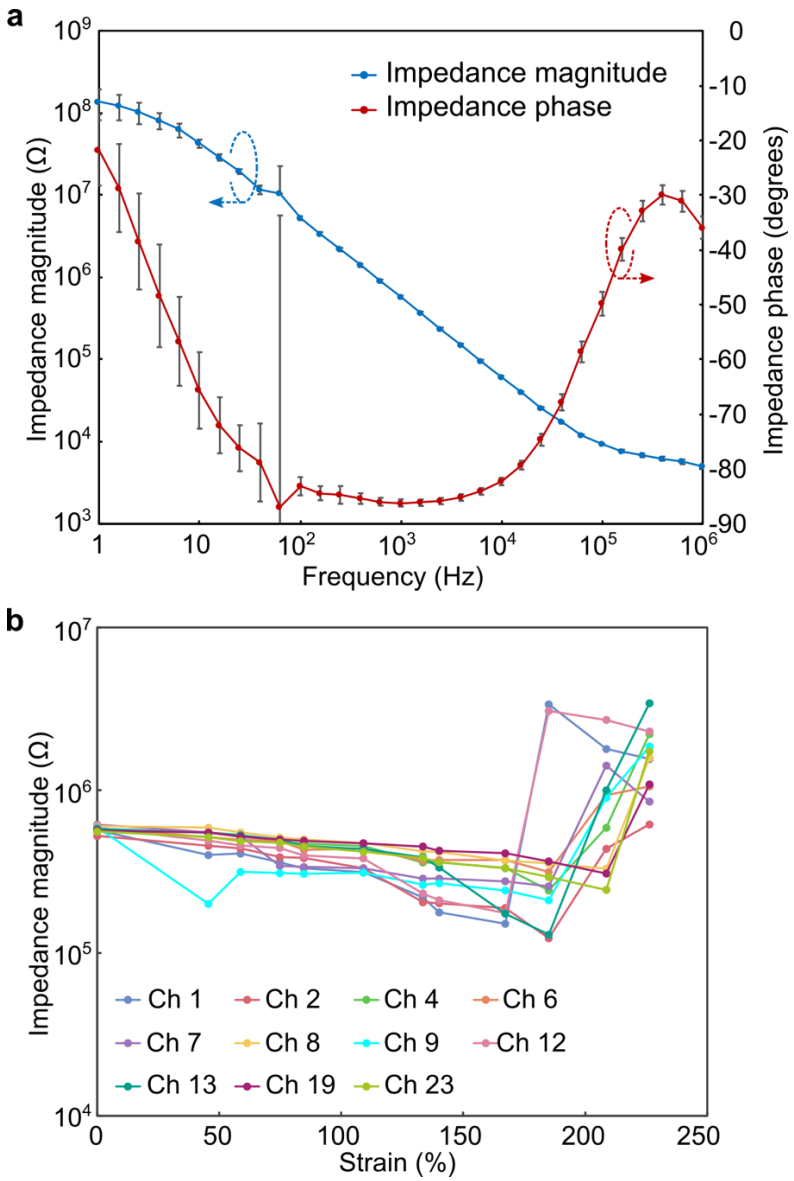

Figure 4.4.1 Impedance of the fabricated single-donut-shaped Kirigami device measured in saline solution. (a) Impedance characteristics without device stretching (0%). Averages and standard deviations of the impedance magnitude and phase characteristics were taken from 11 samples (error bars indicate SD). A deviation of around 60 Hz is due to noise of the measurement system. (b) Strain-dependent impedances measured at 1 kHz in saline solution. Here, the device stretches from 0% to 226%.

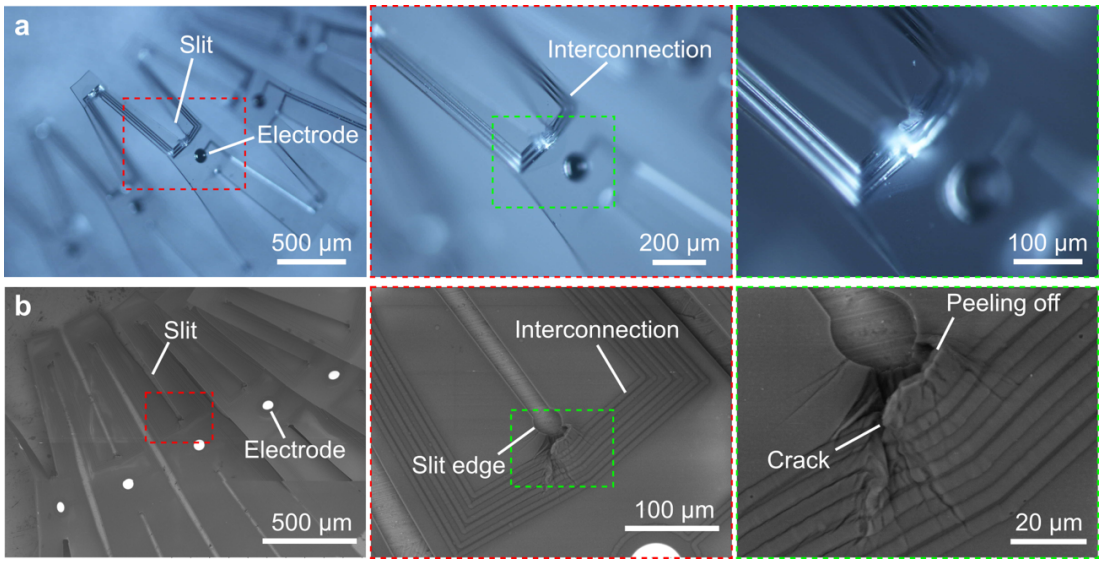

Figure 4.4.2 Slit edge observations after stretching of the Kirigami device up to 200%. (a) Photographs and (b) SEM images taken at the slit edge showing the crack and peeling off of the device's parylene substrate.

4.4.2 Displacement test of the donut Kirigami device

The device deformability on deformable biological tissues was confirmed by conducting displacement tests using an expanding balloon instead of the deformable biological tissues. Two types of displacement tests were performed to confirm the device displacement. These tests involved the strain of the balloon and repeated balloon stretching. In both displacement tests, a donut-shaped Kirigami device (single-donut device with 10 electrode channels shown in Figs 4.3.1a and 4.3.3a) was used. For comparison, a conventional sheet-type Kirigami device was also used (Fig. 3.3.5a). Both donut-shaped and sheet-type Kirigami devices had the same slit length of 1,600 μm. These devices were adhered to the balloon using water between the device and the balloon surfaces.

A schematic diagram of a test investigating the device displacement dependence on the balloon strain is shown in Figure 4.4.3. The devices had markers on their surfaces and the device position could be determined as the perpendicular distance between the marker and the center line of the balloon. The side and cross-sectional views of the balloon before and after the expansion are shown in Figure 4.4.3. Considering the curvature of the balloon surface, the device displacement was defined as the length between the calculated and measured marker positions on the balloon's surface after the balloon's expansion. The calculated marker position with the balloon stretch was derived using the marker position before the balloon stretch and the strain ratio of the balloon.

The device displacement, ΔL, is defined as follows:

$$\Delta L = \frac{D_1|\theta_1 - \theta_0|}{2} \tag{6.1}$$

$$\theta_0 = \sin^{-1}\frac{2L_0}{D_0} \tag{6.2}$$

$$\theta_1 = \sin^{-1}\frac{2L_1}{D_1} \tag{6.3}$$

In the above equations, L_0 and L_1 are the distances from the balloon's center before and after the expansion, D_0 and D_1 are the diameters of the balloon before and after the expansion, and θ_0 and θ_1 are the angles of the balloon's markers before and after the expansion, respectively (Fig. 4.4.3).

The device displacement curves derived from three trials of the balloon expansion using the same donut-shaped Kirigami device (each trial employed five strain cycles of expansion) is shown in Figure 4.4.4. Each curve represents the averages and SD taken from the five strain cycles in each trial. The balloon was expanded to the strain of ~50%,

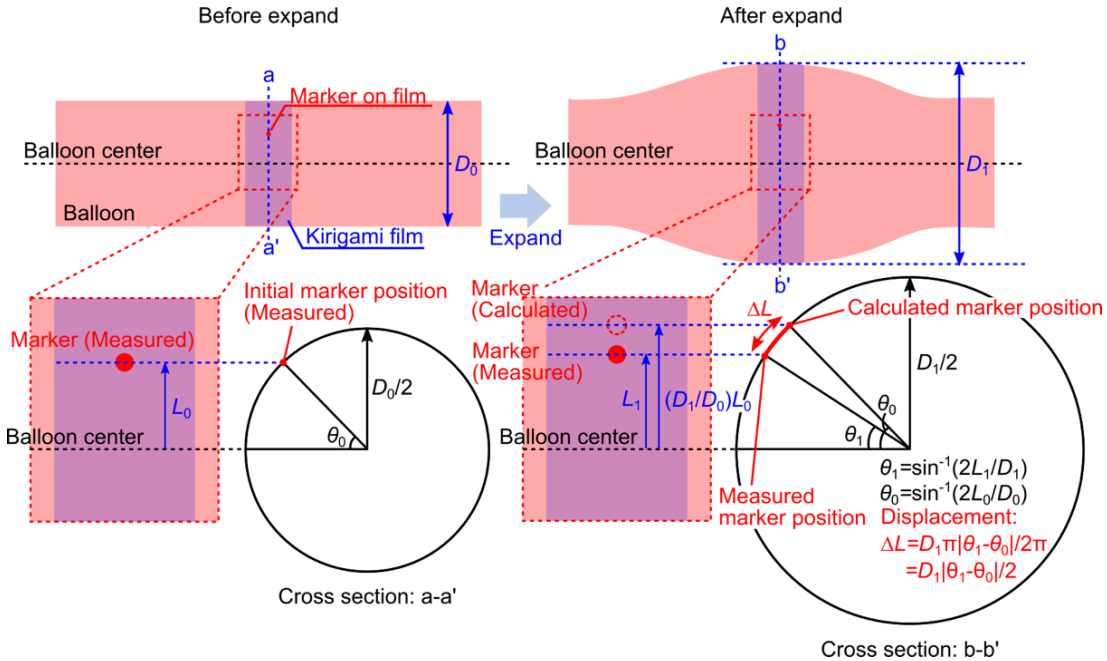

Figure 4.4.3 Schematic diagrams of the displacement test before and after balloon expansion. Considering the curvature of the balloon surface, the device displacement was defined as the length between the calculated and measured marker positions on the balloon's surface after the balloon's expansion.

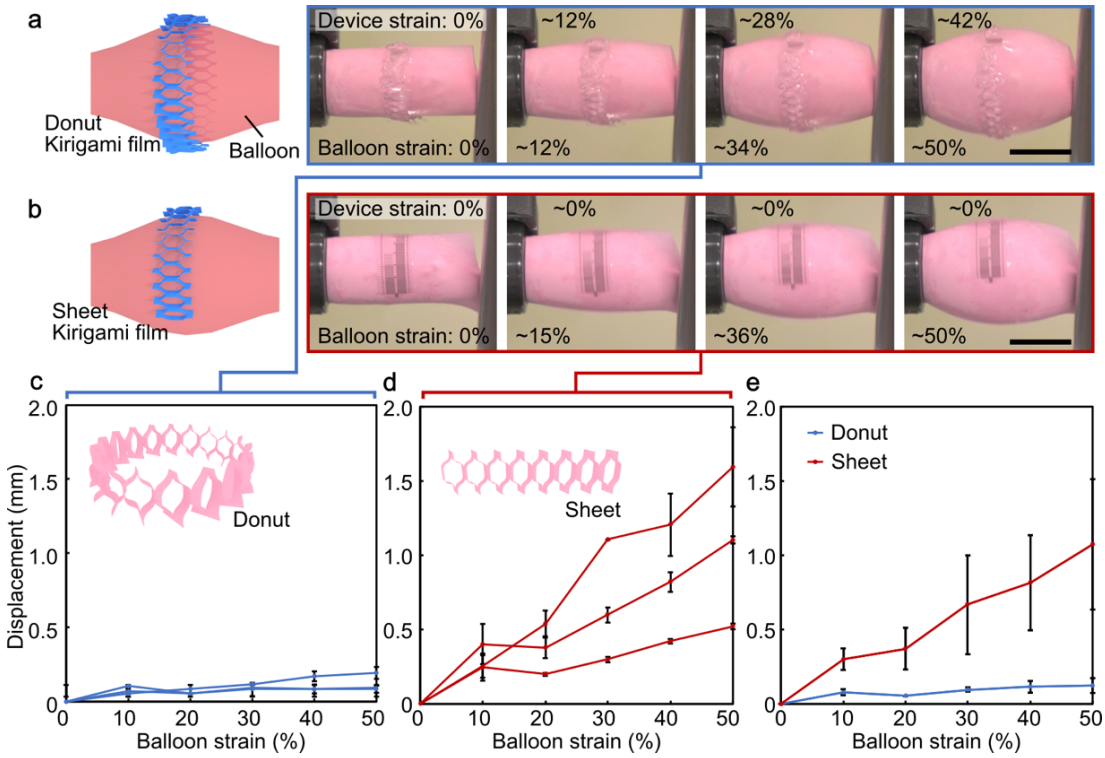

Figure 4.4.4 Displacement test of the Kirigami device on a balloon surface depending on the balloon strain. (a, b) Photographs showing the deformations of the fabricated donut-shaped (a) and sheet-type device (b), when the balloon expands from 0% to 50%. Scale bars = 5 mm. (c, d) Marker displacement of the donut-shaped device (c) and sheet-type devices (d) depending on the strain on the balloon surface. Each curve was derived from three trials of the balloon expansion and represents the averages (five strain cycles in the trial). Error bars indicate SD. (e) Averaged marker displacement for the donut-shaped and sheet-type devices obtained from the three trials in (c) and (d). Error bars indicate SD.

which is five times larger than the reported muscle strain of the human tibialis anterior muscle (~10% strain at maximum contraction intensity) [111]. The donut-shaped Kirigami device showed that the device followed the expansion of the balloon with a displacement of <0.2 mm at the balloon's expansion of ~50% (Figs. 4.4.4a, c). In contrast, the sheet-type device could not follow the expansion of the balloon because of its displacement (Figs. 4.4.4b, d). The displacement of the sheet-type device was >1.5 mm, when the balloon expanded to ~50%. These displacements are shown in Figure 4.4.4e for comparison purposes (each point is averaged from the three trials in Figures 4.4.4c, d). The displacement of the donut-shaped device was ~8 times smaller than that of the sheet-type device.

Schematic images of the repeated displacement test are shown in Figure 4.4.5. 100 balloon expansion cycles were used for each device. The displacement was defined as the difference in distance between the initial marker position on the expanded balloon surface [Marker (Cycle 1), Fig. 4.4.5b] and the marker position in the following cycles [Marker (Cycle n), Fig. 4.4.5b].

The cycle-dependent displacement in the lateral (x-axis) and perpendicular (y-axis) directions against the balloon center line (Fig. 4.4.5b: right) is illustrated in Figures 4.4.6c and d. It is observed that the donut-shaped device exhibited an increased gradual displacement as the cycle number increased (Figs. 4.4.6c, d, blue line). Meanwhile, the displacement of the sheet-type device significantly increased as the trial number increased (Figs. 4.4.6c, d, red line). The sheet type device moved downward and disappeared from the camera view at over 50 cycles ("Cycle 50," in Fig. 4.4.6b). The total displacements calculated with the displacements along the x and y axes (Fig. 4.4.5b) are shown in Figure 4.4.6e. The total displacement of the donut-shaped device was at least five times smaller than the displacement of the sheet-type device. Although the donut-shaped device exhibits some displacement on the balloon, in general, the device follows the balloon's expansion without significant slipping or peeling off. The experimentally measured device displacements (Figs. 4.4.4, 4.4.6) were normalized to the diameter of the balloon, where each device was placed (along the x-axis, as shown in Fig. 4.4.5b).

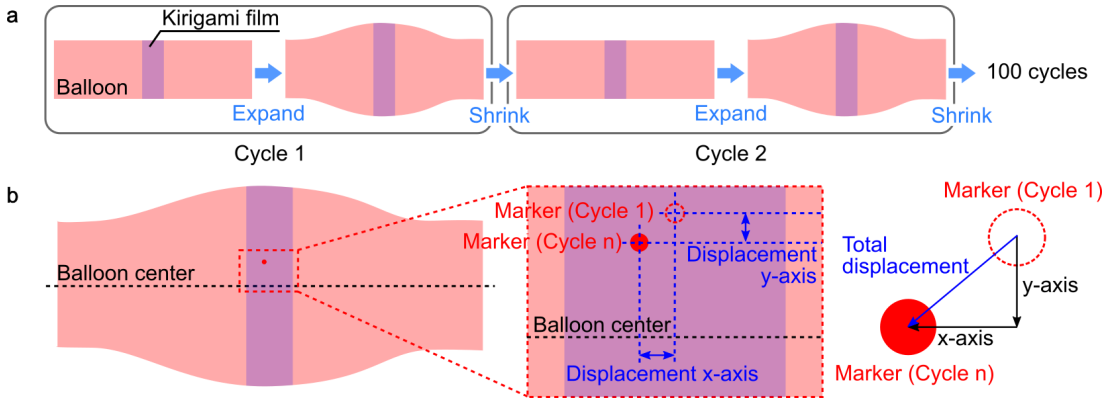

Figure 4.4.5 Repeated displacement test of a Kirigami device on the balloon surface during the balloon 100-cycle stretching. (a) Schematic diagrams of the device on the surface of a balloon, which expands and shrinks repeatedly. (b) Schematic diagram of the displacement as the distance between the initial marker position on the expanded balloon surface [Marker (Cycle 1)] and the marker position in the following cycles [Marker (Cycle n)].

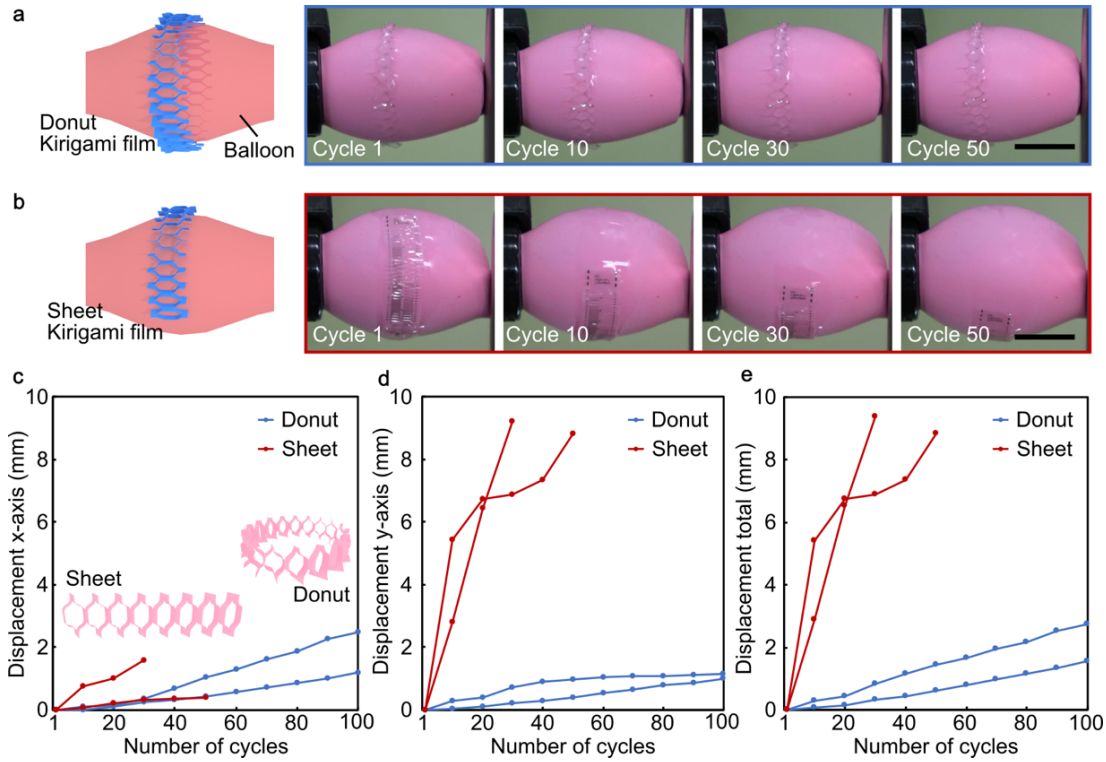

Figure 4.4.6 Displacement test of a Kirigami device on a balloon surface during the balloon 100-cycle stretching. (a, b) Photographs showing the deformations of the donut-shaped (a) and sheet-type (b) devices for a 50-cycle repeated balloon expansion. Scale bars = 5 mm. (c, d) Marker displacements of the x-axis (c) and y-axis (d) for the donut-shaped and sheet-type devices depending on the balloon expansion cycles. Each curve is derived from two trials of the balloon expansion (each trial has 100 cycles of strain). (e) Total marker displacement derived from the displacements in each direction [x-axis (a) and y-axis (b)] for the donut-shaped and sheet-type devices.

4.5 Device packaging using PEG scaffold

In animal experiments, the handling of thin-film devices is a problem because the film geometry (<10 μm in thickness) is not sufficiently self-supporting to be manipulated [31]. In addition, a Kirigami device is more flexible and stretchable compared to the thin-film devices without slit patterns. To overcome the difficulty of the handling of Kirigami devices in animal experiments, the fabricated Kirigami device was embedded in a cylinder of polyethylene glycol (PEG), which is a biocompatible and soluble material (melted by heating and dissolved with liquid) (Fig. 4.5.1).

The fabricated device was successfully embedded into the PEG cylinder. During device embedding, PEG 4,000 and PEG 1,000 with different melting characteristics were used as the scaffold and sacrificial layers, respectively. Initially, melted PEG 1,000 was

coated as the sacrificial layer on a low-temperature polypropylene (PP) tube (iced water in the PP tube) with one side closed [Figs. 4.5.1a(i, ii)]. Next, a Kirigami device was stretched and transformed into a cylindrical shape and the device was transferred onto the sacrificial layer (PEG 1,000) [Fig. 4.5.1a(iii)]. This procedure is described in detail later. Then, PEG 4,000 used as a scaffold layer, was coated over both the device and the sacrificial layer [Fig. 4.5.1a(iv)]. Finally, the fabricated device with the scaffold PEG 4,000 layer was released from the PP tube by melting the sacrificial layer with heating (hot water in the PP tube) [Fig. 4.5.1a(v)]. The PEG cylinder-embedded Kirigami device is shown in Figure 4.5.1b. The inner diameter of the PEG cylinder is ~8 mm and its thickness is ~1 mm.

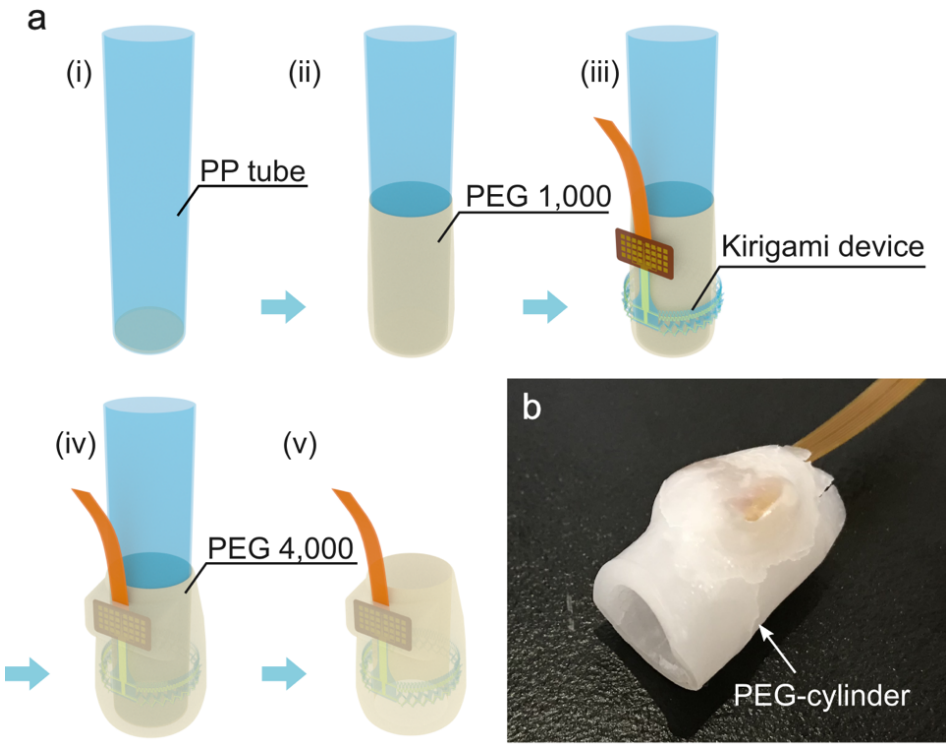

Figure 4.5.1 Device package using a cylindrical PEG scaffold structure. (a) Process steps of the PEG scaffold: (i, ii) coating PEG 1,000 as the sacrificial layer on a low-temperature PP tube (iced water in the PP tube), (iii) attaching the transformed donut-shaped Kirigami device to the PEG layer, (iv) coating PEG 4,000 scaffold layer over both the Kirigami device and the sacrificial layer, and (v) releasing of the Kirigami device with the PEG scaffold from the PP tube by melting the sacrificial layer (PEG 1,000) with PP tube heating (hot water in the PP tube). (b) Photograph of the Kirigami device embedded in the PEG scaffold structure.

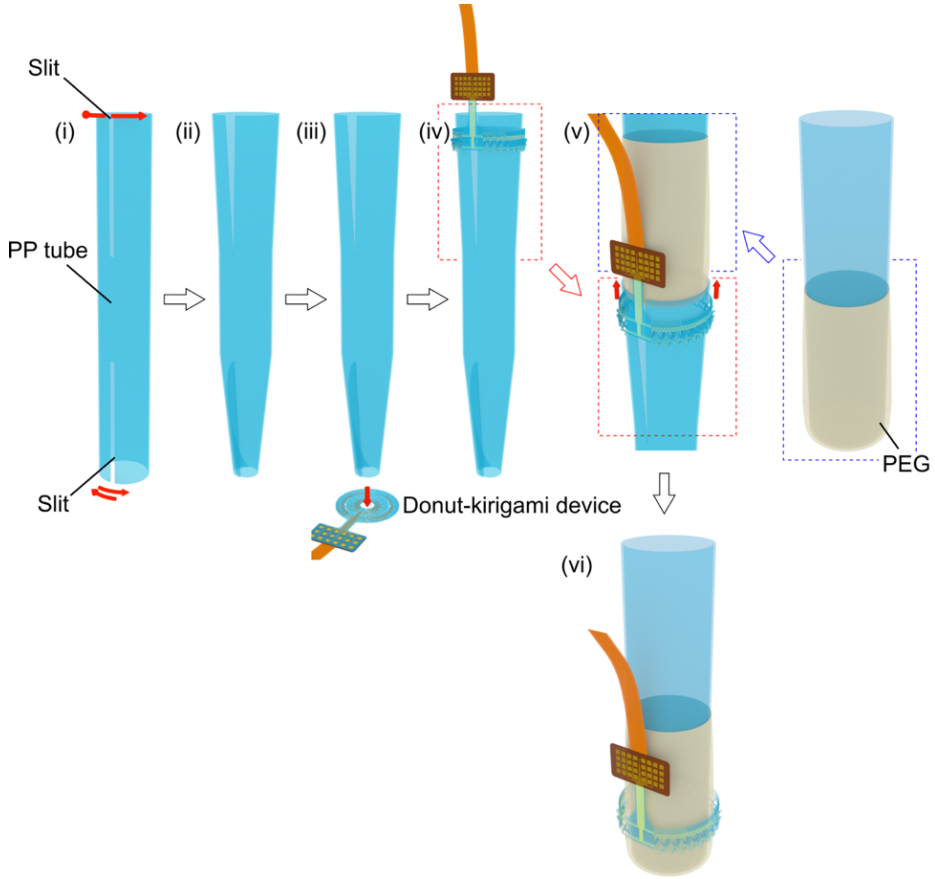

Figure 4.5.2 Transfer of the Kirigami device onto the PEG tube. A PP tube (1st tube) was used. This tube employs slits at both ends, which allow changes in the tube's diameters (i, ii). The 1st tube was used for the transformation of the 2D donut-shaped Kirigami device to the 3D cylindrical shape (iii). The diameter of the Kirigami device transformed to the 3D cylindrical shape was further increased in comparison to the diameter of another PP tube's end with the PEG layer [2nd tube, Fig. 4.5.1(ii)] (iv). Covering the PEG by the 1st PP tube, the Kirigami device could be transferred onto the PEG layer of the 2nd tube (v, vi).

The transformed donut-shaped Kirigami device was transferred onto the PEG using a PP tube (1st tube) with slits at both ends, which helps to adjust the diameter of the tube. This is shown in Figure 4.5.2(i). This tube (1st tube) enables the transformation of the 2D donut-shaped Kirigami device to the 3D cylindrical shape [Figs. 4.5.2(ii-iv)]. Another PP tube coated with the PEG layer (2nd tube mentioned in Fig. 4.5.2a) was also used. The diameter of the 3D Kirigami device surrounding the 1st tube was further increased in comparison to the diameter of the PEG layer of the 2nd PP tube. The Kirigami device could be transferred onto the PEG of the 2nd tube [Fig. 4.5.2(vi)] by

covering the PEG by the 1st PP tube [Fig. 4.5.2(v)].

A dissolving test using a mouse's *in vivo* hind limb was conducted to confirm the dissolving property of the PEG cylinder (Fig. 4.5.3). As a result, the PEG cylinder was dissolved by dropping saline solution and the Kirigami device was exposed from the PEG cylinder within ~15 min. After dissolving the PEG cylinder, the conformal wrapping of the fabricated Kirigami device around the mouse's hind limb was confirmed.

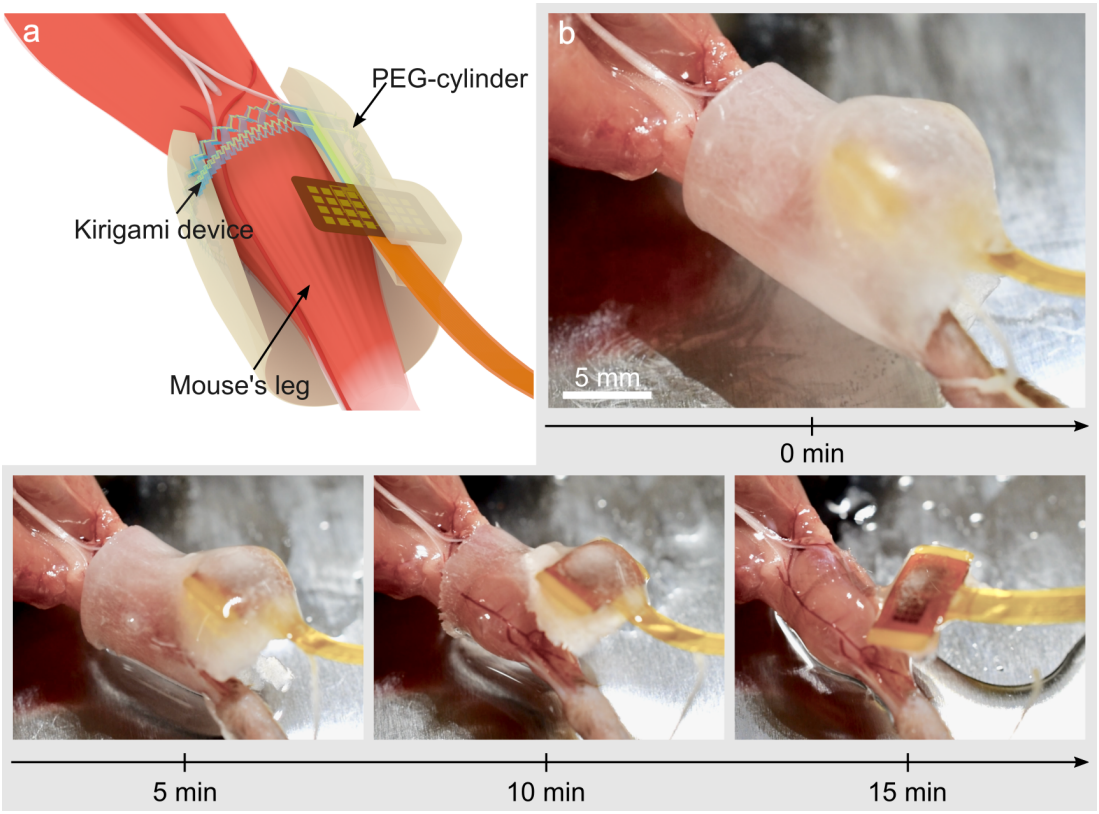

Figure 4.5.3 Dissolving test of the PEG scaffold-embedded Kirigami device on a mouse's hind limb. (a) Schematic diagram of the Kirigami device with the PEG scaffold device attached to the mouse's hind limb. (b) Photographs illustrating the dissolving test of the PEG scaffold. PEG is dissolved by dropping saline solution and the Kirigami device is exposed from the PEG within ~15 min.

4.6 Biological signal recording using donut-shaped Kirigami bioprobe devices

The ECG and EMG signal recordings from a mouse heart and hind limb muscle are demonstrated using the fabricated donut-shaped Kirigami device to confirmed recording capability of the fabricated device from deformable tissues. In the EMG signal recording, EMG signals were recorded during the electrical stimulation to the sciatic nerves to activate the hind limb muscles.

4.6.1 *In vivo* ECG signal recording

The deformation and signal recording capabilities of the device were confirmed by demonstrating the epicardial *in vivo* ECG recording using a mouse's heart. The fabricated device was wrapped around the beating heart (Fig. 4.6.1). The Kirigami device was stretched by ~60% with a strain-stress of ~0.05 MPa. The recorded multi-site waveforms via 23 microelectrodes are shown in Figure 4.6.2. These ECG signals with amplitude of ~ 2.5 mV_{pp} were stably recorded, without significant slip of the device over the beating heart. These ECG signals were recorded via a saline solution, which was used to fill the gap between the electrode and the tissue surface. Some channels were not able to record the signals. This was probably due to the fact that the contact pad was not connected to the FPC during packaging process. Another possible reason was the air gaps between the electrode and the tissue surface.

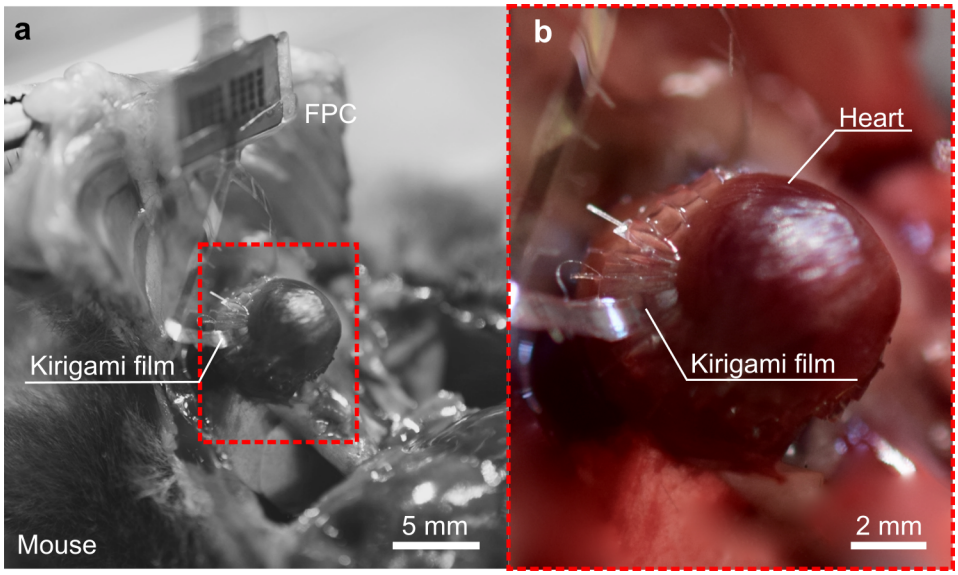

Figure 4.6.1 *In vivo* ECG signal recording from a mouse's heart. (a, b) Photographs of the ECG recording setup, which show the fabricated Kirigami bioprobe film surrounding the beating heart.

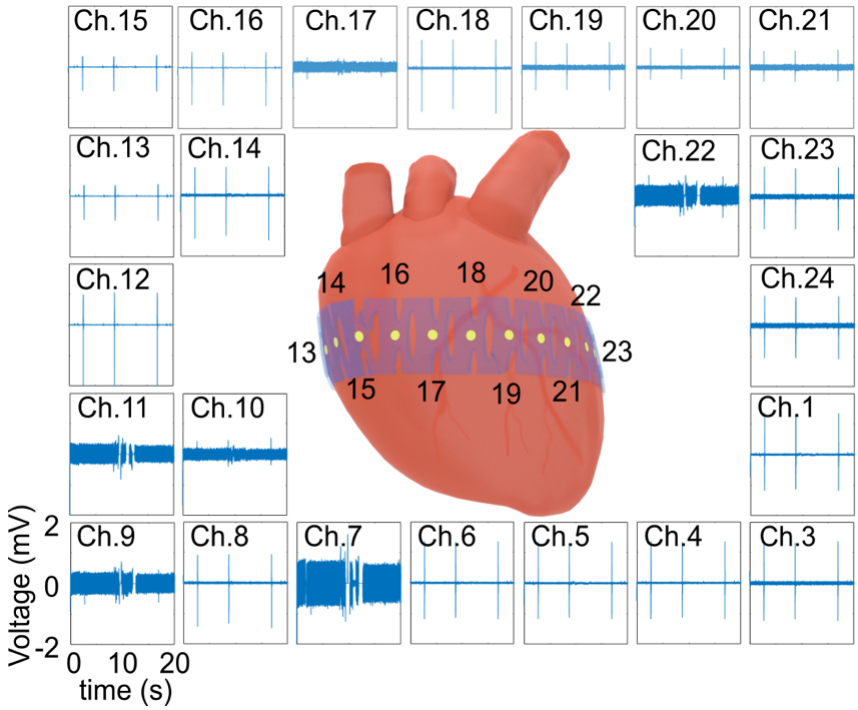

Figure 4.6.2 Multi-channel ECG signal recording via 23 Chs. (Au microelectrodes).

4.6.2 *In vivo* EMG signal recording

The recording capability and deformability of the donut-shaped Kirigami device was also confirmed by EMG signal recording form a mouse's hind limb. The mouse (strain: C57BL, sex: male, weight: 29.0 g) was deeply anesthetized by intraperitoneal injections of chlorprothixene (0.1 ml of 5% solution per 10 g body weight) and urethane (0.05 ml of 10% solution per 10 g body weight). After removing the skin and hamstring muscles of the right limb to expose the lower limb muscles and sciatic nerves, the packaged Kirigami device with the PEG scaffold was placed on the lower limb. Then, the PEG was dissolved by dropping saline solution (~180 ml, room temperature, ~15 min). After dissolving PEG, the Kirigami device was wrapped around the leg muscles (Fig. 4.6.3). The electrodes were placed on the muscles, with Ch. 4 and Ch. 9 electrodes of the array being positioned over the tibialis anterior (TA) and medial gastrocnemius (MG) muscles, respectively (Fig. 4.6.4). An Ag/AgCl wire was attached to the thigh of the leg to operate as a signal reference electrode.

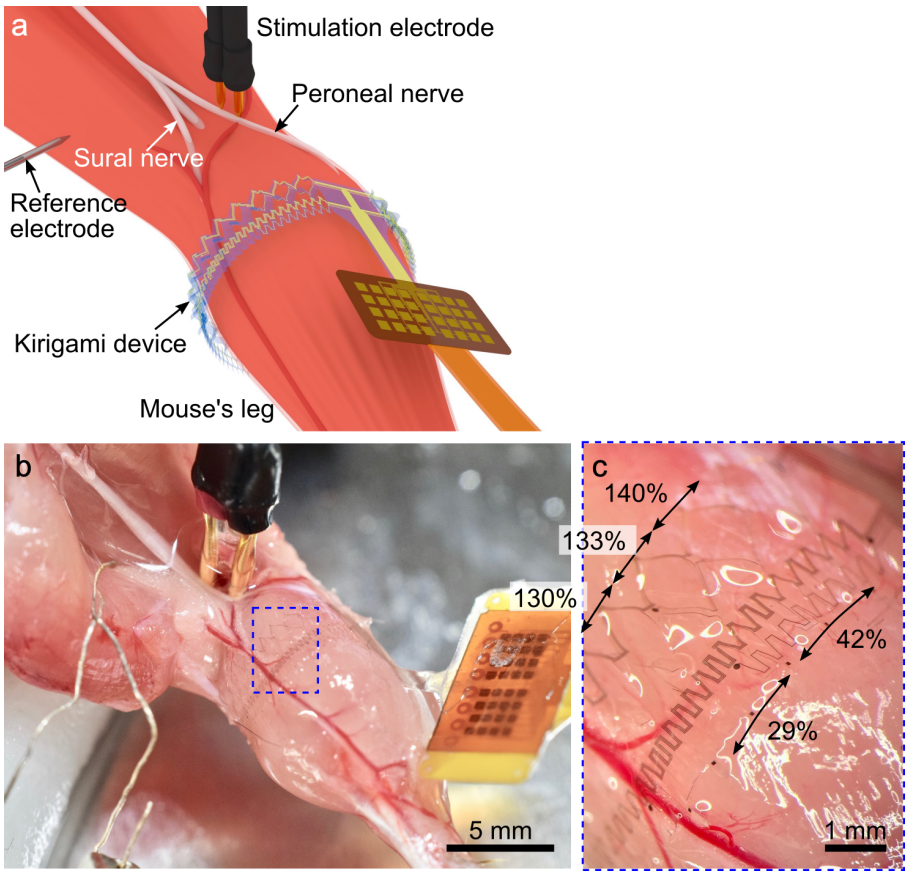

Figure 4.6.3 *In vivo* EMG signal recording from a mouse's hind limb. (a–c) Schematic diagrams and photographs showing the donut-shaped Kirigami device wrapped around a mouse's hind limb.

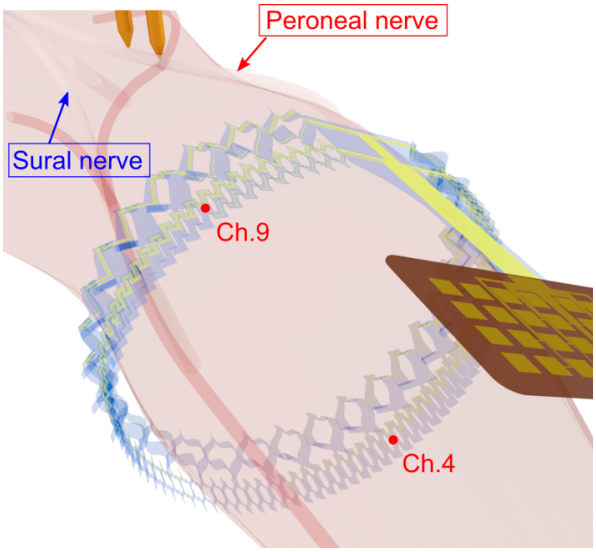

Figure 4.6.4 Schematic diagram showing the positions of two electrodes during the EMG signal recording. Ch. 4 and Ch. 9 electrodes, which were placed opposite to each other on a mouse's hind limb, stimulated the two branches of the sciatic nerve, namely, the peroneal and sural nerves.

The lower limb muscles were activated by electrically stimulating the peroneal and sural nerves (1 ms duration biphasic voltage square wave, 2 s inter trial interval, 320–1,020 mV_{pp} amplitudes, inset in Fig. 4.6.5a) with a handmade bipolar electrode (Au contacts, 1 mm in distance) by an electronic stimulator and isolator (Nihon Koden SEN-4301 and SS-203J). Previous studies confirmed that nerve stimulation causes a muscle response, which passes through afferent fiber, spinal cord, efferent fiber, and neuromuscular junction [112]. Thus, the latency of the EMG signals can be estimated by calculating the conductive velocities of the afferent and efferent fibers and the synaptic delays of the spinal cord and neuromuscular junction. Specific positions of the stimulated area of the spinal cord and the recorded area (electrode positions) are also responsible for the latency. The conductive velocity for sural nerve and peroneal nerve is in the range of 40–50 m/s, and the synaptic delays are ~1 ms for the spinal cord and ~0.75 ms for the neuromuscular junction. The distances between the stimulated area and the spinal cord and between the spinal cord and the neuromuscular junction were 18 mm and 24 mm, respectively. Taking into account these values, the latency of the EMG signal response to the nerve stimulation was calculated to be in the range of 2.6–2.8 ms [113]–[115]. EMG in this range cannot be clearly distinguished from the end point of the stimulation-induced artifact. Therefore, to clearly distinguish the EMG from the artifact, waveforms of 3 ms after the nerve stimulation were used. According to this criterion, the negative peak amplitude of the EMG signal was calculated from the signal during the time range 3–10 ms from the start of the stimulation.

The signals recorded via the electrode in Ch. 9 during each intensity session of the nerve stimulation are presented in Figure 4.6.5a. The threshold voltage, T, was identified as the stimulation intensity at which the smallest EMG response could be observed (Fig. 4.6.5a). The negative peak amplitudes of the recorded EMG signals (3–10 ms), which depend on the stimulus intensity, are shown in Figure 4.6.5b. No increase in the EMG signal amplitude was observed with stimulation voltages of 320–680 mV (stimulus intensity of 0.39T–0.83T). However, the EMG signal amplitude increased with a stimulation voltage of >680 mV. The non-linearities observed between EMG and stimulus intensity suggest that the recorded signals originated from physiological response rather than the artifact [116], [117].

The recorded EMG signals (100 trials) through Ch. 4 and Ch. 9 electrodes, while stimulating the two branches of the sciatic nerve, namely, the peroneal and sural nerves (Fig. 4.6.3a), are shown in Figure 4.6.6. These electrodes, which were placed at opposite sides of the mouse's leg, were positioned over the TA and MG muscles, respectively. The peak-to-peak amplitudes of the recorded EMG signals via the Ch. 4 and Ch. 9 electrodes,

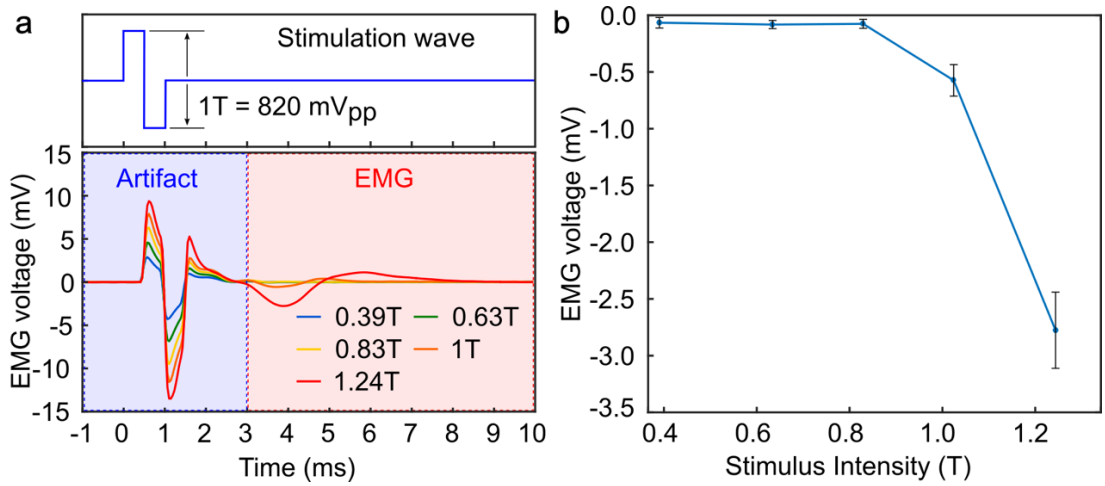

Figure 4.6.5 EMG signals evoked by nerve stimulations. (a) Recorded signals via a Ch. 9 electrode in the device during nerve stimulations. The amplitude of the stimulation signal ranges from 320 mV to 1,020 mV (stimulus intensity of 0.39T–1.24T). (b) Stimulus intensity-dependent EMG signal amplitudes. Averages and SD for EMG signal amplitudes were taken from EMG signals during 100 trials of stimulation; the error bars indicate SD.

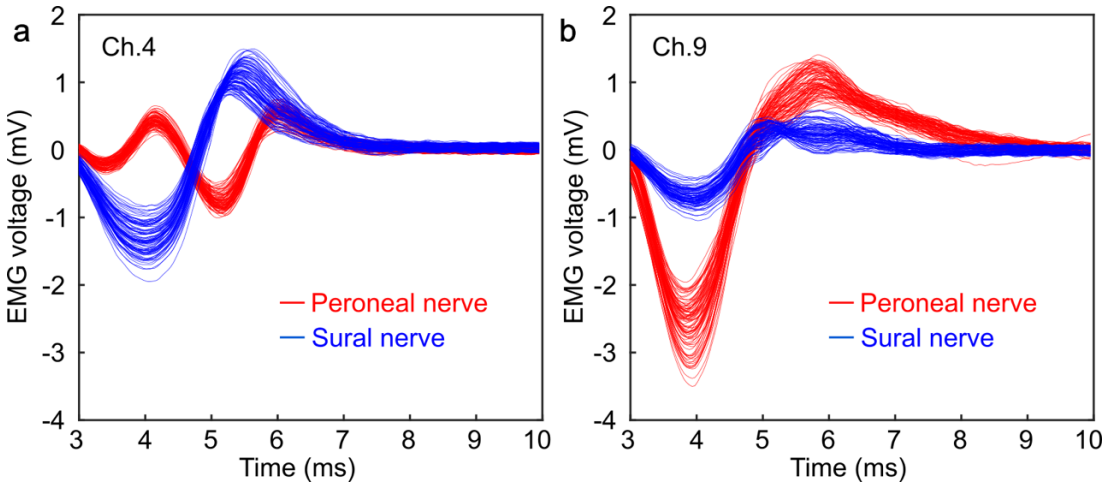

Figure 4.6.6 Recorded EMG signals during 100 trials of stimulations of two branches of the sciatic nerve. (a, b) Recorded EMG signals via the two electrodes (Ch. 4 and Ch. 9). Red and blue lines show the EMG signals evoked by the stimuli to the peroneal and sural nerve, respectively.

while stimulating the two branches of the sciatic nerves, are shown in Figure 4.6.7. Student's *t*-test was used to analyze the statistical differences between EMG signals evoked by either peroneal or sural nerve stimulation. The effect of those stimuli was statistically significant for the recorded signals via each electrode [Student's *t*-test;

df = 198, $p = 1.37 \times 10^{-65}$ (Ch. 4), $p = 1.40 \times 10^{-114}$ (Ch. 9)]. For each stimulation condition, the recorded EMG signals were analyzed by averaging the filtered signals (20–3,000 Hz, first-ordered Butterworth filter) for all 100 trials. In addition, the displacement of the device was <0.1 mm after the 20 nerve stimulation trials as confirmed by the videos and pictures taken from the animal experiment (Fig. 4.6.8).

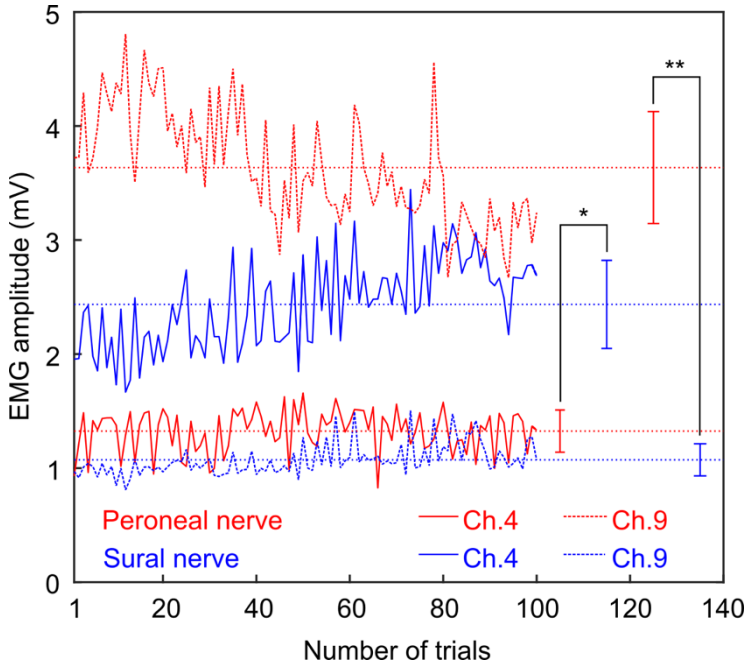

Figure 4.6.7 Peak-to-peak amplitudes of the recorded EMG signals depending on the number of stimulation trial. Horizontal dashed lines represent averages for each EMG signal amplitude. The error bars indicate SD (* : $p = 1.37 \times 10^{-65}$, ** : $p = 1.40 \times 10^{-114}$, Student's *t*-test; df = 198).

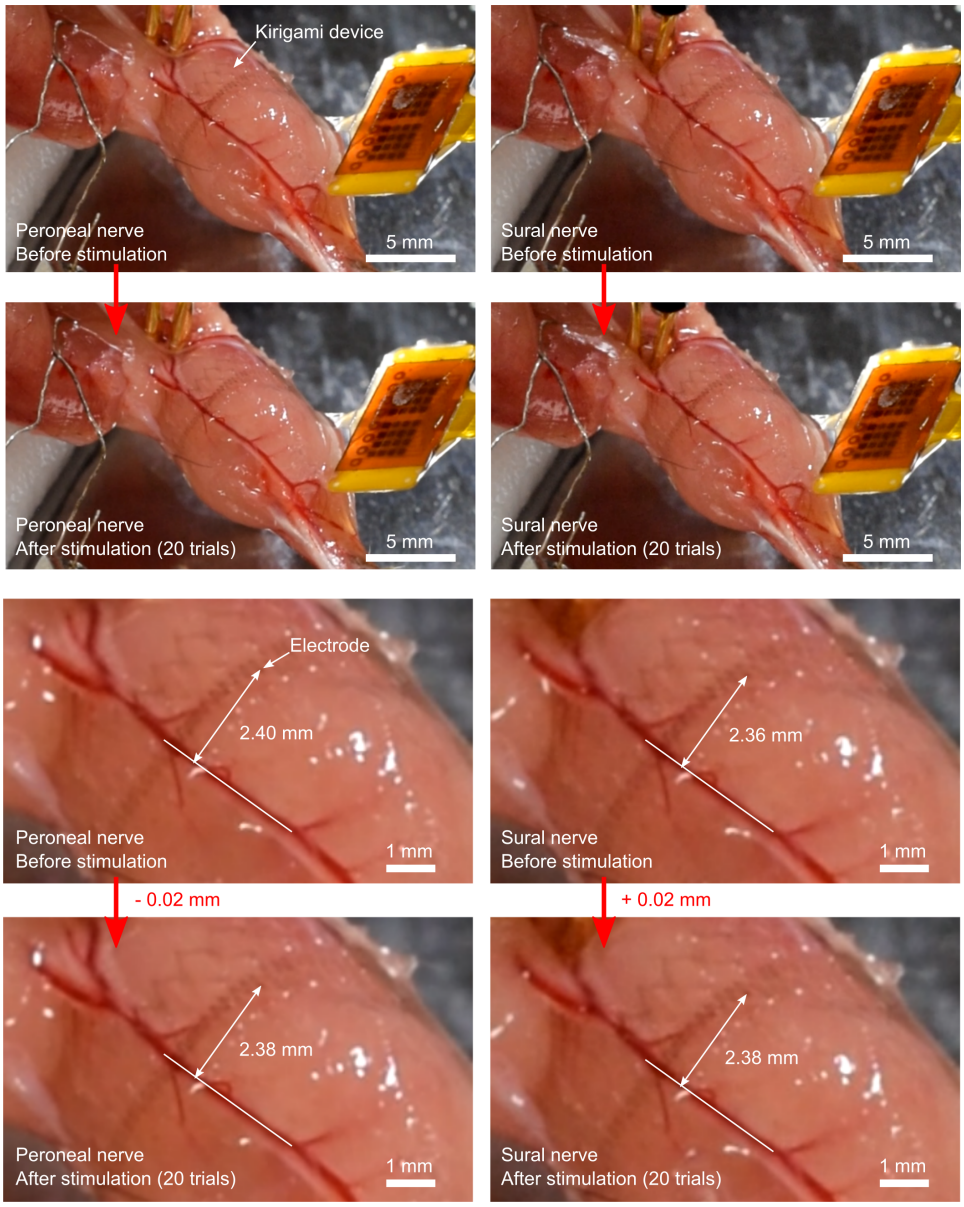

Figure 4.6.8 Electrode displacement after 20 stimulation cycles to the peroneal and sural nerve (top: full view, bottom: enlarged view).

The EMG signals recorded using the donut-shaped Kirigami device were verified by also conducting EMG signal recording using a conventional electrode of 1-mm-diameter Au-pin (Fig. 4.6.9). The Au-electrode was placed on the MG muscle, at the same position as Ch. 9 of the donut-shaped Kirigami device (Fig. 4.6.4). As shown in Figure 4.6.9, the relationship between the recorded EMG signals via the pin electrode and the stimulation intensity is non-linear (Fig. 4.6.9b). This is also the case for EMG signals recorded via the donut-shaped Kirigami device (Fig. 4.6.5b). The waveforms of the recorded EMG signals for 100 trials, while stimulating the two branches of the sciatic

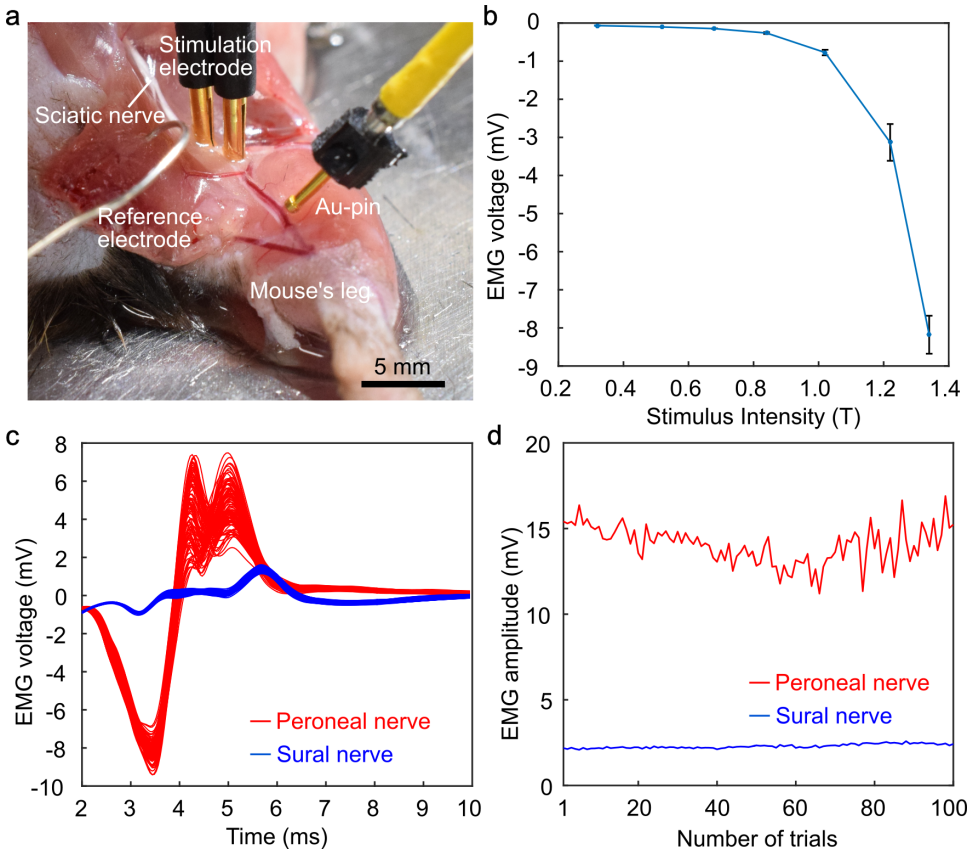

Figure 4.6.9 *In vivo* EMG signal recording from a mouse's hind limb using a 1-mm-diameter Au-electrode. The Au-electrode was placed on a mouse's hind limb, while stimulating the two branches of the sciatic nerve (peroneal and sural nerves). (a) Photograph of the EMG signal recording experiment. (b) Stimulus intensity-dependent EMG signal amplitudes. Averages and SD for EMG signal amplitudes were taken from EMG signals during 100 trials of stimulation; the error bars indicate SD. (c) Recorded EMG signal waveforms during the 100 trials of stimulations to peroneal and sural nerves. (d) Peak-to-peak amplitudes of the recorded EMG signals.

nerve (peroneal and sural nerves), are shown in Figure 4.6.9c. The latency and waveforms of these EMG signals have similar properties to the signals recorded using the donut-shaped Kirigami device. The peak-to-peak amplitudes of the recorded EMG signals, while stimulating the two branches of the sciatic nerve, are shown in Figure 4.6.9d. The relationship between these EMG amplitudes also exhibits the tendency observed in the recording, when the donut-shaped Kirigami device was used. According to these results, the signals recorded using the donut-shaped Kirigami device are considered to be EMG signals evoked by the nerve stimulation.

The recording capability of the Kirigami device was demonstrated using a

mouse's hind limb. The results indicate that the donut-shaped Kirigami device has the capability to record the EMG signals and distinguish the responses evoked by stimuli for different nerves. It was also confirmed that not only the donut-shaped Kirigami device was unaffected by the muscle deformation, but also that it did not affect the muscle function, such as disturbing the muscle's deformation and causing an ischemia. The device's displacement of < 0.1 mm, which was confirmed in the animal experiment, is in the same order of magnitude as the diameter of the muscle fibers (e.g. ~50 μm in gastrocnemius muscles [118]). This indicates that the donut-shaped Kirigami device suffers a very small device displacement on the muscle for the stable recording of the EMG signals. Considering the EMG signal recording analysis, the EMG signal is defined in the range 3–10 ms (Fig. 4.6.5a). This range is used for the detection of the response caused by the nerve stimulation propagating in the direction of the afferent and through the spinal cord (H-reflex). The response caused by the stimulation propagated in the direction of the efferent (M-wave) can be observed in ~1 ms and it could not be distinguished in this analysis due to presence of the artifact. However, the effect of the artifact associated with the electrical stimulations can be ignored for practical applications.

The Kirigami bioprobe with its 3D cylindrical shape enables the fixation of the device's microelectrodes to the target muscles, thereby solving the issue of device displacement. The difficulty of handling the cylindrical and flexible Kirigami device during its attachment to the mouse's hind limb could be overcome using a PEG scaffold (Fig. 4.5.1). The PEG scaffold is also applicable to different shapes and sizes of organs and tissues by varying the shape of the PEG before the device attachment [Fig. 4.5.1(iii)]. The diameter and stretchability (effective modulus) of the Kirigami bioprobe can also be varied by changing the slit design depending on the target tissues and organs. Although the application of the device is limited to tissues and organs with open ends, as demonstrated in the case of the mouse's heart and limb, the device is also applicable to legs, arms, fingers, abdomen, back, and others.

4.7 Conclusions

In this chapter, donut-shaped Kirigami bioprobe devices for both accurate and robust biological signal recording from large and rapid deformable tissues including heart and muscle were proposed. The donut-shape Kirigami structure allows the Kirigami device to be wrapped around the biological tissues and to follow their deformation without significant device displacement over the muscle or physical stress to the tissues. Embedding the Kirigami device in a dissolvable PEG material solved the difficulty of using the flexible, stretchable, and thin-film Kirigami device in an animal experiment. *In*

vivo signal recording using a mouse's heart and hind limb confirmed ECG and EMG signal recording capability without significant electrode displacement and produced a stable signal recording, which was unaffected by tissue deformation.

The advantages of the proposed device (low effective modulus, high strain, and easy fixation to deformable tissues) offers stable biological signal recordings from large deformable tissues in the long-term and chronic applications, although the animal experiment presented in this chapter demonstrated the device's acute recording capability using a mouse's heart and hind limb. In addition to these advantages, the proposed donut-shaped Kirigami approach allowed the integration of an array of dense microelectrodes with the flexible and stretchable device film within the 3D cylindrical shape. The device's electrodes enabled to acquire high-spatiotemporal signals from the target tissues. The proposed device can be used in numerous applications, such as human–machine interface and muscle activity mapping in free moving, which have not been achieved by other electrode devices.

In the next chapter, the integration of the stretchable Kirigami device based on the flexible substrate and rigid components to realize a multifunctional Kirigami device is described. This is as another challenge for the Kirigami device.

Chapter 5:
Optoelectrical Kirigami device

5.1 Introduction

In this chapter, heart disease treatment using a Kirigami device is described, which is another challenge for the Kirigami device. In this application the rigid component of the LED is integrated in the Kirigami film and it extends the possibility of the Kirigami device integration with rigid and unstretchable components, such as Si transistor.

Ventricular arrhythmias, such as fibrillation, are one of the major causes of sudden death. Apart from pharmacological treatments, these diseases often require the implantation of an electrical stimulator. These stimulators are equipped with recording electrodes to detect signs of fibrillation in the ECG signal; they apply an electric shock to the heart via larger paddle electrodes to terminate the fibrillation. Technically, the electric shocks for defibrillation are by far larger than those required for electrical heart pacing. They are also believed to induce irreversible damage to the cardiac muscle, thereby increasing mortality and causing intense pain to the patients, who often recall the experience as a psychological trauma [119], [120]. To overcome the therapy-related problems of electrical stimulation, defibrillation based on the optogenetic intervention using light-sensitive proteins, such as channel-rhodopsin-2, has been proposed in various studies [121], [122]. Implantable test systems comprising LEDs were proposed in the past. They are either placed onto the heart muscle or inserted into it [24].

Here, we propose the optoelectrical Kirigami device for an intimate application of an optoelectrical stimulation and electrophysiological recording on the soft cardiac tissue. When a flexible implant is wrapped around the whole heart, stiffness/Young's modulus mismatch of the flexible device potentially prohibits the free beating of the heart muscle. The low effective Young's modulus of the Kirigami structure, which is comparable to the soft biological tissues, enables device implantation without restriction of the heart beating. In addition, the stretching mechanism based on the bending of the Kirigami beams prevents the failure of interconnects and it is well-suited for integration of rigid,

unstretchable chips, such as LED chips, into the substrate.

In this work, PI was applied as an established material for the realization of the MEMS-based Kirigami structure. As illustrated in Figure 5.1.1, the device employs integrated microelectrodes and interconnecting lines as well as LED chips, which are assembled to electroplated pads using flip-chip bonding. The stretchable optoelectrical Kirigami device is designed to enable simultaneous ECG measurements and optogenetic stimulation for a cardiac tissue. Its mechanical structure employs slit patterns of different lengths, resulting in specific stretching properties that fit well to the shape of the heart. This structure improves device fixation to the targeted tissue and reduces the distance between the electrodes and the tissue surface. The ends of the device are fixed to each other by fastener structures designed as latches that are locked in place once the Kirigami device is wrapped around the heart.

5.2 Design and fabrication of the stretchable optoelectrical Kirigami device

Based on the displacement model and simulations described in Chapter 2, stretchable optoelectrical Kirigami device for the optical stimulation and ECG signal recording from the mouse heart was designed. The designed optoelectrical Kirigami device was fabricated using a microfabrication process, which includes a PI substrate, multi-types of the metal layers for microelectrodes and interconnections of thin platinum and thick gold, and bonded μLEDs.

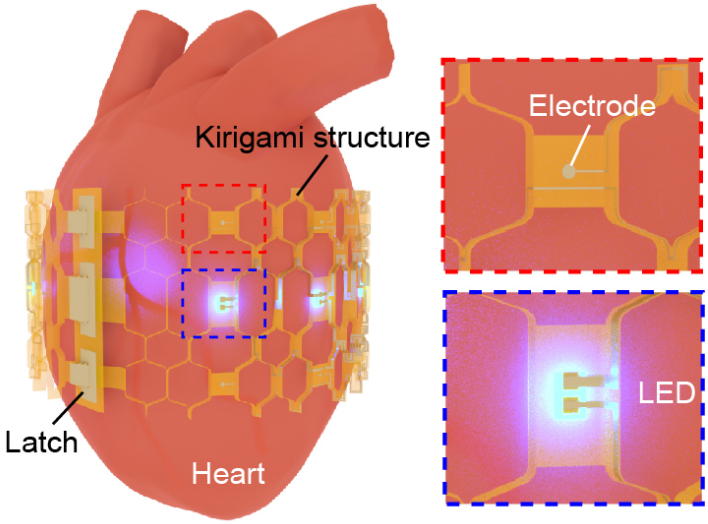

Figure 5.1.1 Schematic diagram of a mouse's heart enwrapped in the highly stretchable optoelectrical Kirigami device, which employs LEDs and microelectrodes.

5.2.1 Design of the stretchable optoelectrical Kirigami device

A stretchable optoelectrical Kirigami device with a Kirigami patterned area of ~6 × 11 mm^2 consisting of $N_r = 3 \times N_c = 20$ cell array was designed (Fig. 5.2.1). The specific deformation of the heart shape was achieved by including two types of cell patterns in the device. The cell in the device's center part has a slit length of 2,200 μm, a

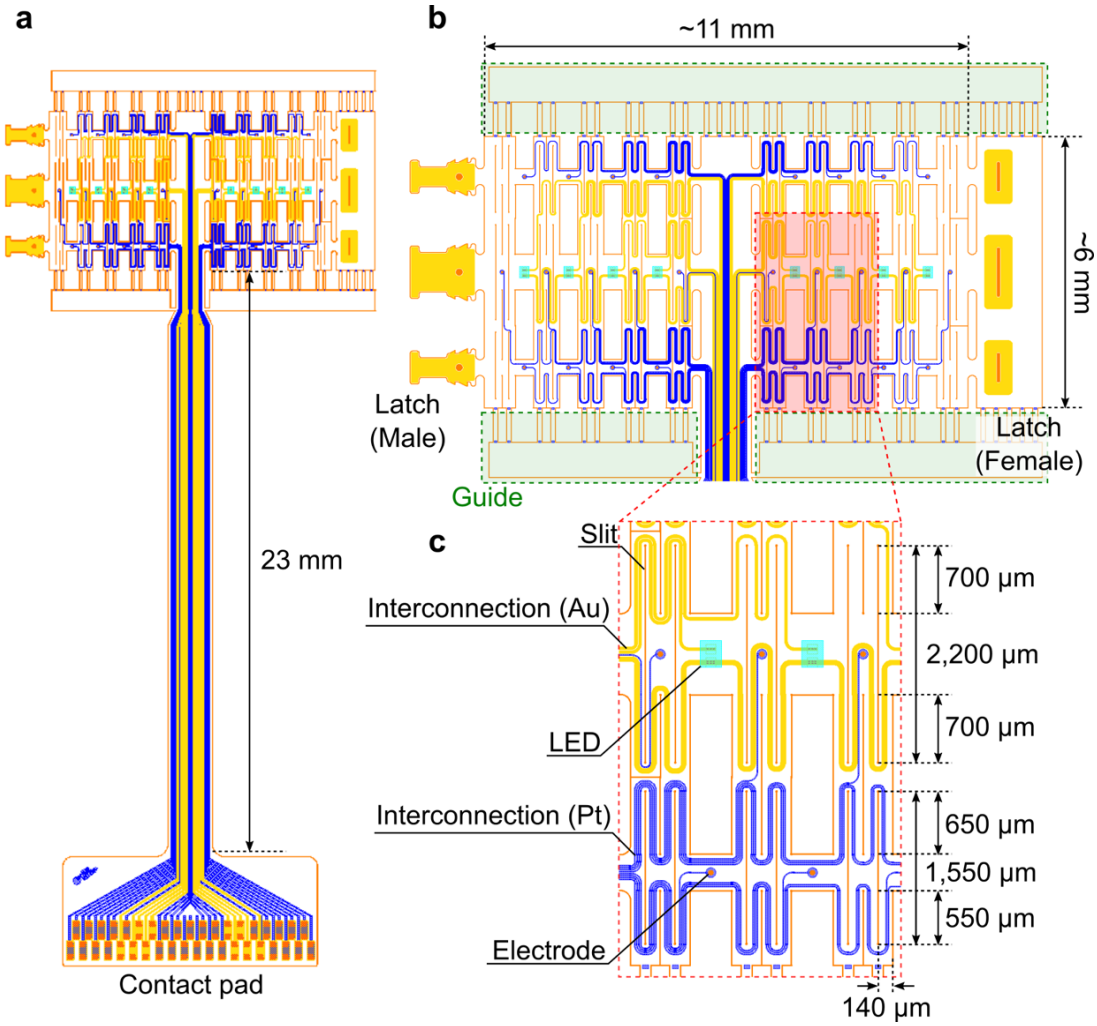

Figure 5.2.1 Design of the stretchable optoelectrical Kirigami device. (a) Full image of the designed Kirigami device with an 8-LED array and 26 electrode channel array. The Kirigami structured site is connected to the contact pad with a 23 mm long interconnection for the animal experiment. (layers colored orange: device contour of the PI, blue: Pt for electrodes, yellow: Au/Pt interconnections for LEDs, light blue: LED). (b) Enlarged view of the Kirigami structured site with the LEDs and electrodes. Guide for easy handling of the Kirigami device is placed in each side (green square). (c) Kirigami structure with electrodes and interconnections.

gap of 800 µm between the slits, a beam length of 700 µm, and a beam width of 140 µm (Fig. 5.2.1c). The other cell in the device's rim part (device top and bottom side in Figure 5.2.1b) has a slit length of 1,550 µm, a gap of 350 µm between the slits, a beam length of 650 µm (inner side) and 550 µm (outer side), and a beam width of 140 µm (Fig. 5.2.1c). In Figure 5.2.1, layers colored orange, blue, yellow, and light blue exhibit the device's contour of the PI, Pt for electrodes, Au/Pt interconnections for LEDs, and LEDs, respectively. This stretchable Kirigami device employs an 8-channel and 10-channel microelectrodes array in the rim parts and the center part and an 8 LED array in the center part. Each recording site, which uses a 50-µm-diameter Pt electrode, is connected to the contact pad with a zigzag interconnection (10-µm wide). LEDs are connected to the contact pad with interconnections of 50 µm and 30 µm in width. Each side of the Kirigami device employs a guide structure for easy handling (green square in Fig. 5.2.1b). The calculated maximum strain of the device's center part and rim part are 110% and 75%, respectively.

5.2.2 Device fabrication

The fabrication process of the stretchable, optoelectrical Kirigami probe is illustrated in Figure 5.2.2. First, a 5-µm-thick PI layer is spin-coated on a Si carrier wafer [Figs. 5.2.2(i, ii)] followed by a Pt-based metallization patterned by lift-off [Fig. 5.2.2(iii)]. The LED interconnections are electroplated with gold (Au, thickness 1 µm) to reduce the line resistance [Fig. 5.2.2(iv)]. Subsequently, a second PI layer (5 µm) is deposited and patterned to realize vias and electrode openings followed by bonding and contact pad formation using again Pt lift-off and Au electroplating process steps [Figs. 5.2.2(v, vi)]. To define the device contour, a dual-layer PI stack is patterned by reactive ion etching [RIE, Fig. 5.2.2(vii)] using a thick photoresist as the masking layer. After peeling off the devices from the Si wafer, LEDs are bonded using a flip-chip bonder [Fineplacer 96λ, Finetech GmbH, Berlin, Germany, Figs. 5.2.2(viii, ix)].

In order to ensure normal operation for the proposed optoelectrical device in a wet environment, LED contacts require an appropriate encapsulation. As schematically illustrated in Figure 5.2.3, this encapsulation is achieved by underfilling the LED chips with a solvent-free, two-component, medical grade epoxy resin (EpoTek 301-2, Epoxy Technologies Inc., Billerica, MA, USA) followed by a thin fluoropolymer layer (Cytop 809M, Asahi Glass Co. Ltd., Tokyo, Japan) applied by drop casting. Finally, the LED chips are coated with a thin layer of silicone (Elastosil RT604, Wacker Chemie AG, Munich, Germany). The encapsulation materials applied are characterized by a high optical transparency. In addition, the mechanical fixation of the LED chips to the PI

substrate is also improved.

A fully encapsulated LED chip is shown in the optical micrograph of Figure 5.2.4. It is obvious that the manual application of the epoxy resin underfill, Cytop, and silicone leads to a certain spreading of the liquid materials. This will be addressed in a future assembly and encapsulation tests by applying either photolithographically defined confinement structures or micro-fabricated molds in order to restrict the encapsulation to a smaller area around the LED chips. In this way, any potential coverage of the closely positioned microelectrodes and Kirigami slits is avoided (Fig. 5.2.5).

The photograph of a fabricated polyimide-based Kirigami device, which is compared with a 1 euro cent coin is shown in Figure 5.2.6. The structure comprises two

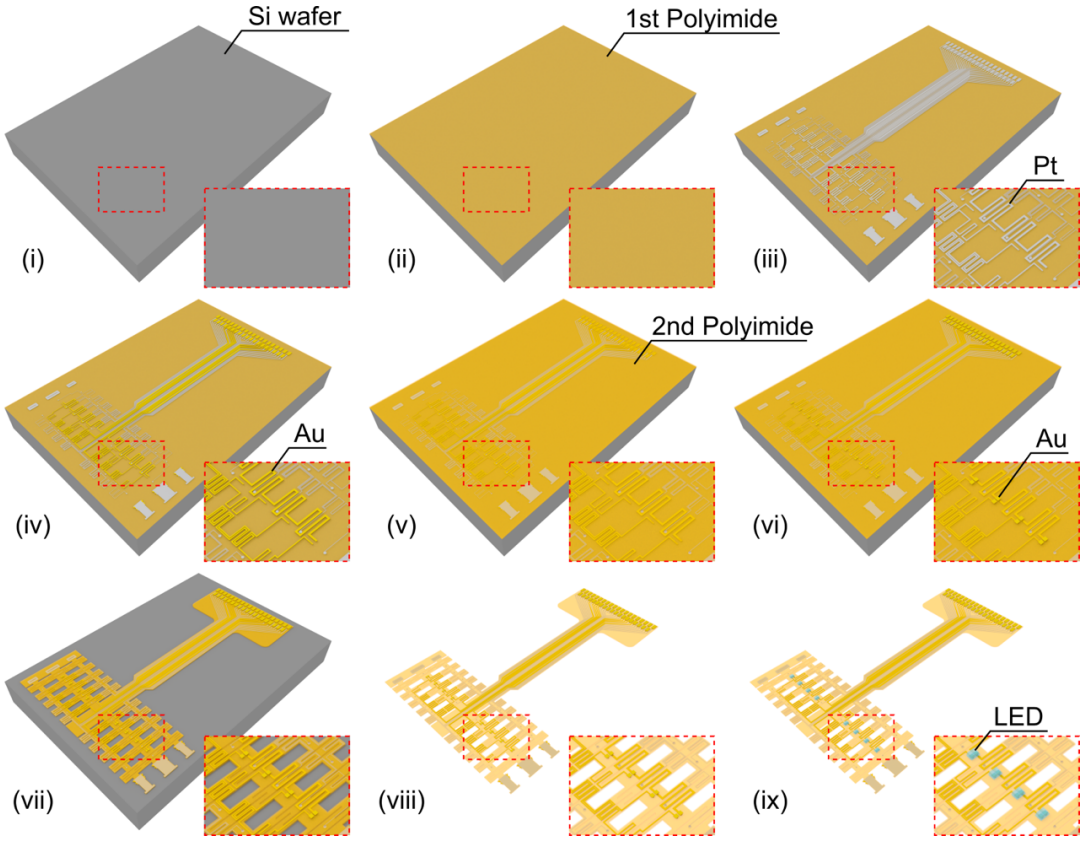

Figure 5.2.2 Fabrication process of the optoelectrical Kirigami probe: (i, ii) spin-coating of the 1st PI layer on the Si wafer, (iii) deposition and patterning of Pt by sputtering and lift-off for the interconnections and microelectrodes, (iv) partial Au electroplating for LED interconnections, (v) spin-coating of the 2nd PI layer, (vi) fabrication of contact pads by Au electroplating, (vii) patterning of the PI stack using RIE, (viii) device release from the Si wafer and, (ix) LED assembly using flip-chip bonding.

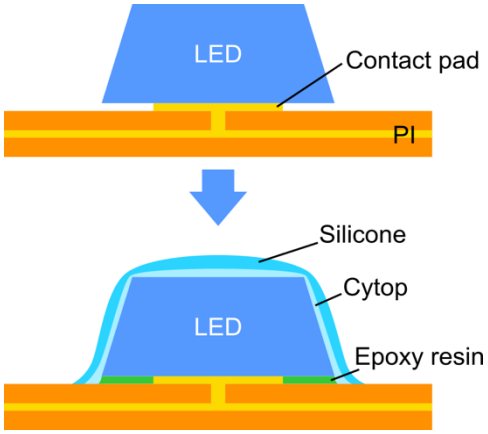

Figure 5.2.3 Schematic side view of the LED encapsulation using epoxy resin (Cytop and silicone).

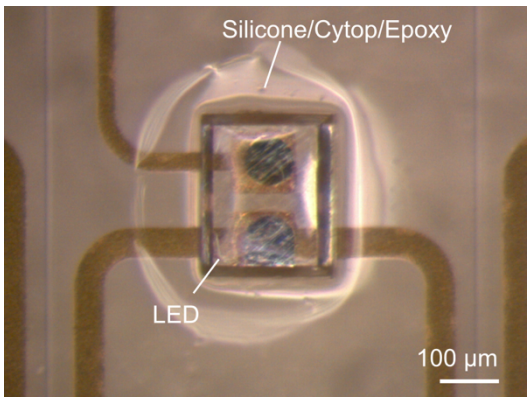

Figure 5.2.4 Optical micrograph (top view) of a LED chip underfilled with epoxy resin and encapsulated in Cytop and silicone.

linear arrays of eight electrodes along lines A-A′ and C-C′ as well as eight LED chips and 10 electrodes along line B-B′. The Kirigami section is connected on the left hand side to an array of contact pads, which fit to a 39-pin zero-insertion-force (ZIF) connector with a contact pitch of 0.25 mm. The interconnecting cable between the Kirigami section and the ZIF interface is 23 mm long and 1.8 mm wide.

The key components of the optoelectrical Kirigami device are shown in Figure 5.2.7 in further detail. The numbers in the upper left corner correspond to those shown in Figure 5.2.6. The photograph in Figure 5.2.7(1) illustrates the central part of the Kirigami device with an embedded Pt electrode (diameter of 50 µm) and LED chips [TR2227 (CREE, Durham, NC, USA) with dimensions of 270 × 220 × 50 μm^3] bonded onto electroplated Au pads using flip-chip bonding. A part of the Kirigami device close to the interconnecting cable, i.e., along line C-C′, which is identical to the part along line

A-A´ in Figure 5.2.6, is shown in Figure 5.2.7(2). The larger male and female types of the latch structures [123] are shown in Figures 5.2.7(3) and (4). All types of latches include a Pt layer support. Furthermore, the male part includes a section with tooth-like structures thickened by Au electroplating.

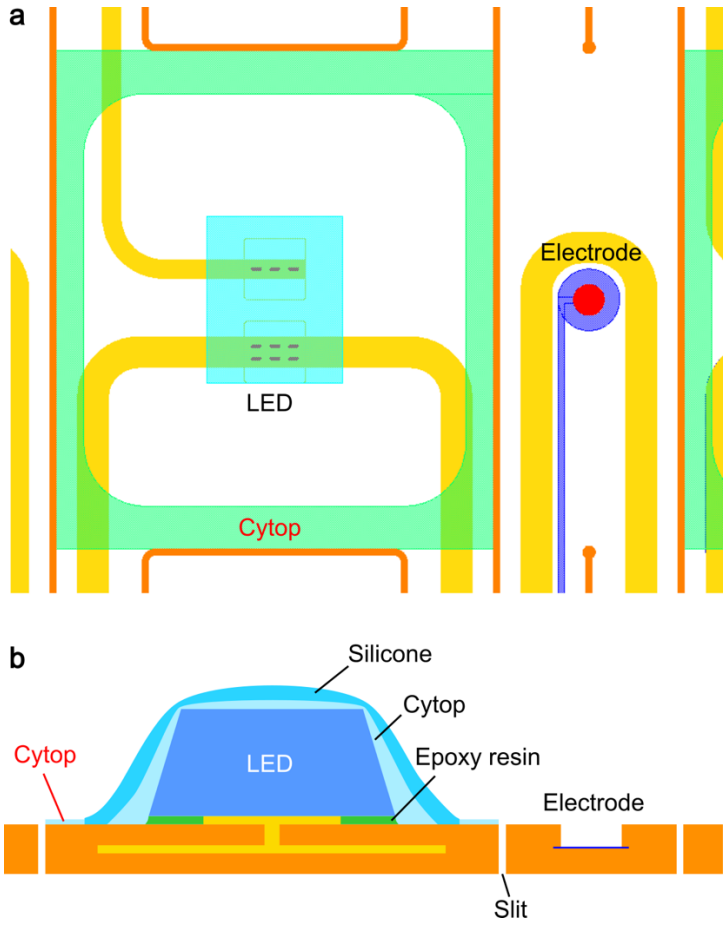

Figure 5.2.5 Confinement structures to restrict the encapsulation to a smaller area around the LED chips, thus avoiding any potential coverage of the closely positioned microelectrodes and Kirigami slits. (a) Design of the confinement structure around the LED. (b) Schematic diagram of the encapsulation using the confinement structure.

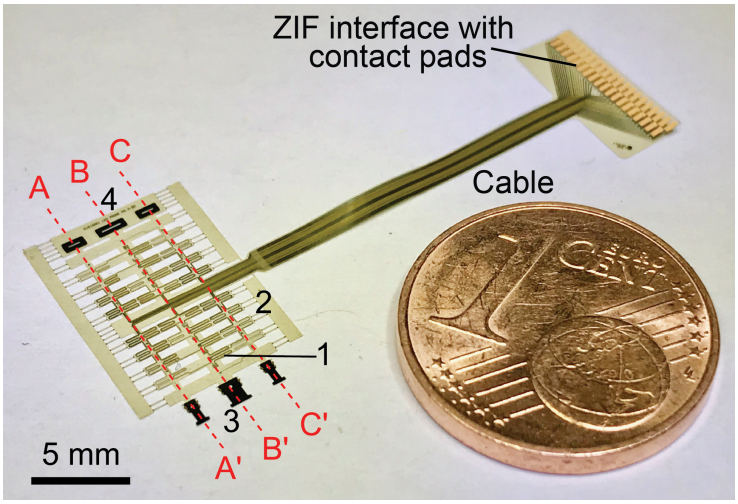

Figure 5.2.6 Photograph of a fabricated optoelectrical Kirigami device (left) and ZIF interface (right) interconnected through a 39-channel cable. Their dimensions are compared with a 1 euro cent coin.

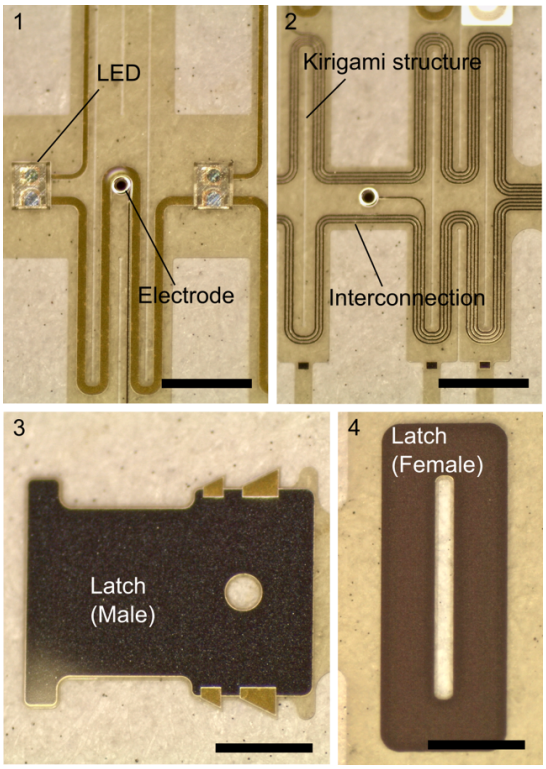

Figure 5.2.7 Optical micrographs of key components of the fabricated Kirigami device (1, 2) Bonded LEDs and embedded electrodes in the Kirigami film, (3, 4) male and female types of the latch structure used for the fixation of the Kirigami device to the heart (scale bar: 500 µm; numbers correspond to locations indicated in Figure 5.6.2).

5.3 Device characterization

To confirm the capability of the components included in the optoelectrical Kirigami device (thin and thickened device interconnections, latch structures, and bonded LEDs), characterization of these components was conducted. As the characterizations of interconnections embedded in Kirigami structures, the resistance of the interconnection was measured using test structures with different interconnection width, thickness and Kirigami design. The fixation force of the latch structure was measured in the tensile test. The bonded LEDs were demonstrated in the functionally test of LEDs.

5.3.1 Resistance of the interconnection embedded in the Kirigami structure

The structures necessary to conduct resistance measurements of the interconnections embedded in the Kirigami structure were also designed (Fig. 5.3.1). The interconnections included three types of line having widths of 10 μm, 30 μm, and 50 μm, respectively. These interconnections were also used in the optoelectrical device, in the two types of Pt metal (Figs. 5.3.1a, c), and in the electroplated Au with a Pt adhesive layer (Figs. 5.3.1b, d). Kirigami structures also have two types of slit lengths [1,500 μm and 1,800 μm with cell widths of 1,900 μm (Figs. 5.3.1a, b) and 2,200 μm (Figs. 5.3.1c, d), respectively]. The beam lengths (550 μm and 700 μm) of these test structures also correspond to the dimensions of the optoelectrical Kirigami device (Fig. 5.2.1). The designs of the structures for resistance measurement are summarized in Table 5.1.

The change of resistance values of the interconnections embedded in the Kirigami structure during five cycles of device stretching up to 250% and 350% is shown in Figure 5.3.2. These values correspond to Kirigami structures with a 1,900 μm (Figs. 5.3.1a, b) and 2,200 μm (Figs. 5.3.1c, d) width, respectively (horizontal axis shows the recorded data number of the resistance sampling). The resistance associated with the 50 μm width electroplating interconnection could not be recorded due to the limited range of the measurement equipment.

The relative resistance changes, $\Delta R/R_0$, during a five-cycle device stretching are shown in Figure 5.3.3. R_0 is the initial resistance without strain and ΔR is the difference between the changed resistance and the initial resistance. All Kirigami structures and interconnection types exhibited ~1% resistance decrease with strains of 250% and 350% for the Kirigami structure with 1,900 μm and 2,200 μm widths, respectively.

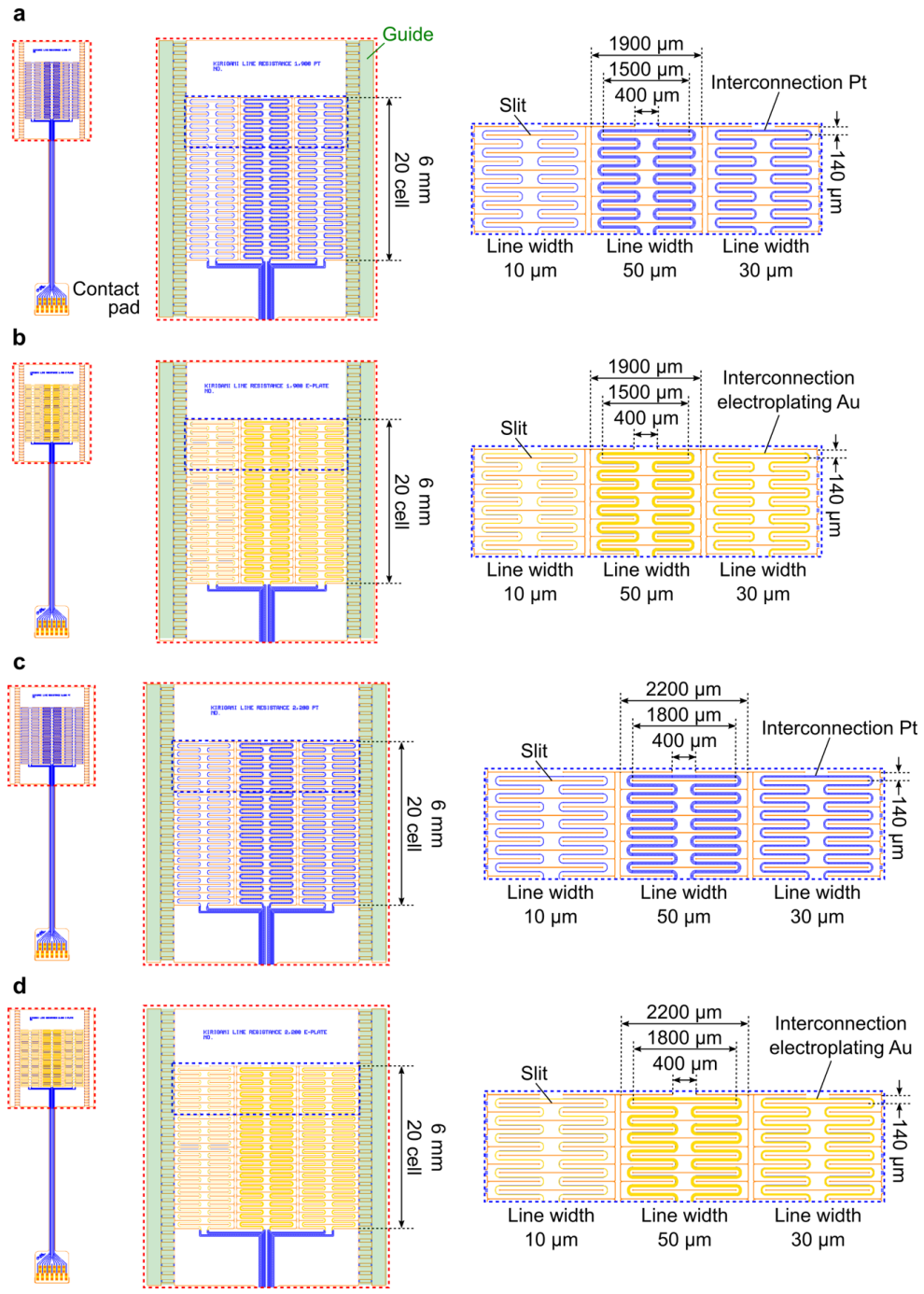

Figure 5.3.1 Test structure for the resistance measurement of the Kirigami structures during the Kirigami stretching. Each design includes three interconnections, which have different widths (10 µm, 30 µm, and 50 µm, respectively). (a) Kirigami structure with a slit length of 1,500 µm (Kirigami cell width of 1,900 µm) composed of Pt interconnections and, (b) electroplated Au interconnections. (c) Kirigami structure with a slit length of 1,800 µm (Kirigami cell width of 2,200 µm) composed of Pt interconnections and (d) electroplated Au interconnections.

Table 5.1 Designs of the interconnections embedded in Kirigami structure

Device	Slit length [μm]	Slit gap [μm]	Beam width [μm]	Film thickness [μm]	Number of cell array column × row	Au electroplating	Line width [μm]	Maximum strain [%]	Figure No.
Kirigami LineResistance _1,900_Pt	1,500	400	140	10	1 × 20	×	10, 30, 50	280	Fig. 5.3.1a
Kirigami LineResistance _1,900_e-plate	1,500	400	140	10	1 × 20	○	10, 30, 50	280	Fig. 5.3.1b
Kirigami LineResistance _2,200_Pt	1,800	400	140	10	1 × 20	×	10, 30, 50	380	Fig. 5.3.1c
Kirigami LineResistance _2,200_e-plate	1,800	400	140	10	1 × 20	○	10, 30, 50	380	Fig. 5.3.1d

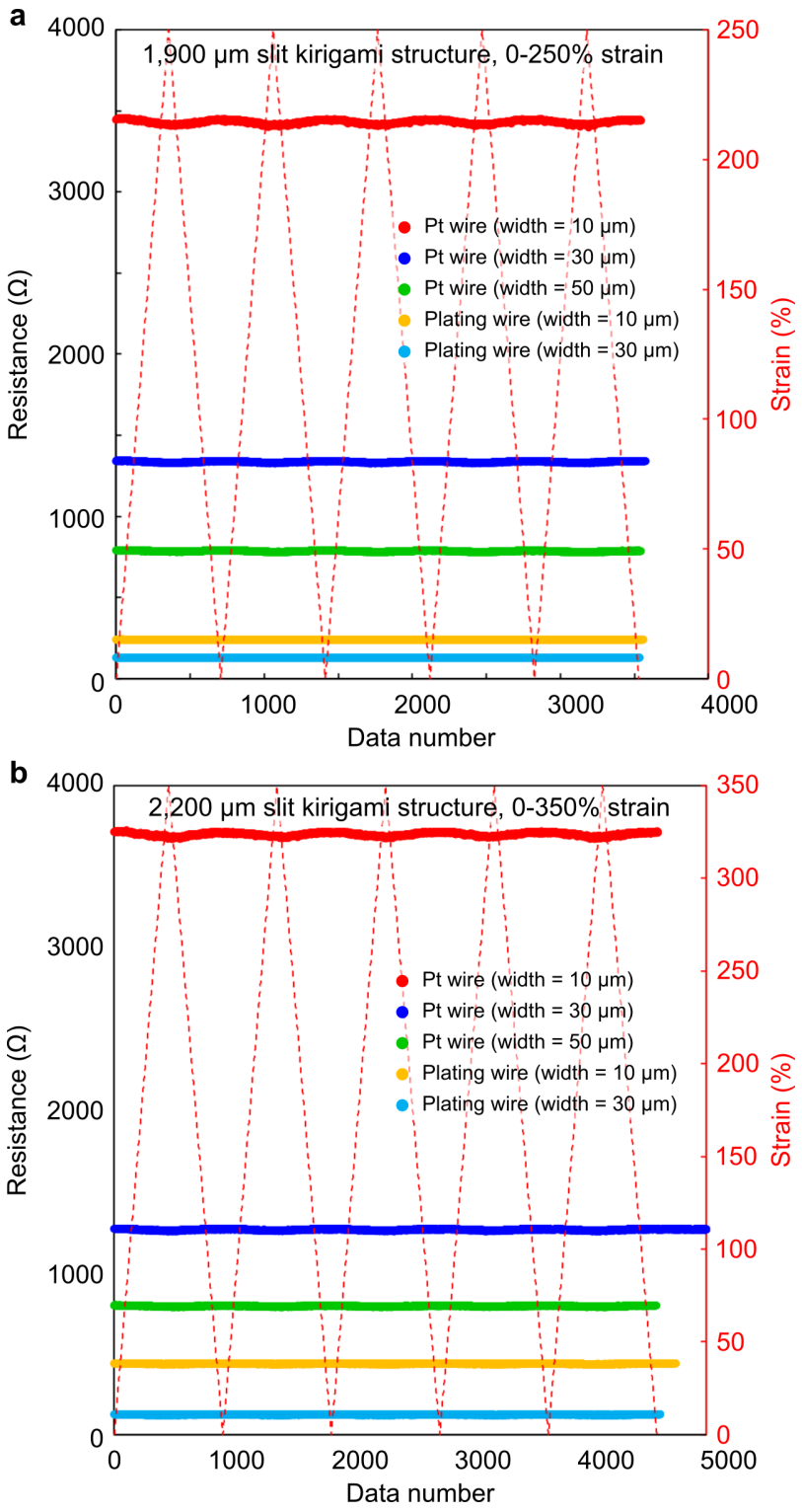

Figure 5.3.2 Resistance values of the interconnections embedded in the Kirigami structure during five cycles of stretching of the Kirigami structure. (a) Kirigami structure with a 1,900 μm width stretched to 250% and, (b) Kirigami structure with a 2,200 μm width stretched to 350%.

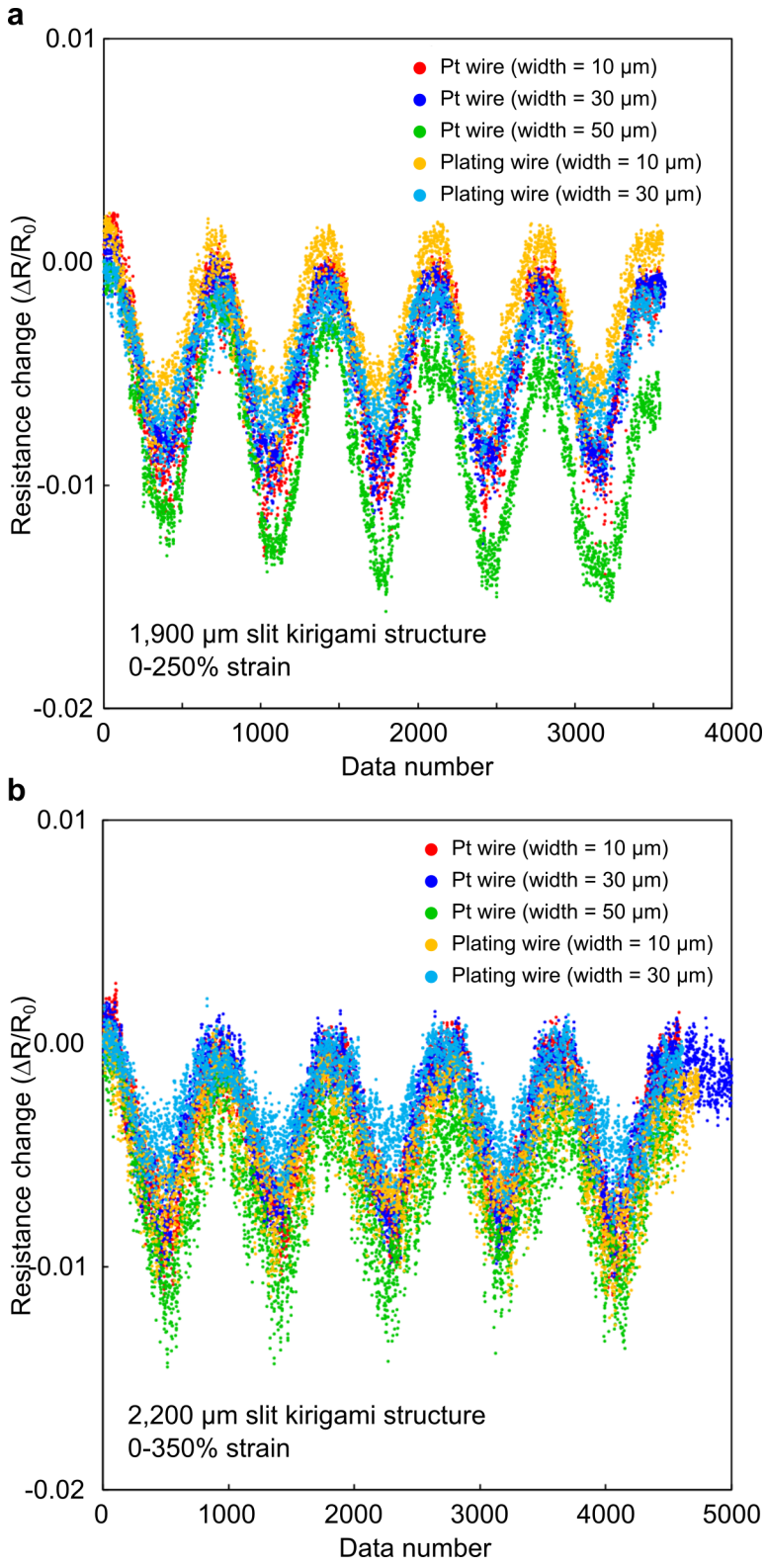

Figure 5.3.3 Relative resistance change during a five-cycle stretching test of Kirigami devices. (a) Kirigami structure with a 1,900 μm width and (b) Kirigami structure with a 2,200 μm width.

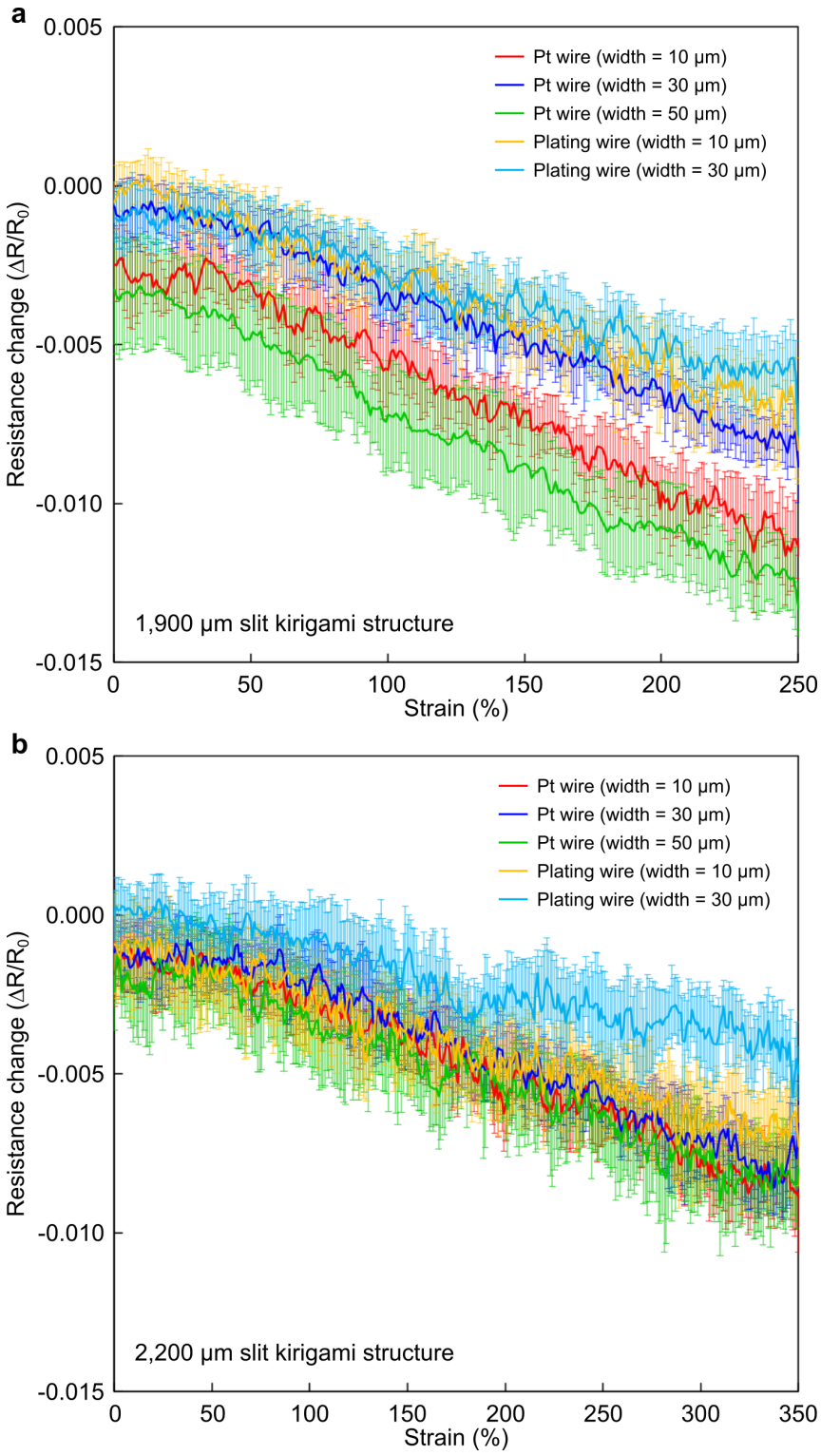

Figure 5.3.4 Averaged relative resistance change during a five-cycle Kirigami device stretching, as a function of strain applied to the Kirigami structure. (a) Kirigami structure with a 1,900 μm width and (b) Kirigami structure with a 2,200 μm width. Error bars indicate SD.

The relative resistance changes, $\Delta R/R_0$, during a five-cycle Kirigami device stretching, as a function of strain applied to the Kirigami structure, is shown in Figure 5.3.4. The resistance change ratio is averaged using the measured data during five strain cycles (Fig. 5.3.3) while the error bars show SD.

A comparison of the resistance change depending on the width of the interconnections embedded in the Kirigami structures during a 200% Kirigami structure strain is shown in Figure 5.3.5. Interconnections embedded in the 1,900 µm width Kirigami structure exhibit a larger resistance change than those embedded in the 2,200 µm width structure. The electroplated interconnections exhibit smaller relative resistance change compared to the interconnections without electroplating (only Pt). Throughout the measurements, the resistance change of the interconnections with a 30 µm width is smaller than that of the interconnections with other widths. Resistance changes of ~1% are small enough for biological signal recordings because the interconnections impedance values are much smaller than those of the microelectrode site (diameter of 50 µm, ~300 kΩ [108]).

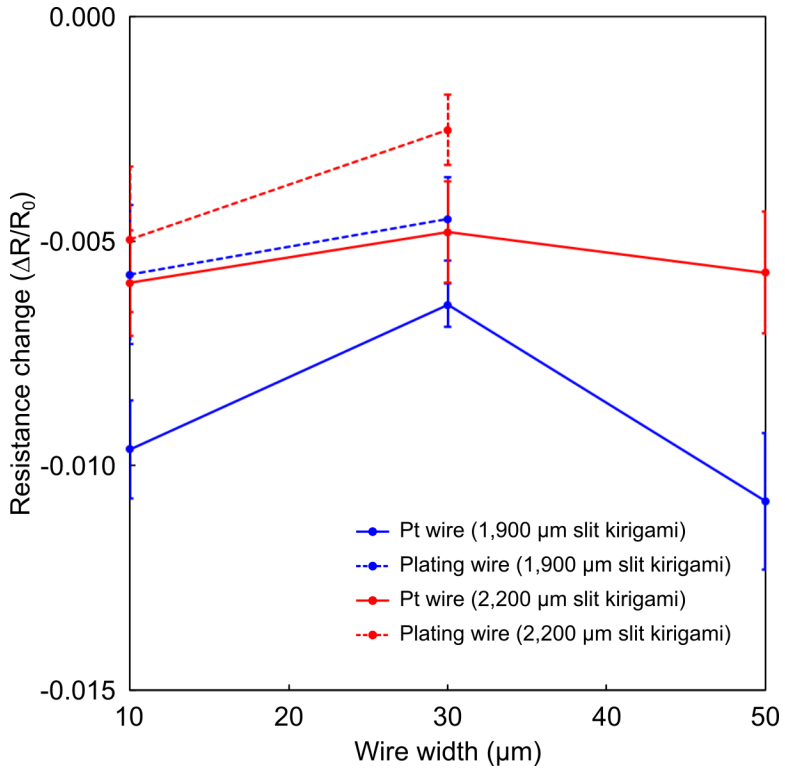

Figure 5.3.5 Relative resistance change depending on the width and thickness of the interconnections and the slit length (cell width) of the Kirigami structure at 200% strain.

5.3.2 Durability of the Kirigami structure

The resistance changes during repeated device stretching were also measured using the test structures shown in Figure 5.3.1. The measured resistance change during the 100-cycle strain for 100%, 200%, and 250% strain (Kirigami structure with 1,900 μm width, Fig. 5.3.6a) and for 100%, 200%, 300%, and 350% strain (Kirigami structure with 2,200 μm width, Fig. 5.3.6b) are shown in Figure 5.3.6. Significant resistance changes were not observed during the cycle strain of a total of 300 and 400 cycles for the 1,900 μm and 2,200 μm width Kirigami structures.

The relative resistance change during a 100-cycle device stretching with a strain of 100%, 200%, and 250% for the 1,900-μm-wide Kirigami structure and 100%, 200%, 300%, and 350% for the 2,200-μm-wide Kirigami structure are shown in Figure 5.3.7. The resistance changes of the interconnections were ~1% and they were not increased or decreased during the device cycle strain of 300 or 400 cycles.

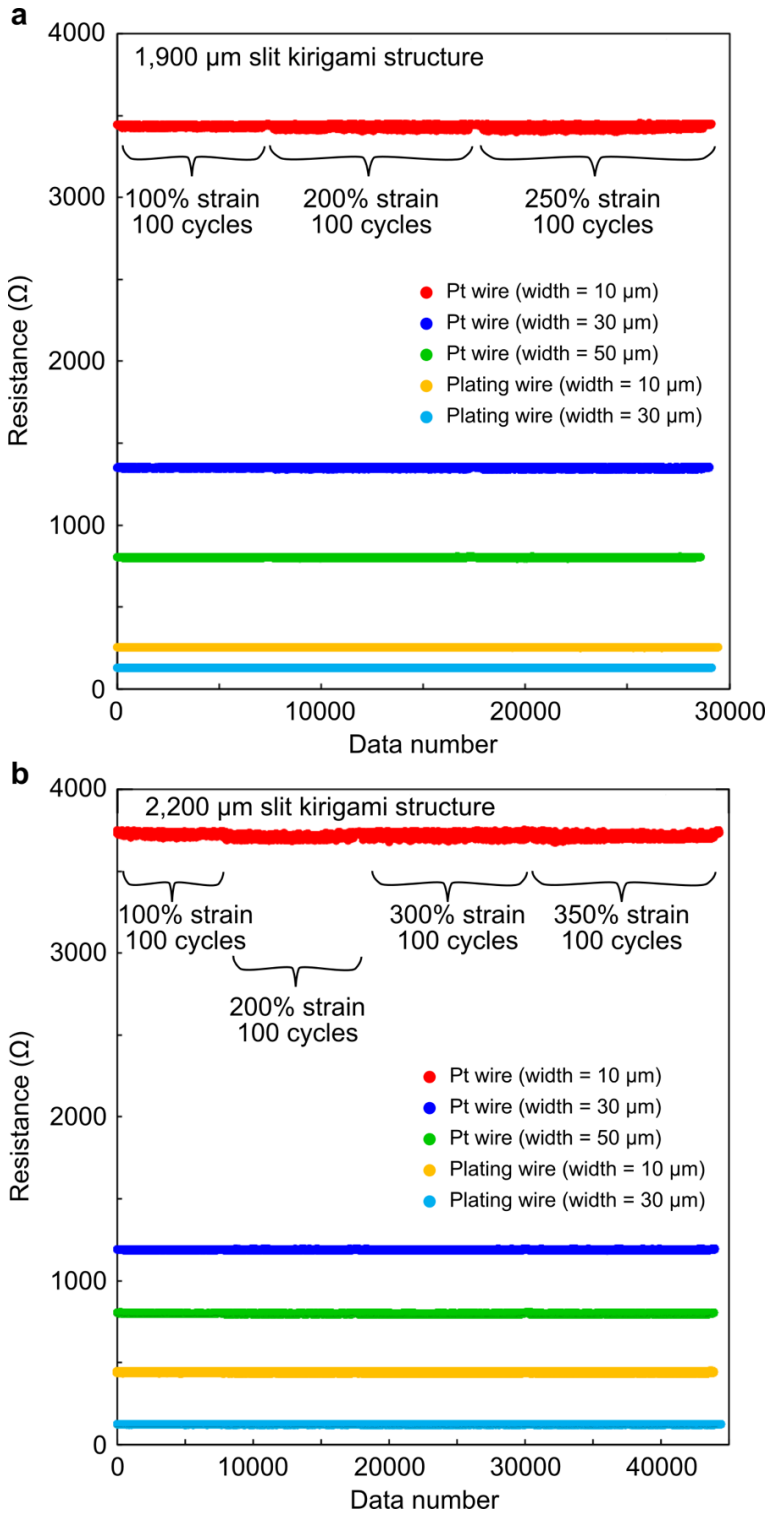

Figure 5.3.6 Resistance of the interconnections embedded in the Kirigami structure during cycle strain. (a) 1,900 μm width Kirigami structure with a 100-cycle strain of 100%, 200%, and 250% (300 strain cycles in total). (b) 2,200 μm width Kirigami structure with a 100-cycle strain of 100%, 200%, 300%, and 350% (400 strain cycles in total).

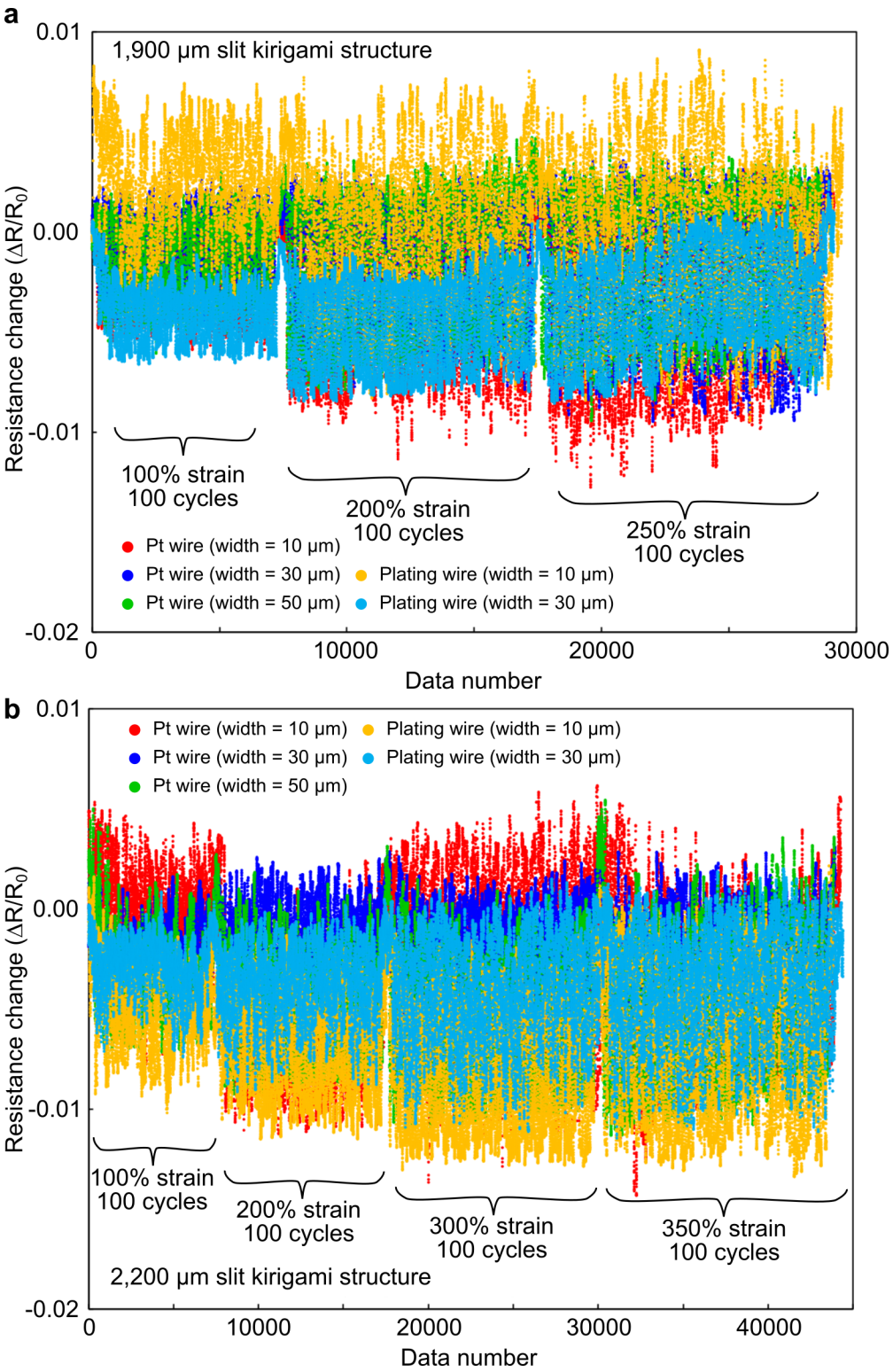

Figure 5.3.7 Relative of the resistance change during the cycle strain. (a) 1,900 μm width Kirigami structure with a 100-cycle strain of 100%, 200%, and 250% and (b) 2,200 μm width Kirigami structure with a 100-cycle strain of 100%, 200%, 300%, and 350%.

5.3.3 Fixation strength of the latch structure

The fixation force of the latch structure, which was used in the optoelectrical Kirigami device for the fixation of the device to the heart surface, was measured. The latch structures consist of two types of latch structures, namely, male and female type. When performing the fixation, the male type latch is inserted into the slit of the female latch structure and the teeth structure of the male type latch catches on the slit edge of the female type latch (Fig. 5.3.8). The male and female types of the latch structures before and after combining each other are shown in Figures 5.3.8a and b. A photograph of the combined latch structures is shown in Figure 5.3.8c. The standard type of tooth structure, which was formed in the male type latch, was reinforced by using the metal layer of the electroplated Au (~1 µm, yellow layer in Figures 5.3.8a, b). In addition, the body of the male type latch and the area around the slit of the female type latch were reinforced by the thin Pt metal layer (~100 nm, blue layer in Figures 5.3.8a, b).

The contribution of the latch design to the fixation force was confirmed by designing three types of the slit width (60 µm, 40 µm, and 20 µm) with a slit length of 650 µm and 1,100 µm (Figs. 5.3.9a–c and 5.3.10a–c). In addition, three types of metal layer designs in the male type latch (metal layer patterned in full body, tooth structure, and without metal) with a slit width of 60 µm (Figs. 5.3.9a, d, e and 5.3.9a, d, e) were used. The designs of the latch structures summarized in Table 5.2. In Figures 5.3.9 and 5.3.10, the layers colored with orange, blue, and yellow exhibit the PI contour, Pt and electroplated Au. In the optoelectrical Kirigami device, the latch structure with a slit

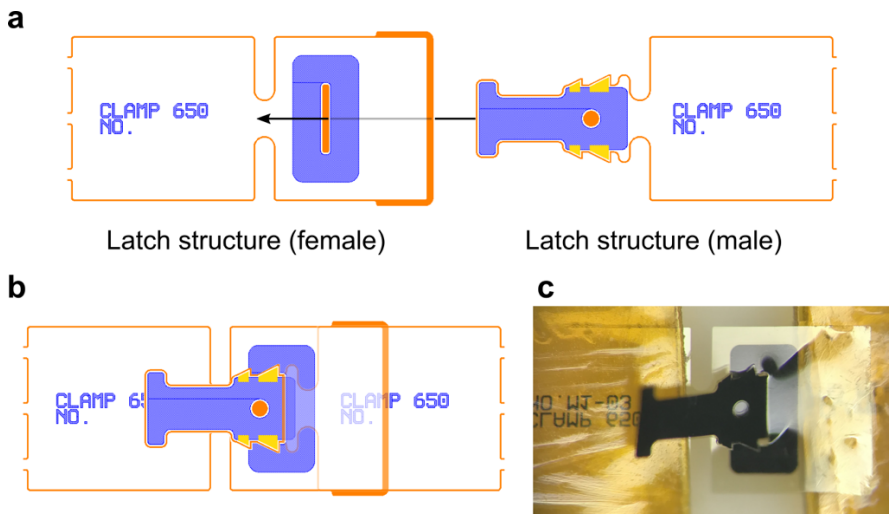

Figure 5.3.8 Combining male and female types of the latch structures. (a) Schematic diagrams before and (b) after the combination of each latch structure type. (c) Photograph of the combined latch structures.

width of 60 µm and a slit length of 650 µm was used in the device rim part (top and bottom side) (Fig. 5.3.9a). The slit length of 1,100 µm was used in center of the device (Fig. 5.3.10a). The fixation force of the latch structures was measured using a combination of a vertical motorized test stand (EMX-1000N, Imada, Aichi, Japan) and a digital force gauge (ZTS-5N, Imada, Aichi, Japan) with a test speed of 0.5 mm/min. Latch

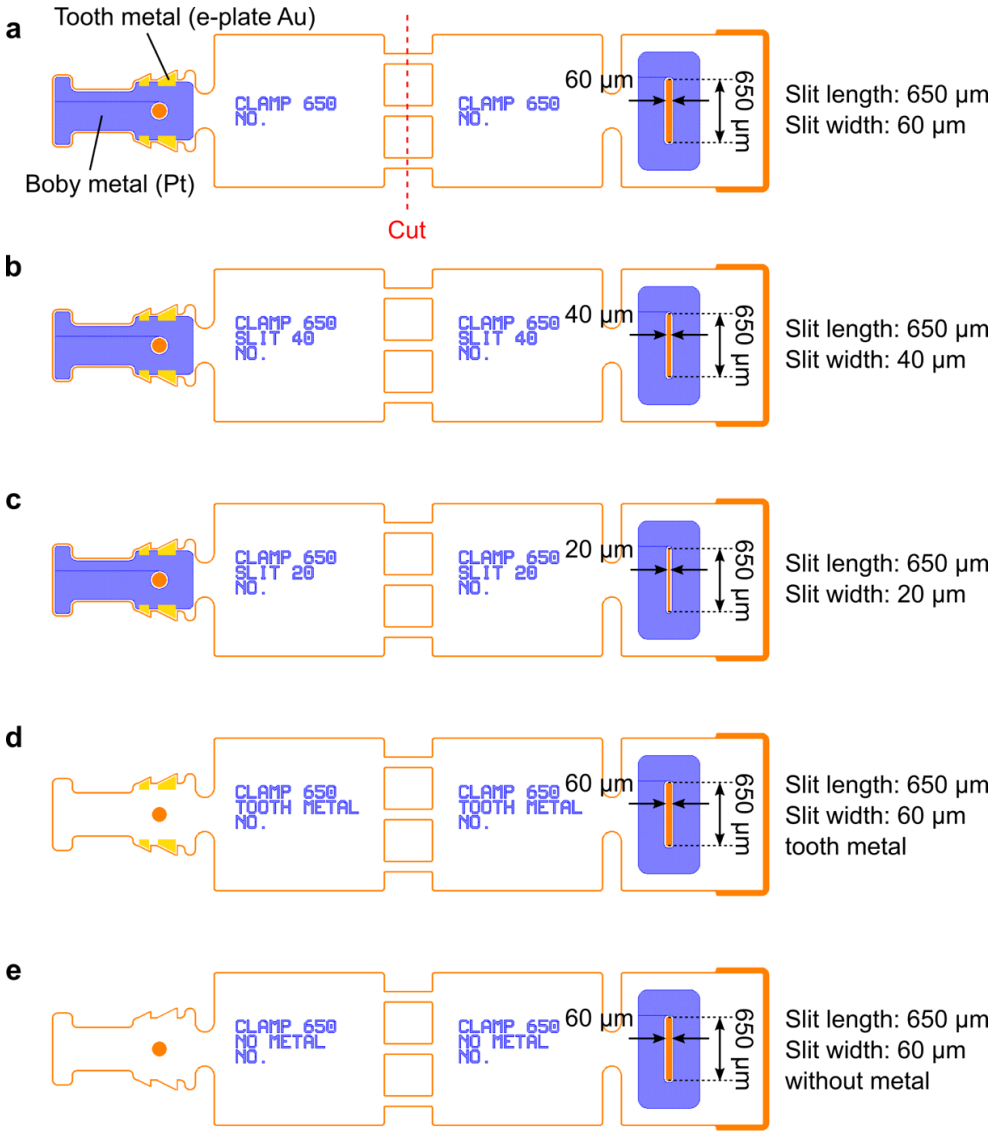

Figure 5.3.9 Latch structures with a slit length of 650 µm. The corresponding male and female types of the latch structure are connected in the design and these structures are separated by cutting before combining. (a) Slit width of 60 µm, (b) 40 µm, and (c) 20 µm. (d) Metal layer only patterned in the tooth of the male latch and (d) male latch without metal layer.

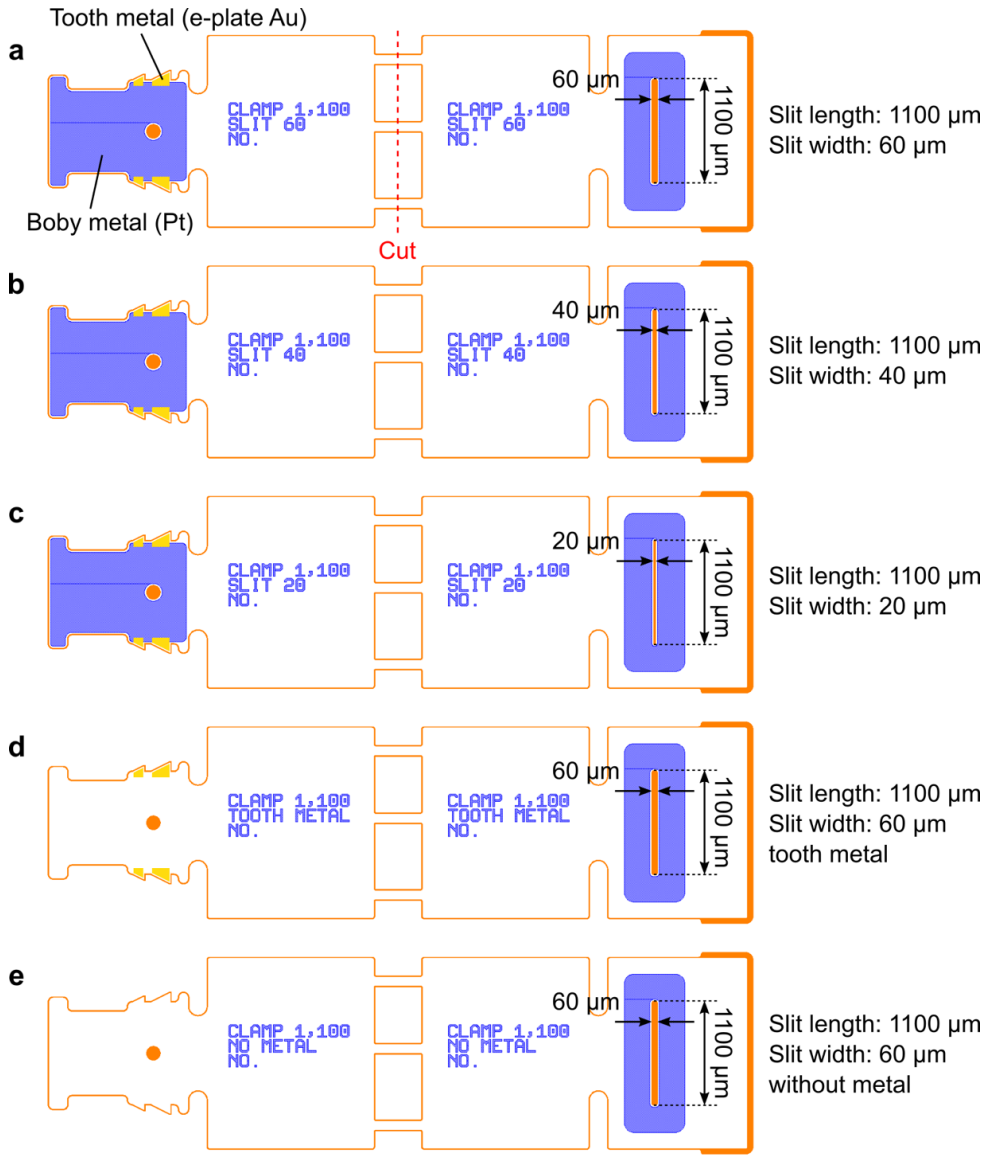

Figure 5.3.10 Latch structures with a slit length of 1,100 μm. (a) Slit width of 60 μm, (b) 40 μm, and (c) 20 μm. (d) Metal layer only patterned in the tooth of the male latch and (d) male latch without metal layer.

structures were combined manually before the tensile tests.

The applied tensile force to the latch structures, which is depending on the displacement of the force gauge, is shown in Figure 5.3.11. These structures have slit widths of 60 μm, 40 μm, and 20 μm and the slit lengths of 650 μm (Fig. 5.3.11a) and 1,100 μm (Fig. 5.3.11b). The applied tensile force to the latch structures, which have a metal pattern in the full body, tooth in the male latch structure, and no metal layer with slit lengths of 650 μm (Fig. 5.3.12a) and 1,100 μm (Fig. 5.3.12b) is shown in

Table 5.2 Designs of latch structures

Device	Latch shape				Tooth shape [μm]				Figure No.
	Slit length [μm]	Slit width [μm]	Body metal	Tooth metal	Small tooth		Large tooth		
					length	width	length	width	
Latch_650_60slit	650	60	○	○	130	60	210	100	Fig. 5.3.9a
Latch_650_40slit	650	40	○	○	130	60	210	100	Fig. 5.3.9b
Latch_650_20slit	650	20	○	○	130	60	210	100	Fig. 5.3.9c
Latch_650_tooth_metal	650	60	×	○	130	60	210	100	Fig. 5.3.9d
Latch_650_no_metal	650	60	×	×	130	60	210	100	Fig. 5.3.9e
Latch_1,100_60slit	1,100	60	○	○	130	60	210	100	Fig. 5.3.10a
Latch_1,100_40slit	1,100	40	○	○	130	60	210	100	Fig. 5.3.10b
Latch_1,100_20slit	1,100	20	○	○	130	60	210	100	Fig. 5.3.10c
Latch_1,100_tooth_metal	1,100	60	×	○	130	60	210	100	Fig. 5.3.10d
Latch_1,100_no_metal	1,100	60	×	×	130	60	210	100	Fig. 5.3.10e

Figure 5.3.12. Three samples were tested for each latch design. Each force–displacement curve has no less than two peaks, since each male type latch structure has two types of teeth structure with different tooth sizes and they cause slit catching twice. The other small peaks were caused by the one side of the tooth structure, which catches the slit. In Figure 5.3.11a, the fixation force of the latch with a slit width of 40 μm is relatively larger than that of the latch with a slit width of 60 μm (Fig. 5.3.13). The separations of the latch structure with a slit length and width of 650 μm and 40 μm, respectively, is shown in Figure 5.3.14. These separations were based on two different mechanisms. Separation of the combined latch occurred, when the male latch structure (including the tooth structure) was deformed to the shape which could go through the slit of the female latch structure (Fig. 5.3.14b) or the slit was teared and expanded to a larger size than that of the male latch structure (Fig. 5.3.14c). When the measured fixation force is relatively large (>0.4 N), it was confirmed that each latch structure was separated accompanied by the breaking of the slit of the female latch structure (Fig. 5.3.14c). The relatively narrow slit width of 40 μm requires a large force, which could cause enough deformation to the male latch structures in order to separate each structure. It also tends to induce the tearing of the slit of the female latch. However, the latch structure with a slit width of 20 μm showed the same or smaller fixation force compared to that of the latch structure with a slit width of 60 μm and 40 μm (Fig. 5.3.13). One possible reason is that cracks occurred in the slit edge, when the male latch structure was combined with the corresponding female structure, because of the very narrow (20 μm) slit width compared to the dimension of the male latch structure (10 μm thickness).

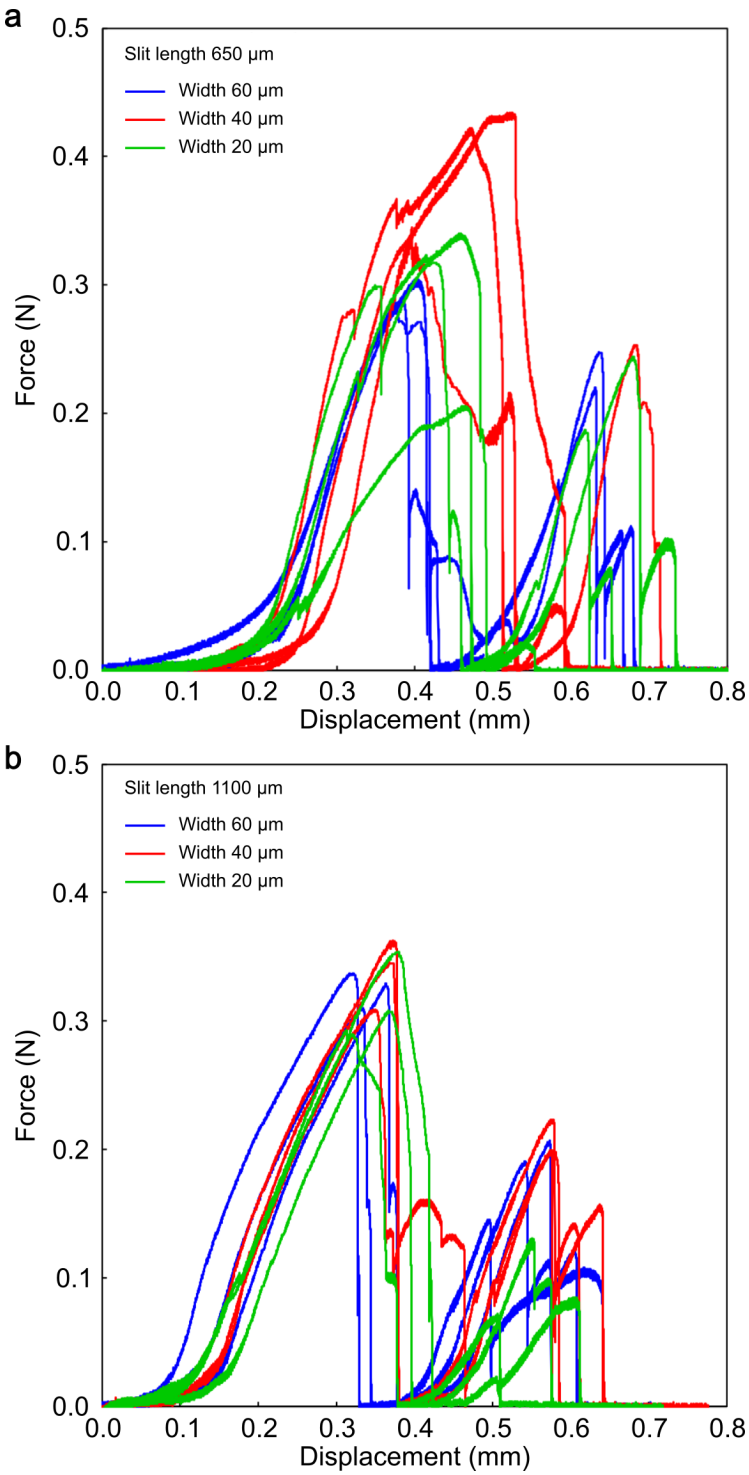

Figure 5.3.11 Fixation force of the latch structures with different slit width and length in the female latch structure. There are three types of latch structures with slit widths of 60 µm (blue line), 40 µm (red line), and 20 µm (green line). Three samples were used in the force measurement for each design. (a) Slit length of 650 µm and (b) slit length of 1,100 µm.

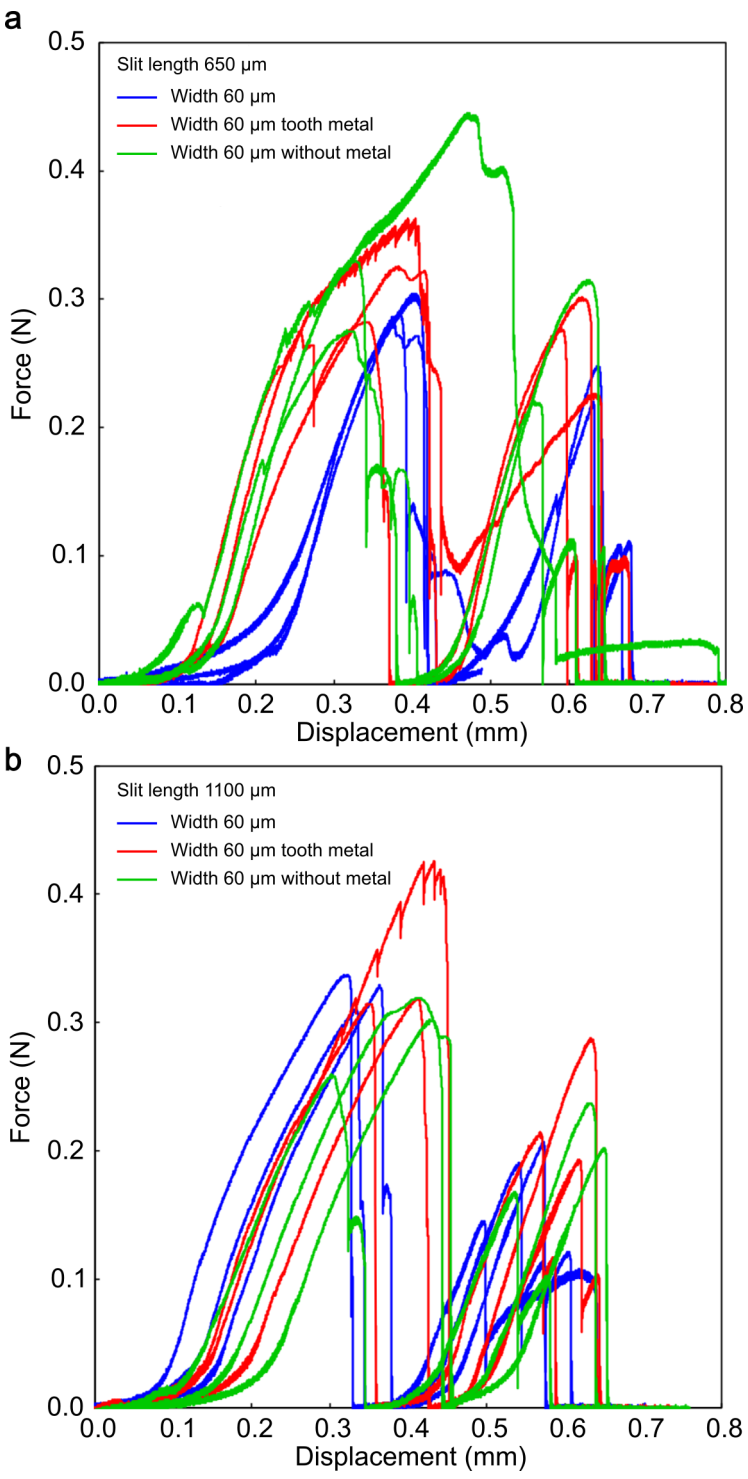

Figure 5.3.12 Fixation force of the latch structures with different metal patterns in the male latch structure. There are three types of latch structures with different metal patterns including full body (blue line), tooth (red line) and no metal layer (green line). Three samples were used in the force measurement for each design. (a) Slit length of 650 µm and (b) slit length of 1,100 µm.

On the other hand, the difference of the metal pattern in the male latch structure did not significantly affect the fixation forces. The 1 μm Au layer embedded in the tooth structure increased bending stiffness by ~36%. This value was estimated by calculation. The difference of the fixation force could also be related to the expansion (damage) of the slit of the female latch during the combining process of each type of latch structures. The metal layer embedded in the tooth structure reinforces the bending stiffness of the tooth structure. However, the slit damage during the combining of the latch structures was also increased.

The fixation forces of the latch structures with a slit length of 1,100 μm in the female latch are shown in Figures 5.3.11b and 5.3.12b. The fixation forces were almost not related to the device design, which includes a slit width and metal layout, compared to the slit length of 650 μm (Fig. 5.3.12). The latch separations based on the tearing of the slit of the female latch were not observed in the test, where the latch with a slit length of 1,100 μm was used. The relatively longer slit length to the tooth size contributes to smooth separations of the male and female latch structures without the tearing of the slit of the female latch structure. The required force to stretch the optoelectrical Kirigami device was ~3 mN with a device strain of 73% for mouse heart (diameter of 6 mm). Therefore, these latch structures have enough fixation force to fix each side of the Kirigami device.

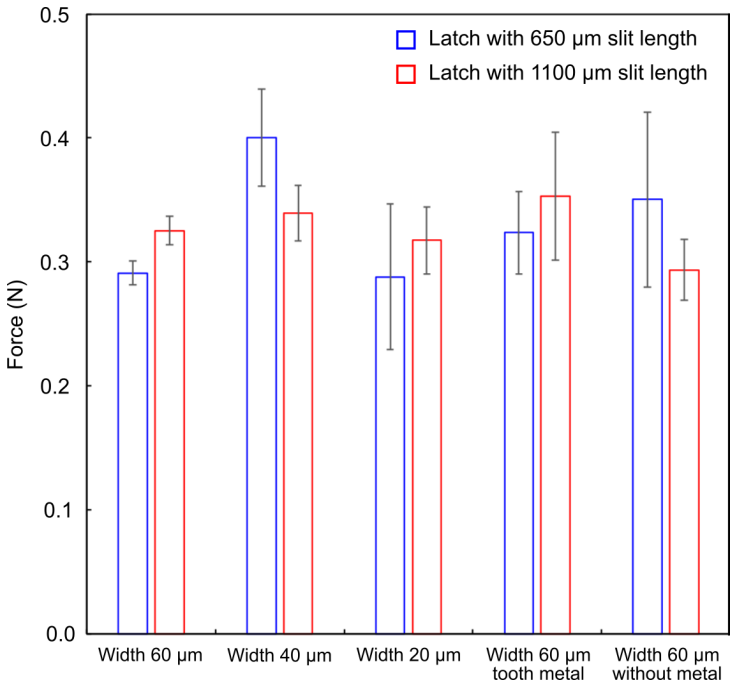

Figure 5.3.13 Maximum fixation force of each latch structure. Blue and red squares show the slit length of 650 μm and 1,100 μm, respectively, in the female type latch structure. Error bars indicate SD.

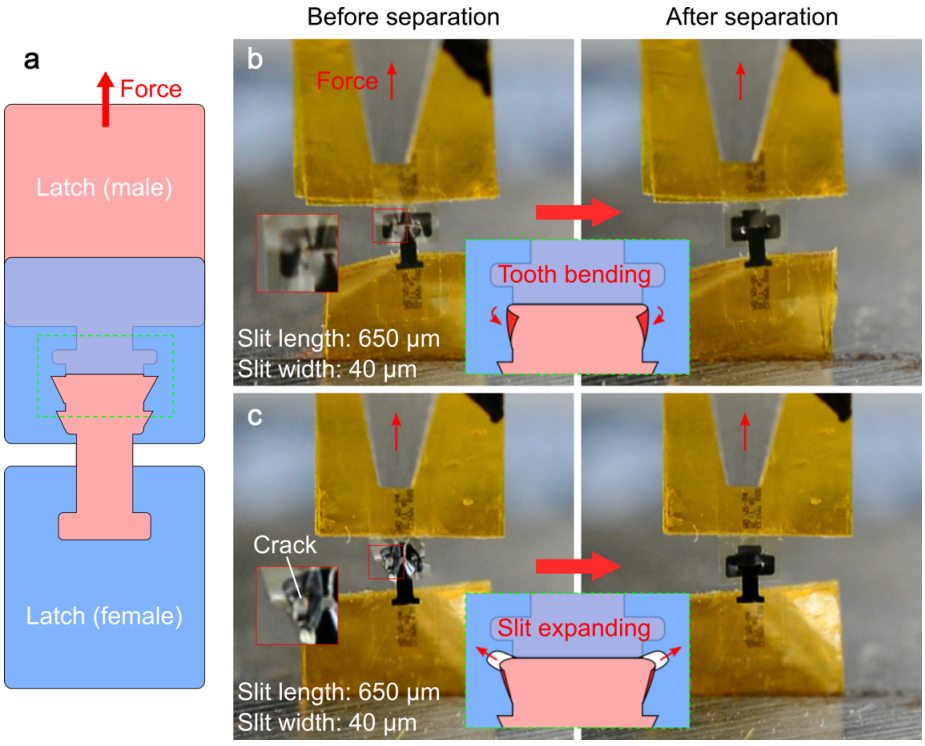

Figure 5.3.14 Schematic diagrams and photographs of the fixation force measurement of the latch structure. Left and right photographs show the combined latch structures just before and after latch separation, respectively. (a) Schematic diagram of the force measurement. (b) Separation due to tooth bending without slit expansion (breaking) and (c) separation due to slit expansion.

5.3.4 LED functionality test

The LED functionality test shown in Figure 5.3.15 demonstrates the successful operation of all eight flip-chip bonded LED chips. As demonstrated previously in [24], optical emittances achieved for these LEDs are in the range of several mW/mm^2 at LED currents of 10 mA modulated with a 30% duty cycle.

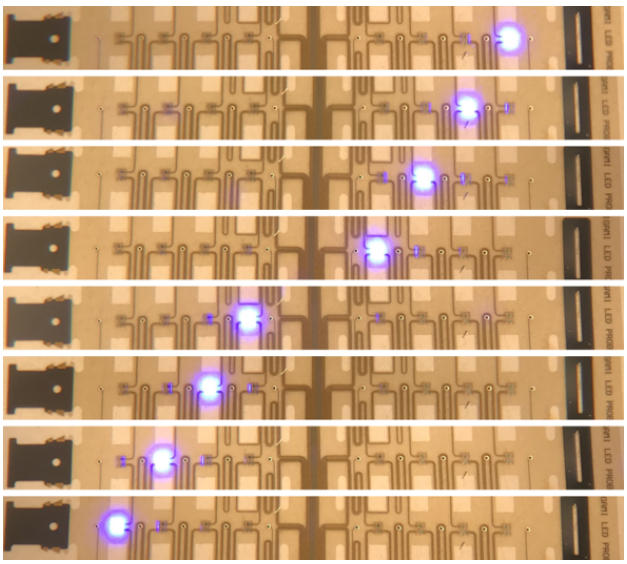

Figure 5.3.15 Functionality test of the eight integrated LED chips on a Kirigami device.

5.4 Conclusions

In this chapter, the design and fabrication of a highly stretchable Kirigami-inspired optoelectrical device intended for opto-physiological experiments in perfused mouse hearts was described. The structures were realized using polyimide substrates with embedded metal lines partially thickened by electroplating in order to minimize the resistance of the lines interfacing the LED chips. Kirigami structures with different slit lengths were designed in an effort to achieve specific stretching properties appropriate for the targeted cardiac tissue. The stretchable optoelectrical Kirigami device was fabricated using micro-electromechanical system processes with LED chips attached to it using flip-chip bonding and a subsequent encapsulation based on epoxy resin, Cytop and silicone. The interconnections embedded in the Kirigami structure exhibited stable characteristics with a resistance change of ~1% under a 250% and 350% strain for each width. In addition, the interconnections exhibited stability under 300- and 400-cycle strains. It was confirmed that the other component of the latch structure had enough strong for fixation to fix each side of the Kirigami device. The LED functionality test revealed an efficiency of 100%. The results successfully demonstrated a highly stretchable device destined for the defibrillation of the cardiac tissue using optogenetic stimulation. This device is expected to reduce the severe side effects caused by the currently used implantable defibrillation systems, which apply high electrical shocks.

Chapter 6: General conclusions and future prospects

6.1 Conclusions

In this thesis, we investigated the stretchable devices to achieve low invasive neuronal interfaces for biological applications using the Kirigami structures. Biological applications using the biological signals such as BMI often request the long-term implantation of the recording device to the biological tissues. To achieve the stable and robust signal recording from the biological tissues for such biological applications, it is required that the device which has the proper electrical characteristics, biocompatibility, and ability to follow tissue deformation. The biocompatibility includes the chemical and the mechanical compatibility. In addition to the small feature of the electrode device, mechanical compatibility also includes the low Young's modulus or low device stiffness which are should be comparable to the biological tissues. High flexibility and stretchability are required for an intimate integration of the device with the soft and deformable biological tissues. These characteristics contribute to the reduction of the physical stress induced to biological tissues and prevent the foreign-body-response. Conventional flexible needle penetrating electrodes and film surface electrodes have the Young's modulus which is about six orders of magnitude higher than that of biological tissues. In addition, the Young's modulus of the stretchable device still higher and its large deformation induce the mechanical failure of rigid device components embedded in the stretchable device due to the mechanical mismatch between the stretchable materials and device components.

The main feature of the Kirigami structure is its high stretchability including high strain ratio and low effective modulus, and stability under the device stretching. In Chapter 2, a mechanical model for the Kirigami structure suitable for the estimation of the structure deformation, which depends on the applied force (stress), was derived to achieve the effective device design. In addition, simulation results of the stress distribution in the Kirigami structure contribute to achieve robust design of the Kirigami

devices.

The stretchability and the recording capability of the Kirigami device were confirmed in the first experiment of the Kirigami bioprobe device described in Chapter 3. Using a fabricated Kirigami bioprobe device, the electrical and mechanical characterizations were conducted. In the electrical characterization, the electrode impedance, which was measured in the saline solution, exhibited remarkable stability under large stretching (500%) using the Kirigami device, which has a maximum calculated strain of 860%. In the mechanical characterization, it was also confirmed that the effective modulus of the fabricated Kirigami devices (3.6–23 kPa) is comparable to those of soft biological tissues (e.g. ~1.5 kPa for the brain and 5–40 kPa for a resting muscle). Kirigami devices exhibited a maximum strain of 470–840% before the breaking of the film. The stretchability of the devices, which are based on stretchable materials, is limited by the intrinsic characteristics of the used materials. On the other hand, the characteristics of the Kirigami structure can be controlled by the device design (e.g. slit length and gap of the Kirigami structure) as confirmed by the mechanical characterizations. Another feature of a Kirigami device is that it consists of slit patterns embedded in the 2D film and makes it compatible with conventional microfabrication processes (e.g. photolithography technique). Therefore, the utilization of a Kirigami structure achieves high density of the microelectrode array in the highly stretchable substrate using relatively simple process steps. In addition, the durability of the Kirigami device was also confirmed during a 4000-cycle strain in the endurance test. The recording capability of the fabricated Kirigami device was also confirmed in the ECoG signal recording under the device stretch. In addition, the recording capability of the device with respect to biological tissues, which exhibit large deformation, was confirmed in the ECG signal recording.

In the second experiment described in Chapter 4, a donut-shaped Kirigami device was proposed to extent the application range of the Kirigami device. The donut-shaped Kirigami device improved the device stability on biological tissues with large deformation, such as the heart and muscles. The stability of the fabricated donut-shaped Kirigami device on the deformable tissue surface was confirmed in the displacement test using a deformable balloon instead of a biological tissue. The results of the displacement test exhibited five to eight times smaller displacement in comparison with the sheet-type Kirigami device proposed in the first experiment. The high stretchability of the Kirigami device results in some manipulation difficulty of the device in the animal experiment. A packaging process using the biocompatible and soluble material of PEG overcame this difficulty. The recording capability and the stability of the fabricated donut-shaped

Kirigami device were also confirmed in the biological signal recordings from large deformable tissues, such as a mouse's heart and hind limb.

An optoelectrical Kirigami device for the heart disease treatment was proposed in the third experiment, which was described in Chapter 5. The integration of the rigid components in the stretchable device to realize a multifunctional device was another challenge for the stretchable devices. The proposed Kirigami device employs an array of LEDs bonded on the fabricated Kirigami film for optical stimulation purposes and electrodes for the ECG signal recording. The characterization of the optoelectrical Kirigami device indicated no significant resistance changes of the device interconnections with the thin and thick metal layer during the Kirigami stretching. Moreover, the resistance change was not increased in the durability test with a strain of 300–400 cycles. It was also confirmed that the latch structures exhibited enough fixation force to enable the device fixation on the heart tissue. The LEDs functionality test revealed an efficiency of 100%. These results successfully demonstrate a highly stretchable device destined for the defibrillation of cardiac tissue using optogenetic stimulation.

Through these results, we confirmed the capability of the Kirigami device as appropriate platform of low invasive neuronal interfaces, which is includes the proper electrical characteristics, high stretchability, stability during the device stretching, controllable device Young's modulus comparable to the biological tissues, mechanical robustness, recording capability from the multiple biological tissues, small displacement on the deformable biological tissues, and integration with the rigid device component. It is believed that the features of the Kirigami device can be extended to applications involving the integration of electrical components with biological tissues. Moreover, the high stretchability, stability, and unique transformation of the Kirigami structure will expand possibilities for stretchable electronics including sensors and actuators.

6.2 Future prospects

A stretchable Kirigami device is based on the out-of-plane (3D) deformation of each beam. Therefore, it is necessary to discuss the effect of this device's roughness on the smooth surface of a biological tissue. An issue, which is associated with the 3D deformation, is that the sharp edge of the tilted beam causes tissue stress. Tissue damage or malfunction was not observed when the Kirigami device was applied to the mouse brain, heart, and muscle of hind limb (Figs. 3.4.1, 3.4.3, 4.6.1, 4.6.3). However, the long-term device implantation could cause some tissue damage. Therefore, the influence of the device implantation to soft biological tissues needs to be confirmed. Also, possible tissue

damage caused by the device implantation needs to be evaluated. In general, tissue damage is evaluated using immuno-staining and fluorescence imaging [33], [124]. The tissue stress associated with the sharp Kirigami's edge can be decreased using elastomer materials with a small Young's modulus (e.g. PDMS [110] and Ecoflex [91]) instead of using parylene and PI. The Young's modulus of the elastomer materials is four to five orders smaller than the Young's modulus of parylene or PI (2.8 GPa). In addition, as shown in equation (2.8), the displacement of the Kirigami structure is inversely proportion to the Young's modulus. Therefore, a lower Young's modulus of a material offers a lower effective modulus for the Kirigami devices. The beam's tilt caused by the device out-of-plane deformation results in insufficient contact of each electrode to the tissue surface. Thus, the quality of the muscle recording is degraded. The electrode contact can be improved by additional device design around the electrodes. With respect to the curb of the out-of-plane deformation of the Kirigami structure, some studies proposed a Kirigami design with an in-plane-deformation [87], [91].

The use of elastomer materials also improves the device durability. No fracture (separation) during a 4,000-cycle device strain was observed during the durability test of the Kirigami structure. However, some cracks were observed around the slit edge of the Kirigami structure. The expansion of the cracks causes breaking of the device interconnections and plastic deformation of the Kirigami film. Using elastomer materials, which have a higher stain ratio without the plastic deformation (large elastic region) than that of the parylene, the device durability was improved.

Minimization of the device package is necessary for device implantation applications, As demonstrated in *in vivo* ECoG, ECG and EMG signal recording, the Kirigami device was electrically connected to the FPC with epoxy manually. The area of the terminal between the parylene Kirigami and the FPC was 5×8 mm^2. Implantation of a device of this size is impossible in mice. A way to minimize the device package is to use the flip-chip bonding technique. The use of wireless technology in conjunction with the Kirigami device will further minimize the invasiveness of the device for long-term applications [125].

The main limitation of the Kirigami device is the difficulty to design the device interconnections. The interconnections of the Kirigami device should be designed between each Kirigami slit and this limits the number of interconnections and electrodes. This issue can be overcome using a multiplexer consisting of transistors [48]. The multiplexer allows the dense electrodes to use fewer interconnections compared to the electrode device without a multiplexer. Many flexible and stretchable transistors proposed in previous studies use Si nanomembrane, SiNWs, indium gallium zinc oxide (IGZO),

CNT, and PEDOT:PSS, which can be applicable to Kirigami devices [48], [126]–[131]. In addition, the use of high conductive materials, such as PEDOT:PSS offer more accurate signal recording, such as the spike signal form the brain surface [49].

The change of the electrode materials also extends the device's applications of stimulating biological tissues [132]. Tissue stimulation can be used to restore the functions lost by the spinal cord injury [133]. It can also be used to artificial tactile feedback for the BMI [134] and the treatment of neurological disorders, such as epilepsy [135].

References

[1] R. Chen, A. Canales, and P. Anikeeva, “Neural recording and modulation technologies,” *Nat. Rev. Mater.*, vol. 2, no. 2, 16093, 2017 .

[2] G. Hong and C. M. Lieber, “Novel electrode technologies for neural recordings,” *Nat. Rev. Neurosci.*, vol. 20, no. 6, pp. 330–345, 2019 .

[3] J. Kim, M. Lee, H. J. Shim, R. Ghaffari, H. R. Cho, D. Son, Y. H. Jung, M. Soh, C. Choi, S. Jung, K. Chu, D. Jeon, S.-T. Lee, J. H. Kim, S. H. Choi, T. Hyeon, and D.-H. Kim, “Stretchable silicon nanoribbon electronics for skin prosthesis,” *Nat. Commun.*, vol. 5, no. 1, 5747, 2014 .

[4] L. F. Nicolas-Alonso and J. Gomez-Gil, “Brain Computer Interfaces, a Review,” *Sensors*, vol. 12, no. 2, pp. 1211–1279, 2012 .

[5] M. A. Lebedev and M. A. L. Nicolelis, “Brain-Machine Interfaces: From Basic Science to Neuroprostheses and Neurorehabilitation,” *Physiol. Rev.*, vol. 97, no. 2, pp. 767–837, 2017 .

[6] L. R. Hochberg, M. D. Serruya, G. M. Friehs, J. A. Mukand, M. Saleh, A. H. Caplan, A. Branner, D. Chen, R. D. Penn, and J. P. Donoghue, “Neuronal ensemble control of prosthetic devices by a human with tetraplegia,” *Nature*, vol. 442, no. 7099, pp. 164–171, 2006 .

[7] L. R. Hochberg, D. Bacher, B. Jarosiewicz, N. Y. Masse, J. D. Simeral, J. Vogel, S. Haddadin, J. Liu, S. S. Cash, P. van der Smagt, and J. P. Donoghue, “Reach and grasp by people with tetraplegia using a neurally controlled robotic arm,” *Nature*, vol. 485, no. 7398, pp. 372–375, 2012 .

[8] B. Xu, A. Akhtar, Y. Liu, H. Chen, W.-H. Yeo, S. I. I. Park, B. Boyce, H. Kim, J. Yu, H.-Y. Lai, S. Jung, Y. Zhou, J. Kim, S. Cho, Y. Huang, T. Bretl, and J. A. Rogers, “An Epidermal Stimulation and Sensing Platform for Sensorimotor Prosthetic Control, Management of Lower Back Exertion, and Electrical Muscle Activation,” *Adv. Mater.*, vol. 28, no. 22, pp. 4462–4471, 2016 .

[9] Y. J. Kim, S. W. Park, H. G. Yeom, M. S. Bang, J. S. Kim, C. K. Chung, and S. Kim, “A study on a robot arm driven by three-dimensional trajectories predicted from non-invasive neural signals,” *Biomed. Eng. Online*, vol. 14, no. 1, 81, 2015 .

[10] C. Cipriani, F. Zaccone, S. Micera, and M. C. Carrozza, “On the shared control of an EMG-controlled prosthetic hand: Analysis of user-prosthesis interaction,”

IEEE Trans. Robot., vol. 24, no. 1, pp. 170–184, 2008 .

[11] J. Gomez-Gil, I. San-Jose-Gonzalez, L. F. Nicolas-Alonso, and S. Alonso-Garcia, "Steering a tractor by means of an EMG-based human-machine interface," *Sensors*, vol. 11, no. 7, pp. 7110–7126, 2011 .

[12] D. Tkach, H. Huang, and T. A. Kuiken, "Study of stability of time-domain features for electromyographic pattern recognition," *J. Neuroeng. Rehabil.*, vol. 7, no. 1, 21, 2010 .

[13] X. Tang, L. Xia, Y. Liao, W. Liu, Y. Peng, T. Gao, and Y. Zeng, "New approach to epileptic diagnosis using visibility graph of high-frequency signal," *Clin. EEG Neurosci.*, vol. 44, no. 2, pp. 150–156, 2013 .

[14] H. S. Mayberg, "Targeted electrode-based modulation of neural circuits for depression," vol. 119, no. 4, pp. 717–725, 2009 .

[15] S. E. Qasim, C. de Hemptinne, N. C. Swann, S. Miocinovic, J. L. Ostrem, and P. A. Starr, "Electrocorticography reveals beta desynchronization in the basal ganglia-cortical loop during rest tremor in Parkinson's disease," *Neurobiol. Dis.*, vol. 86, pp. 177–186, 2016 .

[16] K. Edakawa, T. Yanagisawa, H. Kishima, R. Fukuma, S. Oshino, H. M. Khoo, M. Kobayashi, M. Tanaka, and T. Yoshimine, "Detection of Epileptic Seizures Using Phase–Amplitude Coupling in Intracranial Electroencephalography," *Sci. Rep.*, vol. 6, no. 1, 25422, 2016 .

[17] F. Jiménez, H. Nicolini, A. M. Lozano, F. Piedimonte, R. Salín, and F. Velasco, "Electrical Stimulation of the Inferior Thalamic Peduncle in the Treatment of Major Depression and Obsessive Compulsive Disorders," *World Neurosurg.*, vol. 80, no. 3–4, p. S30.e17-S30.e25, 2013 .

[18] G. Pfurtscheller, G. R. Müller-Putz, R. Scherer, and C. Neuper, "Rehabilitation with brain-computer interface systems," *Computer (Long. Beach. Calif).*, vol. 41, no. 10, pp. 58–65, 2008 .

[19] A. Ramos-Murguialday, D. Broetz, M. Rea, L. Läer, Ö. Yilmaz, F. L. Brasil, G. Liberati, M. R. Curado, E. Garcia-Cossio, A. Vyziotis, W. Cho, M. Agostini, E. Soares, S. Soekadar, A. Caria, L. G. Cohen, and N. Birbaumer, "Brain-machine interface in chronic stroke rehabilitation: A controlled study," *Ann. Neurol.*, vol. 74, no. 1, pp. 100–108, 2013 .

[20] C. D. Swerdlow, S. J. Asirvatham, K. A. Ellenbogen, and P. A. Friedman, "Troubleshooting implanted cardioverter defibrillator sensing problems i," *Circ. Arrhythmia Electrophysiol.*, vol. 7, no. 6, pp. 1237–1261, 2014 .

[21] L. Xu, S. R. Gutbrod, A. P. Bonifas, Y. Su, M. S. Sulkin, N. Lu, H.-J. Chung, K.-

I. Jang, Z. Liu, M. Ying, C. Lu, R. C. Webb, J.-S. Kim, J. I. Laughner, H. Cheng, Y. Liu, A. Ameen, J.-W. Jeong, G.-T. Kim, Y. Huang, I. R. Efimov, and J. A. Rogers, "3D multifunctional integumentary membranes for spatiotemporal cardiac measurements and stimulation across the entire epicardium," *Nat. Commun.*, vol. 5, no. 1, 3329, 2014 .

[22] D. P. Zipes, A. J. Camm, M. Borggrefe, A. E. Buxton, B. Chaitman, M. Fromer, G. Gregoratos, G. Klein, R. J. Myerburg, M. A. Quinones, D. M. Roden, M. J. Silka, C. Tracy, S. C. Smith, A. K. Jacobs, C. D. Adams, E. M. Antman, J. L. Anderson, S. A. Hunt, J. L. Halperin, R. Nishimura, J. P. Ornato, R. L. Page, B. Riegel, S. G. Priori, A. J. Moss, S. G. Priori, J.-J. Blanc, A. Budaj, A. J. Camm, V. Dean, J. W. Deckers, C. Despres, K. Dickstein, J. Lekakis, K. McGregor, M. Metra, J. Morais, A. Osterspey, J. L. Tamargo, and J. L. Zamorano, "ACC/AHA/ESC 2006 Guidelines for Management of Patients With Ventricular Arrhythmias and the Prevention of Sudden Cardiac Death," *J. Am. Coll. Cardiol.*, vol. 48, no. 5, pp. e247–e346, 2006 .

[23] A. Auricchio, P. P. Delnoy, F. Regoli, M. Seifert, T. Markou, and C. Butter, "First-in-man implantation of leadless ultrasound-based cardiac stimulation pacing system: Novel endocardial left ventricular resynchronization therapy in heart failure patients," *Europace*, vol. 15, no. 8, pp. 1191–1197, 2013 .

[24] S. Ayub, P. Ruther, O. Paul, P. Kohl, and C. M. Zgierski-Johnston, "Invasive Optical Pacing in Perfused, Optogenetically Modified Mouse Heart Using Stiff Multi-LED Optical Probes," in *2018 40th Annual International Conference of the IEEE Engineering in Medicine and Biology Society (EMBC)*, 2018, pp. 4836–4839.

[25] V. Mountcastle, "The columnar organization of the neocortex," *Brain*, vol. 120, no. 4, pp. 701–722, 1997 .

[26] D. P. Buxhoeveden and M. F. Casanova, "The minicolumn hypothesis in neuroscience," *Brain*, vol. 125, no. 5, pp. 935–951, 2002 .

[27] P. Hilton-Brown and E. Stålberg, "Motor unit size in muscular dystrophy, a macro EMG and scanning EMG study," *J. Neurol. Neurosurg. Psychiatry*, vol. 46, no. 11, pp. 996–1005, 1983 .

[28] E. Stalberg and L. Antoni, "Electrophysiological cross section of the motor unit," *J. Neurol. Neurosurg. Psychiatry*, vol. 43, no. 6, pp. 469–474, 1980 .

[29] R. A. Normann, E. M. Maynard, P. J. Rousche, and D. J. Warren, "A neural interface for a cortical vision prosthesis," *Vision Res.*, vol. 39, no. 15, pp. 2577–2587, 1999 .

[30] K. D. Wise, D. J. Anderson, J. F. Hetke, D. R. Kipke, and K. Najafi, “Wireless implantable microsystems: High-density electronic interfaces to the nervous system,” *Proc. IEEE*, vol. 92, no. 1, pp. 76–97, 2004 .

[31] D.-H. Kim, J. Viventi, J. J. Amsden, J. Xiao, L. Vigeland, Y.-S. Kim, J. A. Blanco, B. Panilaitis, E. S. Frechette, D. Contreras, D. L. Kaplan, F. G. Omenetto, Y. Huang, K.-C. Hwang, M. R. Zakin, B. Litt, and J. A. Rogers, “Dissolvable films of silk fibroin for ultrathin conformal bio-integrated electronics,” *Nat. Mater.*, vol. 9, no. 6, pp. 511–517, 2010 .

[32] J. J. Jun, N. A. Steinmetz, J. H. Siegle, D. J. Denman, M. Bauza, B. Barbarits, A. K. Lee, C. A. Anastassiou, A. Andrei, Ç. Aydin, M. Barbic, T. J. Blanche, V. Bonin, J. Couto, B. Dutta, S. L. Gratiy, D. A. Gutnisky, M. Häusser, B. Karsh, P. Ledochowitsch, C. M. Lopez, C. Mitelut, S. Musa, M. Okun, M. Pachitariu, J. Putzeys, P. D. Rich, C. Rossant, W. L. Sun, K. Svoboda, M. Carandini, K. D. Harris, C. Koch, J. O’Keefe, and T. D. Harris, “Fully integrated silicon probes for high-density recording of neural activity,” *Nature*, vol. 551, no. 7679, pp. 232–236, 2017 .

[33] A. Campbell and C. Wu, “Chronically Implanted Intracranial Electrodes: Tissue Reaction and Electrical Changes,” *Micromachines*, vol. 9, no. 9, 430, 2018 .

[34] J. W. Salatino, K. A. Ludwig, T. D. Y. Kozai, and E. K. Purcell, “Glial responses to implanted electrodes in the brain,” *Nat. Biomed. Eng.*, vol. 1, no. 11, pp. 862–877, 2017 .

[35] M. D. Ferro and N. A. Melosh, “Electronic and Ionic Materials for Neurointerfaces,” *Adv. Funct. Mater.*, vol. 28, no. 12, 1704335, 2018 .

[36] J. W. Jeong, G. Shin, S. Il Park, K. J. Yu, L. Xu, and J. A. Rogers, “Soft materials in neuroengineering for hard problems in neuroscience,” *Neuron*, vol. 86, no. 1, pp. 175–186, 2015 .

[37] P. Fattahi, G. Yang, G. Kim, and M. R. Abidian, “A review of organic and inorganic biomaterials for neural interfaces,” *Adv. Mater.*, vol. 26, no. 12, pp. 1846–1885, 2014 .

[38] R. Green and M. R. Abidian, “Conducting Polymers for Neural Prosthetic and Neural Interface Applications,” *Adv. Mater.*, vol. 27, no. 46, pp. 7620–7637, 2015 .

[39] C. L. Kolarcik, S. D. Luebben, S. A. Sapp, J. Hanner, N. Snyder, T. D. Y. Kozai, E. Chang, J. A. Nabity, S. T. Nabity, C. F. Lagenaur, and X. T. Cui, “Elastomeric and soft conducting microwires for implantable neural interfaces,” *Soft Matter*, vol. 11, no. 24, pp. 4847–4861, 2015 .

[40] S. P. Lacour, G. Courtine, and J. Guck, “Materials and technologies for soft implantable neuroprostheses,” *Nat. Rev. Mater.*, vol. 1, no. 10, 16063, 2016 .

[41] H. Sawahata, S. Yamagiwa, A. Moriya, T. Dong, H. Oi, Y. Ando, R. Numano, M. Ishida, K. Koida, and T. Kawano, “Single 5 μm diameter needle electrode block modules for unit recordings in vivo,” *Sci. Rep.*, vol. 6, no. 1, 35806, 2016 .

[42] L. Luan, X. Wei, Z. Zhao, J. J. Siegel, O. Potnis, C. A. Tuppen, S. Lin, S. Kazmi, R. A. Fowler, S. Holloway, A. K. Dunn, R. A. Chitwood, and C. Xie, “Ultraflexible nanoelectronic probes form reliable, glial scar–free neural integration,” *Sci. Adv.*, vol. 3, no. 2, e1601966, 2017 .

[43] J. Liu, T. M. Fu, Z. Cheng, G. Hong, T. Zhou, L. Jin, M. Duvvuri, Z. Jiang, P. Kruskal, C. Xie, Z. Suo, Y. Fang, and C. M. Lieber, “Syringe-injectable electronics,” *Nat. Nanotechnol.*, vol. 10, no. 7, pp. 629–635, 2015 .

[44] T. Zhou, G. Hong, T. M. Fu, X. Yang, T. G. Schuhmann, R. D. Viveros, and C. M. Lieber, “Syringe-injectable mesh electronics integrate seamlessly with minimal chronic immune response in the brain,” *Proc. Natl. Acad. Sci. U. S. A.*, vol. 114, no. 23, pp. 5894–5899, 2017 .

[45] T. M. Fu, G. Hong, R. D. Viveros, T. Zhou, and C. M. Lieber, “Highly scalable multichannel mesh electronics for stable chronic brain electrophysiology,” *Proc. Natl. Acad. Sci. U. S. A.*, vol. 114, no. 47, pp. E10046–E10055, 2017 .

[46] A. Fujishiro, H. Kaneko, T. Kawashima, M. Ishida, and T. Kawano, “In vivo neuronal action potential recordings via three-dimensional microscale needle-electrode arrays,” *Sci. Rep.*, vol. 4, no. 1, 4868, 2015 .

[47] T. M. Fu, G. Hong, T. Zhou, T. G. Schuhmann, R. D. Viveros, and C. M. Lieber, “Stable long-term chronic brain mapping at the single-neuron level,” *Nat. Methods*, vol. 13, no. 10, pp. 875–882, 2016 .

[48] J. Viventi, D.-H. Kim, L. Vigeland, E. S. Frechette, J. a Blanco, Y.-S. Kim, A. E. Avrin, V. R. Tiruvadi, S.-W. Hwang, A. C. Vanleer, D. F. Wulsin, K. Davis, C. E. Gelber, L. Palmer, J. Van der Spiegel, J. Wu, J. Xiao, Y. Huang, D. Contreras, J. a Rogers, and B. Litt, “Flexible, foldable, actively multiplexed, high-density electrode array for mapping brain activity in vivo.,” *Nat. Neurosci.*, vol. 14, no. 12, pp. 1599–1605, 2011 .

[49] D. Khodagholy, J. N. Gelinas, T. Thesen, W. Doyle, O. Devinsky, G. G. Malliaras, and G. Buzsáki, “NeuroGrid: Recording action potentials from the surface of the brain,” *Nat. Neurosci.*, vol. 18, no. 2, pp. 310–315, 2015 .

[50] P. J. Rousche, D. S. Pellinen, D. P. Pivin, J. C. Williams, R. J. Vetter, and D. R. Kipke, “Flexible polyimide-based intracortical electrode arrays with bioactive

capability," *IEEE Trans. Biomed. Eng.*, vol. 48, no. 3, pp. 361–370, 2001 .

[51] C. Hassler, R. P. Von Metzen, P. Ruther, and T. Stieglitz, "Characterization of parylene C as an encapsulation material for implanted neural prostheses," *J. Biomed. Mater. Res. - Part B Appl. Biomater.*, vol. 93, no. 1, pp. 266–274, 2010 .

[52] A. T. Al-Halhouli, I. Kampen, T. Krah, and S. Büttgenbach, "Nanoindentation testing of SU-8 photoresist mechanical properties," *Microelectron. Eng.*, vol. 85, no. 5–6, pp. 942–944, 2008 .

[53] S. Budday, R. Nay, R. de Rooij, P. Steinmann, T. Wyrobek, T. C. Ovaert, and E. Kuhl, "Mechanical properties of gray and white matter brain tissue by indentation," *J. Mech. Behav. Biomed. Mater.*, vol. 46, pp. 318–330, 2015 .

[54] M. Shinohara, K. Sabra, J. L. Gennisson, M. Fink, and M. L. Tanter, "Real-time visualization of muscle stiffness distribution with ultrasound shear wave imaging during muscle contraction," *Muscle and Nerve*, vol. 42, no. 3, pp. 438–441, 2010 .

[55] K. Tybrandt, D. Khodagholy, B. Dielacher, F. Stauffer, A. F. Renz, G. Buzsáki, and J. Vörös, "High-Density Stretchable Electrode Grids for Chronic Neural Recording," *Adv. Mater.*, vol. 30, no. 15, 1706520, 2018 .

[56] I. R. Minev, P. Musienko, A. Hirsch, Q. Barraud, N. Wenger, E. M. Moraud, J. Gandar, M. Capogrosso, T. Milekovic, L. Asboth, R. F. Torres, N. Vachicouras, Q. Liu, N. Pavlova, S. Duis, A. Larmagnac, J. Vörös, S. Micera, Z. Suo, G. Courtine, and S. P. Lacour, "Electronic dura mater for long-term multimodal neural interfaces," *Science*, vol. 347, no. 6218, pp. 159–163, 2015 .

[57] J. Park, S. Choi, A. H. Janardhan, S.-Y. Lee, S. Raut, J. Soares, K. Shin, S. Yang, C. Lee, K.-W. Kang, H. R. Cho, S. J. Kim, P. Seo, W. Hyun, S. Jung, H.-J. Lee, N. Lee, S. H. Choi, M. Sacks, N. Lu, M. E. Josephson, T. Hyeon, D.-H. Kim, and H. J. Hwang, "Electromechanical cardioplasty using a wrapped elasto-conductive epicardial mesh," *Sci. Transl. Med.*, vol. 8, no. 344, 344ra86, 2016 .

[58] J. D. Yeager, D. J. Phillips, D. M. Rector, and D. F. Bahr, "Characterization of flexible ECoG electrode arrays for chronic recording in awake rats," *J. Neurosci. Methods*, vol. 173, no. 2, pp. 279–285, 2008 .

[59] D.-H. Kim, N. Lu, R. Ghaffari, Y.-S. Kim, S. P. Lee, L. Xu, J. Wu, R.-H. Kim, J. Song, Z. Liu, J. Viventi, B. de Graff, B. Elolampi, M. Mansour, M. J. Slepian, S. Hwang, J. D. Moss, S.-M. Won, Y. Huang, B. Litt, and J. A. Rogers, "Materials for multifunctional balloon catheters with capabilities in cardiac electrophysiological mapping and ablation therapy," *Nat. Mater.*, vol. 10, no. 4, pp. 316–323, 2011 .

[60] D. Qi, Z. Liu, M. Yu, Y. Liu, Y. Tang, J. Lv, Y. Li, J. Wei, B. Liedberg, Z. Yu, and X. Chen, “Highly stretchable gold nanobelts with sinusoidal structures for recording electrocorticograms,” *Adv. Mater.*, vol. 27, no. 20, pp. 3145–3151, 2015 .

[61] J. W. Jeong, W. H. Yeo, A. Akhtar, J. J. S. Norton, Y. J. Kwack, S. Li, S. Y. Jung, Y. Su, W. Lee, J. Xia, H. Cheng, Y. Huang, W. S. Choi, T. Bretl, and J. A. Rogers, “Materials and optimized designs for human-machine interfaces via epidermal electronics,” *Adv. Mater.*, vol. 25, no. 47, pp. 6839–6846, 2013 .

[62] A. M. F. Wong and J. A. Sharpe, “Representation of the Visual Field in the Human Occipital Cortex,” *Clin. Sci.*, vol. 117, pp. 208–217, 1999 .

[63] O. Kapellou, S. J. Counsell, N. Kennea, L. Dyet, N. Saeed, J. Stark, E. Maalouf, P. Duggan, M. Ajayi-Obe, J. Hajnal, J. M. Allsop, J. Boardman, M. A. Rutherford, F. Cowan, and A. D. Edwards, “Abnormal cortical development after premature birth shown by altered allometric scaling of brain growth,” *PLoS Med.*, vol. 3, no. 8, pp. 1382–1390, 2006 .

[64] T. Sekitani, Y. Noguchi, K. Hata, T. Fukushima, T. Aida, and T. Someya, “A Rubberlike Stretchable Active Matrix Using Elastic Conductors,” *Science*, vol. 321, no. 5895, pp. 1468–1472, 2008 .

[65] N. Matsuhisa, M. Kaltenbrunner, T. Yokota, H. Jinno, K. Kuribara, T. Sekitani, and T. Someya, “Printable elastic conductors with a high conductivity for electronic textile applications,” *Nat. Commun.*, vol. 6, no. 1, 7461, 2015 .

[66] S. Xu, Y. Zhang, J. Cho, J. Lee, X. Huang, L. Jia, J. a Fan, Y. Su, J. Su, H. Zhang, H. Cheng, B. Lu, C. Yu, C. Chuang, T.-I. Kim, T. Song, K. Shigeta, S. Kang, C. Dagdeviren, I. Petrov, P. V Braun, Y. Huang, U. Paik, and J. a Rogers, “Stretchable batteries with self-similar serpentine interconnects and integrated wireless recharging systems,” *Nat. Commun.*, vol. 4, no. 1, 1543, 2013 .

[67] T. Cheng, Y. Zhang, W. Y. Lai, and W. Huang, “Stretchable thin-film electrodes for flexible electronics with high deformability and stretchability,” *Adv. Mater.*, vol. 27, no. 22, pp. 3349–3376, 2015 .

[68] W. M. Choi, J. Song, D.-Y. Khang, H. Jiang, Y. Y. Huang, and J. A. Rogers, “Biaxially Stretchable ‘Wavy’ Silicon Nanomembranes,” *Nano Lett.*, vol. 7, no. 6, pp. 1655–1663, 2007 .

[69] P. Lee, J. Lee, H. Lee, J. Yeo, S. Hong, K. H. Nam, D. Lee, S. S. Lee, and S. H. Ko, “Highly stretchable and highly conductive metal electrode by very long metal nanowire percolation network,” *Adv. Mater.*, vol. 24, no. 25, pp. 3326–3332, 2012 .

[70] F. Xu and Y. Zhu, “Highly conductive and stretchable silver nanowire conductors,” *Adv. Mater.*, vol. 24, no. 37, pp. 5117–5122, 2012 .

[71] D. S. Gray, J. Tien, and C. S. Chen, “High-Conductivity Elastomeric Electronics,” *Adv. Mater.*, vol. 16, no. 5, pp. 393–397, 2004 .

[72] F. Xu, W. Lu, and Y. Zhu, “Controlled 3D buckling of silicon nanowires for stretchable electronics,” *ACS Nano*, vol. 5, no. 1, pp. 672–678, 2011 .

[73] C. F. Guo, T. Sun, Q. Liu, Z. Suo, and Z. Ren, “Highly stretchable and transparent nanomesh electrodes made by grain boundary lithography,” *Nat. Commun.*, vol. 5, no. 1, 3121, 2014 .

[74] F. Xu, X. Wang, Y. Zhu, and Y. Zhu, “Wavy Ribbons of Carbon Nanotubes for Stretchable Conductors,” *Adv. Funct. Mater.*, vol. 22, no. 6, pp. 1279–1283, 2012 .

[75] Q. Cao, H. Kim, N. Pimparkar, J. P. Kulkarni, C. Wang, M. Shim, K. Roy, M. a Alam, and J. a Rogers, “Medium-scale carbon nanotube thin-film integrated circuits on flexible plastic substrates,” *Nature*, vol. 454, no. 7203, pp. 495–500, 2008 .

[76] M. S. Lee, K. Lee, S. Y. Kim, H. Lee, J. Park, K. H. Choi, H. K. Kim, D. G. Kim, D. Y. Lee, S. Nam, and J. U. Park, “High-performance, transparent, and stretchable electrodes using graphene-metal nanowire hybrid structures,” *Nano Lett.*, vol. 13, no. 6, pp. 2814–2821, 2013 .

[77] P. Lee, J. Ham, J. Lee, S. Hong, S. Han, Y. D. Suh, S. E. Lee, J. Yeo, S. S. Lee, D. Lee, and S. H. Ko, “Highly Stretchable or Transparent Conductor Fabrication by a Hierarchical Multiscale Hybrid Nanocomposite,” *Adv. Funct. Mater.*, vol. 24, no. 36, pp. 5671–5678, 2014 .

[78] M. Park, J. Im, M. Shin, Y. Min, J. J. Park, H. Cho, S. Park, M.-B. Shim, S. Jeon, D.-Y. Chung, J. Bae, J. J. Park, U. Jeong, and K. Kim, “Highly stretchable electric circuits from a composite material of silver nanoparticles and elastomeric fibres,” *Nat. Nanotechnol.*, vol. 7, no. 12, pp. 803–809, 2012 .

[79] Liang Guo, G. S. Guvanasen, Xi Liu, C. Tuthill, T. R. Nichols, and S. P. DeWeerth, “A PDMS-Based Integrated Stretchable Microelectrode Array (isMEA) for Neural and Muscular Surface Interfacing,” *IEEE Trans. Biomed. Circuits Syst.*, vol. 7, no. 1, pp. 1–10, 2013 .

[80] S. Il Park, D. S. Brenner, G. Shin, C. D. Morgan, B. A. Copits, H. U. Chung, M. Y. Pullen, K. N. Noh, S. Davidson, S. J. Oh, J. Yoon, K. I. Jang, V. K. Samineni, M. Norman, J. G. Grajales-Reyes, S. K. Vogt, S. S. Sundaram, K. M. Wilson, J. S. Ha, R. Xu, T. Pan, T. Il Kim, Y. Huang, M. C. Montana, J. P. Golden, M. R.

Bruchas, R. W. Gereau, and J. A. Rogers, “Soft, stretchable, fully implantable miniaturized optoelectronic systems for wireless optogenetics,” *Nat. Biotechnol.*, vol. 33, no. 12, pp. 1280–1286, 2015 .

[81] K. Khanafer, A. Duprey, M. Schlicht, and R. Berguer, “Effects of strain rate, mixing ratio, and stress-strain definition on the mechanical behavior of the polydimethylsiloxane (PDMS) material as related to its biological applications,” *Biomed. Microdevices*, vol. 11, no. 2, pp. 503–508, 2009 .

[82] R. Herbert, J.-H. Kim, Y. Kim, H. Lee, and W.-H. Yeo, “Soft Material-Enabled, Flexible Hybrid Electronics for Medicine, Healthcare, and Human-Machine Interfaces,” *Materials (Basel).*, vol. 11, no. 2, 187, 2018 .

[83] S. Moon, H. K. Park, J. H. Song, S. Cho, J. C. Kim, J. Kim, H. Hwang, H. S. Kim, and U. Jeong, “Metal Deposition on a Self-Generated Microfibril Network to Fabricate Stretchable Tactile Sensors Providing Analog Position Information,” *Adv. Mater.*, vol. 30, no. 32, 1801408, 2018 .

[84] R. J. Lang, “A computational algorithm for origami design,” in *Proceedings of the twelfth annual symposium on Computational geometry - SCG ’96*, 1996, pp. 98–105.

[85] M. K. Blees, A. W. Barnard, P. a. Rose, S. P. Roberts, K. L. McGill, P. Y. Huang, A. R. Ruyack, J. W. Kevek, B. Kobrin, D. a. Muller, and P. L. McEuen, “Graphene kirigami,” *Nature*, vol. 524, no. 7564, pp. 204–207, 2015 .

[86] T. C. Shyu, P. F. Damasceno, P. M. Dodd, A. Lamoureux, L. Xu, M. Shlian, M. Shtein, S. C. Glotzer, and N. A. Kotov, “A kirigami approach to engineering elasticity in nanocomposites through patterned defects,” *Nat. Mater.*, vol. 14, no. 8, pp. 785–789, 2015 .

[87] Y. Cho, J.-H. Shin, A. Costa, T. A. Kim, V. Kunin, J. Li, S. Y. Lee, S. Yang, H. N. Han, I.-S. Choi, and D. J. Srolovitz, “Engineering the shape and structure of materials by fractal cut,” *Proc. Natl. Acad. Sci.*, vol. 111, no. 49, pp. 17390–17395, 2014 .

[88] Z. Yan, M. Han, Y. Yang, K. Nan, H. Luan, Y. Luo, Y. Zhang, Y. Huang, and J. A. Rogers, “Deterministic assembly of 3D mesostructures in advanced materials via compressive buckling: A short review of recent progress,” *Extrem. Mech. Lett.*, vol. 11, pp. 96–104, 2017 .

[89] A. Baldwin and E. Meng, “Kirigami Strain Sensors Microfabricated From Thin-Film Parylene C,” *J. Microelectromechanical Syst.*, vol. 27, no. 6, pp. 1082–1088, 2018 .

[90] A. Lamoureux, K. Lee, M. Shlian, S. R. Forrest, and M. Shtein, “Dynamic

kirigami structures for integrated solar tracking," *Nat. Commun.*, vol. 6, no. 1, 8092, 2015 .

[91] R. Zhao, S. Lin, H. Yuk, and X. Zhao, "Kirigami enhances film adhesion," *Soft Matter*, vol. 14, no. 13, pp. 2515–2525, 2018 .

[92] A. Rafsanjani, Y. Zhang, B. Liu, S. M. Rubinstein, and K. Bertoldi, "Kirigami skins make a simple soft actuator crawl," *Sci. Robot.*, vol. 3, no. 15, eaar7555, 2018 .

[93] S. Sosin, T. Zoumpoulidis, M. Bartek, L. Wang, R. Dekker, K. M. B. Jansen, and L. J. Ernst, "Free-standing, parylene-sealed copper interconnect for stretchable silicon electronics," in *2008 58th Electronic Components and Technology Conference*, 2008, pp. 1339–1345.

[94] S. Yamagiwa, M. Ishida, and T. Kawano, "Flexible parylene-film optical waveguide arrays," *Appl. Phys. Lett.*, vol. 107, no. 8, 083502, 2015 .

[95] S. Yamagiwa, M. Ishida, and T. Kawano, "Self-curling and -sticking flexible substrate for ECoG electrode array," in *2013 IEEE 26th International Conference on Micro Electro Mechanical Systems (MEMS)*, 2013, pp. 480–483.

[96] M. Ochoa, P. Wei, A. J. Wolley, K. J. Otto, and B. Ziaie, "A hybrid PDMS-Parylene subdural multi-electrode array," *Biomed. Microdevices*, vol. 15, no. 3, pp. 437–443, 2013 .

[97] H. Toda, T. Suzuki, H. Sawahata, K. Majima, Y. Kamitani, and I. Hasegawa, "Simultaneous recording of ECoG and intracortical neuronal activity using a flexible multichannel electrode-mesh in visual cortex," *Neuroimage*, vol. 54, no. 1, pp. 203–212, 2011 .

[98] B. Rubehn, C. Bosman, R. Oostenveld, P. Fries, and T. Stieglitz, "A MEMS-based flexible multichannel ECoG-electrode array.," *J. Neural Eng.*, vol. 6, no. 3, 036003, 2009 .

[99] D. H. Lim, M. H. Mohajerani, J. LeDue, J. Boyd, S. Chen, and T. H. Murphy, "In vivo Large-Scale Cortical Mapping Using Channelrhodopsin-2 Stimulation in Transgenic Mice Reveals Asymmetric and Reciprocal Relationships between Cortical Areas," *Front. Neural Circuits*, vol. 6, 11, 2012 .

[100] S. Wagner and S. Bauer, "Materials for stretchable electronics," *MRS Bull.*, vol. 37, no. 3, pp. 207–213, 2012 .

[101] M. Abdoli-Eramaki, C. Damecour, J. Christenson, and J. Stevenson, "The effect of perspiration on the sEMG amplitude and power spectrum," *J. Electromyogr. Kinesiol.*, vol. 22, no. 6, pp. 908–913, 2012 .

[102] P. Morel, E. Ferrea, B. Taghizadeh-Sarshouri, J. M. C. Audí, R. Ruff, K.-P.

Hoffmann, S. Lewis, M. Russold, H. Dietl, L. Abu-Saleh, D. Schroeder, W. Krautschneider, T. Meiners, and A. Gail, “Long-term decoding of movement force and direction with a wireless myoelectric implant,” *J. Neural Eng.*, vol. 13, no. 1, 016002, 2016 .

[103] J. M. Hahne, D. Farina, N. Jiang, and D. Liebetanz, “A Novel Percutaneous Electrode Implant for Improving Robustness in Advanced Myoelectric Control,” *Front. Neurosci.*, vol. 10, 114, 2016 .

[104] R. Merletti, A. Botter, A. Troiano, E. Merlo, and M. Alessandro, “Technology and instrumentation for detection and conditioning of the surface electromyographic signal : State of the art,” *Clin. Biomech.*, vol. 24, no. 2, pp. 122–134, 2009 .

[105] K. Nagamine, S. Chihara, H. Kai, H. Kaji, and M. Nishizawa, “Totally shape-conformable electrode/hydrogel composite for on-skin electrophysiological measurements,” *Sensors Actuators B Chem.*, vol. 237, pp. 49–53, 2016 .

[106] K. I. Jang, H. N. Jung, J. W. Lee, S. Xu, Y. H. Liu, Y. Ma, J. W. Jeong, Y. M. Song, J. Kim, B. H. Kim, A. Banks, J. W. Kwak, Y. Yang, D. Shi, Z. Wei, X. Feng, U. Paik, Y. Huang, R. Ghaffari, and J. A. Rogers, “Ferromagnetic, Folded Electrode Composite as a Soft Interface to the Skin for Long-Term Electrophysiological Recording,” *Adv. Funct. Mater.*, vol. 26, no. 40, pp. 7281–7290, 2016 .

[107] M. Wade, Y.-C. Li, and G. M. Wahl, “The Effects of Electrode Size and Orientation on the Sensitivity of Myoelectric Pattern Recognition Systems to Electrode Shift,” *Nat. Rev. Cancer*, vol. 13, no. 2, pp. 83–96, 2013 .

[108] Y. Morikawa, S. Yamagiwa, H. Sawahata, R. Numano, K. Koida, M. Ishida, and T. Kawano, “Ultrastretchable Kirigami Bioprobes,” *Adv. Healthc. Mater.*, vol. 7, no. 3, 1701100, 2018 .

[109] Y. Morikawa, S. Yamagiwa, H. Sawahata, M. Ishida, and T. Kawano, “An origami-inspired ultrastretchable bioprobe film device,” in *2016 IEEE 29th International Conference on Micro Electro Mechanical Systems (MEMS)*, 2016, pp. 149–152.

[110] R. Sun, S. C. Carreira, Y. Chen, C. Xiang, L. Xu, B. Zhang, M. Chen, I. Farrow, F. Scarpa, and J. Rossiter, “Stretchable Piezoelectric Sensing Systems for Self-Powered and Wireless Health Monitoring,” *Adv. Mater. Technol.*, vol. 4, no. 5, 1900100, 2019 .

[111] B. J. Raiteri, A. G. Cresswell, and G. A. Lichtwark, “Three-dimensional geometrical changes of the human tibialis anterior muscle and its central

aponeurosis measured with three-dimensional ultrasound during isometric contractions," *PeerJ*, vol. 4, e2260, 2016 .

[112] R. M. Palmieri, C. D. Ingersoll, and M. A. Hoffman, "The Hoffmann reflex: Methodologic considerations and applications for use in sports medicine and athletic training research," *J. Athl. Train.*, vol. 39, no. 3, pp. 268–277, 2004 .

[113] H. Steffens, P. Dibaj, and E. D. Schomburg, "In vivo measurement of conduction velocities in afferent and efferent nerve fibre groups in mice," *Physiol. Res.*, vol. 61, no. 2, pp. 203–214, 2012 .

[114] B. Katz and R. Miledi, "The Measurement of Synaptic Delay, and the Time Course of Acetylcholine Release at the Neuromuscular Junction," *Proc. R. Soc. B Biol. Sci.*, vol. 161, no. 985, pp. 483–495, 1965 .

[115] M. J. Wayner and R. Emmers, "Spinal synaptic delay in young and aged rats.," *Am. J. Physiol.*, vol. 194, no. 2, pp. 403–405, 1958 .

[116] A. M. Tan, S. Chakrabarty, H. Kimura, and J. H. Martin, "Selective corticospinal tract injury in the rat induces primary afferent fiber sprouting in the spinal cord and hyperreflexia," *J. Neurosci.*, vol. 32, no. 37, pp. 12896–12908, 2012 .

[117] C. C. Smith, R. W. P. Kissane, and S. Chakrabarty, "Simultaneous Assessment of Homonymous and Heteronymous Monosynaptic Reflex Excitability in the Adult Rat," *eneuro*, vol. 5, no. 5, pp. 1–10, 2018 .

[118] E. Dirren, J. Aebischer, C. Rochat, C. Towne, B. L. Schneider, and P. Aebischer, "SOD1 silencing in motoneurons or glia rescues neuromuscular function in ALS mice," *Ann. Clin. Transl. Neurol.*, vol. 2, no. 2, pp. 167–184, 2015 .

[119] G. M. Marcus, D. W. Chan, and R. F. Redberg, "Recollection of pain due to inappropriate versus appropriate implantable cardioverter-defibrillator shocks," *PACE - Pacing Clin. Electrophysiol.*, vol. 34, pp. 348–353, 2011 .

[120] M. R. Sohail, C. A. Henrikson, M. J. Braid-Forbes, K. F. Forbes, and D. J. Lerner, "Mortality and cost associated with cardiovascular implantable electronic device infections," *Arch. Intern. Med.*, vol. 171, pp. 1821–1828, 2011 .

[121] C. Crocini, C. Ferrantini, R. Coppini, M. Scardigli, P. Yan, L. M. Loew, G. Smith, E. Cerbai, C. Poggesi, F. S. Pavone, and L. Sacconi, "Optogenetics design of mechanistically-based stimulation patterns for cardiac defibrillation," *Sci. Rep.*, vol. 6, no. 1, 35628, 2016 .

[122] T. Bruegmann, P. M. Boyle, C. C. Vogt, T. V. Karathanos, H. J. Arevalo, B. K. Fleischmann, N. A. Trayanova, and P. Sasse, "Optogenetic defibrillation terminates ventricular arrhythmia in mouse hearts and human simulations," *J. Clin. Invest.*, vol. 126, no. 10, pp. 3894–3904, 2016 .

[123] H. Yu, W. Xiong, H. Zhang, W. Wang, and Z. Li, “A parylene self-locking cuff electrode for peripheral nerve stimulation and recording,” *J. Microelectromechanical Syst.*, vol. 23, no. 5, pp. 1025–1035, 2014 .

[124] V. S. Polikov, P. A. Tresco, and W. M. Reichert, “Response of brain tissue to chronically implanted neural electrodes,” *J. Neurosci. Methods*, vol. 148, no. 1, pp. 1–18, 2005 .

[125] B. D. Farnsworth, D. M. Talyor, R. J. Triolo, and D. J. Young, “Wireless in vivo EMG sensor for intelligent prosthetic control,” in *TRANSDUCERS 2009 - 2009 International Solid-State Sensors, Actuators and Microsystems Conference*, 2009, pp. 358–361.

[126] D. H. Kim, J. H. Ahn, H. S. Kim, K. J. Lee, T. H. Kim, C. J. Yu, R. G. Nuzzo, and J. A. Rogers, “Complementary logic gates and ring oscillators on plastic substrates by use of printed ribbons of single-crystalline silicon,” *IEEE Electron Device Lett.*, vol. 29, no. 1, pp. 73–76, 2008 .

[127] S.-W. Hwang, H. Tao, D.-H. Kim, H. Cheng, J.-K. Song, E. Rill, M. A. Brenckle, B. Panilaitis, S. M. Won, Y.-S. Kim, Y. M. Song, K. J. Yu, A. Ameen, R. Li, Y. Su, M. Yang, D. L. Kaplan, M. R. Zakin, M. J. Slepian, Y. Huang, F. G. Omenetto, and J. a. Rogers, “A Physically Transient Form of Silicon Electronics,” *Science*, vol. 337, no. 6102, pp. 1640–1644, 2012 .

[128] F. Patolsky, “Detection, Stimulation, and Inhibition of Neuronal Signals with High-Density Nanowire Transistor Arrays,” *Science*, vol. 313, no. 5790, pp. 1100–1104, 2006 .

[129] K. Nomura, A. Takagi, T. Kamiya, H. Ohta, M. Hirano, and H. Hosono, “Amorphous Oxide Semiconductors for High-Performance Flexible Thin-Film Transistors,” *Jpn. J. Appl. Phys.*, vol. 45, no. 5B, pp. 4303–4308, 2006 .

[130] S. H. Jin, J. Shin, I.-T. Cho, S. Y. Han, D. J. Lee, C. H. Lee, J.-H. Lee, and J. A. Rogers, “Solution-processed single-walled carbon nanotube field effect transistors and bootstrapped inverters for disintegratable, transient electronics,” *Appl. Phys. Lett.*, vol. 105, no. 1, 013506, 2014 .

[131] D. Khodagholy, T. Doublet, P. Quilichini, M. Gurfinkel, P. Leleux, A. Ghestem, E. Ismailova, T. Hervé, S. Sanaur, C. Bernard, and G. G. Malliaras, “In vivo recordings of brain activity using organic transistors,” *Nat. Commun.*, vol. 4, no. 1, 1575, 2013 .

[132] S. Venkatraman, J. Hendricks, Z. A. King, A. J. Sereno, S. Richardson-Burns, D. Martin, and J. M. Carmena, “In vitro and in vivo evaluation of PEDOT microelectrodes for neural stimulation and recording,” *IEEE Trans. Neural Syst.*

Rehabil. Eng., vol. 19, no. 3, pp. 307–316, 2011 .

[133] C. Ethier, E. R. Oby, M. J. Bauman, and L. E. Miller, "Restoration of grasp following paralysis through brain-controlled stimulation of muscles," *Nature*, vol. 485, no. 7398, pp. 368–371, 2012 .

[134] J. E. O'Doherty, M. A. Lebedev, P. J. Ifft, K. Z. Zhuang, S. Shokur, H. Bleuler, and M. a L. Nicolelis, "Active tactile exploration using a brain–machine–brain interface," *Nature*, vol. 479, no. 7372, pp. 228–231, 2011 .

[135] R. S. Fisher and A. L. Velasco, "Electrical brain stimulation for epilepsy," *Nat. Rev. Neurol.*, vol. 10, no. 5, pp. 261–270, 2014 .

Acknowledgments

This thesis was written in the Department of Electrical and Electronic Information Engineering, Toyohashi University of Technology.

First, I would like to express my sincere gratitude to my supervisor Associate Professor Takeshi Kawano, Department of Electrical and Electronic Information Engineering, Toyohashi University of Technology. His support through balanced guidance, encouragement, and valuable suggestions has been invaluable for me to continue this research.

I would like to express my sincere gratitude to my supervisor of the Leading Program Dr. Patrick Ruther, Microsystem Materials Laboratory, Department of Microsystems Engineering (IMTEK), University of Freiburg, Germany, Dr. Hidekazu Kaneko, Neuro-rehabilitation Research Group, Human Informatics Research Institute, National Institute of Advanced Industrial Science and Technology, Professor Hiroyuki Muto, Institute of Liberal Arts and Science, Toyohashi University of Technology and Associate Professor Rika Numano, Department of Environmental and Life Science, Toyohashi University of Technology, for their precise review.

I am grateful to Professor Oliver Paul, Microsystem Materials Laboratory, Department of Microsystems Engineering (IMTEK), University of Freiburg, Germany, for his hosting my studying abroad.

I would like to express my sincere thanks and gratitude to Professor Makoto Ishida, Professor Kazuaki Sawada, Associate Professor Kazuhiro Takahashi, Assistant Professor Daisuke Akai, for their valuable suggestions and discussions throughout my research work.

I would like to express my cordial thanks to Associate Professor Kowa Koida, Assistant Professor Hirohito Sawahata (currently Ibaraki National College of Technology), Dr. Shota Yamagiwa (currently KIOXIA Corporation), Dr. Yoshihiro Kubota (currently KIOXIA Corporation), for their valuable suggestions and discussions on device fabrication and biological experiments throughout my research work.

I am grateful to Technical Engineer Dr. Takeshi Hizawa, Mr. Mitsuaki Ashiki, Mr. Hiroyuki Takase for their technical support and advice.

I would like to express my appreciation to Research Professor Hiromu Ishii, Professor Shigeki Nakauchi, and Professor Seiichi Nakagawa for their beneficial advice.

I am thankful to my group members, Mr. Shinnosuke Idogawa, Mr. Ko Suzuki,

Mr. Koji Yamashita, Mr. Junichiro Shikata, Mr. Yuta Kotani, Mr. Yoshitaka Ito, Mr. Syuhei Tsuruhara, Mr. Kento Onozaki, Mr. Rioki Sanda, Mr. Yuta Hompo, Ms. Claire King, Mr. Yu Seikoba, Mr. Ryohei Tonai, Mr. Tomoaki Banno, Mr. Akihiro Fuchigami, Mr. Khong Yi Nern, Ms. Akemi Suzuki for their assistance and co-operation during my research work.

I am grateful to the Professors at Integrated Electronics Corse for their valuable guidance and advice.

I am also grateful to the members of the Microsystem Materials Laboratory for their advice during my study abroad at the University of Freiburg, Germany.

I am also thankful to Dr. Hajime Tsukada, Ms. Yuki Izawa, Ms. Yuri Tanaka, Ms. Chiharu Iwase and Mr. Yukiharu Ozaki for their help and activities in the Leading Program.

I would also like to thank Enago (www.enago.jp) for the English language review.

Finally, I wish to offer thanks to my family for their love and support.

January, 2020

Yusuke Morikawa

List of Publications and Awards

Journal Papers:

[1] **Y. Morikawa**, S. Yamagiwa, H. Sawahata, R. Numano, K. Koida, M. Ishida, and T. Kawano, 2018. Ultrastretchable Kirigami Bioprobes. Advanced Healthcare Materials, vol. 7, no. 3, 1701100, 2018.

[2] **Y. Morikawa**, S. Yamagiwa, H. Sawahata, R. Numano, K. Koida, M. Ishida, and T. Kawano, "Donut‐Shaped Stretchable Kirigami: Enabling Electronics to Integrate with the Deformable Muscle", Advanced Healthcare Materials, vol. 8, no. 23, 1900939, 2019

International Conference Proceedings:

[1] **Y. Morikawa**, S. Yamagiwa, H. Sawahata, M. Ishida and T. Kawano, "An origami-inspired ultrastretchable bioprobe film device", Micro Electro Mechanical Systems (MEMS), 2016 IEEE 29th International Conference on, pp. 149-152, 2016.

[2] Y. Seki, S. Yamagiwa, **Y. Morikawa**, H. Sawahata, R. Numano, M. Ishida and T. Kawano, "Hook and loop microfastener: Flexible microelectrodes tied to a nerve", Micro Electro Mechanical Systems (MEMS), 2017 IEEE 30th International Conference on, pp. 117-120, 2017.

[3] **Y. Morikawa**, S. Yamagiwa, H. Sawahata, R. Numano, K. Koida, M. Ishida and T. Kawano, "Stretchable micro-doughnuts Kirigami bioprobe", Micro Electro Mechanical Systems (MEMS), 2018 IEEE 31th International Conference on, pp. 186-189, 2018.

[4] K. Yamashita, H. Sawahata, S. Yamagiwa, **Y. Morikawa**, R. Numano, K. Koida, T. Kawano, "Sewing Bioprobe", Micro Electro Mechanical Systems (MEMS), 2019 IEEE 32th International Conference on, pp. 621-624, 2019.

[5] **Y. Morikawa**, S. Ayub, O. Paul, T. Kawano and P. Ruther, "Highly stretchable Kirigami structure with integrated LED chips and electrodes for optogenetic experiments on perfused hearts", IEEE Solid State Sensors, Actuator and Microsystems (Transducers)'19, pp. 2484-2487, Berlin, Germany, 2019.

Domestic Conference Proceedings:

[1] **Y. Morikawa**, S. Yamagiwa, H. Sawahata, M. Ishida and T. Kawano, "Ultra-stretchable bioprobe film", The 63th JSAP Spring Meeting, March 2016.

[2] **Y. Morikawa**, S. Yamagiwa, H. Sawahata, M. Ishida and T. Kawano, "Characterizations of Kirigami-based ultrastretchable bioprobe film device", The 33th Sensor Symposium, October 2016.

[3] Y. Seki, S. Yamagiwa, **Y. Morikawa**, H. Sawahata, R. Numano, K. Koida, M. Ishida and T. Kawano, "Hook and loop microfastener-based nerve recording device", The 78th JSAP Autumn Meeting, September 2017.

[4] Y. Seki, S. Yamagiwa, **Y. Morikawa**, H. Sawahata, R. Numano, K. Koida, M. Ishida and T. Kawano, "Microfasteners for flexible nerve recording device", The 34th Sensor Symposium, October 2017.

[5] **Y. Morikawa**, S. Yamagiwa, H. Sawahata, R. Numano, K. Koida and T. Kawano, "Stretchable donut-shaped Kirigami electrode for the ECG signal recording", The 80th JSAP Autumn Meeting, September 2019.

[6] **Y. Morikawa**, S. Yamagiwa, H. Sawahata, R. Numano, K. Koida and T. Kawano, "Fabrication and characterizations of stretchable donut-shaped Kirigami EMG electrode", The 36th Sensor Symposium, November 2019.

Awards and Honors:

[1] December 2014, Graduation Research Presentation Award, Toyohashi University of Technology.

[2] October 2016, Encouragement award, The 33th Sensor Symposium.

[3] March 2017, Students Award, Toyohashi University of Technology.

[4] April 2017, IEEJ Excellent Presentation Award, IEEJ.

[5] January 2018, The 31th IEEE International Conference on Micro Electro Mechanical Systems, MEMS 2018, Student Paper Award Finalist.

[6] March 2019, Students Award, Toyohashi University of Technology.

Appendix A
Process chart
(Kirigami bioprobe device)

No	Step	Condition	Time	Remarks
1	Parylene evaporation	Dimer 9.0 g Furnace 690°C Chamber gauge 135 °C Vaporizer 175 °C Vacuum 25 Pa		For 5 μm
2	O_2 ashing	Gas flow: O_2 40 sccm RF: 150 W Mode: Plasma	60 sec	Hydrophilization
3	Sputtering	Ti: RF 0.15/0 kW, 1.0 Pa Pt: RF 0.15/0 kW, 1.0 Pa	20 min × 2 15 min	Cooling 10 min between each sputtering
4	Photolithography	Bake before coating 80°C OAP 1st 1000 rpm 2nd 4000 rpm OFPR 52cp 1st 1000 rpm 2nd 4000 rpm Prebake 80 °C Exposure LI: 20 Developing NMD-3 Rinse DIW Post bake 80 °C	10 min 5 s 25s 10s 45s 2 min 1 min 50 s 2 min 10 min	
5	Pt etching	CCP-RIE Gas flow: Ar 20 sccm Pressure: 4.0 Pa RF power: 50W	10 min × 2	
6	O_2 ashing	Gas flow: O_2 40 sccm RF: 150 W Mode: RIE Gas flow: CF_4 40 sccm RF: 150 W Mode: RIE	15 min×2 15 min	Resist etching Ti etching
7	Parylene evaporation	Same as No. 1		
8	Sputtering	Ti: RF 0.15/0 kW, 1.0 Pa	20 min × 3	Cooling 10 min between

				each sputtering
9	Photolithography	Same as No. 4		
10	O_2 ashing	Gas flow: CF_4 40 sccm RF: 150 W Mode: RIE	10 min × 2	Ti etching
		Gas flow: O_2 40 sccm RF: 150 W Mode: RIE	20 min × 5	Parylene etching
		Gas flow: CF_4 40 sccm RF: 150 W Mode: RIE	10 min	Ti etching
11	Release	Using ethanol		